Karlsruher Mineralogische und Geochemische Hefte
Schriftenreihe des Instituts für Mineralogie und Geochemie
36

Annett Steudel

Selection strategy and modification of layer silicates for technical applications

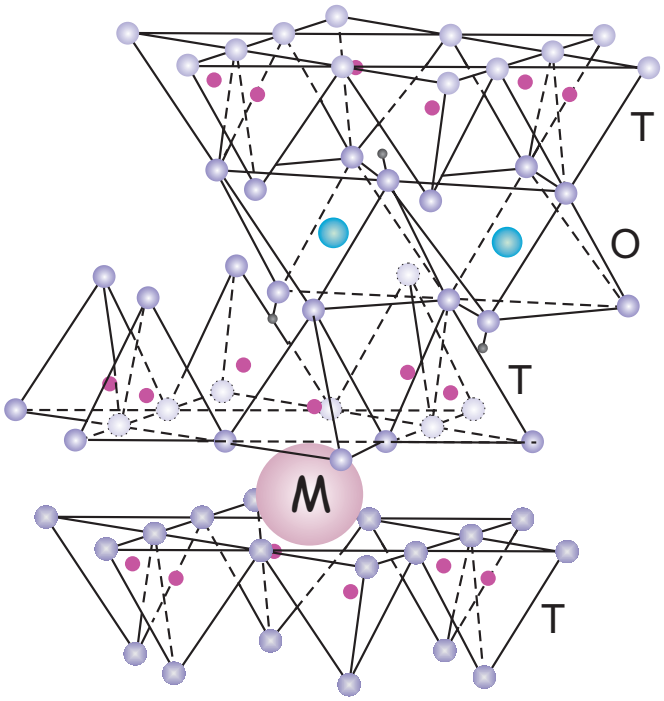

universitätsverlag karlsruhe

Annett Steudel

Selection strategy and modification of layer silicates for technical applications

Karlsruher Mineralogische und Geochemische Hefte

Schriftenreihe des Instituts für Mineralogie und Geochemie,

Universität Karlsruhe (TH)

Band 36

Selection strategy and modification of layer silicates for technical applications

by
Annett Steudel

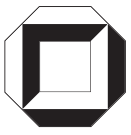

universitätsverlag karlsruhe

Dissertation, Universität Karlsruhe (TH),
Fakultät für Bauingenieur-, Geo- und Umweltwissenschaften
Tag der mündlichen Prüfung: 05.12.2008
Referenten: Prof. Dr. W. Smykatz-Kloss, Prof. Dr. H. Stanjek

Anschrift der Schriftleitung:
Karlsruher Mineralogische und Geochemische Hefte
Institut für Mineralogie und Geochemie
Universität Karlsruhe (TH)
D – 76128 Karlsruhe

Anschrift des Autors:
Annett Steudel
Kompetenzzentrum für Materialfeuchte (CMM)
Universität Karlsruhe
c/o
Forschungszentrum Karlsruhe GmbH
Institut für Funktionelle Grenzflächen (IFG)
Hermann-von-Helmholtz-Platz 1
D – 76344 Eggenstein-Leopoldshafen

Impressum

Universitätsverlag Karlsruhe
c/o Universitätsbibliothek
Straße am Forum 2
D-76131 Karlsruhe
www.uvka.de

Universitätsverlag Karlsruhe 2009
Print on Demand

ISSN: 1618-2677
ISBN: 978-3-86644-352-5

Vorwort

In diesem Rahmen möchte ich zuerst Herrn Prof. Dr. Rolf Nüesch, der leider unerwartet von uns gegangen ist, für die Vergabe der Arbeit danken.

Ein besonderer Dank gebührt Frau Dr. Katja Emmerich. Sie hat mich vor und während meiner Promotion am Forschungszentrum Karlsruhe großartig unterstützt. Besonders dankbar bin ich für die gute Zusammenarbeit, für die zahlreichen gemeinsamen Gespräche und Diskussionen, sowie für die kritische Durchsicht des Manuskripts.

Ebenfalls sehr dankbar bin ich für die Unterstützung von Herrn Dr. Peter G. Weidler. Ich möchte mich für die gute Zusammenarbeit und für die lehrreichen Diskussionen sowie für die Durchsicht einiger Manuskriptteile bedanken

Herrn Dr. Reinhard Kleeberg (Institut für Mineralogie, TU Bergakademie Freiberg) möchte ich auch ganz herzlich danken. Er stellte mir den Kontakt zum Institut für Technische Chemie, Bereich Wasser- und Geotechnologie am Forschungszentrum Karlsruhe her. Zudem möchte ich mich auch für die Nutzung der McCrone Mühle sowie für die Diskussionen am Telefon und auf Tagungen bedanken.

Bedanken möchte ich mich auch bei Herrn Prof. Dr. Werner Smykatz-Kloss (Institut für Mineralogie und Geochemie – IMG, Universität Karlsruhe), dass er nach dem Ableben von Herrn Prof. Dr. Rolf Nüesch das Hauptreferat übernommen hat.

Für die Übernahme des Korreferats möchte ich mich bei Herrn Prof. Dr. Helge Stanjek (RWTH Aachen) bedanken.

Für die Unterstützung und Betreuung während meines Forschungsaufenthalts am Forschungsinstitut TNO in Eindhoven (Niederlande) möchte ich mich bei Herrn Lawrence F. Batenburg und Herrn Dr. Hartmut R. Fischer bedanken. Zudem bedanke ich mich auch bei allen Kollegen, die mich während dieser Zeit unterstützt haben.

Während meines Auslandsaufenthalts wurde ich finanziell vom Deutschen Akademischen Austauschdienst (DAAD) durch ein Doktorandenstipendium (D/06/45522; Referat 312) unterstützt. Dafür möchte ich mich ganz herzlich bedanken.

Frau Dr. Melissa Denecke (Institut für Nukleare Entsorgung, Forschungszentrum Karlsruhe) möchte ich für die Durchsicht meines Manuskripts in Bezug auf die englische Sprache danken.

Sehr dankbar bin ich auch Herrn Dr. Michael Plötze (ETH Zürich) und seinen Kollegen für die Durchführung von KAK-Messungen mit Ammoniumacetat sowie für die Einweisung in diese Methode.

Herrn Stefan Heißler, Herrn Dr. Werner Faubel und Herrn Dr. Frank Friedrich (IR-Cluster) vom Institut für Technische Chemie, Bereich Wasser- und Geotechnologie danke ich für die Einführung in die Infrarotmesstechnik, sowie für die Hilfestellungen bei der Interpretation der FTIR Daten.

Für die Durchführung der zahlreichen Röntgenfluoreszenzmessungen danke ich Frau Nora Groschopf und ihren Kollegen am Institut für Geowissenschaften und Mineralogie der Universität Mainz ganz herzlich.

Frau Marita Heinle und Frau Gudrun Hefner vom Institut für Technische Chemie, Bereich Wasser- und Geotechnologie am Forschungszentrum Karlsruhe bin ich sehr dankbar für die Durchführung der zahlreichen ICP-OES Messungen und Fluoridmessungen.

Frau Dr. Ute Schwotzer und ihren Kollegen (Labor für Wasser und Umwelt, Forschungszentrum Karlsruhe) danke ich für die chemische Analyse des Hectorits.

Frau Cherifa Bachir, Herrn Dr. Markus Hauser-Fuhlberg sowie Herrn Volker Jansen danke ich für die Durchführung der BET-Messungen.

Besonders danken möchte ich meiner lieben Zimmerkollegin Doreen Rapp für die zahlreichen Gespräche und Diskussionen, sowie für die Durchsicht einiger Manuskriptteile.

Frau Dr. Felicitas Wolters danke ich ganz lieb für die Hilfestellungen am Anfang meiner Promotion hinsichtlich Durchführung der Schichtladungsmessungen und Berechnung von Strukturformeln.

Frau Dr. Durime Buqezi-Ahmeti, meiner Zimmerkollegin Kerstin Petrick und Maike Krauß danke ich für die Hilfe im Labor. Lorenzo Rieg danke für die Hilfe bei der Literaturrecherche und für Hilfsarbeiten im Labor.

Danken möchte ich auch Frau Astrid Biedermann sowie Herrn Dr. Hartmut Gliemann und Herrn Dr. Rainer Schuhmann.

Rosa Rotondo möchte ich auch ganz lieb danken für die großartige Unterstützung bei der Betreuung meiner Tochter Pietrina. Sie ermöglichte mir dadurch mehrere längere Arbeitstage im Labor.

Zu ganz besonderem Dank bin ich auch meinen Eltern Eva-Maria Steudel und Wolfgang Steudel verpflichtet, die mich während meiner gesamten Studien- und Promotionszeit großartig unterstützten und mir somit vieles ermöglicht haben.

Ein ganz großer Dank gebührt Frank Friedrich, der immer für mich da war, mich tatkräftig unterstützt hat und meine Launen meisterhaft ertragen hat.

Ich möchte diese Arbeit meiner Tochter Pietrina widmen.

Table of Contents

Summary

Clay minerals show a large variability, e.g., in chemical composition, morphology, layer charge, layer charge density and exchange behaviour. Thus, for technical applications a comprehensive characterisation is essential. The focus of this work was the structural characterisation and modification of different and apparently similar clay minerals, allowing technical applications. A couple of possibilities are described subsequently.

In this study, samples were selected with respect to their layer charge and morphology. Sixteen bulk materials were pre-selected, which contained either swellable clay minerals (smectite, vermiculite) or non-swelling clay minerals (kaolinite, illite, sepiolite, palygorskite, magadiite). A comprehensive characterisation of all materials was carried out. Based on these results, several samples were selected for further investigations.

The investigations revealed that the cation exchange behaviour of vermiculite is a function of the charge and size of the interlayer cations, which is differed from the exchange behaviour of smectite. Thus, special attention was paid to the cation exchange behaviour of vermiculite. The selected vermiculite was ground and purified. However, the exchange of all interlayer cations against Cu-triethylenetetramine (Cu-trien) was solely possible after the homoionic exchange with monovalent cations such as Na^+ and Li^+. Based on these results, vermiculite can be used to prepare pillared clays, which will upgrade the spectrum of charge density remarkably.

Another topic of this work was a comprehensive determination of layer and edge charge and exchange properties of clay minerals, because the exchange capacity is the most important feature of swellable clay minerals. Changes in exchange properties of layer charge reduced materials of two homoionic smectites were investigated. The influence of Li^+ and Cu^{2+} in the interlayer was compared. The CEC of the materials decreased with increasing temperature. The decreasing CEC is combined with an apparent reduced layer charge. The amount of Li^+ or Cu^{2+}, which moved into the octahedral vacancies or in the hexagonal cavities of the tetrahedral sheet of the smectite, is equivalent to the CEC reduction. The decrease of CEC of Volclay was larger over the temperature range compared to the Indian Bentonite. Therefore, more Li^+ or Cu^{2+} moved into the structure of the Volclay smectite than in the smectite from the Indian Bentonite. Both smectites have the same octahedral charge, but exhibit different layer charge, tetrahedral charge and iron content. One or more of these three parameters constrained the migration of Li^+ or Cu^{2+} in the structure. Layer charge reduction can be used to prepare material with a certain layer charge. However, materials of the same apparent layer charge differed in their hydration behaviour.

In addition to the layer charge, the charges of the edges were investigated using the purified and fractionated material of two smectites (Volclay, Indian Bentonite), one vermiculite and one sepiolite. Two methods were used to determine the edge charge of these clay minerals:

1) Cation exchange capacity (CEC) was measured in dependency of pH using Cu-triethylenetetramine (Cu-trien) in the pH range between 4 and 11.

2) Hydroxyl groups were exchanged by fluoride in the second method for edge charge determination.

Both methods give similar results and can be applied to estimate the charge of the edges, however, with some constraints for vermiculite and sepiolite. HCl, NaOH and NaF attack the octahedral and tetrahedral sheets. The release of elements occurs incongruently for acids or bases and congruently for NaF. The ion release is too low (< 0.01% related to the concentration in the structural formula) to cause substantial dissolution of the clay minerals. Thus, clay minerals remain nearly unaltered during the exchange reactions. The characterisation of the edges can be used as screening method prior to edge modification to achieve a homogeneous and oriented arrangement by edge-to-edge or surface-to-edge connections e.g., in clay polymer-nanocomposites.

A further topic in this study concerned the modification of swellable and non-swelling clay minerals with mineral acids, e.g., HCl and H_2SO_4. The alteration of the clay mineral structures was controlled by the individual character of each mineral. Acid treatment resulted in a successive dissolution of the octahedral and tetrahedral sheets. The number of substitutions by Mg^{2+} or Fe^{3+} in the octahedral and by Al^{3+} in the tetrahedral sheet of the clay minerals promoted the dissolution of the layers and the formation of X-ray amorphous silica phase. The results showed that the release of the octahedral cations occurred in the following order: $Mg^{2+} > Fe^{3+} > Al^{3+}$, i.e. dioctahedral clay minerals are more stable against acid attack than trioctahedral clay minerals.

The acid treated swellable clay minerals like smectite retain the ability to exchange cations. The acid treated materials possessed a simple chemical composition with layered structure. These materials have a low CEC and a high specific surface area (A_S), resulting in a lower charge density compared to the raw materials. Thus, the acid treated materials have the ability to adsorb very large organic molecules (e.g., dodecylamine), which can be used as precursor for clay-polymer nanocomposites.

The observed development of micropores and increase in specific surface area implied the delamination of the non-swellable clay minerals, which occurred more slowly in contrast to smectite and vermiculite. The protonation of the SiO-groups of the tetrahedral sheet at low

pH (< 2) resulted in a delamination of the particles. The protons caused a positive charge of the layers, which tend to repulse each other.

An adjusted residual Al_2O_3 content was proved applicable for a reliable estimation of residual kaolinite and smectite in bulk materials after acid treatment. The calculated amount of these minerals was comparable with the XRD quantification and with the CEC measurements in relation to smectite content.

Acid treatment of non-swelling layer silicates can be used to produce materials with a simple chemical composition that retain the layered structure. These materials consisted of delaminated particles resulting in a high specific surface area. Thus, they can be used as precursor for clay-polymer nanocomposites. Polymer incorporation will be investigated in the near future.

Zusammenfassung

Tonminerale weisen eine große Variabilität z.B. in Bezug auf chemische Zusammensetzung, Morphologie, Schichtladung, Ladungsdichte und Austauschverhalten auf, so dass eine umfassende Charakterisierung für technische Anwendungen unumgänglich ist. Der Fokus dieser Arbeit lag deshalb auf der Analyse und auf der Modifizierung von unterschiedlichen und scheinbar ähnlichen Tonmineralien in Hinblick auf mögliche Anwendungen. Somit werden nachfolgend einige Anwendungsmöglichkeiten beschrieben.

Die Auswahl der Minerale erfolgte in Bezug auf Schichtladung und Morphologie. Daher wurden sechzehn Proben ausgewählt, die quellfähige (Smectit, Vermiculit) oder nicht quellfähige Tonminerale (Kaolinit, Illit, Sepiolith, Palygorskit, Magadiit) enthalten. Alle vorliegenden Proben wurden umfassend charakterisiert und für die nachstehenden Untersuchungen verwendet.

Während der Charakterisierung zeigte sich, dass sich das Kationenaustauschverhalten des ausgewählten Vermiculits deutlich von dem des Smectits unterscheidet, obwohl beide zu den quellfähigen Tonmineralen zählen. Daher wurde das Kationenaustauschverhalten näher untersucht. Der vorliegende Vermiculit wurde aufgemahlen und gereinigt, aber erst durch die Belegung mit einwertigen Kationen wie Na^+ oder Li^+ war es möglich, alle Zwischenschichtkationen gegen Cu-Triethylentetramin (Cu-Trien) auszutauschen. Aufgrund dieser Ergebnisse kann Vermiculit zur Herstellung von „Pillared Clays“ verwendet werden. Somit wird die Bandbreite der Ladungsdichte deutlich erweitert.

Ein weiteres Thema der Arbeit beinhaltet Schichtladungs- und Kantenladungsmessungen sowie Austauscheigenschaften von Tonmineralien. In diesem Zusammenhang wurde das Austauschvermögen von ladungsreduzierten Smectiten untersucht. Zur Herstellung dieser Materialien wurden zwei homoionisch belegte Smectite verwendet. Neben dem Austauschverhalten wurde der Einfluss von Li^+ und Cu^{2+} in der Zwischenschicht untersucht. Die Kationenaustauschkapazität (KAK) der Materialien sinkt mit zunehmender Temperatur und ist verbunden mit einer scheinbaren Ladungsreduzierung. Der Anteil an Li^+ und Cu^{2+}, das in die freien Stellen der Oktaederschicht oder in die hexagonalen Löcher der Tetraederschicht wandert, ist äquivalent zur Reduzierung der KAK. Die KAK des Volclays sinkt schneller über den ausgewählten Temperaturbereich als die des Indischen Bentonits. Das bedeutet, das mehr Li^+ und Cu^{2+} in die Smectitstruktur des Volclays, als in die des Indischen Bentonits wandert. Beide Smectite haben die gleiche Oktaederladung, aber sie unterscheiden sich in ihrer Schichtladung, im Anteil an tetraedrischer Ladung und in der Höhe des Eisengehaltes. Einer oder mehrere dieser drei Parameter behindern das

Einwandern von Li^+ und Cu^{2+} in die Smectitstruktur. Damit bietet die gezielte Schichtladungsreduzierung die Möglichkeit, Materialien mit einer definierten Schichtladung herzustellen. Proben mit einer scheinbar gleichen Schichtladung können dabei unterschiedliche Dehydratationseigenschaften aufweisen.

Zusätzlich zur Schichtladung wurde die Kantenladung untersucht. Verwendet wurde das gereinigte und fraktionierte Material von zwei Smectiten (Volclay, Indischer Bentonit), von einem Vermiculit und einem Sepiolith. Zwei Methoden wurden zur Bestimmung der Kantenladung an diesen Tonmineralien angewandt:

1) Die erste Methode basiert auf einer Kationenaustauschreaktion. Die KAK wurde in Abhängigkeit vom pH-Wert, unter Verwendung von Cu-Triethylentetramin (Cu-Trien) im Bereich von pH 4 bis pH 11, gemessen.

2) Die zweite Methode basiert auf einer Anionenaustauschreaktion. Dabei wurden die an den Kanten befindlichen Hydroxylgruppen gegen Fluorid ausgetauscht.

Beide Methoden führen zu ähnlichen Ergebnissen und können zur Bestimmung der Kantenladung angewandt werden. Allerdings gibt es Einschränkungen für Vermiculit und Sepiolith. HCl, NaOH und NaF können die Oktaeder- und Tetraederschicht angreifen. Die Freisetzung der Elemente erfolgt dabei inkongruent für Säuren und Basen und kongruent für NaF. Die freigesetzte Ionenkonzentration ist zu niedrig (< 0,01% bezogen auf den Gehalt pro Formeleinheit), um die Tonminerale erheblich aufzulösen. Somit bleiben diese während der Austauschreaktionen nahezu unverändert. Die Charakterisierung der Kanten kann als Vorstufe zu deren Modifizierung verwendet werden, um eine homogene und orientierte Verteilung über Kanten-Kanten- oder Flächen-Kanten-Vernetzungen, z.B. in Tonmineral-Polymer-Nanokompositen zu erreichen.

Diese Arbeit beschäftigt sich außerdem mit der Modifizierung von quellfähigen und nicht quellfähigen Tonmineralien mit Hilfe mineralischer Säuren (HCl, H_2SO_4). Die Änderung der Tonmineralstruktur wird durch den individuellen Charakter jedes Minerals kontrolliert. Im Allgemeinen verursacht Säurebehandlung die Auflösung der Oktaeder- und Tetraederschichten. Die Anzahl der Substitutionen durch Mg^{2+} oder Fe^{3+} in der Oktaederschicht und durch Al^{3+} in der Tetraederschicht bewirken die Freisetzung der Oktaederkationen und die Bildung einer Silicatphase. Die Ergebnisse zeigen, dass die Oktaederkationen in folgender Reihenfolge freigesetzt werden: $Mg^{2+} > Fe^{3+} > Al^{3+}$, das heißt dioktaedrische Tonminerale sind stabiler gegenüber Säureangriffe als trioktaedrische Tonminerale.

Säurebehandelte, quellfähige Tonminerale wie Smectite haben noch immer die Fähigkeit Kationen auszutauchen. Die erhaltenen Materialien verfügen über eine einfache chemische

Zusammensetzung und behalten ihre Schichtstruktur. Die Materialien haben eine niedrige KAK und eine große spezifische Oberfläche (A_s) und somit eine niedrigere Ladungsdichte verglichen mit dem Ausgangsmaterial. Folglich haben diese Materialien die Fähigkeit große organische Moleküle (z.B. Dodecylamin) zu adsorbieren und können als Vorstufe für Tonmineral-Polymer-Nanokompositen verwendet werden.

Die Entwicklung der Mikroporen und der spezifischen Oberfläche unterstützt die Delamination der nicht quellfähigen Tonmineralien, die deutlich langsamer als bei Smectiten und Vermiculiten erfolgt. Die Protonierung der SiO-Gruppen der Tetraederschicht bei niedrigem pH (< 2) bewirkt die Delamination der Partikel. Die Protonen verursachen eine positive Ladung der Schichten, wodurch sich diese gegenseitig abstoßen.

Der korrigierte, noch vorhandene Al_2O_3-Gehalt wurde zur Abschätzung des verbleibenden Kaolinit- und Smectitgehaltes im Gesamtmaterial genutzt. Der berechnete Gehalt von diesen Mineralien ist vergleichbar mit der Quantifizierung und mit den KAK-Messungen in Bezug auf den Smectitgehalt.

Auch die Säurebehandlung von nicht quellfähigen Schichtsilicaten kann zur Herstellung von Materialien mit einer einfachen chemischen Zusammensetzung genutzt werden, die ihre Schichtstruktur behalten. Diese Materialien bestehen aus delaminierten Partikeln, wodurch eine große spezifische Oberfläche erzeugt wird. Somit können diese als Vorstufe für Tonmineral-Polymer-Nanokompositen genutzt werden. Die Einarbeitung dieser Materialien in Polymere wird in näherer Zukunft untersucht.

1 Introduction

Layer silicates like kaolinite, smectite, vermiculite, illite and sepiolite are natural nanoparticles and are characterised by their layered structure. They are of great importance for the improvement of material properties, e.g., in clay-polymer composites (Pinnavaia and Beall, 2001).

Clay minerals are low-cost materials, which differ in their morphological, mineralogical, chemical and thermal properties, as well as in their exchange behaviour. Because of their large variability (e.g., in chemical composition), clay minerals are often used in their natural form in many industrial applications like ceramic industries, food industries, chemical industries and paper industries (Jasmund and Lagaly, 1993). However, it is not possible in all cases to use the minerals without modification (e.g., acid or alkali treatment).

For example, acidic activated clay minerals are widely used as bleaching earth (Siddiqui, 1968; Komadel et al., 1997; Ravichandran and Sivasankar, 1997; Kaufhold, 2001), catalysts (Adams, 1987) or catalyst supports (Rhodes et al., 1991; Rhodes and Brown, 1992) and in carbonless copying paper (Fahn and Fenderl, 1983).

Alkali treatment (e.g., by soda) of bentonites with a high content of smectite affects the structure of smectite crystals by changing the layer sequence (Lagaly et al., 1981). Soda activated bentonites are used for geotechnical applications. The production of molecular sieves (MCM-41) by NaOH treatment of smectite or kaolinite (Kang et al., 2005; Adjdir et al., 2008) also uses clay minerals as a low cost Si^{4+} and Al^{3+} source.

In the following paragraphs, the key aspects of the present work are described with some important references. Each chapter starts with an introduction, including several references.

This work dealt with two topics. The first focused on the selection and characterisation of natural layer silicates. The second part included the modification of clay minerals for technical applications.

Several clay minerals were selected for the investigation with respect to layer charge and morphology. The origin of the selected clay minerals is shown in Chapter 2. A detailed description to chemical pre-treatment and particle size separation are also included in this chapter. Morphological and surface investigations were carried out using environmental scanning electron microscopy (ESEM) and specific surface area investigation (BET). Qualitative and quantitative phase analysis was done using X-ray diffraction analysis (XRD). A number of chemical analytical methods (X-ray fluorescence analysis (XRF), inductively coupled plasma - optical emission spectroscopy (ICP-OES), determination of cation

exchange capacity (CEC) and layer charge (ξ)) were applied to investigate the chemical composition, the interlayer composition and the exchange behaviour. The thermal properties were investigated using simultaneous thermal analysis (STA). Fourier transform infrared spectroscopy (FTIR) was used to characterise the clay near structural order. A detailed description of all these methods is given in Chapter 3. Summaries of these methods are also given in Chapter 5 and 6.

Results of the comprehensive basic characterisation are described in Chapter 4 and include description of morphological, mineralogical, chemical and thermal properties, as well as description of the exchange behaviour. Special attention was paid to the cation exchange reactions of vermiculite and to the thermal transformation of sepiolite.

An important feature of smectite, vermiculite and sepiolite is their ability to exchange cations. Layer and edge charge and exchange properties of clay minerals are presented in Chapter 5.

Several layer charge reduced materials were prepared according to the methods of Madejová et al. (1996). Two smectites with different layer charges and tetrahedral charges were used to investigate the correlation between chemical composition resulting layer charges and charge reduction by heat treatment.

Homoionically exchanged samples of smectite, vermiculite and sepiolite were investigated to characterise the edges. Two methods were used to characterise the edge charge of these materials. One method was the measurement of the CEC in dependency of pH (Kaufhold, 2001; Amman et al. 2005). The second method was the exchange of hydroxyl groups against fluoride (Weiss et al., 1956).

Chapter 6 includes the structural modification of several clay minerals with mineral acids (Madejová et al., 1998; Snäll and Liljefors, 2000; Yebra-Rodríquez et al., 2003; Makó et al., 2006; Önal and Sarikaya, 2007; Superti et al., 2007). The aim was to prepare materials with a simple chemical composition, which have a similar layered morphology as the untreated material and which still have the ability to adsorb organic molecules. The investigations resulted in detailed information on the stability of each clay mineral during acid treatment.

The goal of this work was the structural characterisation and modification of different and apparent similar clay minerals, allowing technical applications.

References

Adams J. M. (1987) Synthetic organic chemistry using pillared, cation-exchanged and acid-treated montmorillonite catalysts – A review. Applied Clay Science **2**, pp. 309-342.

Adjdir M., Ali-Dahmane T., Friedrich F., Scherer T. and Weidler P. (2008) The synthesis of Al-MCM-41 from Volclay – a low-cost Al and Si source. Microporous and Mesoporous Materials, submitted.

Amman L., Bergaya F. and Lagaly G. (2005) Determination of the cation exchange capacity of clays with copper complexes revisited. Clay Minerals **40**, pp. 441-453.

Fahn R. and Fenderl K. (1983) Reaction products of organic dye molecules with acid-treated montmorillonite. Clay Minerals **18**, pp. 447-458.

Jasmund K. and Lagaly G. (1993) Tonminerale und Tone: Struktur, Eigenschaften, Anwendung und Einsatz in Industrie und Umwelt. Steinkopff Verlag, Darmstadt, pp. 490.

Kang F., Wang Q. and Xiang S. (2005) Synthesis of mesoporous Al-MCM-41 materials using metakaolin as aluminium source. Materials Letters **59**, pp. 1462-1429.

Kaufhold S. (2001) Untersuchungen zur Eignung von natürlich alterierten sowie mit Oxalsäure aktivierten Bentoniten als Bleicherde für Pflanzenöle. Dissertation, Fakultät für Bergbau, Hüttenwesen und Geowissenschaften der Rheinisch-Westfälischen Technischen Hochschule Aachen, pp. 178.

Komadel P., Janek M., Madejová J., Weekes A. and Breen C. (1997) Acidity and catalytic activity of mildly acid-treated Mg-rich montmorillonite and hectorite. Journal of Chemical Society, Faraday Transactions. **93**(23), pp. 4207-4210.

Lagaly G., Müller-Vonmoos M., Kahr G. and Fahn R. (1981) Vorgänge bei der Sodaaktivierung von Bentoniten am Beispiel eines Bentonits von Neuseeland. Keramische Zeitschrift **33**(5), pp. 278-283.

Madejová J., Bujdák J., Janek M. and Komadel P. (1998) Comparative FT-IR study of structural modifications during acid treatment of dioctahedral smectites and hectorite. Spectrochimica Acta **54**, pp. 1397-1406.

Madejová J., Bujdák J., Petit S. and Komadel P. (1996) Effects of chemical composition and temperature of heating on the infrared spectra of Li-saturated dioctahedral smectites - (II) Near-infrared region. Clay Minerals **35**(5), pp. 753-761.

Makó E., Senkár Z., Kristóf J. and Vágvölgyi V. (2006) Surface modification of mechanochemically activated kaolinites by selective leaching. Journal of Colloid and Interface Science **294**, pp. 362-370.

Önal M. and Sarikaya Y. (2007) Preparation and characterization of acid-activated bentonite powders. Powder Technology **172**, pp. 14-18.

Pinnavaia T. J. and Beall G. W. (2001) Polymer-Clay-Nanocomposites. Wiley Series in Polymer Science, John Wiley and Sons Inc., pp. 349.

Ravichandran J. and Sivasankar B. (1997) Properties and catalytic activity of acid-modified montmorillonite and vermiculite. Clays and Clay Minerals **45**(6), pp. 854-858.

Rhodes C. N. and Brown D. R. (1992) Structural characterisation and optimisation of acid-treated montmorillonite and high-porosity silica supports for $ZnCl_2$ alkylation catalysts. Journal of the Chemical Society, Faraday Transactions. **88**, pp. 2269-2274.

Rhodes C. N., Franks M., Parkes G. M. B. and Brown D. R. (1991) The effect of acid treatment on the activity of clay supports for $ZnCl_2$ alkylation catalysts. Journal of Chemical Society, Chemical Communications, pp. 804-807.

Siddiqui M. K. H. (1968) Bleaching Earths. Pergamon Press, Oxford, 32

Snäll S. and Liljefors T. (2000) Leachability of major elements from minerals in strong acids. Journal of Geochemical Exploration **71**, pp. 1-12.

Superti G. B., Olivereira E. C. and Pastore H. O. (2007) Aluminium magadiite: An acid solid layered material. Chemistry of Material **19**, pp. 4300-4315.

Weiss A., Mehler A., Koch G. and Hofmann U. (1956) Über das Anionenaustauschvermögen der Tonmineralien. Zeitschrift für anorganische und allgemeine Chemie **284**, pp. 247-271.

Yebra-Rodríquez A., Martín-Ramos J. D., Del Rey F., Viseras C. and López-Galindo A. (2003) Effect of acid treatment on the structure of sepiolite. Clay Minerals **38**, pp. 353-360.

2 Material

2.1 Samples

Natural nanoparticles (layer silicates) were used for the investigations. They differ in morphology and layer charge. The selected clay minerals belong to the 2:1 layer silicates, with the exception of kaolinite, belonging to the 1:1 layer silicates. The layers of 1:1 layer silicates consist of one tetrahedral and one octahedral sheet, whereas in 2:1 layers silicates one octahedral sheet is surrounded by two tetrahedral sheets. These layers are connected by exchangeable interlayer cations. Seven bentonites with a high content of smectite, one vermiculite, one illite, one sepiolite and three kaoline samples with a high content of kaolinite (Table 2.1) were selected. Additionally, a synthetic magadiite was used.

Table 2.1 Origin of samples.

Sample ID	Name	Source	Supplier
1_Calci	Bentonite (“Calcigel”)	Germany	Südchemie
2_EXM757	Montmorillonite	Germany	Südchemie
3_SWy-2	Bentonite	USA	Source Clay Repository of the Clay Mineral Society
4_Vol	Bentonite (“Volclay”)	USA	Südchemie
5_WYO	Bentonite	USA	Wyoming
6_IndBent	Bentonite (“Indian Bentonite”)	India	F. Wolters / Institute for Foundry Technology (IFG)
7_NHec	Hectorite (natural)	USA	Elementis
8_Verm	Vermiculite	Russia	S. Dultz / University Hannover
9_Illite	Illite (“Arginotec NX”)	France	Commercial product of B.+M. Nottenkämper
10_PangelS9	Sepiolite (“Pangel S9”)	Spain	Tolsa
11_Pansil	Sepiolite (“Pansil”)	Spain	Tolsa
12_Palygorskite	Palygorskite (“Smectagel”)	Spain	Tolsa
13_Pol	Kaoline (“Polwhite B”)	GB	IMERYS
14_Kaolex	Kaoline (“Kaolex BN”)	USA	Kentucky-Tennessee Clay Company
15_Rogers	Kaoline (“Rogers”)	USA	Kentucky-Tennessee Clay Company
16_Mag	Magadiite (synthetic)	---	TNO Science and Industry (NL)

2.2 Chemical pre-treatment and particle size separation

Purification of the bulk material

Grain size separation of the bulk material is necessary to concentrate single phases like smectite or sepiolite with small particle sizes. With decreasing particle size the charge of their edges increase. For characterisation, the edges of the material must be coated homoionically (e.g., with sodium).

Before separation of the fractions, disturbing phases such as carbonates, iron oxides and organic matter have to be removed. These substances may cause aggregation of the clay minerals and hence an inadequate dispersion of the sample powders. The elimination of these impurities was performed according to, Mehra and Jackson (1960), Tributh and Lagaly (1986a), Emmerich (2000) and Wolters et al. (2008).

Only four samples (4_Vol, 6_IndBent, 8_Verm, 10_PangelS9) from the 16 samples were selected for purification and separation because it was necessary for the subsequent investigations a) characterisation of layer charge reduced materials and b) characterisation of the edges (Chapter 5). These four samples were treated in the same way to make sure that they underlie the same reaction conditions. The removal of impurities was done in the following order:

1. removal of carbonates
2. removal of iron oxides
3. removal of organic matter.

300 g of these samples were purified. For the purification, every sample was divided into three beakers. A detailed description of the methods is given below.

Removal of carbonate

Calcium carbonate was dissolved by an acetic acid-acetate buffer and then was washed with sodium chloride and deionised water.

$$CaCO_3 + 2CH_3COOH \rightarrow Ca(CH_3COO)_2 + CO_2 + H_2O$$

Equipment:

Scale, beaker (5 l), graduated cylinder, graduated flask, pH-meter, magnetic stirrer, centrifuge tube (600 ml), centrifuge (Multifuge 3S-R Heraeus/Kendro).

Chemicals:

Sodium acetate p.a. (CH_3COONa), acetic acid (100%) p.a. (CH_3COOH), sodium chloride p.a. (NaCl), deionised water.

Brief description:

The acetate buffer was prepared by mixing a 2 M sodium acetate solution with a 2 M acetic acid solution at a ratio of 2 to 1. The buffer was adjusted to pH 4.8. A volume between 1000 and 1500 ml of the buffer was added to 100 g sample in a beaker and then stirred without heating. The amount of carbonate in the samples was very low; therefore the reaction was finished after one day. Thereafter, the suspensions were centrifuged and washed 4 times with a 1 M sodium chloride solution and one time with deionised water. The centrifugation was carried out at 4500 rpm between 10 and 30 min.

Error:

The pH of the acetate buffer should not be lower than 4.8 to avoid solution of the clay mineral structure. Carbonates such as dolomite and siderite cannot be dissolved during short reaction times.

Removal of iron oxide

The removal of iron oxide and aluminium hydroxides was performed with a buffered dithionite-citrate system according to Mehra and Jackson (1960). The reduction of iron oxide occurred by sodium dithionite and the complexation of Fe^{2+} by sodium citrate. Sodium hydrogen carbonate was used to buffer the consumed hydrogen ions during the oxidation of sodium dithionite to sodium sulphate.

Equipment:

Scale, beaker (5 l), graduated cylinder, graduated flask, pH-meter, magnetic stirrer, centrifuge tube (600 ml), centrifuge (Multifuge 3S-R Heraeus/Kendro).

Chemicals:

Tri-sodium citrate p.a. ($C_6H_5O_7Na_3$), sodium hydrogen carbonate p.a. ($NaHCO_3$), sodium dithionite LAB ($Na_2S_2O_4$), sodium chloride p.a. (NaCl), deionised water.

Brief description:

The carbonate free samples were transferred together with about 1 l 0.3 M Tri-sodium-citrate-dehydrate solution into a beaker. Subsequently, 125 ml sodium hydrogen carbonate solution were added. The suspensions were stirred and 25 g of the solid dithionite carefully added. After one day the suspensions were centrifuged and washed again 4 times with a 1 M NaCl solution and one time with deionised water. The centrifugation was carried out at 4500 rpm between 10 and 30 min.

Error:

Short reaction times might cause insufficient removal of iron oxides and aluminium hydroxides.

Removal of organic matter

Organic matter can be destroyed effectively by hydrogen peroxide.

Equipment:

Beaker (5 l), graduated cylinder, magnetic stirrer, centrifuge tube (600 ml), centrifuge (Multifuge 3S-R Heraeus/Kendro).

Chemicals:

Hydrogen peroxide 30% p.a. (H_2O_2), sodium chloride p.a. (NaCl), deionised water.

Brief description:

After the removal of iron oxides the washed sample was resuspended in 1000 ml deionised water. Between 270 and 360 ml hydrogen peroxide solution were added stepwise to the suspension to adjust the suspension to 5%. The amount of organic matter in the used samples was very low; therefore the reaction was finished under stirring in one day. In case of intense reaction, the solutions have to be adjusted to 10% in order to remove the remaining organic matter. After reaction the suspensions were centrifuged and washed 4 times with a 1 M sodium chloride solution and one time with deionised water. The centrifugation was carried out at 4500 rpm between 20 and 30 min. In some cases it is necessary to add solid sodium chloride to the suspensions after the removal of organic matter for centrifugation. The hydrogen peroxide ions affected the buoyancy of the clay particles therefore the overlaying solution is cloudy. Solid sodium chloride caused a faster sedimentation of the material.

Error:

Residues of organic matter may remain.

Separation of < 2 µm and < 0.2 µm fractions

The < 2 µm fraction was obtained by sedimentation from the purified samples and the < 0.2 µm fraction by centrifugation of the < 2 µm fraction.

After purification the samples are saturated with sodium, as this is important for stable dispersions. However, high amounts of sodium chloride in the suspensions caused a coagulation of the particle; therefore it is important to dilute the suspensions with deionised water.

The settling time for the particles follows the Stoke's law. The settling time for a particle in a gravity field is determined by:

$$t = \frac{18\eta_0}{(\rho - \rho_0)\cdot g} \cdot \frac{h}{d^2} \qquad (1).$$

The gravity force (g) is included in the calculation. The calculation of the settling time for sedimentation in the centrifuge is based on the following formula:

$$t = \frac{18\eta_0}{(\rho - \rho_0)\cdot 4r\pi^2 \cdot (R/60)^2} \cdot \frac{dh}{d^2} \qquad (2).$$

The centrifugal acceleration [$4r\pi^2 \cdot (R/60)^2$] with the radius of the particles (r) and R/60 as rotation per minute is included in the calculation. The formulas (1) and (2) include the viscosity of water (η_0), the density of the clay mineral (ρ) and water (ρ_0), the equivalent particle diameter (d) and the settling distance of the particles (h). Sedimentation of the particles depends on the temperature (Stoke's law), as $\eta_0 = f(T)$. With increasing temperature the sedimentation time decreases.

Particle size separation

Equipment:

Beaker (5 l), timer, thermometer, U-shaped glass pipe, water jet pump, centrifuge (Multifuge 3S-R Heraeus/Kendro), buckets, tube for dialysis (Nadir, pore size 2.5 nm), plastic pots, drying oven, agate mill or agate mortar.

Chemicals:

Sodium chloride p.a. (NaCl), deionised water.

Brief description:

After purification, the samples were mixed with deionised water and then shaken overnight. The homogeneous suspensions were transferred into 5 l beakers, diluted so that the concentration of solid was less than 1% and stirred. The sedimentation of the < 2 µm fraction was calculated in dependence of the temperature. For temperature measurement, a thermometer was placed into a beaker of water. One part of the < 2 µm suspensions was coagulated with sodium chloride to reduce the volume. The second half of the < 2 µm suspension was centrifuged at a constant temperature (20 °C) and a constant rotation speed of 4500 rpm for 25 min to obtain the < 0.2 µm fraction. The time for centrifugation was calculated according to Tributh and Lagaly (1986b). After centrifugation, the < 0.2 µm suspensions were also coagulated with sodium chloride. The suspensions were transferred into a dialysis tube, which was treated beforehand in boiling deionised water twice for few hours to remove organic molecules. The material was dialysed until the conductivity of the surrounding deionised water was below 5 µS/cm. This process is time consuming and needs between 2 and 3 weeks. During dialysis, it is very important to change the deionised water constantly (every day or every second day). The chloride free samples were dried at 60 °C. After drying, the fractions were milled slightly in an agate mortar.

Error:

Larger particles (e.g., > 2 µm) were separated when the centrifugation or sedimentation time was too short. Acceleration and deceleration also have an influence on the separation of the < 0.2 µm fraction, both cause that larger particles are in the fraction < 0.2 µm.

The purification of four samples (~ 300 g) and the separation of the < 2 µm and < 0.2 µm fraction took between 5 and 6 months.

References

Emmerich K. (2000) Die geotechnische Bedeutung des Dehydroxylierungsverhalten quellfähiger Tonminerale. Dissertation, Veröffentlichungen des Instituts für Geotechnik (IGT) der ETH Zürich, pp. 143.

Mehra O. P. and Jackson M. L. (1960) Iron oxide removal from soils and clays by a dithionite-citrate-system buffered with sodium bicarbonate. 7th National Conference on Clays and Clay Minerals, pp. 317-327.

Tributh H. and Lagaly G. (1986a) Aufbereitung und Identifizierung von Boden- und Lagerstättentonen Teil I - Aufbereitung der Proben im Labor. GIT Fachzeitschrift für das Laboratorium **30**, pp. 524-529.

Tributh H. and Lagaly G. (1986b) Aufbereitung und Identifizierung von Boden und Lagerstättentonen Teil II - Korngrößenanalyse und Gewinnung von Tonsubfraktionen. GIT Fachzeitschrift für das Laboratorium **30**, pp. 771-776.

Wolters F., Lagaly G., Kahr G., Nueesch R. (†) and Emmerich K. (2009) A comprehensive characterisation of dioctahedral smectites. Clays and Clay Minerals, in print.

3 Methods

Table 3.1 Techniques to characterize clay minerals.

Method		Sample preparation and reactants	direct information	indirect information
Morphology and surface				
Environmental Scanning Electron Microscopy	ESEM	Powder (without sputtering)	Morphology	-
Determination of Specific surface area	BET	Powder	Specific surface area	-
Mineralogy				
X-Ray Diffraction Analysis	XRD	Powder sample texture sample	Qualitative and quantitative phase analysis	Chemical composition
Chemical composition				
X-Ray Fluorescence Analysis	XRF	Melting pellets	Chemical composition	Structural formula of pure phases
Inductively Coupled Plasma - Optical Emission Spectroscopy	ICP-OES	Supernatant solutions	Soluble and / or exchanged cations	Cation exchange capacity
Short range order				
Fourier Transform Infrared Spectroscopy	FTIR / DRIFT	KBr-Pellets, Powder with KBr	Structural information	Structural changes
Thermal reactions				
Simultaneous Thermal Analysis	STA	Powdered samples	Phase transformations, release of water	Clay mineral content, thermal stability
Exchange behaviour and interlayer composition				
Determination of Cation Exchange Capacity	CEC	Copper-triethylenetetramine, Ammonium acetate	Cation exchange capacity	Layer charge
Determination of Layer Charge	ξ	Alkylammonium ions	Layer charge	Calculation of the cation exchange capacity

Table 3 summarized the methods used to characterise the clay materials. A brief description of each technique follows.

3.1 Morphology and surface

3.1.1 Environmental Scanning Electron microscopy (ESEM)

The examination of the particle morphology was carried out by ESEM using a Philips ESEM XL 30 FEG. This kind of SEM uses a chamber atmosphere of 1 to 3 Torr water vapour instead of high vacuum. The microscope is equipped with a special gaseous secondary electron detector (GSE-detector); therefore sputtering of the samples with conductive material (gold, carbon) is not necessary. Thus, it can be used for the investigation of moisture sensitive samples like clay minerals. A chamber atmosphere of 1 Torr and an acceleration voltage of 20 KV were applied.

There are two kinds of sample holders for the sample preparation. One of the holders consists of aluminium, which was laminated with an adhesive carbon foil. Very small amounts of the clay powder were dispensed onto the foil. The other holder was made of polished brass and was coated with a 0.1% clay suspension.

3.1.2 Specific Surface Area (BET)

Nitrogen adsorption using a Quantochrome Autosorb-1MP and BET evaluation was used to measure specific surface area (A_S or SSA in most literature) (Brunauer et al., 1932; Gregg and Sing, 1991). Eleven adsorption points in the range of p/p_0 from 0.05 to 0.32 were used for BET evaluation. The outgassing conditions were 24 h under vacuum at 95 °C. The t-plot according to De Boer et al. (1966) was applied to estimate the external specific surface area (A_E) and the part of the micro-pore area (A_{MP}).

3.2 Mineralogy

3.2.1 X-Ray Diffraction Analysis (XRD)

XRD was used to determine the mineralogical composition of the natural materials. For the XRD measurements, powder and textured samples of the starting materials were prepared. The measurements were performed on a Siemens D5000 diffractometer (CuKα radiation) equipped with a graphite secondary monochromator. The powder patterns were recorded between 5 and 80° 2θ (step size: 0.03° 2θ / 5 s). The texture patterns were recorded between 2 and 35° 2θ (step size: 0.03° 2θ / 3 s).

Qualitative phase analysis was done by using Brindley and Brown (1980) and Diffrac Plus Evaluation software (Version 10.0) by Bruker. Quantification of the samples was done with the Rietveld program “Autoquan” (Agfa NDT Pantak Seifert GmbH_Co.KG, Version 2.7.0.0).

The Rietveld method is based on a mathematical method, which calculates a pattern by the optimisation of crystal structure parameters, profile form functions and background functions (Kleeberg and Bergmann, 2002). This calculated diffractogram is adjusted by increment match to the measured pattern until the best match within defined limits is achieved.

The Rietveld analysis is a method for a stepwise refinement of crystal structures. According to Kleeberg and Bergmann (2002) every point in the diffractogram is specified by the following equation:

$$Y_i = \sum_p \left[S_p \sum_k \left[L_i P_k H_k \left| F_k \right|^2 G\left(\Delta\Theta_{ik}\right) Po_k \right] \right] + y_{bi} \qquad (3)$$

(Kleeberg and Bergmann, 2002)

with
	y_i	intensity on the measuring point i
	S_p	scale factor (proportional to the scattering volume of the phase)
	L_k, P_k, H_k	Lorentz-, polarisation and. multiplicity factors (line k)
	$\|F_k\|^2$	structure factor
	$G(\Delta\Theta_{ik})$	profile function
	Po_k	preferred orientation correction
	y_{bi}	intensity of the background.

"Autoquan" combines the analytical properties of the plain Rietveld program BGMN with a simple operator interface.

Powder samples

Equipment:

Sample holder, glass slide, sandpaper.

Brief description:

The powder was loosely filled into the sample holder. The powder was then carefully pressed with the long edge of a glass slide into the sample holder; therefore removing surplus material at the same time. The result of the preparation is the formation of a plane surface. This surface was roughed up with sandpaper to obtain a random orientation. The powder sample should be prepared without force or textures.

An internal standard (ZnO) was used to quantify the content of amorphous SiO_2 in the powder samples. For these measurements, the powdered samples were mixed with ZnO in the ratio of 9:1.

Textured samples

Equipment:

Glass slide (diameter: 25 mm), cap (5 ml), spatula, ultrasonic finger, desiccator.

Chemicals:

Ethylene glycol, deionised water.

Brief description:

100 mg powder (tip of a spatula) were dispersed in 3 ml deionised water. The suspension was treated with the ultrasonic finger (UP 200s, Dr Hielscher GmbH; amplitude: 90; cycle: 0.9) for one minute to yield a homogenous suspension. Afterwards the dispersion was pipetted onto a glass slide and dried at room temperature under atmospheric conditions. The textured sample was measured air-dried, after treatment with ethylene glycol and after heating at 375 °C and 550 °C for 3 h. For the treatment with ethylene glycol the oriented sample was stored for 2 or 3 days in a desiccator with ethylene glycol.

3.3 Chemical composition

3.3.1 X-Ray Fluorescence Analysis (XRF)

The chemical composition of the natural materials and the < 2 µm and < 0.2 µm fractions were investigated with XRF. The chemical composition of the crude sample is important to verify the quantification of the sample. From quantitative analysis by XRD, the chemical composition of the sample based on stoichiometric formula of the phases can be calculated and compared with the measured chemical composition of the XRF analysis. The investigation of the fractions is important for the calculation of the structural formula of clay minerals.

In XRF the sample X-ray emission following excitation with primary radiation source is detected. The emitted X-ray radiation can be used to identify elements in the sample and quantity their amount. The wavelengths of the emitted fluorescence radiation are specified for an element atomic number in the sample. The concentration of selected elements can be determined by the intensity of their characteristic radiation on the basis of extensive adjustment and calibration programs. The concentration range differs from element to element and ranges from 0.0001 to 100%.

The XRF analyses were performed on a MagiXPRO spectrometer from Phillips equipped with a rhodium X-ray tube (stimulation power: 3.2 KW) using molten pellets. The loss of ignition was determined separately by storing a sample in an oven at 1000 °C for 2 h. The

general measurement conditions of the basic elements are listed in Table 3.2. The calibration occurs with 59 international standards.

Table 3.2 General measurement conditions of the elements indicated.

Element	Line	Crystal	Detector	kV	mA
Na	Kα	PX1	Flow	32	100
Mg	Kα	PX1	Flow	32	100
Al	Kα	PE002	Flow	32	100
Si	Kα	PE002	Flow	32	100
P	Kα	Ge111	Flow	32	100
K	Kα	LiF200	Flow	32	100
Ca	Kα	LiF200	Flow	32	100
Ti	Kα	LiF200	Duplex	37	86
Cr	Kα	LiF200	Duplex	57	56
Mn	Kα	LiF220	Duplex	57	56
Fe	Kα	LiF220	Duplex	60	53
Ni	Kα	LiF200	Duplex	57	56

As the samples strongly differ in their amount of SiO_2, they were measured with two different programs. One was used for samples with SiO_2 contents larger than 60% and the other for materials with SiO_2 amounts below 60%. The information about the possible sources of error of the calibration of the basic elements for SiO_2-rich and SiO_2-poor samples is listed in Tables 3.3 and 3.4.

Table 3.3 Possible calibration sources of error for SiO_2-rich samples (SiO_2 > 60%).

Oxide	Average concentration [%]	Root mean square [%]	Testing time [s]	Calibration range [%]	Root mean square relative [%]
SiO_2	75	0.28	12	60 - 100	0.4
TiO_2	0.55	0.01	8	0.01 - 1	1.8
Al_2O_3	12	0.11	24	3 - 22	0.9
Fe_2O_3	3.7	0.04	8	0.2 - 8	1.1
MnO	0.16	0.003	16	0.01 - 0.4	1.9
MgO	1.35	0.04	24	0.05 - 3	3.0
CaO	4	0.04	8	0.10 - 9	1.0
Na_2O	4.5	0.04	24	0.10 - 10	0.9
K_2O	6.9	0.05	8	0.6 - 13	0.7
P_2O_5	0.7	0.006	16	0.01 - 1.4	0.9

Table 3.4 Possible calibration sources of error for SiO_2-poor samples (SiO_2 < 60%).

Oxide	Average concentration [%]	Root mean square [%]	Testing time [s]	Calibration range [%]	Root mean square relative [%]
SiO_2	52	0.19	12	32 - 60	0.4
TiO_2	1.9	0.027	8	0.02 – 4.0	1.4
Al_2O_3	16	0.18	24	0.2 - 30	1.1
Fe_2O_3	9	0.09	8	0.2 - 20	1.0
MnO	0.17	0.006	16	0.03 – 0.2	3.5
MgO	20	0.09	24	0.04 - 50	0.5
CaO	8	0.08	8	0.1 - 16	1.0
Na_2O	4.5	0.06	24	0.02 - 10	1.3
K_2O	6.6	0.06	8	0.01 - 14	0.9
P_2O_5	0.75	0.01	12	0.01 – 1.5	1.3
Cr_2O_3	0.12	0.005	12	0.002 - 3.5	4.2
NiO	0.12	0.002	12	0.002 – 0.35	1.7

Equipment:

Scale, Pt crucible, smelting gadget (Vulcan 4MA, HD Electronic).

Chemicals:

Lithium tetraborate (Spectromelt A10, Merck) supra pure ($Li_2B_4O_7$).

Brief description:

The powdered samples were mixed with lithium tetraborate in the ratio of 1 to 7. The whole material was molten stepwise in a platinum crucible at a smelting apparatus. After this procedure, the melt was transferred into a platinum jacket and cooled.

Error:

Too short of smelting time lead to incomplete melting.

3.3.2 Inductively Coupled Plasma - Optical Emission Spectroscopy (ICP-OES)

ICP-OES is a method to quantify ion concentrations in solutions. The general parameters of the spectrometer used are listed in Table 3.5. The characteristic wavelengths for the analysed ions are listed in Table 3.6.

Table 3.5 Experimental parameters for ICP-OES.

ICP emission spectrometer	Jobin Yvon, Typ JY 38 S		
Monochromator	Czerny-Turner-specification (1 m)		
HF generator	Frequency	MHz	40.68
	Power	W	1000
ICP torch	Demountable torch with ceramic injector tube		
Nebulizer chamber	Cyclone chamber		
Nebulizer	Burgener Graphit Mira Mist HS		
Argon gas flow	Plasma	[l/min]	14.0
	Protective gas	[l/min]	0.2
	Nebulizer gas	[l/min]	0.71
Sample uptake	Flexible-tube pump	[ml/min]	1

ICP-OES was used for the investigation of the exchanged cations in the supernatant solution after the exchange with copper triethylenetetramine and the determination of the released cations during the acid treatment.

The analysis of the exchanged cations (Na^+, Ca^{2+}, Mg^{2+}, K^+ and Li^+) gives information about the kind of interlayer cations and about the ratio of the cations relative to one another. The amount of all exchanged cations allows verification of the measured cation exchange capacity. The investigation of the cations released by acid treatment (Si^{4+}, Al^{3+}, $Fe^{2+/3+}$, Mg^{2+}, Ca^{2+}, Na^+, K^+ and Li^+) gives information about the kind and amount of cations within the octahedral sheet and interlayer.

Table 3.6 Characteristic wavelengths of the analysed ions.

Elements	Wavelength [nm]
Silicon	251.611
Aluminium	259.940
Magnesium	279.533
Calcium	317.933
Iron	396.152
Sodium	589.592
Lithium	670.784
Potassium	766.490

Equipment:

Vials (20 ml), pipette (5 ml) with pipette tips, centrifuge (Multifuge 3S-R Heraeus/Kendro), ICP emission spectrometer (Jobin Yvon, Typ JY 38 S).

Chemicals:

Nitric acid (65%) supra pure (HNO_3), deionised water.

Brief description:

For the analysis of the exchanged cations, 5 ml of the supernatant solution were separated with a pipette from the clay. The solution was filled in vials and diluted with deionised water in 1:1, 1:2 or 1:4. Volumes, expending on concentration, estimated from the cation exchange capacity. Between 10 and 20 ml solution were used for the measurements of Na^+, Ca^{2+}, Mg^{2+}, K^+ and Li^+. 10 to 20 µl of nitric acid were added to stabilise the solutions. Nitric acid caused decolourisation of the solutions, indicating that means the copper complex was destroyed (Section 3.6.1).
For the determination of the released cations (Si^{4+}, Al^{3+}, $Fe^{2+/3+}$, Mg^{2+}, Na^+, Ca^{2+}, K^+, Li^+), the solutions, as separated from the residual clay fragments, were analysed by ICP-OES after centrifugation. The supernatant solutions were concentrated; therefore the solutions were diluted with dilution factors 1:20, 1:50 or 1:100 using deionised water. 20 ml solution were used in the analyses.

Error:

The precision of the method averaged 3 meq/100g for the sum of the exchanged cations. In some cases, the amount of the exchanged cations is higher than the measured cation exchange capacity, because the sample contained small amounts of soluble phases such as carbonates and sulphates. These phases also released elements like Ca.

3.4 Short range order

3.4.1 Fourier Transform Infrared Spectroscopy (FTIR)

FTIR spectroscopy can be divided into near infrared (NIR: 8000 - 4000 cm^{-1}), mid infrared (MIR: 4000 - 400 cm^{-1}) and far infrared spectroscopy (FIR: 400 - 50 cm^{-1}). The MIR spectroscopy represents an established tool for the study of the clay lattice and of molecules adsorbed on its surface. In this work only MIR spectroscopy was used to characterise the structural changes of the natural and treated materials.

The FTIR spectra were recorded on a Bruker IFS66/S spectrometer equipped with a deuterated triglycinesulfonate detector (DTGS) using pressed KBr-pellets (3 mg sample : 300 mg KBr). Thirty-two scans were recorded in the 4000 - 400 cm^{-1} spectral range with a resolution of 4 cm^{-1}. A pure KBr pellet was used for the background measurement.

For a higher resolution of the bands in the Si-O stretching region (1200 - 800 cm^{-1}), a diffuse reflectance accessory from Spectra-Tech Inc. (DRIFT) was used. In this case, 2.5 mg of a sample was mixed with 500 mg KBr. The powder was filled loosely into a sample cup to obtain a random orientation. The FTIR spectra were recorded on a Bruker IFS66/S spectrometer equipped with a DTGS detector. Sixty-four scans were recorded in the 4000 - 400 cm^{-1} spectral range with a resolution of 4 cm^{-1} using a scanner velocity of 4 kHz and a lens aperture of 12 mm. After preparation and prior to the measurement, each sample was flushed with nitrogen for 2 min. Pure KBr was used for the background measurements. The raw DRIFT data were transformed using Kubelka-Munk-Function (Kubelka and Munk, 1931; Petrick, 2007).

3.5 Thermal reactions

3.5.1 Simultaneous Thermal Analysis (STA)

STA is a combination of thermogravimetry (TG) with differential thermal analysis (DTA) or differential scanning calorimetry (DSC). In this study, the thermal behaviour of the clay minerals was observed with a STA 449 C Jupiter from Netzsch connected to a quadrupole mass spectrometer (QMS 403 C, Aeolos, Netzsch). The samples were measured at a defined temperature-time-program with a defined heating rate. The mass spectrometer allows detection of released gases such as H_2O, CO_2 and SO_2 during the measurements.

STA is a very useful device to characterise clay minerals. The STA measurements give information on the release of water, phase transformations, decomposition and recrystallisation. Clay minerals contain various kinds of water, which are released at different temperature ranges. First dehydration occurs up to temperatures of around 300 °C. During dehydration adsorbed water from the mineral surfaces and interlayer water from inner surfaces are released in endothermic reactions. The dynamic mass loss during the dehydration is equal to the static determined water content at 200 °C. Dehydroxylation occurs between 330 and 850 °C. During dehydroxylation structural water associated with hydroxyl groups migrates out of the mineral structure. The dehydroxylation temperature gives information about the stability of clay minerals and is associated with the structure of the octahedral layer of dioctahedral 2:1 clay minerals (Drits et al., 1995). Fe-rich smectites such as nontronite release structural water between 450 and 600 °C, while Al-rich smectites release water between 500 and 750 °C. Trioctahedral smectites (Mg-rich) such as saponite or hectorite show dehydroxylation temperatures between 750 and 850 °C (Smykatz-Kloss, 1974; Köster and Schwertmann, 1993; Niederbudde, 2002).

In some cases, the dehydroxylation temperature gives additional information about the crystallinity of the clay mineral, especially of kaolinite (Jasmund and Lagaly, 1993). The dehydration and the dehydroxylation can occur stepwise, which is dependent on the clay mineral structure. In addition to dehydration and dehydroxylation, some clay minerals like sepiolite and palygorskite show the release of coordinated water, which is connected to the edges of the octahedral sheet (Frost and Ding, 2003).

It is also possible to obtain qualitative information on impurities like sulphides, sulphates and carbonates from STA measurements. In addition, the STA is connected to a pulse box (PulseTa, Netzsch) for injection of CO_2, which can be used for the quantification of carbonates. At the end of the measurements a 30 min isotherm segment is added. During this time a defined content of CO_2 (0.5 ml) is injected by the pulse box and repeated 5 times. On the basis of the averaged peak area detected and the peak area from the dynamic segment, the CO_2 volume of the sample can be calculated. The amount of carbonate in the sample can be calculated using the density of CO_2 and the molar mass of the identified carbonates (calcite, dolomite, magnesite and siderite). The different carbonates can be identified from their different decomposition temperatures (Smykatz-Kloss, 1974).

At the beginning of the measurement, there is an added isotherm 10 minute segment to redress the balance. Prior to the measurements, the samples are stored above a saturated magnesium nitrate solution ($Mg(NO_3)_2$, 53%) in a desiccator to equilibrate at constant humidity conditions. The general measurement conditions are listed in Table 3.7.

Table 3.7 Experimental parameters.

Dynamic segment	Start temperature	[°C]	35
	End temperature	[°C]	1100
	Heating rate	[K/min]	10
Isotherm segment at	35 °C	[min]	10
	1100 °C	[min]	30
Atmosphere	Nitrogen as protective gas	[ml/l]	20
	Synthetic air as purging gas	[ml/l]	50
Sample holder	Pt/Rh		
Crucible	Pt/Rh with lid		
Reference material	Empty crucible with lid		
Net weight	Bentonite	[mg]	100
	Kaolinite, vermiculite, illite, magadiite	[mg]	50
	Sepiolite, palygorskite	[mg]	30

According to Wolters and Emmerich (2007), the dehydroxylation temperature of dioctahedral smectites can be used to estimate the cis- and trans-vacant character. The proportions were determined by fitting the MS curve of water (m/e = 18) using PeakFit

program 4.0 from Jandel Scientific. Details of the peak fit program are described in the appendix. The fitting procedure includes the determination of the peak areas in the range of 350 and 900 °C. The ratio between the areas of the peaks reflects the ratio between trans- and cis-vacant layers. The border between both varieties was defined by 600 °C according to Drits et al. (1998). The limits of the amount of cis- and trans-vacant layers in the dioctahedral smectites are displayed in Table 3.8 (Wolters and Emmerich, 2007).

Table 3.8 Limits of the amount of cis- and trans-vacant layers in the dioctahedral smectites according to Wolters and Emmerich (2007).

	Cis-vacant (cv)	Cis-trans-vacant (cv/tv)	Trans-cis-vacant (tv/cv)	Trans-vacant (tv)
Percentage area [w] of MS curve of water (m/e=18) [%]	w_{cv} 100 - 75	w_{cv} 74 - 50	w_{cv} 49 - 25	w_{cv} 24 - 0
	w_{tv} 0 - 25	w_{tv} 26 - 50	w_{tv} 51- 75	w_{tv} 76 - 100

3.6 Exchange behaviour and interlayer composition

3.6.1 Cation Exchange Capacity (CEC)

Clay minerals have the ability to adsorb cations, which can be exchanged by other cations. This ability can be described as cation exchange capacity (CEC), which is an important property of clay minerals, especially of smectites and vermiculites.

The total CEC consists of two parts: the exchange capacity of the interlayer and that of the edges. The exchange of the interlayer cations is independent of the pH-value, whereas the amount of cations, which are located at the edges, strongly depends on pH. For example, smectites have up to 20% charge at their edges. This means 20% of the total exchange capacity measured at pH 7 results from the edges (Lagaly, 1981). In the acid pH range, the edges are positively charged; thus the edges do not contribute to the measured CEC. In the basic pH range, the edges are negatively charged; therefore in this pH range all edges contribute to the CEC.

The CEC of the natural materials was measured with 0.01 M copper triethylenetetramine solution according to Meier and Kahr (1999). The concentration of copper triethylenetetramine in the supernatant solution was measured by photometry. The CEC is determined by:

$$CEC\left[meq/100g\right] = \frac{2 \cdot \left[\left(0.01mol/l \cdot 5ml - c_{Cu-Trien} \cdot \left(5ml + 10ml\right)/1000\right) \cdot 100\right]}{m_{dried}\left[g\right]} \quad (4)$$

$$m_{dried}\left[g\right] = m_{netweight}\left[g\right] \cdot \frac{\left(100 - w_{\min}\left[\%\right]\right)}{100\%} \quad (5)$$

$$c_{Cu-Trien}[mmol/l] = a \cdot Abs \quad (6)$$

with

$c_{Cu\text{-}Trien}$	concentration of copper triethylenetetramine
m_{dried}	mass of dried sample
$m_{net\ weight}$	mass of air dried sample
w_{min}	water content
a	slope of the calibration curve
Abs	measured absorbance of the overlaying solution.

The calculation of the CEC includes the volume of deionised water (10 ml) and copper triethylenetetramine (5 ml), as well as the molarity of copper triethylenetetramine. For the calculation of the CEC, it is necessary to measure the water content of the clay sample, because the CEC refers to the dry sample weight. The water content can be measured with simultaneous thermal analysis or by oven drying.

Due to its size, the copper triethylenetetramine molecule can not be exchanged completely in natural vermiculites. Therefore the CEC of the vermiculite was determined with the ammonium acetate method. This CEC is here defined by:

$$CEC[meq/100g] = \frac{V_{H_2SO_4}[ml] \cdot n_{H_2SO_4}[mol] \cdot 100}{m_{dried}[g]} \quad (7)$$

$$V_{H_2SO_4}[ml] = V_{Sample}[ml] - V_{Blank}[ml] \quad (8)$$

with

V_{H2SO4}	revised Volume (Consumption) of H_2SO_4
n_{H2SO4}	Molarity of H_2O_4 (0.0067 mol)
m_{dried}	mass of dried sample
V_{Sample}	measured Volume of H_2SO_4 of the used sample
V_{Blank}	measured Volume of H_2SO_4 of the blank sample.

Copper triethylenetetramine method

Equipment:

Scale, weighing glasses, desiccator, centrifuge tube (50 ml), shaking table, disposable cuvettes (1.5 ml semi-micro, Plastibrand), centrifuge (Multifuge 3S-R Heraeus/Kendro), UV-vis Spectrometer Genesys 10UV (Thermo).

Chemicals:

0.01 M $(CuSO_4)\cdot 5H_2O$, triethylenetetramine purum, saturated $Mg(NO_3)_2$ (53% r.h.), deionised water.

Brief description:

Before CEC measurements, the hydration state of the samples is allowed to equilibrate by storing the samples over magnesium nitrate between 3 and 5 days. Thereafter, a specified amount of material is weighed into 50 ml centrifuge tubes. The amount of sample depends on the expected CEC. If the CEC

is higher than 50 meq/100 g, the net weight averages 50 mg. If the CEC is less than 50 meg/100 g, a larger amount of material has to be used. 10 ml deionised water and 5 ml 0.01 M copper triethylenetetramine (Cu-trien) are then added and the resulting suspensions shaken for 3 h. After this procedure, a complete exchange of the Cu^{2+}-complex with the exchangeable cations is guaranteed. Afterwards, the suspensions are centrifuged at a constant rotation speed of 4500 rpm for 10 min. The clear blue supernatant is transferred into cuvettes and is measured in a photometer at a wavelength of 580 nm. A calibration curve to calculate the Cu-trien concentrations in the clay samples was prepared by mixing 10 ml deionised water with several volumes of Cu-trien (0.5, 1, 2, 3, 4 and 5 ml), which were measured. At our laboratory repeated measurements of two bentonites (Volclay, Calcigel) have been done during the last year. Volclay has an average value of 85 meq/100g and Calcigel has an average value of 63 meq/100g. Thus, these clays are measured as standards to check the correctness of my measurements. The CEC measurement of a sample was always done twice.

Error:

The correctness of the method was determined by repeated measurements (> 75) of two standards (Volclay and Calcigel) in our laboratory. The precision is defined to be ± 3 meq/100g.

Ammonium acetate method

Equipment:

Scale, centrifuge tube (50 ml), shaking table, centrifuge (Multifuge 3S-R Heraeus/Kendro), distillation apparatus, evaporating dish, burette, Erlenmeyer flasks (100 ml), Kjeldahl flasks, pipette (5 ml, 10 ml), magnetic stirrer, drying oven, volumetric flask (100 ml), polyethylene bottles.

Chemicals:

1 M CH_3COONH_4 (pH=7, p.a.), CH_3CH_2OH (pure), H_2SO_4 (0.0067 M, p.a.), H_3BO_3 (pH=4.75, 4%, p.a.), NaOH (50%, p.a.), indicator (25 mg methylred and 125 mg bromocresol green in 25 ml ethanol), HNO_3 (Suprapur®, Merck), deionised water.

Brief description:

The preparation of the samples follows the instructions of MacKenzie (1951) and Emmerich (2000). 60 mg material was weighed in 50 ml centrifuge tubes. Between 25 and 30 ml ammonium acetate solution were added. The suspensions were shaken during 24 h. After this procedure, a complete exchange of the ammonium with the exchangeable cations is guaranteed. The next day, the solutions were centrifuged with 4500 rpm for 10 min. The clear supernatant was exchanged by 25 to 30 ml 1 M ammonium acetate solution. The procedure was repeated four times. Afterwards, the materials were washed 4 times with 25 to 30 ml ethanol. All supernatant solutions were collected in evaporation bowls and dried at 90 °C. The solid residue was prepared for ICP-OES. It was redissolved with 3 ml nitric acid and deionised water and transferred into a volumetric flask (100 ml) and filled to the mark. The solutions were stored in polyethylene bottles.

The ammonium exchanged material was transferred into Kjeldahl flasks together with 30 ml deionised water and was mixed with 2 ml NaOH solution before the measurement started. Ammonium was

eliminated from the interlayer by the sodium and transformed to ammoniac. The released NH_3 was transferred into an Erlenmeyer flask by water vapour distillation (Kjeldahl). The Erlenmeyer flask contained already 2 ml boric acid and the indicator for titrimetric determination of NH_3 by H_2SO_4. In addition to the samples, a blank was measured. The blank consisted of 30 ml deionised water and 2 ml NaOH solution. After the distillation, each solution in the Erlenmeyer flask was blue and the pH was basic. The titration occurred from basic to acid and the colour changed from blue to red. The measurement of the CEC of a sample was always done twice. The water content of the clay sample was measured with STA, because smectite and vermiculite can release water up to 250 °C. The CEC determined referred to the dry sample weight.

Error:

A CEC value being too high was determined, when the surplus ammonium was not completely washed out. A lower CEC value is obtained, when the exchange with ammonium was not complete.

3.6.2 Layer Charge Determination (ξ)

The layer charge of smectite in bentonite and vermiculite was determined by the alkylammonium method (Lagaly and Weiss, 1970; Lagaly, 1989 and 1994). Interlayer cations like sodium, calcium, magnesium were exchanged by alkylammonium ions of various chain lengths. The intercalation of the alkylammonium ions results in an expansion of the interlayer and to a shift of the characteristic basal XRD peaks (d_{001} peak), which was measured after washing and drying. With increasing alkyl chain length, the basal spacings increase. Short chains cause monolayer (1.36 nm) and longer chains are oriented in bilayers (1.77 nm). Very long chains produce pseudotrimolecular layers (2.17 nm) and a paraffin-type configuration (> 2.2 nm), which can be observed in vermiculites.

In most cases, a heterogeneous charge distribution in smectites exists because the interlayer cation density varies from interlayer space to interlayer space. The transition from monolayer to bilayer is required to determine the charge distribution or the cation density. For homogeneous charge distribution, the cation density and the charge density are equal.

The peak migration curve according to Lagaly (1981) was used to calculate the cation density. The method of Lagaly and Weiss (1970) is very time-consuming, because this procedure requires the exchange with 14 different alkylammonium chains for each sample, the preparation and measuring of 14 texture samples and then subsequent calculation.

Therefore, Olis et al. (1990) developed an empirical method for the rapid estimation of the layer charge of expandable clays like smectites or vermiculites. Here, the exchange is done with only one alkylammonium chain (n_c = 12 or n_c = 18). The mean layer charge (MLC) can be determined for the monolayer to bilayer transition by the following formula (Olis et al., 1990):

n_c= 12: $$MLC = \frac{d(001) - 5.52}{32.98} \quad (9)$$

n_c = 18: $$MLC = \frac{d(001) - 8.21}{34.22} \quad (10)$$

and for the bilayer to pseudotrimolecular layer transition by the following equation (Olis et al., 1990):

n_c = 12: $$MLC = \frac{d(001) - 8.71}{20.25} \quad (11)$$

n_c = 18: $$MLC = \frac{d(001) - 8.71}{29.65} \quad (12).$$

Equipment:

Scale, weighing glasses, desiccator, centrifuge tube (10 ml), centrifuge (Multifuge 3S-R Heraeus/Kendro), drying oven, X-ray diffractometer (Siemens D5000), sample holder.

Chemicals:

Alkylammonium ions (chain lengths 4 to 18, Aldrich and Merck), formic acid, ethanol, di-phosphor pentaoxyde p.a. (P_2O_5).

Brief description:

For the determination of the layer charge, aqueous solutions of n-alkylammonium formiate were used because of their good solubility, especially of longer chains (Wolters et al., 2008). Fourteen various alkylammonium solutions from n_c = 4 to n_c = 18 (except n_c = 17) were prepared for the measurements according to Lagaly and Weiss (1971) and Wolters et al. (2008).

100 mg of the clay sample were mixed with 3 ml alkylammonium solution and stored at 60 °C. After 2 or 3 days the alkylammonium solution was replaced. First, by separating the clay from the alkylammonium solution by centrifugation and washing with ethanol one time. The fresh suspensions were stored again at 60 °C for three days. After this procedure, a complete exchange of the alkylammonium ions with the exchangeable cations is guaranteed. Afterwards, the solutions are washed free of the excess alkylammonium ions with ethanol. Sixteen washing cycles were necessary. After centrifugation, the clay samples were dispersed in 3 ml ethanol together with small amounts of muscovite (~ 10 mg) to prepare textured samples for XRD. The muscovite was used as line standard. After drying at room temperature, the samples were stored in a desiccator above P_2O_5 until the XRD-patterns were recorded. The prepared samples are stable for only 2 days.

The XRD measurements were performed on a Siemens D5000 diffractometer (CuKα radiation) equipped with a graphite secondary monochromator. The patterns were recorded between 2 and 12° 2θ with a step size of 0.04° 2θ / 8 s.

Annotation:

For the determination of the layer charge, vermiculite samples need a longer reaction time for the exchange with alkylammonium ions in comparison to smectites. For smectite, the exchange is completed in one week, while vermiculite needs more than one month.

Error:

Too short reaction times may result in an incomplete exchange, especially for high charge expandable clays like vermiculite. The correction of the particle size is necessary for particles < 0.1 µm and for chain length above n_c = 9. For the < 0.2 µm fraction, the values for the particle size correction were taken from Lagaly (1994).

References

Brindley G. W. and Brown G. (1980) Crystal structures of clay minerals and their X-ray identification. Mineralogical Society, Monograph 5, London, pp. 539.

Brunauer S., Emmett P. H. and Teller E. (1932) Adsorption of gases in multimolecular layers. Journal of the American Chemical Society **60**, pp. 309-319.

De Boer J. H., Lippens B. C., Linsen B. G., Broekhoff J. C. P., Van den Heuvel A. and Osinga Th. J. (1966) The t-curve of multimolecular N_2-adsorption. Journal of Colloid and Interface Science **21**, pp. 405-414.

Drits V. A., Besson G. and Muller F. (1995) An improved model for structural transformations of heat-treated aluminous dioctahedral 2:1 layer silicates. Clay and Clay Minerals **43**, pp. 718-731.

Drits V. A., Lindgreen H., Salyn A. L., Ylagan R. and McCarty D. K. (1998) Semiquantitative determination of trans-vacant and cis-vacant 2:1 layers in illites and illite-smectites by thermal analysis and X-ray diffraction. American Mineralogist **83**, pp. 1188-1198.

Emmerich K. (2000) Die geotechnische Bedeutung des Dehydroxylierungsverhaltens quellfähiger Tonminerale. Dissertation, Veröffentlichungen des Instituts für Geotechnik (IGT) der ETH Zürich, pp. 143.

Frost R. L. and Ding Z. (2003) Controlled rate thermal analysis and differential scanning calorimetry of sepiolites and palygorskites. Thermochimica Acta **397**, pp. 119-128.

Gregg S. J. and Sing K. S. W. (1991) Adsorption, surface area and porosity. 2nd ed. Academic Press, London, pp. 330.

Jasmund K. and Lagaly G. (1993) Tonminerale und Tone: Struktur, Eigenschaften, Anwendung und Einsatz in Industrie und Umwelt. Steinkopff Verlag, pp. 490.

Kleeberg R. and Bergmann J. (2002) Quantitative phase analysis using the Rietveld method and a fundamental parameter approach. Proceedings of the II International School on Powder Diffraction, pp. 63-76.

Köster H. M. and Schwertmann U. (1993) Beschreibung einzelner Tonminerale. Jasmund K. and Lagaly G. (ed.), Tonminerale und Tone: Struktur, Eigenschaften, Anwendung und Einsatz in Industrie und Umwelt, Steinkopf Verlag, Darmstadt, pp. 33-58.

Kubelka P. and Munk F. (1931) Ein Beitrag zur Optik von Farbanstrichen. Zeitschrift für technische Physik **12**, pp. 593-601.

Lagaly G. (1981) Characterization of clays by organic compounds. Clay Minerals **16**, pp. 1-21.

Lagaly G. (1989) Erkennung und Identifizierung von Tonmineralen mit organischen Stoffen. Jahrestagung der deutschen Ton- und Tonmineralgruppe (DTTG), pp. 86-130.

Lagaly G. (1994) Layer charge determination by alkylammonium ions in layer charge characteristics of 2:1 silicate clay minerals. Mermut A. R. (ed.), The Clay Minerals Society **6**, Aurora, pp. 1-46.

Lagaly G. and Weiss A. (1970) Anordnung und Orientierung kationischer Tenside auf ebenen Silicatoberflächen Teil IV. Kolloid-Zeitschrift und Zeitschrift für Polymere **243**, pp. 48-55.

Mackenzie R. C. (1951) A micromethod for determination of cation-exchange capacity of clay. Journal of Colloid Science **6**, pp. 219-222.

Meier L. P. and Kahr G. (1999) Determination of the cation exchange capacity (CEC) of clay minerals using the complexes of copper(II) ion with triethylenetetramine and tetraethylenepentamine. Clays and Clay Minerals **47**(3), pp. 386-388.

Niederbudde E. A., Stanjek H. and Emmerich K. (2002) Tonmineral Methodik, Handbuch der Bodenkunde.

Olis A. C., Malla P. B. and Douglas L. A. (1990) The rapid estimation of the layer charges of 2:1 expanding clays from a single alkylammonium ion expansion. Clay Minerals **25**, pp. 39-50.

Petrick K. (2007) Vergleich von STA-Messungen und FTIR-spektroskopischen Messungen zur Strukturbestimmung der Oktaederschicht von Montmorillonit. Diplomarbeit, Fakultät für Bauingenieur-, Geo- und Umweltwissenschaften der Universität Karlsruhe, pp. 175.

Smykatz-Kloss W. (1974) Differential thermal analysis: Application and results in mineralogy. Wyllie P. J. (ed.), Minerals, Rocks and Inorganic materials, Springer Verlag, Berlin, pp. 185.

Wolters F., Lagaly G., Kahr G., Nueesch R. (†) and Emmerich K. (2009) A comprehensive characterisation of dioctahedral smectites. Clays and Clay Minerals, in print.

Wolters F. and Emmerich K. (2007) Thermal reactions of smectites – Relation of dehydroxylation temperature to octahedral structure. Thermochimica Acta **462**, pp. 80-88.

4 Mineralogical characterisation and selection strategy

The results of Vermiculite are submitted to Clays and Clay Minerals in the form of one publication:

Steudel A., Weidler P., Schuhmann R. and Emmerich K. (2009) Cation exchange reactions of vermiculite in dependents of mechanical and chemical pre-treatment. Clays and Clay Minerals, submitted.

4.1 Introduction

Prior to the characterisation of the clay mineral edges and modification of the clay minerals, it is necessary to know the characteristic properties of the bulk material. Information on the samples studied is given in Table 2.1 (Chapter 2). The methods to characterise each sample are listed in Table 4.1.

Table 4.1 Samples and applied characterisation methods.

Method / Sample	XRD	CEC	Layer charge	STA	FTIR	ESEM	XRF	ICP-OES	BET
1_Calci	X	X	X	X	X	X	X	X	X
2_EXM757	X	X	X	X	X	X	X	X	X
3_SWy-2	X	X	X	X	X	X	X	X	X
4_Vol	X	X	X	X	X	X	X	X	X
5_WYO	X	X	X	X	X	X	X	X	X
6_IndBent	X	X	X	X	X	X	X	X	X
7_NHec	X	X	X	X	X	X	X	X	X
8_Verm	X	X*	X	X	X	X	X	X	X
9_Illite	X			X	X	X	X		X
10_PangelS9	X	X	X	X	X	X	X	X	X
11_Pansil	X	X	X	X		X	X	X	X
12_Palygorskit	X	X	X	X		X	X	X	X
13_Pol	X	X		X	X	X	X	X	X
14_Kaolex	X	X		X	X	X	X	X	X
15_Rogers	X	X		X	X	X	X	X	X
16_Mag	X	X		X	X	X	X	X	X

* CEC was measured with the ammonium acetate method.

The complete data set for each sample is given in the appendix. The results of the characterisation are discussed exemplarily for one sample of each mineral group. A grain

size separation has been carried out for several samples. From six bentonites, one vermiculite and one sepiolite (1_Calci, 2_EXM757, 4_Vol, 5_WYO, 6_IndBent, 7_NHec, 8_Verm, 10_PangelS9), the < 2 µm fraction was separated and the < 0.2 µm fraction was separated from the samples 3_SWy-2, 4_Vol, 6_IndBent and 10_PangelS9.

4.2 Bentonites and Smectites

Morphology and surface

Smectites are Al-bearing layer silicates and the main phases in the < 2 µm fraction of bentonites. The natural bentonites in this study contain about 80% of the < 2 µm fraction. They consist of thick but small agglomerates of smectites with irregular shape and partly sharp grain boundaries. Figure 4.1 displays the typical morphology of the smectite particles in the bentonite sample EXM757. Due to their small particle size, the specific surface area of the smectites in the raw bentonites ranged between 20 and 65 m^2/g. All BET data are given in the appendix.

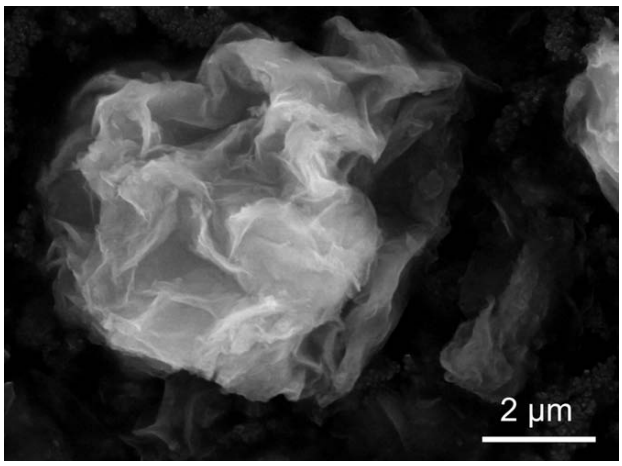

Figure 4.1 ESEM image showing the typical smectite morphology in the bentonite sample EXM757 (2_EXM757).

Mineralogy

The mineralogy of the bentonites is shown in Table 4.2. The qualitative analysis of the XRD patterns using Brindley and Brown (1980) showed that one of the smectites is a trioctahedral (d_{060} = 0.152 nm) natural hectorite (7_Nhec). According to Brindley and Brown (1980), all further smectites are dioctahedral (d_{060} between 0.149 and 0.150 nm).

Table 4.2 Phase content of the natural bentonites.

Phases[#] \ Sample	1_Calci [%]	2_EXM757 [%]	3_SWy-2 [%]	4_Vol [%]	5_WYO [%]	6_IndBent [%]	7_NHec [%]
Smectite (Na-rich, di)	-	86.5 ± 1.3	79.4 ± 2.1	60.0 ± 4.2	67.2 ± 2.2	82.2 ± 3.6	-
Smectite (Na-rich, tri)	-	-	-	-	-	-	93.9 ± 1.3
Smectite (Ca-rich, di)	24.6 ± 10.8	-	-	19.8 ± 3.6	-	6.7 ± 3.0	-
Smectite (Mg-rich, di)	38.9 ± 10.2	-	-	-	-	-	-
Kaolinite	3.8 ± 0.8	-	-	-	-	4.4 ± 0.8	-
Muscovite / Illite	13.7 ± 1.5	-	3.7 ± 1.4	2.8 ± 0.9	5.4 ± 1.4	-	-
Quartz	5.9 ± 0.7	2.3 ± 0.3	10.5 ± 1.0	4.4 ± 0.5	6.6 ± 0.8	1.1 ± 0.3	-
Cristobalite	-	11.2 ± 1.3	-	-	3.6 ± 0.6	-	-
K-Feldspars (Orthoclase)	-	-	4.2 ± 1.4	4.0 ± 0.9	-	-	-
K-Feldspars (Microcline Int1)	-	-	-	-	3.9 ± 0.7		-
Plagioclase (Albite)	2.5 ± 0.7	-	-	4.1 ± 0.8	-	-	-
Plagioclase (Oligoclase)	-	-	-	-	8.0 ± 1.8	-	-
Plagioclase (Anorthite)	-	-	-	-	-	3.9 ± 1.2	-
Calcite	3.3 ± 0.5	-	2.2 ± 0.4	1.3 ± 0.4	3.5 ± 0.6	-	3.1 ± 0.8
Dolomite	7.3 ± 0.5	-	-	-	-	-	-
Ankerite (Fe 0.54)	-	-	-	-	-	-	0.7 ± 0.6
Maghemite	-	-	-	-	-	0.9 ± 0.3	-
Hematite	-	-	-	-	-	0.8 ± 0.3	-
Gypsum	-	-	-	3.6 ± 0.6	0.9 ± 0.4	-	-
Clinoptilolite	-	-	-	-	1.0 ± 0.5	-	-
Analcime (cubic)	-	-	-	-	-	-	2.1 ± 0.7

In parenthesis the structure model used for Rietveld analysis is given.

Rietveld quantification revealed smectite contents between 64 and 94% for these seven bentonites (Table 4.2). All bentonites have similar impurities such as quartz, feldspars, mica and calcite. The bentonites 2_EXM757 and 5_WYO contain quartz and cristobalite as impurities (Figure 4.2).

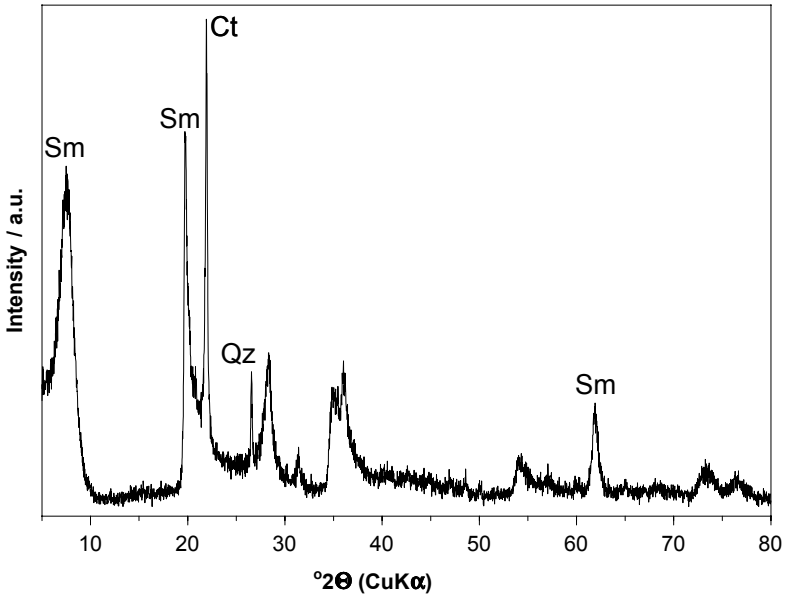

Figure 4.2 X-ray pattern (powder sample) of the bentonite EXM 757 (2_EXM757); Sm: characteristic Smectite peaks with increasing 2θ (001), (020,110,021), (060); Qz: Quartz; Ct: Cristobalite.

Chemical composition

The chemical composition of the bentonites, determined by XRF, is given in Table 4.3. The main octahedral cation of the dioctahedral smectites is aluminium. In the octahedral sheet of the hectorite, the main cation is magnesium. It can partly be substituted by lithium. In this sample 1.1% lithium has been determined by ICP-OES.

Table 4.3 XRF-analysis of the natural bentonites.

Oxides		1_Calci	2_EXM757	3_SWy-2	4_Vol	5_WYO	6_IndBent	7_NHec
SiO_2	[%]	49.35	61.01	61.26	56.50	59.85	43.08	55.03
Al_2O_3	[%]	16.61	17.15	17.98	18.56	15.21	15.59	1.99
MgO	[%]	4.15	2.08	2.41	2.26	5.41	2.40	22.84
Fe_2O_3	[%]	5.09	3.76	3.79	3.56	1.61	13.74	0.81
TiO_2	[%]	0.38	0.16	0.15	0.15	0.17	0.94	0.08
MnO	[%]	0.05	0.01	0.03	0.01	0.33	0.12	0.02
Na_2O	[%]	0.26	2.95	1.34	1.88	2.17	3.29	3.31
CaO	[%]	4.26	0.74	1.54	1.14	2.37	1.23	1.88
K_2O	[%]	1.52	0.17	0.59	0.52	0.52	0.10	0.42
P_2O_5	[%]	0.06	0.52	0.04	0.04	0.07	0.06	0.87
LOI	[%]	17.7	11.4	10.3	15.4	12.3	18.8	12.7

The dioctahedral smectites differ in the components of their interlayers and of their octahedral sheets. The interlayer cations and the cations of the octahedral sheet are listed in Tables 4.4 and 4.5 for the seven clays, respectively. The bentonite EXM757 consists of a Na-rich smectite, while the bentonite Calcigel (1_Calci) consists of a Ca-rich smectite with a

high content of magnesium (28%) in the interlayer. In comparison to the other dioctahedral smectites, this smectite has a higher content of iron and magnesium in the octahedral sheet.

In the Wyoming bentonites (3_SWy-2, 4_Vol, 5_WYO), sodium and calcium are the main interlayer cations and also the Indian Bentonite (6_IndBent) consists mainly of a Na-rich smectite. Furthermore, one third of the aluminium in the octahedral sheet of the Indian Bentonite is substituted by iron; therefore this dioctahedral smectite belongs to the iron rich smectites compared to the other used dioctahedral smectites.

Table 4.4 Composition of the interlayer [%] of the smectites.

Sample	Na^+ [%]	Ca^{2+} [%]	Mg^{2+} [%]	K^+ [%]	M^{2+} (Ca, Mg) : M^+ (Na) ratio
1_Calci	11	58	28	2	8 : 1
2_EXM757	83	14	2	1	1 : 6
3_SWy-2	48	31	19	2	1 : 1
4_Vol	61	31	6	2	1 : 2
5_WYO	67	29	4	-	1 : 2
6_IndBent	90	8	1	1	1 : 11
7_NHec	90	7	3	-	1 : 13

Table 4.5 Composition of the octahedral sheet in [%] of the used smectites.

Sample	Al^{3+} [%]	Fe^{3+} [%]	Mg^{2+} [%]	Li^+ [%]
1_Calci	65	15	20	-
2_EXM757	77	11	12	-
3_SWy-2	74	11	15	-
4_Vol	79	10	11	-
5_WYO	76	13	11	-
6_IndBent	64	24	13	-
7_NHec	2	1	87	10

The chemical composition of the < 2 and < 0.2 µm fractions combined with the layer charge (Köster, 1977; Wolters et al., 2008) was used to calculate the structural formula of the smectites. The results are listed in Table 4.6. Only the chemical data of the fractions could be used for the calculation, because the crude materials contained other mineral phases.

Table 4.6 Structural formula of the smectites.

Sample	Fraction	Structural formula
1_Calci	< 2 µm	$Me^{+}_{0.26}(Si_{3.84}Al^{3+}_{0.16})(Al^{3+}_{1.38}Fe^{3+}_{0.30}Mg^{2+}_{0.43})[O_{10}(OH)_2]$
2_EXM757	< 2 µm	$Me^{+}_{0.32}(Si_{3.95}Al^{3+}_{0.05})(Al^{3+}_{1.53}Fe^{3+}_{0.22}Mg^{2+}_{0.24})[O_{10}(OH)_2]$
3_SWy-2	< 0.2 µm	$Me^{+}_{0.29}(Si_{3.79}Al^{3+}_{0.21})(Al^{3+}_{1.53}Fe^{3+}_{0.23}Mg^{2+}_{0.32})[O_{10}(OH)_2]$
4_Vol	< 0.2 µm	$Me^{+}_{0.25}(Si_{3.95}Al^{3+}_{0.05})(Al^{3+}_{1.58}Fe^{3+}_{0.20}Mg^{2+}_{0.23})[O_{10}(OH)_2]$
5_WYO	< 2 µm	$Me^{+}_{0.28}(Si_{3.89}Al^{3+}_{0.11})(Al^{3+}_{1.53}Fe^{3+}_{0.26}Mg^{2+}_{0.23})[O_{10}(OH)_2]$
6_IndBent	< 0.2 µm	$Me^{+}_{0.34}(Si_{3.71}Al^{3+}_{0.29})(Al^{3+}_{1.32}Fe^{3+}_{0.49}Mg^{2+}_{0.26})[O_{10}(OH)_2]$
7_NHec	< 2 µm	$Me^{+}_{0.26}(Si_{3.90}Al^{3+}_{0.10})(Mg^{2+}_{2.64}Li^{+}_{0.29}Al^{3+}_{0.05}Fe^{3+}_{0.04})[O_{10}(OH)_2]$

Short range order

The chemical differences in the octahedral sheet can be observed in the FTIR spectra in the wavenumber region between 1200 and 400 cm^{-1} (Figure 4.3). In this range, dioctahedral smectites show sharp vibration bands. Their assignments are listed in Table 4.7 (Farmer, 1974; Komadel et al., 1990; Komadel et al., 1996; Madejová et al., 1998; Tyagi et al., 2006).

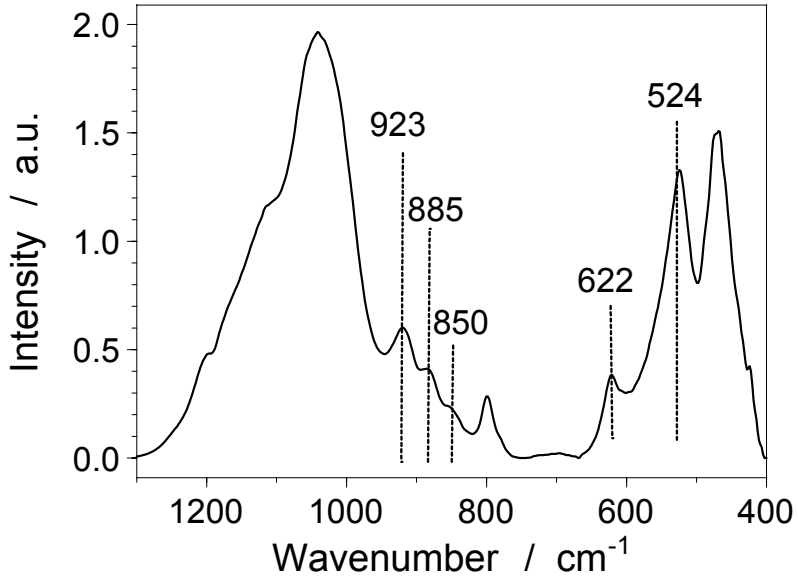

Figure 4.3 FTIR spectrum of the bentonite EXM757 (2_EXM757).

Table 4.7 Positions and assignments of the vibrational bands in the lattice region of the dioctahedral smectites.

Wavenumber [cm^{-1}]	Assignment*
1103	Si-O stretching vibration (out-of-plane)
1037	Si-O stretching vibration (in-plane)
923	AlAlOH bending
885	AlFeOH bending
850	AlMgOH bending
622	R-O-Si with R = Al, Mg, Fe
526	Si-O-Al vibration (Al tetrahedral cation)
470	Si-O-Si bending vibration

* Komadel et al., 1990; Madejová et al., 1998; Tyagi et al., 2006.

Various bands around 923, 885, 850, 622 and 526 cm^{-1} can be attributed to vibrations of aluminium in the octahedral sheet. For example, the band near 923 cm^{-1} can be assigned to an AlAlOH bending vibration and gives information on the content of aluminium in the octahedral sheet. The vibrations at 885 and 850 cm^{-1} reflect a partial substitution of aluminium by iron (AlFeOH bending vibration) and magnesium (AlMgOH bending vibration). The absorption band around 622 cm^{-1} can be attributed to a R-O-Si vibration (R = Al, Fe, Mg) and indicates a perpendicular vibration of the octahedral cations and their connection to the tetrahedral sheet. The band near 524 cm^{-1} can be assigned to a Si-O-Al vibration of aluminium in the tetrahedral sheet. All the other bands near 1103 (shoulder), 1037 and 470 cm^{-1} are strong Si-O bending and stretching vibrations.

In contrast to the spectra of dioctahedral smectites, the FTIR spectra (Figure 4.4) of trioctahedral smectites generally show broad and rounded absorption bands (Wilson, 1994). Their assignments are listed in Table 4.8 (Farmer, 1974; Komadel et al., 1990; Komadel et al., 1996; Madejová et al., 1998; Tyagi et al., 2006).

Table 4.8 Positions and assignments of the vibrational bands in the lattice region of trioctahedral smectites.

Wavenumber [cm^{-1}]	Assignment (Komadel et al., 1996; Madejová et al.,1998; Farmer, 1974)
1124	Si-O stretching vibration (out-of-plane)
1000	Si-O stretching vibration (in-plane)
696	SiO bending vibration (out of plane)
659	OH bending vibration
526	MgO
466	SiO bending vibration (in plane)
450 – 460	Si-O-Mg vibration

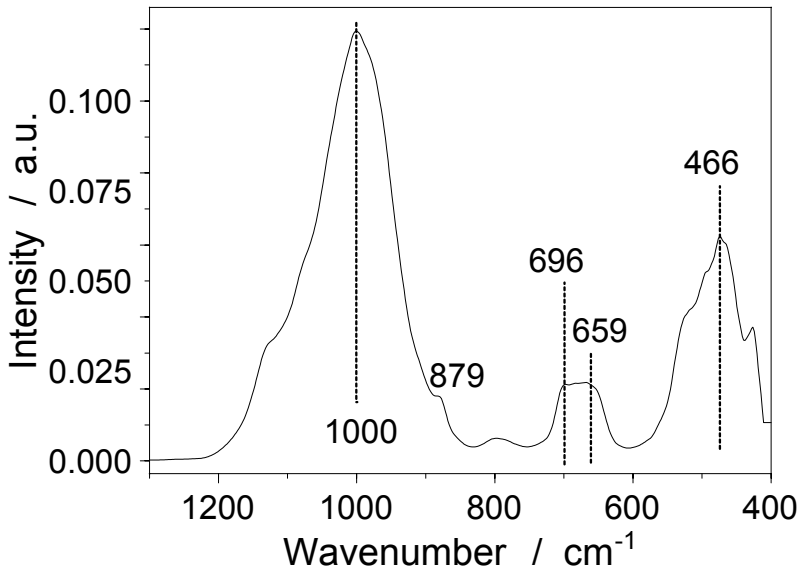

Figure 4.4 FTIR spectrum of the natural hectorite (7_NHec).

Similar to spectra of dioctahedral smectites, one sharp band with a shoulder to higher wavenumber is observable in the region around 1000 cm^{-1} for the trioctahedral smectites. This band at 1000 cm^{-1} and the shoulder are attributed to SiO-stretching vibrations. A further small shoulder at 879 cm^{-1} supports the presence of calcite in this sample. In the OH-bending region from 900 to 400 cm^{-1}, a broad band occurs with two maxima (696 and 659cm^{-1}). The band at lower wavenumbers can be assigned to an OH bending vibration (Komadel et al., 1990; Madejová et al., 1996), while Farmer (1974) attributed the vibration at 696 cm^{-1} to a complex bending vibration of Si_2O_5 units. The strong band at 466 cm^{-1} is generally attributed to a Si-O (in plane) bending vibration. Madejova et al. (1998) interpreted this vibrational mode as Si-O-Mg band, which is overlapped by a strong Si-O-Si vibration.

Thermal reactions

The chemical composition of the interlayers and of the octahedral sheet of the smectite has an influence on the thermal behaviour. In dependence of the temperature, smectites show four characteristic reactions during thermal analysis (Figure 4.5): dehydration, dehydroxylation, decomposition and recrystallisation (Niederbudde et al., 2002; Wolters et al., 2008).

While most of the smectites in this study showed one dehydration peak below 300 °C, the two smectites with the highest layer charge (5_WYO, 6_IndBent, Table 4.12) showed two dehydration peaks in this temperature range (Table 4.9). Here, the release of adsorbed water from the mineral surfaces and interlayer water from the inner surfaces occurred stepwise.

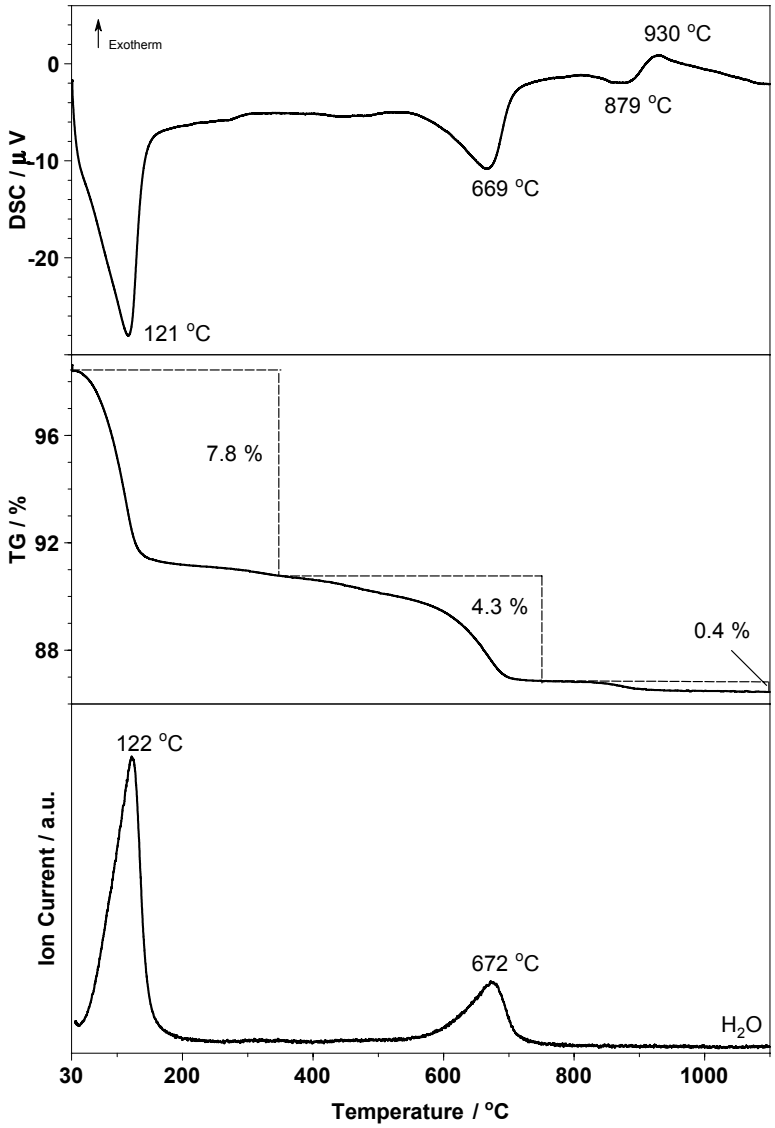

Figure 4.5 DSC, TG and MS (H_2O and CO_2) curve of EXM757 (2_EXM757).

Table 4.9 Thermal analysis data of the smectites.

Sample	Dehydration [°C]		Dehydroxylation [°C]		Decomposition [°C]	Recrystallisation [°C]
1_Calci	136	-	517	653	860	919
2_EXM757	121	-	-	669	879	930
3_SWy-2	132	-	-	696	904	944
4_Vol	144	-	-	707	909	951
5_WYO	138	243	-	691	885	943
6_IndBent	151	279	511	649	853	908
7_NHec	138	-	-	691	902	972

In general, the dehydroxylation temperature is influenced by the chemical composition and by the structure of the octahedral sheet. According to Smykatz-Kloss (1974), the dehydroxylation temperature shifts to higher temperature with an increasing content of

magnesium and to lower temperature with an increasing content of iron in the octahedral sheet. Higher dehydroxylation temperature of Al-rich smectites can be associated with the arrangement of the cations in the octahedral sheet (Drits et al., 1995).

In the seven samples, the release of structural water (dehydroxylation) occurred between 500 and 750 °C (Table 4.9). The DSC curves of two smectites 1_Calci and 6_IndBent showed two dehydroxylation peaks, which are associated with maxima in the MS curves of the released water. These peaks indicate a two-step dehydroxylation. In comparison, the other smectites showed only one dehydroxylation peak at temperatures above 660 °C. The smectite in the Indian Bentonite and in the Calcigel had more iron in the octahedral sheet than the other smectites (Table 4.5); therefore one dehydroxylation peak was around 510 °C. The dehydroxylation temperature can also be used to estimate the cis- and trans-vacant character of the dioctahedral smectites (Table 4.10). According to Drits et al. (1998), the border between both varieties was defined by 600 °C. A classification of dioctahedral smectites with respect to the occupancy of cis- and trans-positions was created by Wolters and Emmerich (2007).

Table 4.10 Proportions of trans-vacant (W_{tv}) and cis-vacant (W_{cv}) parts and classification.

Sample	original material		fraction < 2 µm		fraction < 0.2 µm		Classification
	W_{cv} [%]	W_{tv} [%]	W_{cv} [%]	W_{tv} [%]	W_{cv} [%]	W_{tv} [%]	
1_Calci	50	50	61	39	-	-	cv/tv
2_EXM757	95	5	98	2	-	-	Cv
3_SWy-2	90	10	-	-	94	6	Cv
4_Vol	92	8	99	1	99	1	Cv
5_WYO	93	7	-	-	93	7	Cv
6_IndBent	34	66	34	66	33	67	tv/cv

Most of the starting materials are cis-vacant. Only the Indian Bentonite (6_IndBent) and the Calcigel have more trans-vacant positions. The Indian Bentonite can be assigned to the group of trans-cis-vacant smectites. The starting material of Calcigel has cis- and trans-vacant portions in equal shares. According to Wolters and Emmerich (2007), the Calcigel belongs to the cis-trans-vacant smectites.

Decomposition started at temperatures between 850 and 920 °C, where a loss of crystalline order in the smectite phases occurred. Recrystallisation took place between 910 and 980 °C, which indicated the formation of anhydrous high temperature phases (Table 4.9).

Exchange behaviour and interlayer cations

The exchange capacity and the layer charge give information about the exchange behaviour of the smectites in the bentonites. They have a measured CEC between 60 and 95 meq/100g (Table 4.11). The layer charges of the Volclay (0.26 - 0.27 eq/FU) and Indian Bentonite were measured by the alkylammonium method (Lagaly and Weiss, 1970; Lagaly, 1989 and 1994) (see Chapter 3). The layer charge of the other materials (between 0.28 and 0.38 eq/FU) was measured according Olis et al. (1990) using the alkylammonium ions with a chain length of n_c = 12 (see Chapter 3). Each can be used to estimate the other value (Table 4.11 and 4.12).

We assumed that the measured CEC and layer charge are only caused by the existence of the smectite phases. The differences of the CEC between the crude material and the fractions (< 2 µm and < 0.2 µm) are caused by the presence of additional mineral phases. These impurities lead to a dilution of the smectite and, as a result, the CEC of the raw material was slightly lower.

The measured layer charge disregarded the charge of the mineral edges. Therefore, the measured layer charge is lower in the clay-rich fractions (< 2 µm and < 0.2 µm) than the calculated charge from CEC. The calculated CEC of these fractions was also lower than the measured CEC.

Table 4.11 Cation exchange capacity of the original material and of the < 2 µm and < 0.2 µm fraction.

Sample	CEC [meq/100g]					
	original material		fraction < 2 µm		fraction < 0.2 µm	
	Measured	Calculated	measured	calculated	measured	calculated
1_Calci	63	81	88	83	-	-
2_EXM757	84	81	84	81	-	-
3_SWy-2	78	78	-	-	91	83
4_Vol	85	78	85	70	90	70
5_WYO	68	75	80	72	-	-
6_IndBent	91	94	96	86	98	86
7_NHec	89	73	90	70	-	-

The layer charge of the raw material can be estimated, but must be interpreted with care. The measured layer charge of the starting material was higher than the calculated layer charge due to the preparation of the alkylammonium samples. The impurities did not cause a dilution. These values are in agreement with the layer charge values of the fractions (< 2 µm and < 0.2 µm). Therefore, most of the starting smectites had a higher calculated than a

measured CEC. The measured CEC of the raw materials of EXM757 (2_EXM757), Volclay (4_Vol) and hectorite (7_NHec) were higher than the calculated CEC, because in the calculated values the charges of the edges were not considered.

Table 4.12 Measured and calculated layer charge of the crude material and of the < 2 µm and < 0.2 µm fractions.

Sample	Layer charge ξ [eq/FU]					
	original material		fraction < 2 µm		fraction < 0.2 µm	
	measured	Calculated	measured	Calculated	Measured	calculated
1_Calci**	0.30	0.23	0.31	0.33	-	-
2_EXM757**	0.30	0.31	0.30	0.31	-	-
3_SWy-2**	0.29	0.29	-	-	0.31	0.34
4_Vol*	0.27	0.32	0.26	0.32	0.26	0.33
5_WYO**	0.28	0.25	0.27	-	-	-
6_IndBent*	0.36	0,35	0.33	0.37	0.33	0.38
7_Nhec**	0.28	0.34	0.27	0.35	-	-

* For the measurement all alkylammonium chains were used (Lagaly, 1994).
** Measurements according to Olis et al. (1990), using alkylammonium ion with the chain length n_c =12.

4.3 Vermiculite

4.3.1 Morphological, mineralogical, chemical and thermal properties

Morphology and surface

The vermiculite is a Mg-rich layer silicate. In contrast to smectite, vermiculite has a lower content of < 2 µm fraction (< 10%) and a larger particles size (> 20 µm). Due to the large particle size, a pre-treatment (grinding) is necessary.

The crude vermiculite particles, after grinding with the CGS 10 from Netzsch (see Chapter 4.3.2), consist of thick agglomerates with a layered appearance and with an irregular shape (Figure 4.6).

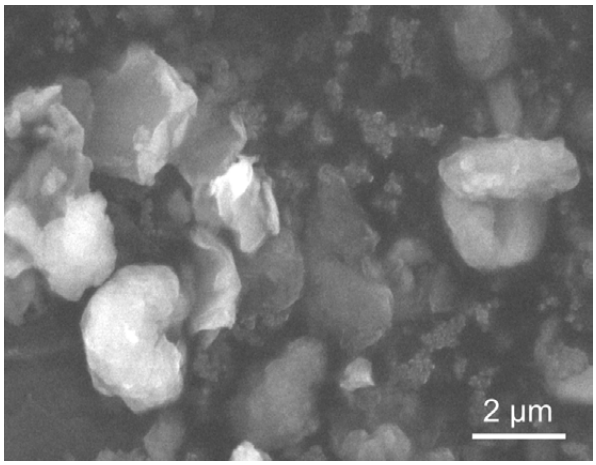

Figure 4.6 ESEM image shows the morphology of the vermiculite (8_Verm).

The specific surface area of the vermiculite increased to 36 m^2/g due to reduced particle size after grinding. This value is similar to that of the bentonites. After grinding, the natural material had a higher content of micropores (24 m^2/g) in comparison to the other materials like smectite.

Mineralogy

The vermiculite (8_Verm) used in this study is a trioctahedral mineral with a high magnesium content in the octahedral sheet. In comparison to the smectites, this vermiculite has a higher layer charge due to substitutions in the octahedral and tetrahedral sheets. The vermiculite sample consists of 84% vermiculite and contains calcite (2%) and phlogopite (14%) as impurities (Figure 4.7).

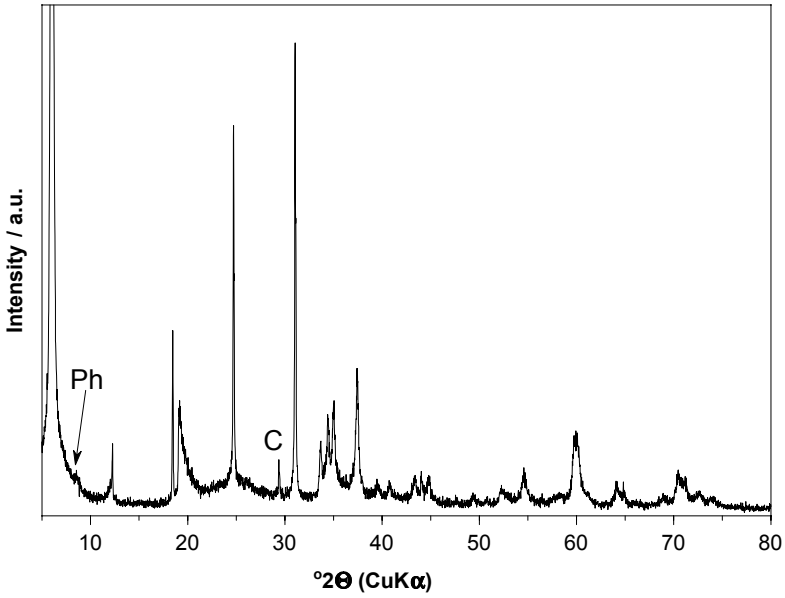

Figure 4.7 X-ray pattern (powder sample) of the vermiculite (8_Verm);
Ph: Phlogopite; Ca: Calcite; all not indexed peaks originated from Vermiculite.

Grinding Experiments

The starting material of the vermiculite used has a low < 2 µm fraction content. Particle size separation revealed an amount of less than 10%. The aim of the grinding experiment was to find a grinding method to increase this content without affecting changes in the structure of the vermiculite.

Several mills were used (Table 4.13). The agate mill was used in combination with a sieve of a mesh size of 63 µm. Furthermore, the material for the McCrone mill was first ground with the agate mill for 1 h to obtain material with a particle size smaller than 400 µm.

Table 4.13 The kind of mill used in this study.

Mill		Company
Agate Mill		Fritsch
McCrone Mill		McCrone Scientific Ltd
Wet Mill	PE 075	Netzsch
Dry Mill	CGS 10	Netzsch

A volume of 3 ml of this powder and 10 ml deionised water were filled in a grinding vessel. The suspension was milled in the McCrone mill for 15, 20 and 25 min with a rotation speed of 4800 min^{-1}. For 100 g powder, the grinding process requires 2 days when each charge is ground for 15 min. The wet mill was used with a rotation speed of 1000 min^{-1}. After 20, 40 and 60 min, samples were taken. Several rotation speeds (16000, 17000, 18000 min^{-1}) were tested in the dry mill CGS 10. After 15 and 30 min, a sample was taken (Figure 4.8).

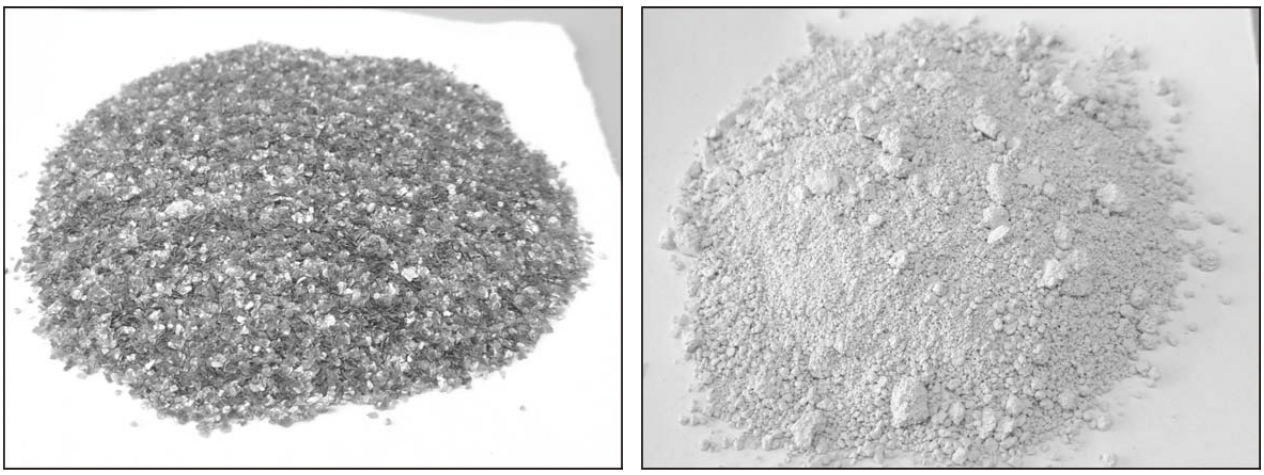

Figure 4.8 The raw vermiculite before (left) and after (right) the grinding procedure. The material was ground with the dry mill CGS 10 from Netzsch.

After grinding, the changes in the structure and the particle size distribution of the ground material were investigated using X-ray diffraction analysis and a laser scattering particle size distribution analyser LA-950 from Horiba.

The X-ray patterns of the powder samples (Figure 4.9) showed that the intensity of the hkl peaks increased, while the intensity of the basal reflections decreased slightly with decreasing particle size. The primary domains are still present. The particles are equal in length and width; indicating the particles cannot be oriented completely.

In general, the use of the agate mill in combination with a sieve (< 63 µm) was very time consuming (30 g in 1 h) and the content of the < 2 µm fraction could not be increased (Table 4.14).

Table 4.14 Grain size distribution of the vermiculite after grinding in an agate mill in combination with a sieve (< 63 µm).

Fraction	%
> 63 µm	3
63 – 20 µm	44
20 – 2 µm	37
< 2 µm	16

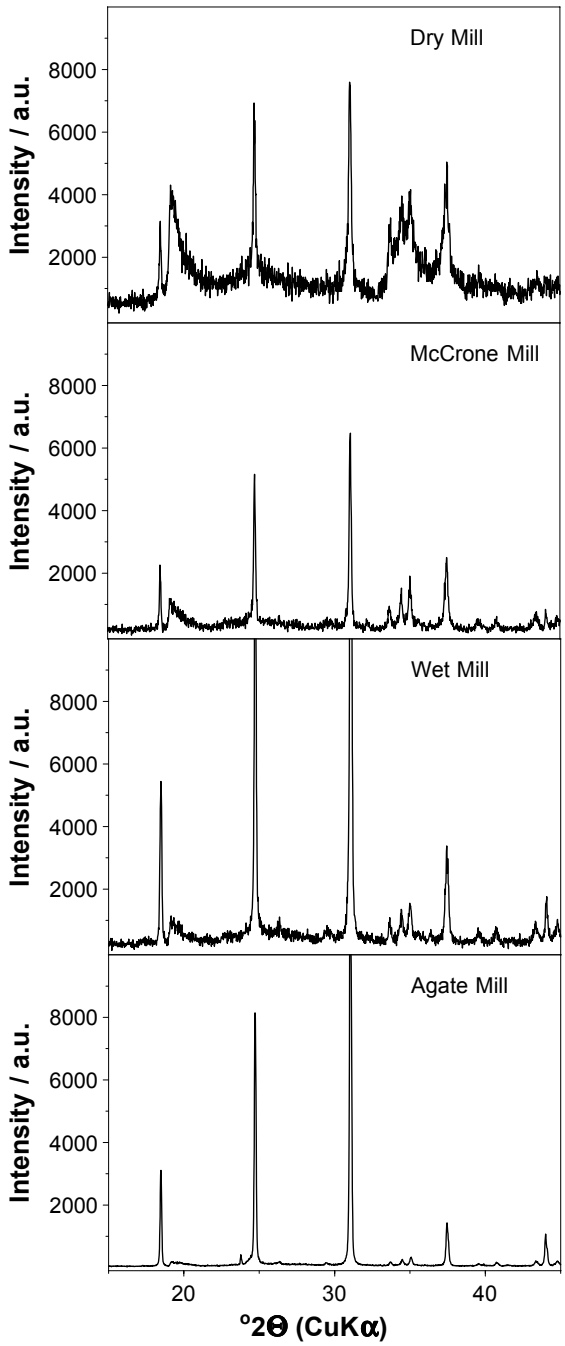

Figure 4.9 Influence of the grinding procedure on the vermiculite structure.

The particle size measurements showed that nearly 83% of the particles milled for 15 minutes in the McCrone mill were smaller than 20 µm (Figure 4.10a). The amount of this fraction increased about 15% with increasing grinding time (25 min). In spite of this increase, the amount was still insufficient for particle size separation. Due to its small volume, the use of the McCrone mill was too time consuming to significantly increase the content of the fraction < 2 µm.

Grinding in the wet mill reduced grain size to below 90 µm. 20 min of wet grinding revealed an amount of 40% of the < 20 µm fraction, which increased to nearly 70% after

60 min. However, the content of the < 2 µm fraction was again insufficient for particle size separation (Figure 4.10b).

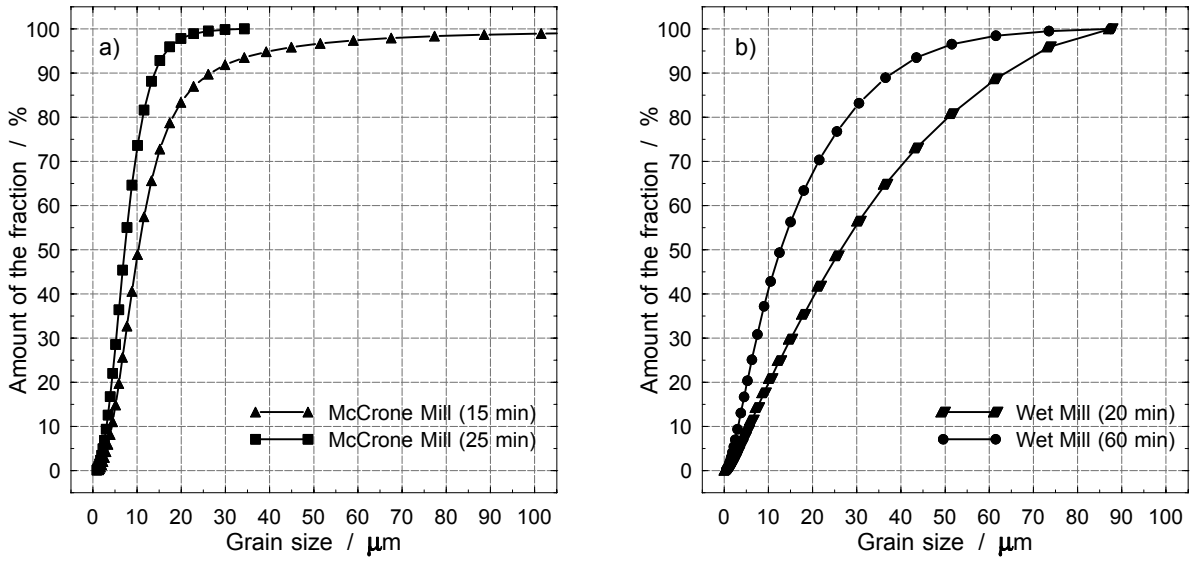

Figure 4.10 Particle size distributions a) after 15 and 25 min grinding time using the McCrone mill and b) after 20 and 60 min grinding time using the wet mill from Netzsch.

At the beginning of the grinding experiment, a part of the raw material was ground with the dry mill CGS 10 for 15 min with a rotation speed of 16000 min^{-1} and the particle size distribution was determined. The particle size of this material was completely less than 20 µm and the content of the fraction size < 2 µm was about 25% (Figure 4.11).

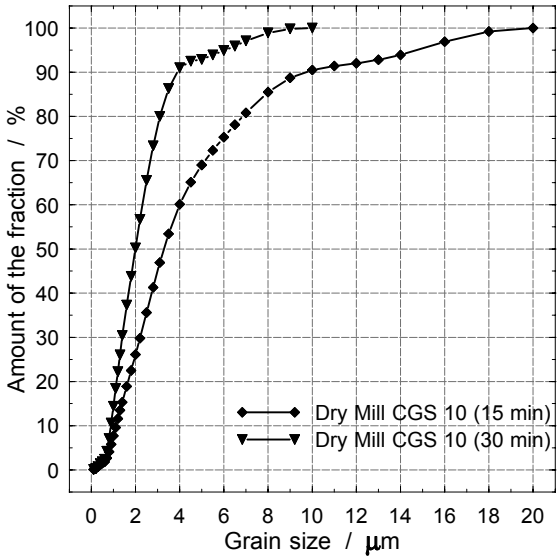

Figure 4.11 Particle size distributions after 15 and 30 min grinding time using the dry mill CGS 10 from Netzsch.

Further dry grinding with the CGS 10 mill reduced the grain size to below 10 µm (Figure 4.11). Also the content of the < 2 µm fraction increased to nearly 50% with increasing grinding time. In this case, a particle size separation was possible. Furthermore, the grinding

procedure with the dry mill from Netzsch was not time consuming; 5 kg vermiculite were ground in one day.

The differences in the particle size distribution after the grinding procedure with several mills are displayed in Figure 4.12.

The McCrone mill can be used for rapid particle size reduction of small sample amounts for qualitative and quantitative phase analysis, but not to enrich the < 2 µm fraction. The wet mill from Netzsch can also be used for particle size reduction, but in comparison to the McCrone mill it needs significantly more time. The dry mill CGS 10 can be used to enrich the < 2 µm fraction.

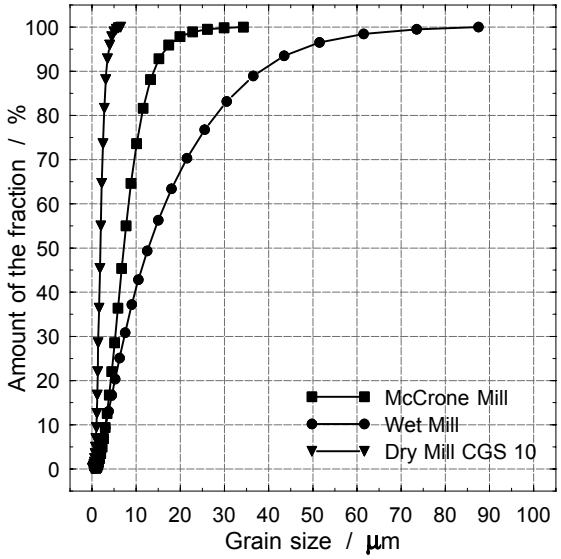

Figure 4.12 Comparison between the particle size distribution using the McCrone mill (25 min), the wet mill (60 min) and the dry mill (30 min).

Chemical composition

The chemical composition of the natural vermiculite sample is given in Table 4.15.

Table 4.15 XRF-analysis of the natural vermiculite.

Oxides		8_Verm
SiO_2	[%]	36.89
Al_2O_3	[%]	10.21
MgO	[%]	26.08
Fe_2O_3	[%]	5.14
TiO_2	[%]	0.55
MnO	[%]	0.06
CaO	[%]	0.57
K_2O	[%]	0.26
P_2O_5	[%]	0.02
LOI	[%]	20.2

Due to the large grain size of the vermiculite sample, it was not possible to separate the < 0.2 µm fraction. Thus, the < 2 µm fraction was used to characterise the edges (see Chapter 5). Furthermore, this fraction was used to calculate the structural formula of the vermiculite according to Köster (1977). The stoichiometric composition was calculated as follows:

$$Me^{+}_{0.70}(Si_{3.04}Al^{3+}_{0.96})(Mg^{2+}_{2.65}Fe^{3+}_{0.31}Al^{3+}_{0.01})[O_{10}(OH)_2]\,.$$

Short range order

The FTIR spectra show only a few sharp and characteristic vibrations (Figure 4.13). The absorption bands are broad and rounded (Wilson, 1994). In comparison to dioctahedral clay minerals like smectite, trioctahedral clay minerals show a distinctive OH-band, which is broad, strong and at lower wavenumbers (995 cm^{-1}).

In the region between 900 - 550 cm^{-1}, several small (823 cm^{-1}) and broad bands (736 and 665 cm^{-1}) occur, which can be attributed to OH bending vibrations and their interactions with octahedral cations (Farmer, 1974; Wilson, 1994; Ravichandran and Sivasankar, 1997). The other intense band at 466 cm^{-1} can be attributed to a Si-O bending vibration.

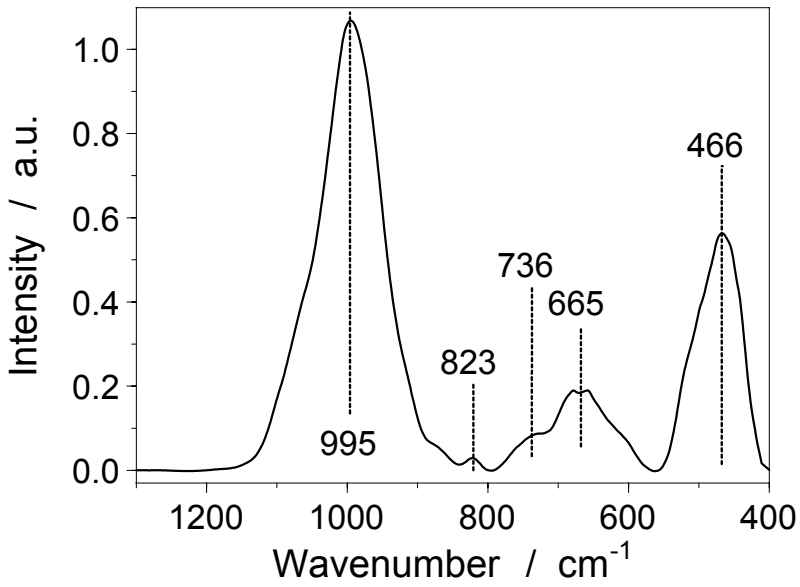

Figure 4.13 FTIR spectrum of the vermiculite sample (8_Verm).

Thermal reactions

The thermal behaviour of vermiculite was similar to that of the high charged smectites, as well as of the trioctahedral smectites. The DSC curve showed two endothermic peaks at low temperature (Figure 4.14). Both peaks are associated with maxima in the MS curve and with a mass loss of 14%. These two peaks can be assigned to the release of adsorbed and interlayer water. The dehydration of vermiculite occurred stepwise, which was also observed for high charged smectites like Indian Bentonite (6_IndBent). The reason is the higher layer charge, thereby the interlayer water is bound stronger and the complete release occurs at higher temperature.

The MS-curve of H_2O showed that the loss of the hydroxyl groups occurred very slowly and over a large temperature range (750 to 900 °C). The dehydroxylation is associated with a mass loss of 6%. The final stage of dehydroxylation is followed by decomposition and recrystallisation.

In contrast to smectite the final stage of dehydroxylation, decomposition and recrystallisation occurred in vermiculite over a smaller temperature range (800 to 860 °C).

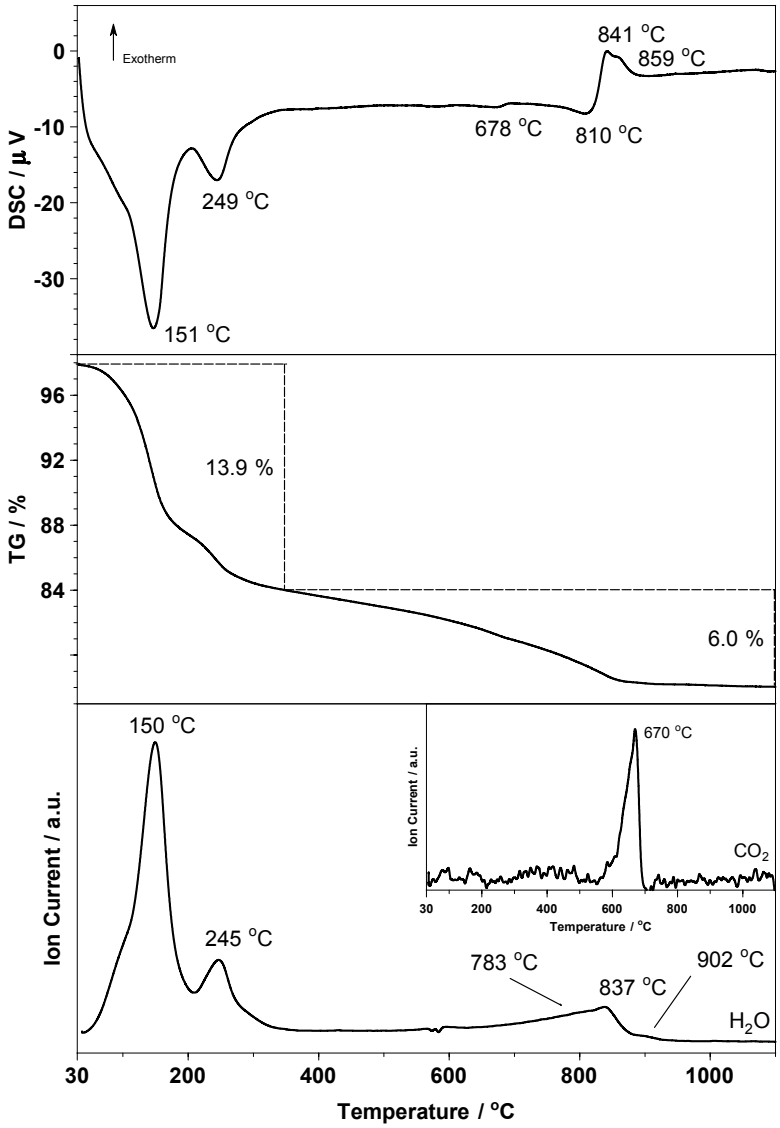

Figure 4.14 DSC, TG and MS (H_2O and CO_2) curve for the vermiculite (8_Verm).

The DSC curve showed a small endothermic peak at 670 °C, which is associated with a peak in the MS curve of CO_2. These results show that the vermiculite sample contained calcite, in agreement with the X-ray diffraction data.

4.3.2 Cation exchange reactions

Copper triethylenetetramine (Cu-trien) and ammonium acetate can be used to measure the CEC of swellable clay minerals like smectite and vermiculite (see Chapter 3).

The Cu-trien treated vermiculite samples were shaken for 3 h. Calculation of the CEC shows that only some Cu-trien replaced interlayer cations (Table 4.16).

Table 4.16 Preliminary results of the CEC of vermiculite using Cu-triethylenetetramine, shaking time: 3 h.

Sample	Vermiculite* (1)	Vermiculite* (2)	Vermiculite* (3)
CEC [meq/100g]	31	63	53

* Samples were not purified according to Tributh and Lagaly (1986).
(1) Vermiculite < 63 µm (using agate mill in combination with a sieve with mesh size 63 µm).
(2) Vermiculite < 2 µm (separation of the fraction < 2 µm by sedimentation).
(3) Vermiculite < 10 µm (using dry mill CGS 10).

For the determination of the layer charge, vermiculite samples need a longer reaction time for the exchange with alkylammonium ions in comparison to smectites. For smectite, the exchange is complete in one week, while vermiculite needs more than one month. Thus, we would expect that the exchange procedure with Cu-trien also needs much longer time for vermiculite. However, an increased shaking time caused no remarkable variations.

Table 4.17 Measured CEC of vermiculite at various shaking times.

Shaking time	3 h	7 d	14 d	21 d	28 d
Vermiculite* (1) [meq/100g]	31	47	56	53	52
Vermiculite* (2) [meq/100g]	63	63	75	65	66

* Samples were not purified according to Tributh and Lagaly (1986).
(1) Vermiculite < 63 µm (using agate mill in combination with a sieve with mesh size 63 µm).
(2) Vermiculite < 2 µm (separation of the fraction < 2 µm by sedimentation).

The exchange of alkylammonium ions was performed at 60 °C, because heating improves the exchange with Cu-trien. The samples were shaken for 24 h. After that, the samples were stored at 60 °C for several weeks. To check the stability of the Cu-trien solution against heat, the same procedure was applied on a standard smectite sample (Volclay). These measurements showed that Cu-trien is stable at higher temperatures (60 °C), but again the intrinsic CEC of vermiculite was not achieved (Figure 4.15).

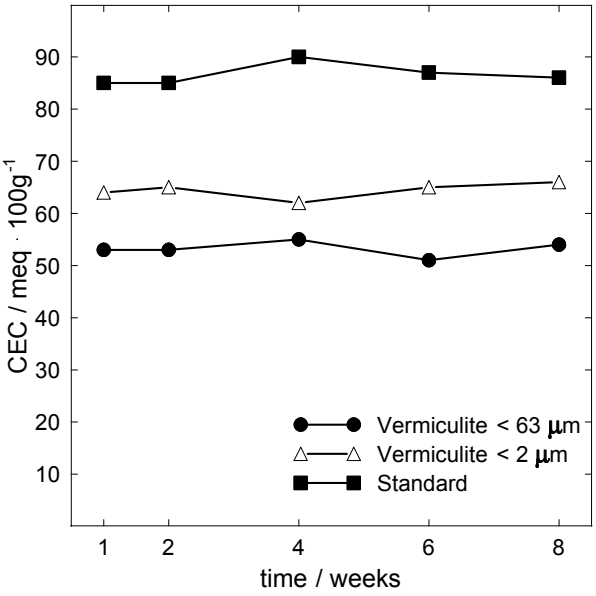

Figure 4.15 CEC of the vermiculite as a function of time, as well as the temperature stability check of Cu-triethylenetetramine, using a standard sample (Volclay).

According to these results, Cu-trien cannot be used to determine the CEC of this non-purified vermiculite. A possible reason is the size of the Cu-trien molecules. Cu-trien has a planar cyclic structure with a size between 4.0 and 4.5 nm^2, i.e. this molecule has an equivalent area per charge between 2.0 and 2.25 nm^2. Vermiculite has an equivalent area per charge of 3.1 nm^2 (Lagaly, 1994). This value is remarkably lower than that of smectites, which have an equivalent area between 4.5 and 8.0 nm^2 (Lagaly, 1994). A further reason could be the charge of the vermiculite per formula unit. This charge lies between 0.6 and 0.9 for vermiculite and between 0.2 and 0.6 for smectite. This means, the vermiculite has between 1.2 and 1.8 and the smectite between 0.4 and 1.2 charges per unit cell. This results in stronger electrostatic interactions in the interlayer of vermiculite than in the interlayer of smectite. The released energy of the Cu-trien molecule is too low to reduce the bond energy between the layers. Therefore, the molecule cannot be intercalated completely. In summary, the high charge content, the low equivalent area per charge and the size of the Cu-trien molecule prevent the exchange.

In addition, the CEC of purified vermiculite samples were measured with Cu-trien (Table 4.18). Therefore, the sample, which was milled with the CGS 10, was purified according to Tributh and Lagaly (1986) and the < 2 µm fraction was separated (see Chapter 2). The measured CEC of the purified vermiculite is comparable to that determined with ammonium acetate (Table 4.24).

Table 4.18 CEC of the purified vermiculite sample using Cu-triethylenetetramine, shaking time: 3 h.

Sample	Vermiculite # (8_Verm purified)	Vermiculite # (8_Verm < 2 µm)
CEC [meq/100g]	157	151

Samples were purified according to Tributh and Lagaly (1986).

The measurements were also repeated with varying shaking times (3, 6, 24, 48, 72 and 96 h). Again a standard sample (Volclay) was measured under same conditions, to check the stability of Cu-trien during the shaking time (Figure 4.16).

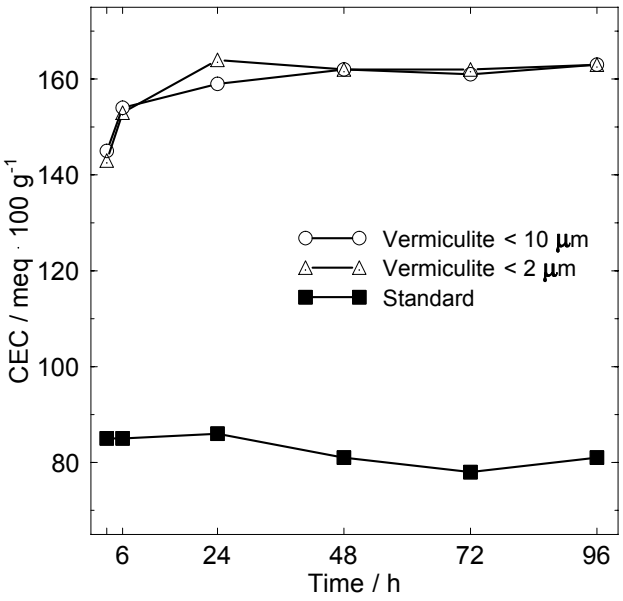

Figure 4.16 CEC of the purified and milled vermiculite samples as a function of time, as well as the stability check of Cu-triethylenetetramine using a standard sample (Volclay).

Purification according to Tributh and Lagaly (1986) includes 3 steps (removal of carbonate, removal of organic matter and removal of iron). To identify, which purification step enhanced Cu-trien exchange, three samples were prepared by applying only one step to each of them. Afterwards, the samples were dried and the CEC with Cu-trien was measured. For this, the samples were shaken for 48 h. According to the results displayed in Table 4.19, all purification steps caused an exchange with Cu-trien. The best result was achieved after the removal of carbonate.

Table 4.19 CEC of the differently purified vermiculite samples (< 10 µm) using Cu-triethylenetetramine, shaking time: 48 h.

Sample	CEC [meq/100g]
Vermiculite# (8_Verm - completely purified)	163
Vermiculite# (8_Verm - removal of carbonate)	160
Vermiculite# (8_Verm - removal of iron)	141
Vermiculite# (8_Verm - removal of organic matter)	142

Vermiculite < 10 µm partially purified according to the applied steps of the procedure described by Tributh and Lagaly (1986) (see Chapter 2).

Each purification step yields homoionic sodium exchanged material, because excess reagents were removed by washing with NaCl. To understand the influence of the interlayer cations of the exchange behaviour of the vermiculite, the purified bulk material and the purified < 2 µm fraction were homoionically exchanged with several cations (Na^+, Li^+, Ca^{2+}, Mg^{2+} and Cu^{2+}). For these measurements, the samples were shaken for 48 h.

Table 4.20 CEC of the differently homoionic exchanged vermiculite samples using Cu-triethylenetetramine, shaking time: 48 h.

	CEC [meq/100g]		
Cation	Vermiculite * (8_Verm)	Vermiculite # (8_Verm purified)	Vermiculite # (8_Verm < 2 µm)
Na^+	88	165	164
Li^+	87	-	161
Ca^{2+}	55	64	71
Mg^{2+}	54	71	71
Cu^{2+}	24	-	47

* Samples were not purified according to Tributh and Lagaly (1986).
\# Samples were purified according to Tributh and Lagaly (1986).

The measurements showed that the type of interlayer cation influenced the exchange with Cu-trien. Only a small amount of Cu-trien exchanged by the untreated homoionically exchanged vermiculite sample, but the Na^+ and Li^+ exchanged material showed a higher CEC compared with the Mg^{2+} and Ca^{2+} exchanged material. The purification in combination with monovalent cations (Na^+, Li^+) permitted the complete exchange. Bivalent cations such as Ca^{2+}, Mg^{2+}, Cu^{2+} prevent the exchange with Cu-trien. These results showed that the charge of the cations influenced the exchange. The higher charge results in stronger electrostatic interactions in the interlayer. The released energy of the Cu-trien molecule is too low to reduce the bond energy between the layers. Therefore, the molecule can not be intercalated completely.

The chemical composition of the differently purified vermiculites, as well as of the several homoionically exchanged, purified and fractionated vermiculite samples were measured to

calculate the structural formula. Tables 4.21, 4.22 and 4.23 contain the structural formulae to show the interlayer composition of the materials.

Table 4.21 Structural formulae of several purified vermiculite samples according to Köster (1977) and Wolters et al. (2008).

8_Verm	Structural formulae
completely purified	$Na^{+}_{0.68}Ca^{2+}_{0.01}(Si_{3.04}Al^{3+}_{0.96})(Mg^{2+}_{2.64}Fe^{3+}_{0.31}Al^{3+}_{0.02})[O_{10}(OH)_2]$
removal of carbonate	$Na^{+}_{0.71}Ca^{2+}_{0.01}K^{+}_{0.01}(Si_{3.05}Al^{3+}_{0.95})(Mg^{2+}_{2.60}Fe^{3+}_{0.31}Al^{3+}_{0.03})[O_{10}(OH)_2]$
removal of iron	$Na^{+}_{0.64}Ca^{2+}_{0.03}K^{+}_{0.01}(Si_{2.97}Al^{3+}_{0.99})(Mg^{2+}_{2.77}Fe^{3+}_{0.30})[O_{10}(OH)_2]$
removal of organic matter	$Na^{+}_{0.62}Ca^{2+}_{0.03}K^{+}_{0.01}(Si_{2.95}Al^{3+}_{1.00})(Mg^{2+}_{2.79}Fe^{3+}_{0.31})[O_{10}(OH)_2]$

Table 4.22 Structural formulae of several homoionically exchanged and purified bulk material of the vermiculite according to Köster (1977) and Wolters et al. (2008).

8_Verm purified#	Structural formulae
Na	$Na^{+}_{0.68}Ca^{2+}_{0.01}(Si_{3.04}Al^{3+}_{0.96})(Mg^{2+}_{2.64}Fe^{3+}_{0.31}Al^{3+}_{0.02})[O_{10}(OH)_2]$
Ca	$Ca^{2+}_{0.36}(Si_{3.0}Al^{3+}_{0.99})(Mg^{2+}_{2.69}Fe^{3+}_{0.31})[O_{10}(OH)_2]$
Mg	$Mg^{2+}_{0.34}Ca^{2+}_{0.01}(Si_{3.05}Al^{3+}_{0.95})(Mg^{2+}_{2.60}Fe^{3+}_{0.31}Al^{3+}_{0.04})[O_{10}(OH)_2]$

Vermiculite < 10 µm purified according to Tributh and Lagaly (1986).

Table 4.23 Structural formulae of the several homoionic exchanged and fractionated (< 2 µm) vermiculite samples according to Köster (1977) and Wolters et al. (2008).

8_Verm < 2 µm#	Structural formulae
Na	$Na^{+}_{0.68}Ca^{2+}_{0.01}(Si_{3.04}Al^{3+}_{0.96})(Mg^{2+}_{2.65}Fe^{3+}_{0.31}Al^{3+}_{0.01})[O_{10}(OH)_2]$
Ca	$Ca^{2+}_{0.35}(Si_{3.01}Al^{3+}_{0.99})(Mg^{2+}_{2.68}Fe^{3+}_{0.31})[O_{10}(OH)_2]$
Mg	$Mg^{2+}_{0.34}Ca^{2+}_{0.01}(Si_{3.05}Al^{3+}_{0.95})(Mg^{2+}_{2.60}Fe^{3+}_{0.31}Al^{3+}_{0.04})[O_{10}(OH)_2]$
Cu	$Cu^{2+}_{0.36}(Si_{3.04}Al^{3+}_{0.94})(Mg^{2+}_{2.67}Fe^{3+}_{0.32})[O_{10}(OH)_2]$
Li	$Li^{+}_{0.66}Ca^{2+}_{0.02}K^{+}_{0.01}(Si_{3.02}Al^{3+}_{0.98})(Mg^{2+}_{2.67}Fe^{3+}_{0.31})[O_{10}(OH)_2]$

Vermiculite < 2 µm purified according to Tributh and Lagaly (1986).

In summary, the purification and the homoionic exchange with sodium or lithium allowed the complete exchange with Cu-trien and the estimation of the CEC. These CEC values are comparable with the CEC of ammonium acetate (Table 4.24).

The CEC of unpurified vermiculite can very well be measured very well with ammonium acetate. The unpurified vermiculite had a measured CEC of 159 meq/100g. The purified < 2 µm fraction had a value of 176 meq/100g. These variations are caused by additional phases in the starting material contributing to a decrease in CEC. In contrast, the purified raw material has a CEC of 173 meq/100g. The sum of the exchanged cations is comparable with

the measured CEC values and reveals information on the composition of the interlayers (Table 4.24).

Table 4.24 Composition of the interlayer and sum of the exchanged cations as well as the cation exchange capacity of the vermiculite samples using the ammonium acetate method.

Sample	Vermiculite * (8_Verm)	Vermiculite # (8_Verm purified)	Vermiculite # (8_Verm < 2 µm)
Na [meq/100g]	-	151	157
K [meq/100g]	2	0	0
Ca [meq/100g]	20	3	4
Mg [meq/100g]	98	11	14
Al [meq/100g]	33	-	-
Sum of exchanged cations [meq/100g]	153	165	175
CEC [meq/100g]	159	173	176

* Sample was not purified according to Tributh and Lagaly (1986).
\# Sample was purified according to Tributh and Lagaly (1986).

4.4 Illite

The illite sample used in this study exhibits dioctahedral 2:1 layer. This illite had a very small particle size and is characterised by a layer charge between 0.6 and 0.9, which is higher than that of smectite, but lower than that of muscovite. Illite has lower potassium contents in the interlayer than the muscovite, because the potassium can be substituted by H_3O^+. Its layer charge is in the same range as vermiculite. The differences between illite and vermiculite are the different interlayer cations. Illite has potassium cations in the interlayer sheets and is not swellable, while vermiculite is swellable with mainly Mg interlayer cations. The negative charge of both is caused in both minerals by substitutions in the octahedral and in the tetrahedral sheet.

Morphology and surface

Due to its small particle size and the slat-like shape, the illite has a larger specific surface area (95 m^2/g) than vermiculite and smectite (Figure 4.17, Table 4.25).

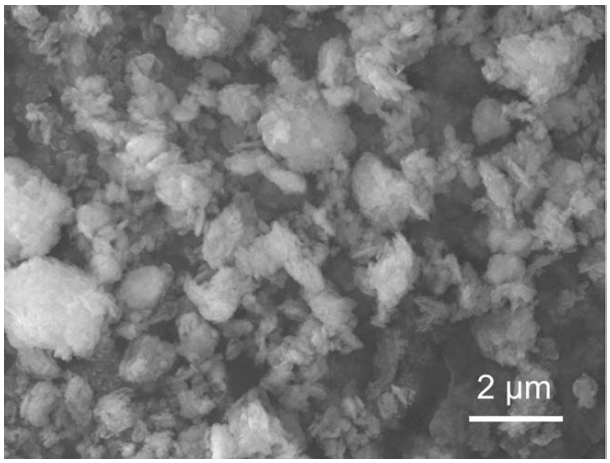

Figure 4.17 ESEM image shows the morphology of the illite (9_Illite).

Table 4.25 Grain size distribution of the natural illite.

Sample		d_{10}	d_{50}	d_{90}
9_Illite	[nm]	51	144	420

Mineralogy and chemical composition

Rietveld quantification of the natural sample revealed 76% illite (Table 4.26). The main impurity is phlogopite (7.9%); further minerals are kaolinite (5.4%), feldspars (5.5%) and calcite (2.4%) (Figure 4.18). Results of the chemical analysis of the illite are contained in Table 4.27. Remarkable is the relatively high iron content; the Mg and Ca contents may be attributed to phlogopite and calcite, respectively.

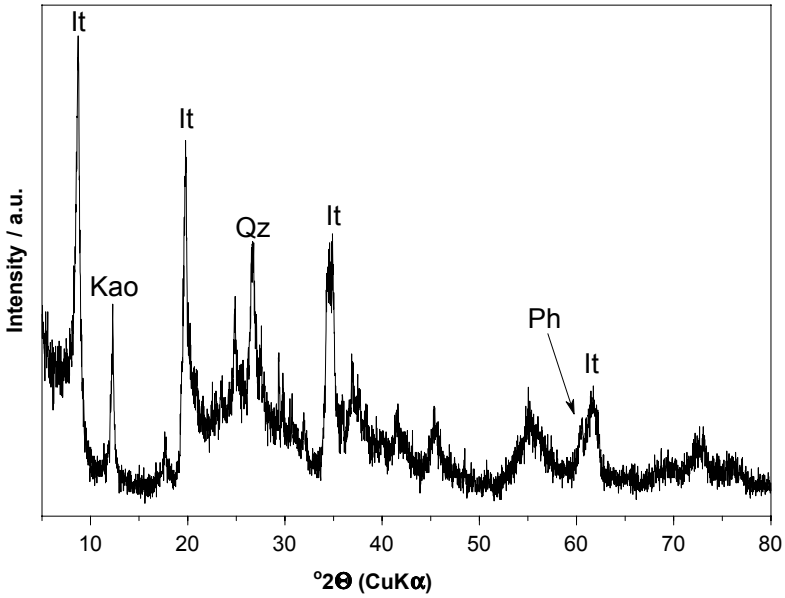

Figure 4.18 X-ray pattern (powder sample) of the illite (9_Illite);
It: characteristic illite peaks with increasing 2θ (001), (002), (130), (060);
Qz: Quartz; Kao: Kaolinite; Ph: Phlogopite (060).

Table 4.26 Quantification of the natural illite.

Sample	9_Illite
Illite	76.4 ± 2.0
Phlogopite	7.8 ± 1.2
Kaolinite	5.4 ± 0.7
K-feldspar (Orthoclase)	4.4 ± 0.6
Plagioclase (Anorthite)	1.1 ± 0.9
Calcite	2.4 ± 0.4
Anhydrite	1.4 ± 0.3
Apatite	0.7 ± 0.4
Quartz	0.4 ± 0.3

In parenthesis the structure model used for Rietveld analysis is given.

Table 4.27 XRF-analysis of the natural illite.

Elements		9_Illite
SiO_2	[%]	47.56
Al_2O_3	[%]	22.02
MgO	[%]	3.27
Fe_2O_3	[%]	7.93
TiO_2	[%]	0.8
MnO	[%]	0.06
Na_2O	[%]	0.00
CaO	[%]	1.46
K_2O	[%]	6.82
P_2O_5	[%]	0.41
LOI	[%]	11.1

Short range order

The FTIR spectrum of the raw illite shows a number of sharp bands in the region between 1200 and 400 cm^{-1} (Figure 4.19). Their assignments are listed in Table 4.28 (Farmer, 1974; Komadel et al., 1996; Liu, 2001). The OH bending vibrations at 912, 877 and the weak absorption bands near 825 and 750 cm^{-1} are associated with vibrations of cations (aluminium, magnesium, iron) in the octahedral position. The assignment of the bands at 825 and 750 cm^{-1} is not yet clear. They may be attributed to AlMgOH deformations, or in analogy to muscovite spectra to Al-O-Si vibrations (Farmer, 1974; Wilson, 1994).

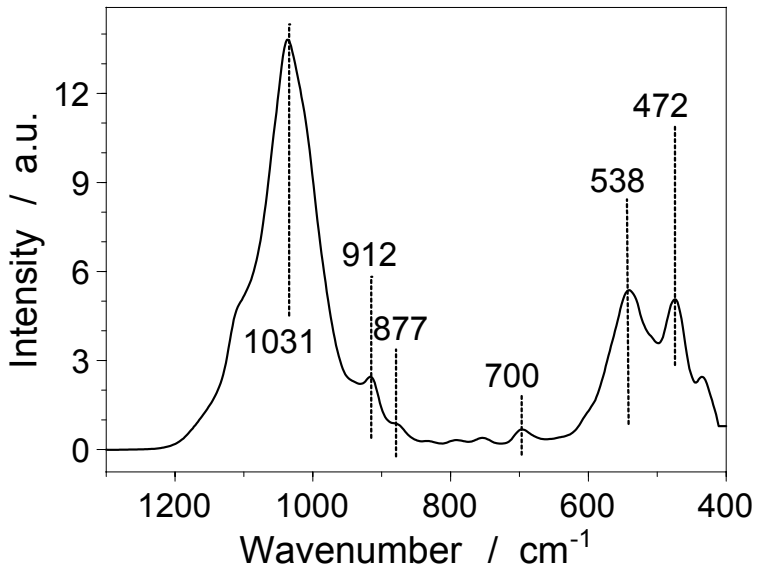

Figure 4.19 FTIR spectrum of the illite (9_Illite).

Table 4.28 Positions and assignments of the vibrational bands in the lattice region of the raw illite.

Wavenumber [cm^{-1}]	Assignment*
1101	Si-O stretching vibration (out-of-plane)
1031	Si-O stretching vibration (in-plane)
912	AlAlOH bending
877	AlFeOH bending
823	AlMgOH vibration
750	Al-O-Si vibration
700	OH bending
538	Si-O bending
472	Si-O-Si vibration
431	Si-O bending

* Farmer, 1974; Wilson, 1994; Liu, 2001.

The weak band at 700 cm^{-1} can be assigned to another OH bending vibration. The vibration at 538 cm^{-1} is attributed to a Si-O-Al bending vibration of silicon and aluminium in the tetrahedral sheet. All the other strong bands at 1031 with a weak shoulder at 1101, at 472 and 431 cm^{-1} are attributed to strong Si-O vibrations.

Thermal reactions

The DSC curve for the 9_Illite sample showed two endothermic peaks below 550 °C. Both are correlated to maxima in the MS curve. The first peak at lower temperature is associated with the release of adsorbed water (97 °C). The second peak at 508 °C displays the release of hydroxyl groups. Another small endothermic peak at 659 °C is associated with the release of CO_2 (Figure 4.20). This reaction shows the decomposition of a carbonate. In this case, the carbonate was calcite, as verified by XRD. Furthermore, the decomposition and the recrystallisation of the illite occurred at 883 and 914 °C.

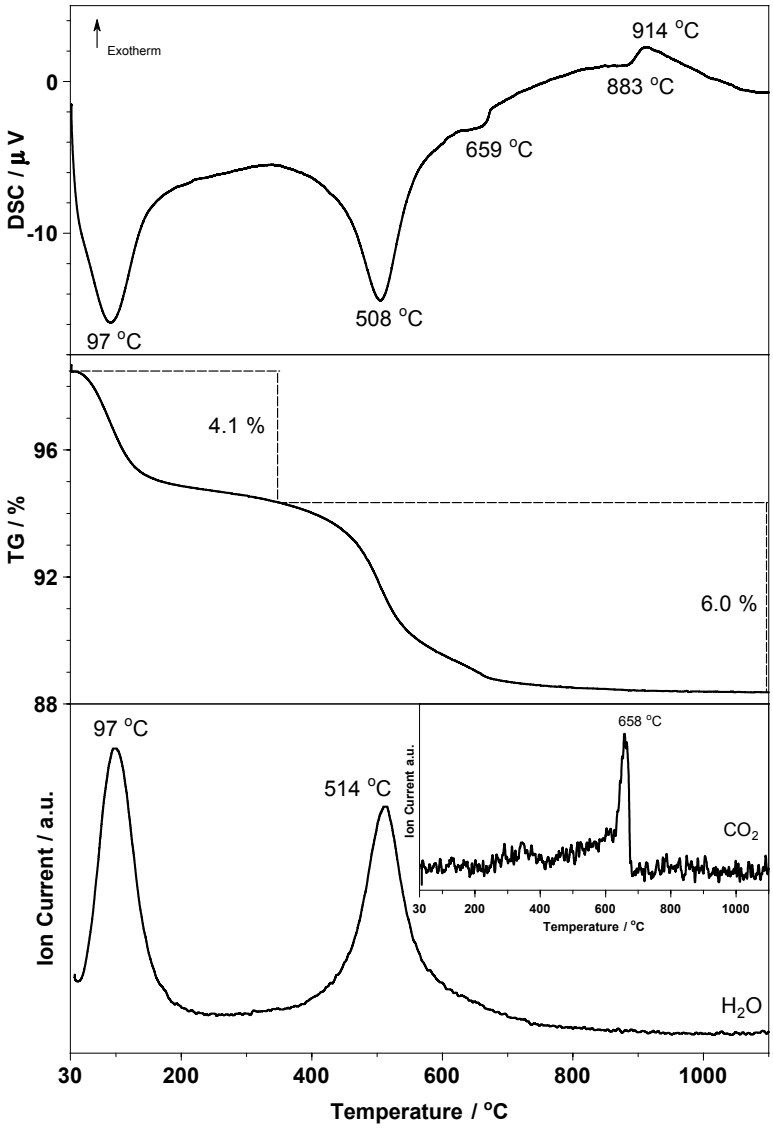

Figure 4.20 DSC, TG and MS (H_2O and CO_2) curve of the illite (9_Illite).

4.5. Sepiolite and Palygorskite

4.5.1 Morphological, mineralogical, chemical and thermal properties

Morphology and surface

Sepiolite and Palygorskite are hydrous Mg-bearing and Al-Mg-bearing silicates with a fibrous morphology and distinctive layered appearance (Figure 4.21).

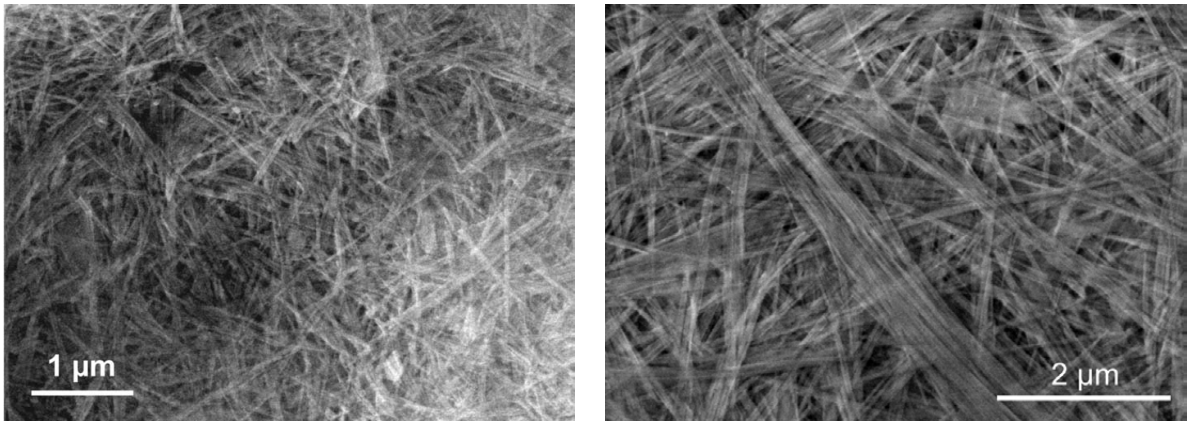

a) Sepiolite (10_Pangel S9) b) Palygorskite (12_Palygorskite)

Figure 4.21 ESEM images show the morphology a) of sepiolite (10_PangelS9) and b) of palygorskite (12_Palygorskite).

Both are layer silicates, but they also have structural affinities to inosilicates (Vivaldi and Hach-Ali, 1970). The sepiolite has eight octahedral positions per formula unit, which are mainly occupied by magnesium. In contrast, the palygorskite has only five octahedral positions per formula unit, which are partly occupied by aluminium and magnesium. The single layers consist of an octahedral sheet, which is surrounded by two tetrahedral sheets. They are linked via oxygen atoms. This results in triple (sepiolite) or double (palygorskite) pyroxene-type chains with channels along the c-axis. The channels can be filled with water, exchangeable cations or organic molecules.

The specific surface area of these fibrous clay minerals is remarkably higher than that of smectite (Paragraph 4.2), vermiculite (Paragraph 4.3) or kaolinite (Paragraph 4.6). The high values are caused by the channel-like structure (Table 4.29).

Table 4.29 BET data of the crude sepiolites and palygorskite.

BET data		10_PangelS9	11_Pansil	12_Palygorskite
External area	[m^2/g]	133	115	143
Micropore area	[m^2/g]	167	146	178
Specific surface area	[m^2/g]	300	261	321

Mineralogy

All three samples show a characteristic d_{110} peak in their X-ray pattern (see Appendix). The d_{110} peak of sepiolite is located at 1.21 nm and that of palygorskite at 1.05 nm.

The sepiolite Pangel S9 (10_PangelS9) consists of 90% sepiolite and has only muscovite and calcite as impurities. The other sepiolite sample (11_Pansil) consists of 72% sepiolite and has a slightly higher content (28% vs. 10%) of impurities including muscovite, quartz, orthoclase, albite and calcite (Table 4.30). In contrast, the palygorskite sample exhibits more impurities than the two sepiolites; only 50% palygorskite is present in this sample (12_Palygorskite). The quantification of the raw material was adjusted with the chemical composition.

Table 4.30 Quantification of the natural sepiolites and palygorskite.

Phases[#] \ Sample	10_PangelS9 [%]	11_Pansil [%]	12_Palygorskite [%]
Sepiolite	90.7 ± 2.2	71.6 ± 2.4	-
Palygorskite	-	-	47.0 ± 2.7
Muscovite / Illite	8.2 ± 2.1	8.6 ± 1.7	-
Kaolinite	-	-	2.9 ± 1.3
Chlorite	-	-	8.1 ± 2.7
K-Feldspars (Orthoclase)	-	6.9 ± 1.4	5.9 ± 1.4
Plagioclase (Albite)	-	7.1 ± 1.4	-
Quartz	-	4.1 ± 1.1	22.6 ± 1.6
Calcite	1.1 ± 0.8	1.7 ± 0.7	-
Dolomite	-	-	10.5 ± 1.1
Jarosite	-	-	3.1 ± 0.8

In parenthesis the structure model used for Rietveld analysis is given.

Chemical composition

The chemical composition is shown in Table 4.31. The chemical composition of the purified and fractionated material of the sepiolite Pangel S9 sample was used to calculate its structural formula. According to Stevens (1945), the stoichiometric composition of the fraction < 0.2 µm is given as:

$$Me^{+}_{0.11}(Si_{5.91}Al^{3+}_{0.09})(Mg^{2+}_{3.63}Al^{3+}_{0.18}Fe^{3+}_{0.06})[O_{15}(OH)_2]\cdot 2H_2O + 4H_2O\,.$$

Table 4.31 XRF-analysis of the natural sepiolites and palygorskite.

Oxides		10_PangelS9	11_Pansil	12_Palygorskite
SiO_2	[%]	53.59	57.51	52.76
Al_2O_3	[%]	2.51	3.17	8.54
MgO	[%]	22.93	19.23	8.62
Fe_2O_3	[%]	0.81	0.59	2.79
TiO_2	[%]	0.12	0.12	0.52
MnO	[%]	0.03	0.01	0.09
Na_2O	[%]	0.09	0.36	0.12
CaO	[%]	0.34	0.90	2.83
K_2O	[%]	0.63	1.07	0.80
P_2O_5	[%]	0.05	0.04	0.02
LOI	[%]	18.9	17.0	22.9

Thermal reactions

Sepiolite and palygorskite showed a similar thermal behaviour, but different to that of smectite and vermiculite. The dehydroxylation of palygorskite started at lower temperature than that of sepiolite (Figure 4.22).

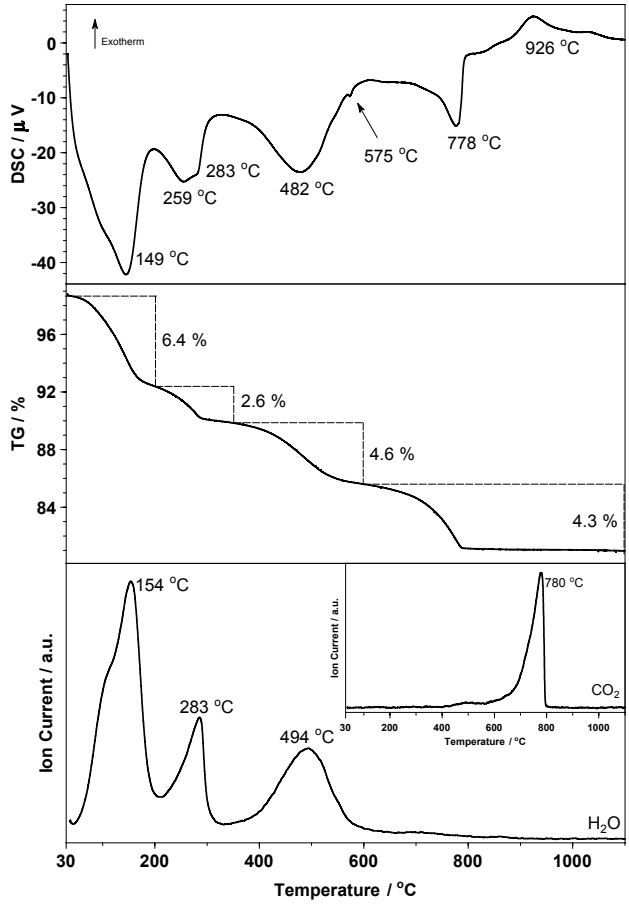

Figure 4.22 DSC, TG and MS curve of palygorskite (12_Palygorskite).

The DSC curve of palygorskite showed two endothermic peaks in the region below 300 °C. Both are associated with maxima in the MS curve of water. The peak at lower temperature (149 °C) mirrored the release of adsorbed and zeolitic water and the broad peak at higher temperature with two maxima showed the release of coordinated water. In contrast to sepiolites, palygorskite did not release its coordinated water stepwise (see Chapter 4.5.1).

The complete dehydroxylation occurred below 500 °C. Above 500 ° C, there is no water left. The two further endothermic peaks can be assigned to the transformation of low to high quartz (575 °C) and to the decomposition of the carbonate mineral calcite (778 °C). This latter peak is associated with a maximum at 780 °C in the MS curve of CO_2.

The decomposition of palygorskite is overlapped by the decomposition of calcite. According to Jones and Galan (1988), palygorskite is amorphous above 700 °C. The exothermic peak at 926 °C can be attributed to the recrystallisation of the material.

Exchange behaviour and interlayer cations

Cu-triethylenetetramine is used to estimate the CEC of sepiolite and palygorskite (Table 4.32). Similar to the previously discussed minerals, the variations between the raw material and the isolated fractions are caused by the presence of additional phases in the natural material, which contribute a decrease in measured CEC. Compared to the non-purified material, the purified bulk material of the sepiolite Pangel S9 (10_PangelS9) had a CEC of 16 meq/100g.

Table 4.32 CEC of sepiolites and palygorskite.

Sample	CEC raw material [meq/100g]	CEC fraction < 2 µm [meq/100g]	CEC fraction < 0.2 µm [meq/100g]
10_PangelS9	14	16 *	19 *
11_Pansil	11	19	-
12_Palygorskite	5	10	-

* The separation of the three fractions occurred after purification of the raw material.

The CEC of these materials is located in the lower range of the published CEC values for sepiolites and palygorskite (Vivaldi and Hach-Ali, 1970). The CEC of palygorskite is reported to vary from below 10 to 35 meq/100g and that for sepiolite between 25 and 45 meq/100 g.

Cations in these minerals can be exchanged against alkylammonium ions, but the alkyl chains are too short to produce bilayers. Therefore, the layer charge of sepiolite and palygorskite cannot be measured with the alkylammonium method. Thus, the layer charge has to be estimated from the measured CEC (Table 4.33) and from the chemical

composition. For the purified < 0.2 µm fraction of the sepiolite Pangel S9, a layer charge of 0.12 eq/FU was calculated from the structural formula.

Table 4.33 Calculated layer charge of sepiolite and palygorskite, using CEC values.

Sample	ξ [eq/FU] raw material	ξ [eq/FU] fraction < 2 µm	ξ [eq/FU] Fraction < 0.2 µm
10_PangelS9	0.18	0.21 *	0.24 *
11_Pansil	0.14	0.24	-
12_Palygorskite	0.04	0.08	-

* The separation of the fractions occurred after purification of the raw material.

4.5.2 Thermal transformation of sepiolite

The characterisation of all clay materials investigated in this study revealed that the thermal behaviour of sepiolite was different to that of smectite and vermiculite. The thermal behaviour was investigated by various high temperature techniques, including STA, XRD and FTIR spectroscopy. Upon heating, the mineral undergoes complex structural changes (Nagata et al., 1974; Serna et al., 1975). Therefore, these three techniques were combined in a comparative investigation of phase transitions, structural changes and dehydration reactions during heating of a sepiolite sample (Pangel S9) from 30 to 900 °C in order to understand the thermal behaviour of sepiolite.

Methods

The thermal behaviour of sepiolite was observed with a STA equipment (STA 449 C Jupiter, Netzsch), which was connected to a quadrupole mass spectrometer (QMS 403 C, Aeolos, Netzsch). Thirty mg were heated to 1100 °C (Pt-crucible with lid) with a heating rate of 10 K/min. N_2 was used as protective gas (20 ml/min) and synthetic air as purging gas (50 ml/min).

The XRD measurements were performed on a Bruker AXS D8 diffractometer (CuKα radiation) equipped with a high-temperature chamber (MRI TC1200). Patterns were recorded between 5 and 50° 2θ (step size: 0.013° 2θ/s). A temperature range from 80 to 900 °C was chosen, with a heating rate < 1 K/min. A data set containing 31 patterns was obtained. Prior to and after heating, XRD patterns at room temperature were recorded. Silicon powder was used as calibration standard.

In comparison to the temperatures of the DSC signals, the reaction temperatures in the X-ray patterns lie somewhat lower. This can be explained by the lower heating rate (< 1 K/min, DSC: 10 K/min). Thus, the material has more time to react during the X-ray measurements.

FTIR spectra were recorded on a Bruker IFS66/S spectrometer equipped with a DTGS detector using KBr-pellets. Thirty-two scans were recorded in the 4000 - 400 cm^{-1} range with a resolution of 4 cm^{-1}. Four sepiolite samples were heated at 350, 500, 700 and 820 °C for 2 h and then quenched. From each heated specimen, a KBr pellet was pressed (1 mg sample : 300 mg KBr).

Results and Discussion

The DSC curve (Figure 4.23) shows the release of adsorbed and zeolitic water up to 200 °C, which is associated with a mass loss of 9% (A). At higher temperatures, two endothermic peaks occurred at 304 and 344 °C. The first is correlated to a maximum at 332 °C in the MS curve and displayed the partial release of coordinated water (B). The very small peak at 344 °C, which is not associated with any release of gases, can be attributed to the transformation of the sepiolite to its anhydrous form (Nagata et al., 1974).

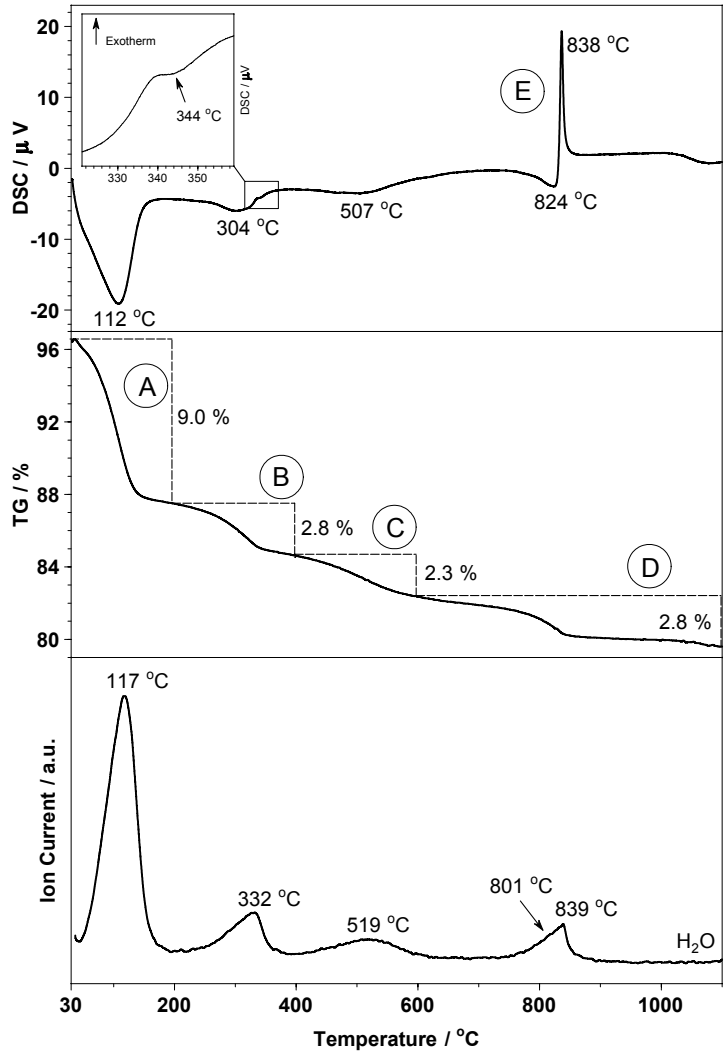

A)
$Mg_8 (OH)_4 [Si_{12} O_{30}] * 4 H_2O + 8 H_2O$

↓ - 8 H_2O

$Mg_8 (OH)_4 [Si_{12} O_{30}] * 4 H_2O$

B)
$Mg_8 (OH)_4 [Si_{12} O_{30}] * 4 H_2O$

↓ - 2 H_2O

$Mg_8 (OH)_4 [Si_{12} O_{30}] * 2 H_2O$

C)
$Mg_8 (OH)_4 [Si_{12} O_{30}] * 2 H_2O$

↓ - 2 H_2O

$Mg_8 (OH)_4 [Si_{12} O_{30}]$

D)
$Mg_8 (OH)_4 [Si_{12} O_{30}]$

↓ - 2 H_2O

$Mg_8 [Si_{12} O_{30}] + 2 H_2O + O_2$

E)
$Mg_8 [Si_{12} O_{30}] + O_2$

↓

8 ($Mg [Si O_3]$) + 4 SiO_2

Figure 4.23 DSC, TG and MS curve of sepiolite (10_PangelS9), as well as the stoichiometric formula of sepiolite and the several steps of water release (A trough E).

The anhydrous phase occurred, when half of the coordinated water at the edges of the octahedral sheets is removed (Frost and Ding, 2003). The second part of the coordinated water is released at 508 °C, while in the MS curve the maximum occurred at 519 °C. The release of coordinated water is associated with a mass loss of 5.1% (C).

The MS curve indicated a two-step dehydroxylation of sepiolite. One part of the hydroxyl groups is released at 801 °C, the other at 839 °C. The dehydroxylation is associated with a mass loss of 2.8% (D). In contrast to smectites, the transition from dehydroxylation to decomposition and to recrystallisation (formation of enstatite $Mg[SiO_3]$; Brauner and Preisinger, 1956) occurred in sepiolites over a much smaller temperature range (800 °C - 840 °C) (E). This is attributed to the unique "channel-like" structure of sepiolite.

The X-ray pattern (Figure 4.24) recorded at room temperature showed the characteristic d_{110} peak of sepiolite at 1.21 nm.

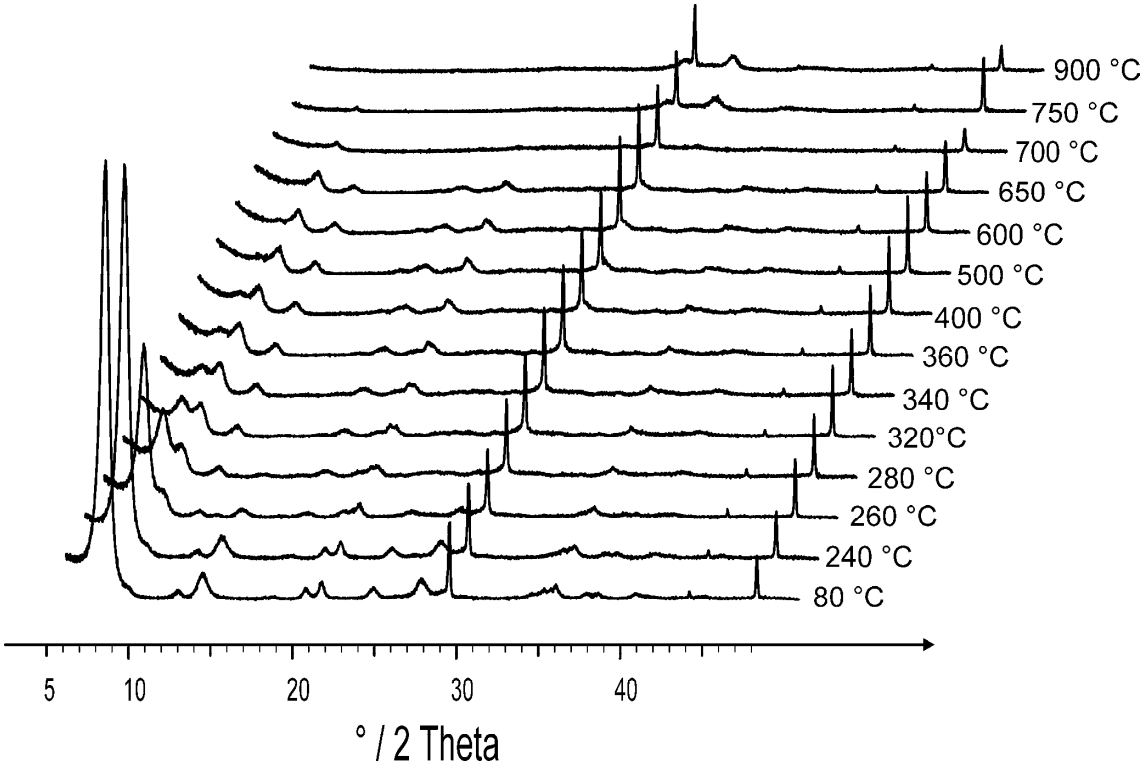

Figure 4.24 Sequence of XRD patterns of sepiolite in dependence on the temperature.

During heating up to 280 °C, the intensity of the d_{110} peak strongly decreased while the intensity of the d_{001} peak at 1.01 nm slightly increased. In addition, a new d_{110} peak occurred at 0.82 nm. This new peak reflects the transformation from sepiolite into a sepiolite anhydrous form. At about 500 °C, the d_{110} peak at 1.21 nm completely disappeared, while the intensity of the other two peaks (d_{001} = 1.01 nm and d_{110} = 0.82 nm) increased slightly. Within the temperature range from 600 to 650 °C, the intensity of the 0.82 and 1.01 nm peaks gradually decreased. At 700 °C, the 0.82 nm peak disappeared completely and two new

peaks at 0.32 nm (d_{220}) and 0.29 nm (d_{-221}) appeared indicating the occurrence of the high temperature mineral enstatite (Brauner and Preisinger, 1956).

As expected, the FTIR spectra showed distinct changes in the OH stretching region with increasing temperature (Figure 4.25a). The band at 3745 cm^{-1} can be attributed to a Si-OH vibration. The intensity of this vibration increased with increasing temperature, because of new hydrogen bonds associated with the folded structure of the anhydrous sepiolite phase. The bands at 3687 and 3629 cm^{-1} can be assigned to Mg-OH stretching modes. Both disappeared below 500 °C, which reflect the complete release of the coordinated water at the edges of the octahedral sheets (Frost et al., 1998).

Above 350 °C, three new OH stretching vibrations at 3675, 3596 and 3533 cm^{-1} occurred because the adsorbed and zeolitic water are lost and a part of the vibrations are then free to vibrate. The band at 3675 cm^{-1} can be attributed to a MgO stretch vibration. The other bands at 3596 and 3533 cm^{-1} are assigned to OH stretching vibrations.

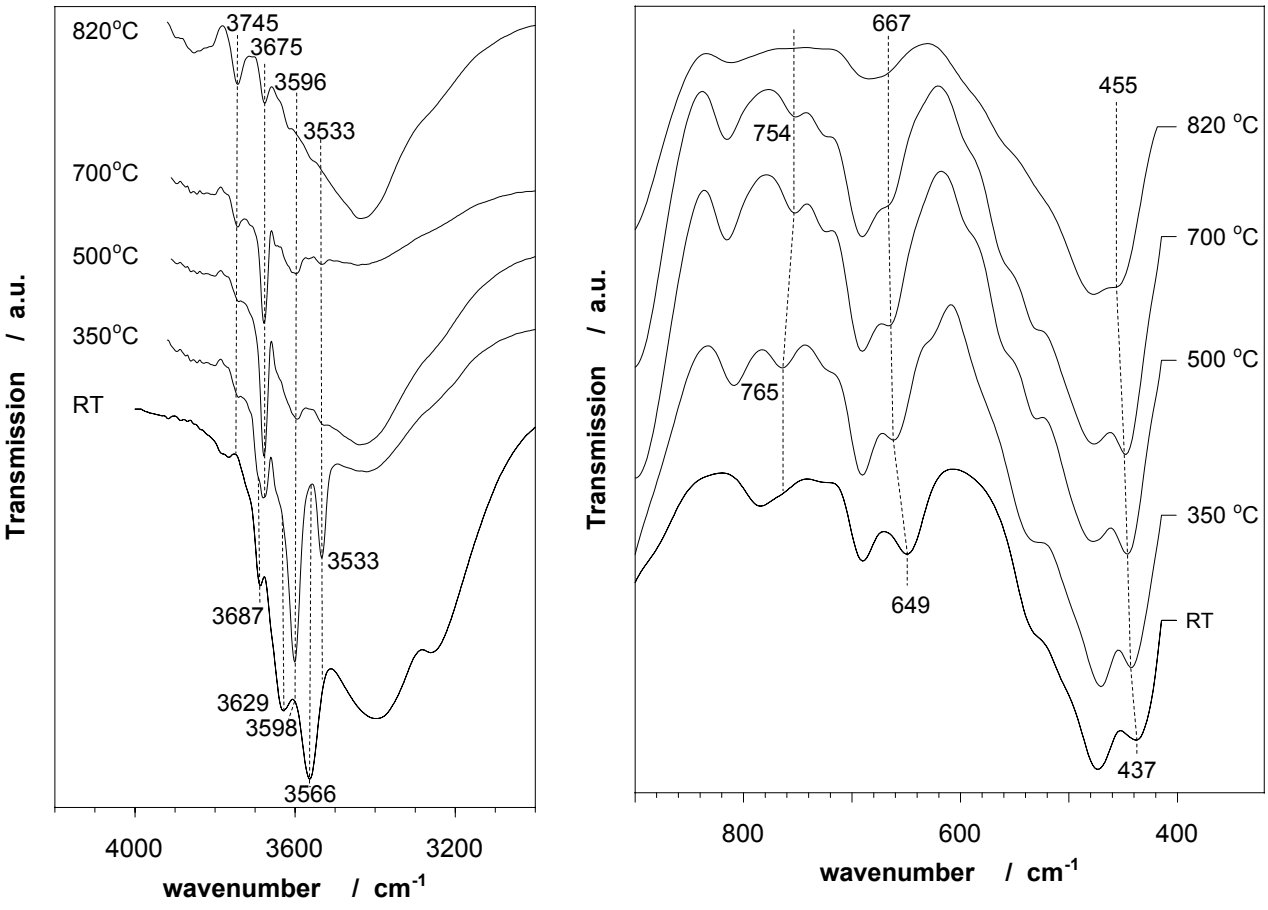

a) OH stretching region b) OH bending region

Figure 4.25 FTIR spectra of sepiolite and thermal treated sepiolite a) in the region between 3000 and 4000 cm^{-1} and b) 400 and 900 cm^{-1}.

The new vibrations are associated with the formation of the folded structure of an anhydrous sepiolite phase (Nagata et al., 1974), which can be observed in the DSC curve at 344 °C. The lower bands disappeared above 700 °C. This temperature reflects the ongoing release of hydroxyl groups. Another band at 3566 cm^{-1} can be attributed to a OH stretching of coordinated water. It disappeared at 350 °C, reflecting the partial release of coordinated water.

The heat treatment and the release of hydroxyls obviously affect the SiO-structure of sepiolite (Figure 4.25b). The band at 765 cm^{-1} can be attributed to an OH deformation, which occurred at 350 °C and shifted to lower wavenumbers. This vibration reflected the formation of hydrogen bonds within the new folded structure of the anhydrous phase. The band at 649 cm^{-1} can be assigned to an OH translation, which shifts to 667 cm^{-1} with increasing temperature. The vibration reflected the release of water molecules bound to Mg-O sites. The band at 437 cm^{-1} can be attributed to an O-Si-O bend, which shifts to 455 cm^{-1} with increasing temperature. The vibration is caused by distortions and weakening of the Si-O-Mg bonds between tetrahedral and octahedral sheets (Vicente-Rodriguez et al., 1996).

Conclusions

Changes in X-ray patterns show the transformation of sepiolite into an anhydrous sepiolite phase at about 280 °C. This is confirmed by the results of DSC measurements, which suggest that new XRD peaks occur, when half of the coordinated water is removed. Furthermore, two dehydration steps and two dehydroxylation steps are observed over the temperature range from 300 to 850 °C. FTIR spectroscopic results indicate that remarkable structural changes occur. Especially, the formation of the anhydrous sepiolite phase is characterized by a rotation and folding of the original sepiolite structure and by the formation of new O-Si-O bonds.

4.6 Kaolin and Kaolinite

Kaolinite belongs to the 1:1 layer silicates with a layer charge of 0. Three kaolin samples, which contain kaolinite with varying particle size, were investigated. Polwhite has 40% of the < 2 µm fraction, whereas the other two samples possess about 80% of the < 2 µm fraction. The d_{10}, d_{50} and d_{90} values of the three kaolin samples are shown in Table 4.34.

Table 4.34 Grain size distribution of the natural kaolin samples.

Sample		d_{10}	d_{50}	d_{90}
13_Pol	[nm]	244	1109	2022
14_Kaolex	[nm]	104	314	1317
15_Rogers	[nm]	97	390	1377

Morphology and surface

The crude kaolinites consist of platy particles with a pseudohexagonal habit (Figure 4.26, Appendix). Different particle sizes influenced the measured specific surface area. The specific surface area of the raw kaolinites ranged from 10 to 25 m^2/g. Two kaolinites (14_Kaolex, 15_Rogers) have smaller particles, which caused a higher specific surface area compared to the other kaolinite (13_Pol).

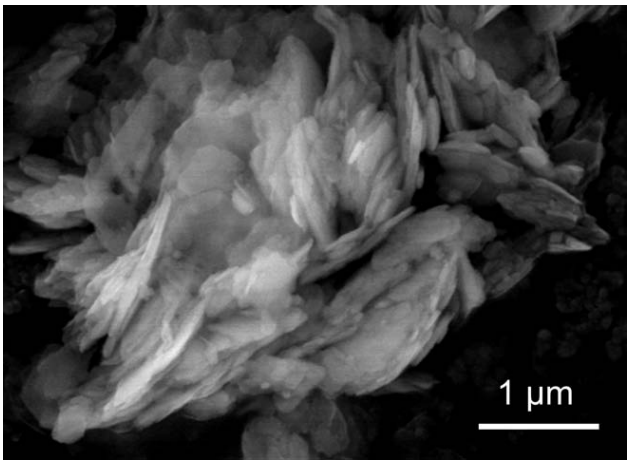

Figure 4.26 ESEM image shows the morphology of the kaolinite Rogers (15_Rogers).

Mineralogy and chemical composition

The kaolinite content of the kaolin raw materials ranged from 71 to 87%. All samples have similar impurities like quartz, mica, feldspars, smectite and anatase (Table 4.35).

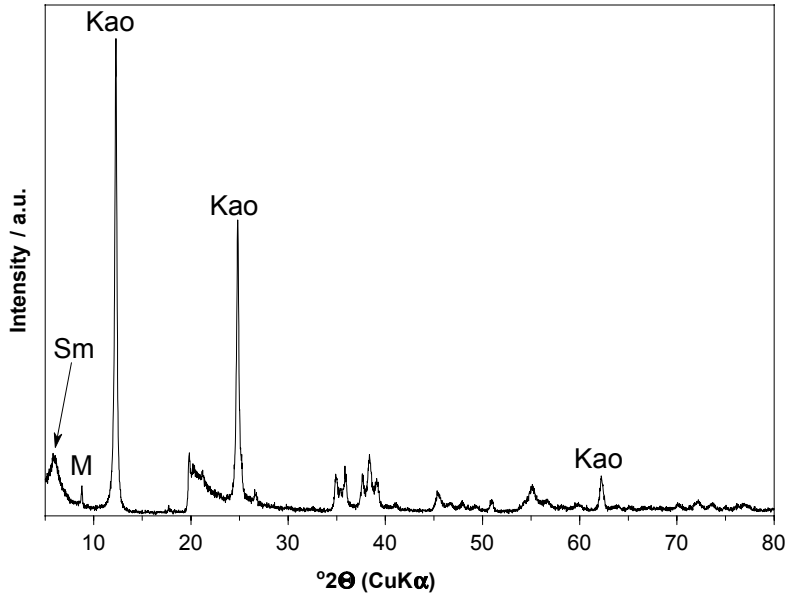

Figure 4.27 X-ray pattern (powder sample) of the kaolin Rogers (15_Rogers);
Kao: characteristic kaolinite peaks with increasing 2θ (001), (002), (060);
Qz: Quartz; M: Muscovite/Illite; Sm: Smectite.

The existence of smectite as impurity was verified by the measured CEC (Table 4.36) using a CEC of 82 meq/100g for the calculation. The X-ray pattern of the kaolin Rogers is shown in Figure 4.27. The chemical composition of the used kaolin is listed in Table 4.37.

Table 4.35 Quantification of the natural kaolin samples.

Phases[#] \ Sample	13_Pol [%]	14_Kaolex [%]	15_Rogers [%]
Kaolinite	71.4 ± 1.4	85.3 ± 1.3	86.1 ± 2.6
Muscovite \ Illite	9.2 ± 0.7	-	-
Fe-rich Muscovite \ Illite	-	6.6 ± 1.1	3.3 ± 1.0
Smectite	6.9 ± 1.1	5.1 ± 1.0	9.1 ± 2.9
Orthoclase	10.8 ± 0.6	-	-
Quartz	1.7 ± 0.4	1.5 ± 0.3	-
Anatase	-	1.5 ± 0.3	1.4 ± 0.3

In parenthesis the structure model used for Rietveld analysis is given.

Table 4.36 CEC of the kaolin samples.

Sample	13_Pol	14_Kaolex	15_Rogers
CEC [meq/100g]	6	4	10
Smectite [%]	7	5	12

Table 4.37 XRF-analysis of the natural kaolin.

Oxides		13_Pol	14_Kaolex	15_Rogers
SiO_2	[%]	49.72	44.72	45.69
Al_2O_3	[%]	33.85	36.34	35.98
MgO	[%]	0.30	0.08	0.33
Fe_2O_3	[%]	0.96	1.58	0.97
TiO_2	[%]	0.04	1.58	1.39
MnO	[%]	0.02	0.00	0.00
Na_2O	[%]	0.00	0.00	0.00
CaO	[%]	0.03	0.00	0.16
K_2O	[%]	3.02	0.47	0.27
P_2O_5	[%]	0.16	0.10	0.07
LOI	[%]	11.9	14.2	15.1

The potassium content of the kaolin sample Polwhite was noticeably higher than that of the other two samples (Kaolex and Rogers). The mica in the kaolin samples Kaolex and Rogers was to be an illite or an iron-rich muscovite. Up to 8.5% iron can be incorporated into the mica (muscovite) structure (Rösler, 1979). Kaolin sample (13_Pol) contained K-rich feldspar (orthoclase) besides a mica phase.

K-feldspar and muscovite have the same potassium content in mol per formula unit, but the potassium content related to the molecular weight of the formula unit varied strongly, because 1 mol K^+ in the muscovite corresponds to nearly 11.8% K_2O and 1 mol K^+ in K-feldspar corresponds to 16.9% K_2O. The different influence of the K contents is depicted by an example based on two fictive samples. The chemical data of these two samples are listed in Table 4.38. Sample A has a total K_2O content of 2.7% and sample B of 0.5%. Sample A includes muscovite (8%) and K-feldspar (10%). Sample B includes only muscovite (4%) as K-rich phase. Eight percent muscovite contain nearly 1% K_2O and 10% K-feldspar contain nearly 1.7% K_2O that means the content of potassium in the muscovite is lower than in K-feldspar.

Table 4.38 Chemical data of the two fictive samples A and B.

Sample	A	B
Muscovite [%]	8	4
K-feldspar [%]	10	-
K_2O content from Muscovite [%]	0.95	0.47
K_2O content from K-Feldspar [%]	1.69	-
Total amount of K_2O [%]	2.7	0.5

An increasing amount of K-feldspar has a higher influence on the total K_2O content than the increase of muscovite. Therefore, the difference in the chemistry between sample A and B are noticeable higher than in the quantification, which is valid for sample 13_Pol and 14_Kaolex, too.

Short range order

The FTIR spectra of the raw kaolin samples (Figure 4.28, Appendix) generally showed a number of sharp vibration bands, especially in the region between 400 and 1200 cm^{-1}. Their assignments are listed in Table 4.39 (Farmer, 1974; Makó et al., 2006).

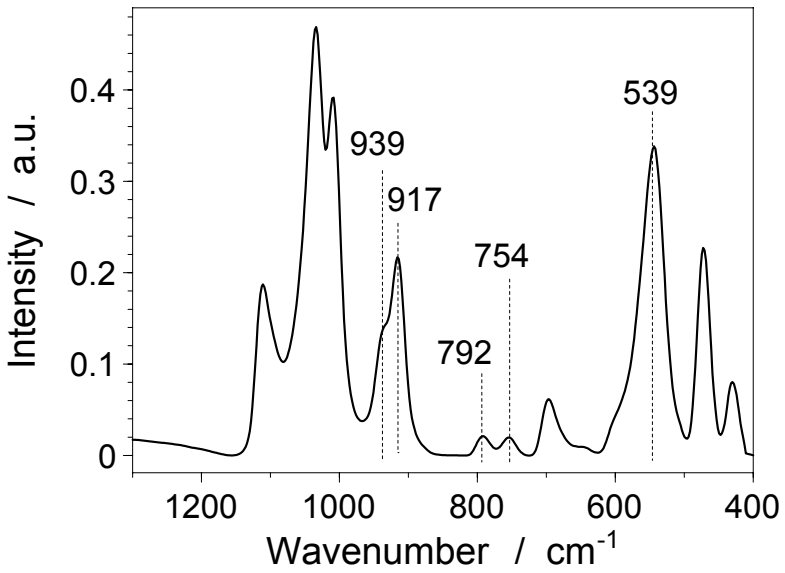

Figure 4.28 FTIR spectra of the kaolin Rogers (15_Rogers).

The bands at 939, 917, 792, 754 and 539 cm^{-1} are to be connected to aluminium in tetrahedral and octahedral positions. The vibrations at 939 and 917 cm^{-1} can be assigned to OH deformations, which also give information on the content of aluminium in the octahedral sheet. The lower bands at 792 and 754 cm^{-1} can be assigned to Si-O-Al vibrations. They indicate linkage between octahedral aluminium and tetrahedral silicon via an oxygen atom. The vibration at 539 cm^{-1} can be attributed to a Si-O-Al bending vibration within the tetrahedral sheet. All the other bands at 1110, 1030, 472 cm and 431 cm^{-1} are strong Si-O vibrations.

Table 4.39 Positions and assignments of the vibrational bands in the lattice region of the raw kaolinite.

Wavenumber [cm^{-1}]	Assignment*
1110	(apical) Si-O out-of-plane
1030	Si-O in-plane
939	inner surface OH deformation
917	inner OH deformation
792	Si-O-Al vibrations
754	Si-O-Al vibrations
698	OH translation
644	inner surface OH vibration
539	Si-O-Al (out-of-plane) bending (Al in the tetrahedral sheet)
472	Si-O (in-plane) bending associate with OH
431	Si-O bending

* Farmer, 1974; Makó et al., 2006.

Thermal reactions

All three kaolin samples showed an endothermic peak around 545 °C and an exothermic peak between 970 and 990 °C in the DSC curve (Figure 4.29). The first is correlated to a maximum in the same range in the MS curve of H_2O and indicates the release of hydroxyl groups. The sharp peak at higher temperature is not associated with any release of gases and can be attributed to the recrystallisation of the mullite phase.

The dehydroxylation temperature gives additional information on the kaolinite crystallinity (Smykatz-Kloss, 1974). Ordered kaolinites show a dehydroxylation maximum between 570 and 600 °C. In comparison, the dehydroxylation maximum of disordered kaolinites is shifted to lower temperatures (between 540 and 570 °). All three kaolinites in this study showed a dehydroxylation below 570 °C. Additionally, disordered kaolinites show a weak endothermic peak below 200 °C, which indicates the release of some adsorbed water. All three kaolinites in this study showed a small dehydration between 80 and 100 °C. In addition to the peak at 98 °C, the kaolin Rogers showed a further dehydration peak at 156 °C. This endothermic peak, which is associated with the release of water, is an indication of the existence of a smectite phase in this particular sample. This was supported by X-ray diffraction and by cation exchange measurements.

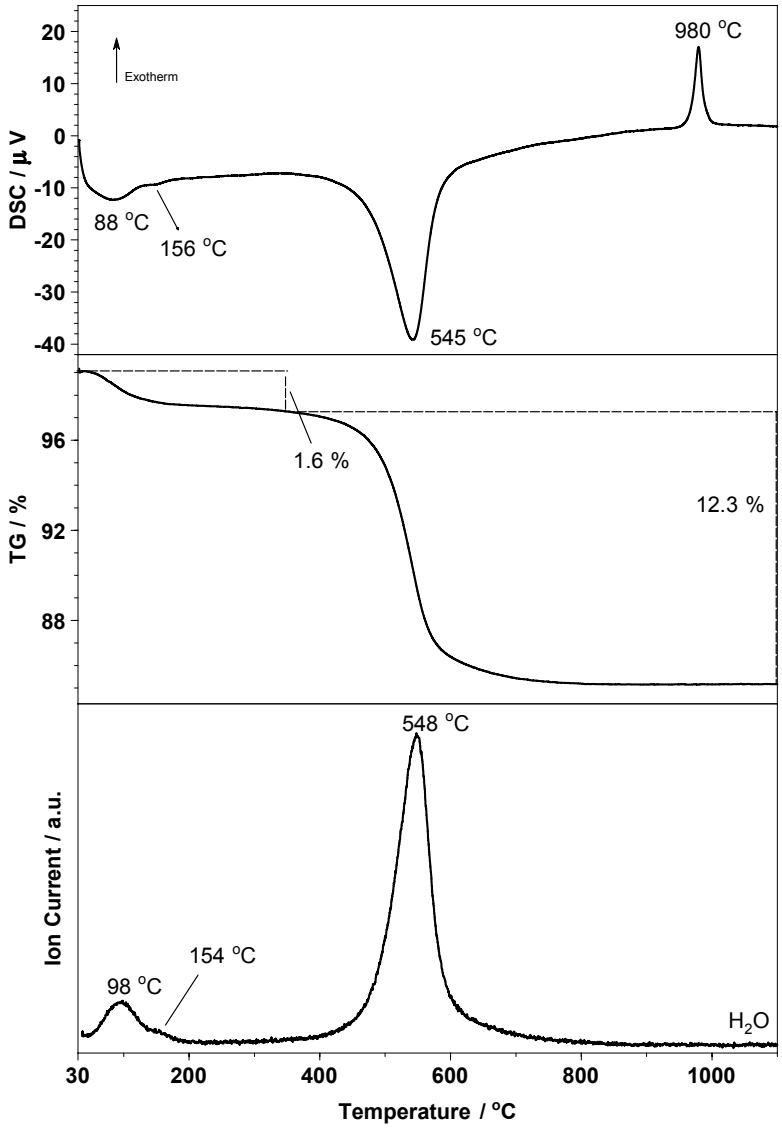

Figure 4.29 DSC, TG and MS curve of the kaolin Rogers (15_Rogers).

4.7 Magadiite

The Magadiite (16_Mag) in this work is a synthesised silicic acid with sodium, which has the ability to exchange organic molecules (e.g., copper triethylenetetramine). The measured CEC is 54 meq/100g. Natural magadiite was found in the area of the Lake Magadi in Kenya (Eugster, 1967).

Morphology and surface

Magadiite has a layered appearance. The magadiite consists of agglomerated particles with an irregular shape and partly sharp grain boundaries (Figure 4.30). The morphology of the magadiite is similar to that of smectite in bentonites.

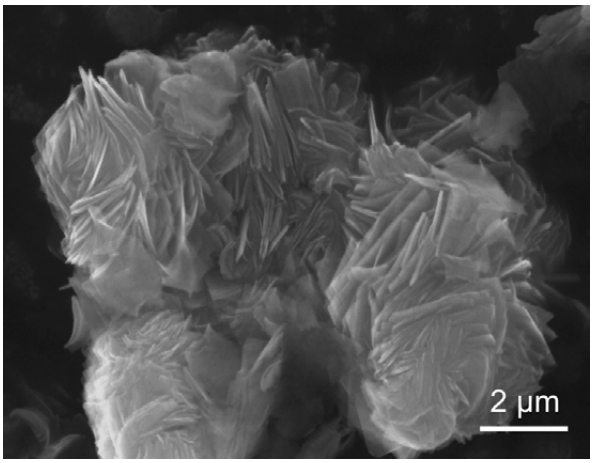

Figure 4.30 ESEM image shows the morphology of the magadiite (16_Mag).

The natural magadiite has a specific surface area of 30 m^2/g, which is close to that of smectite. In comparison to smectites, magadiite is more porous, having a higher amount of micropores (14 m^2/g).

Mineralogy

X-ray powder data were published by Brindley (1969) and are identical with the magadiite investigated in this work (Figure 4.31). The d_{001} peak is the strongest line in the X-ray pattern with a basal spacing of 0.156 nm.

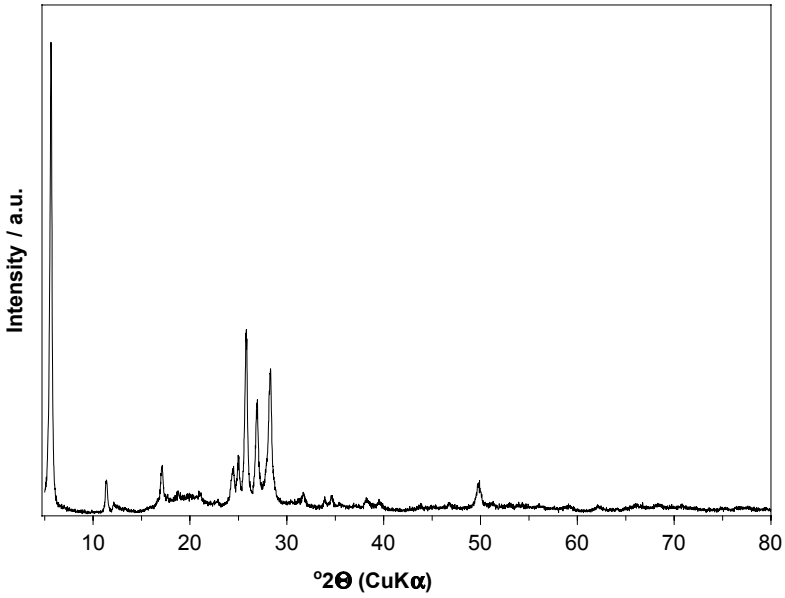

Figure 4.31 X-ray pattern (powder sample) of the magadiite (16_Mag). All peaks originated from magadiite.

Chemical composition

The chemical composition is shown in Table 4.39. The magadiite contains silicon and sodium as main elements, as well as low amounts of aluminium and iron (Table 4.40). Its has the following structural formula: $NaSi_7O_{13}(OH)_3 \cdot 3H_2O$ (Eugster, 1967) or $NaSi_7O_{13}(OH)_3 \cdot 4H_2O$ (Brindley, 1969), respectively.

Table 4.40 XRF-analysis of the magadiite.

Oxides		16_Mag
SiO_2	[%]	77.91
Al_2O_3	[%]	0.36
Fe_2O_3	[%]	0.20
TiO_2	[%]	0.03
Na_2O	[%]	6.09
K_2O	[%]	0.02
LOI	[%]	15.4

Short range order

According to previous studies (Eypert-Blaison et al., 2001; Superti et al., 2007), the FTIR spectra of magadiite (Figure 4.32) can be divided into three parts. In the first region (1000 - 1300 cm^{-1}), four absorption bands at 1236, 1201, 1172 and 1081 cm^{-1} are observed, which can be assigned to the antisymmetric stretching vibrations of Si-O-Si bridges. In the second region (700 - 1000 cm^{-1}), four vibrations at 941, 819, 786 and 707 cm^{-1} are visible. These bands can be attributed to symmetric stretching vibrations of the Si-O-Si bridges.

In the third region between 400 and 700 cm^{-1}, bands at 620, 578, 543 and 457 cm^{-1} are observed. These absorption bands can be assigned to Si-O-Si and O-Si-O bending vibrations.

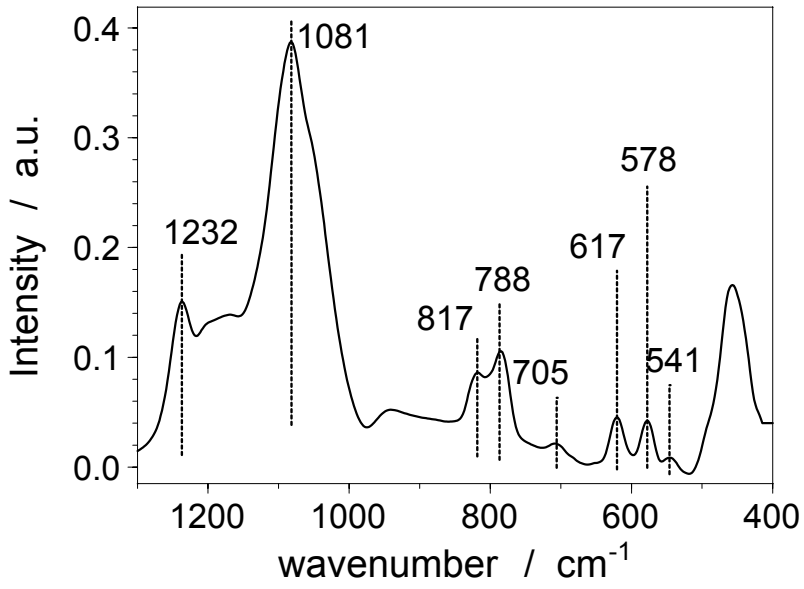

Figure 4.32 FTIR spectra of the magadiite (16_Mag).

Thermal reactions

The DSC curve showed three endothermic peaks in the temperature range between 100 and 310 °C (Figure 4.33). These peaks are correlated to maxima in the MS curve and represent the release of adsorbed and interlayer water molecules. The dehydration occurred stepwise and is associated with a mass loss of 13.5%.

A weak mass loss of 1% was observed in the temperature range between 350 and 650 °C. This mass loss is associated with a small peak in the MS curve. The release of water here is attributed to the dehydroxylation of silanol groups of the magadiite framework in combination with the formation of siloxane bonds (Superti et al., 2007).

Two further peaks are observed at higher temperatures in the DSC curve. Both peaks are not associated with the release of any gases. The peak at 721 °C is endothermic and can be attributed to the decomposition of magadiite. This decomposition peak is followed by an exothermic peak at 722 °C, which can be assigned to the recrystallisation of the magadiite phase to a quartz-like phase.

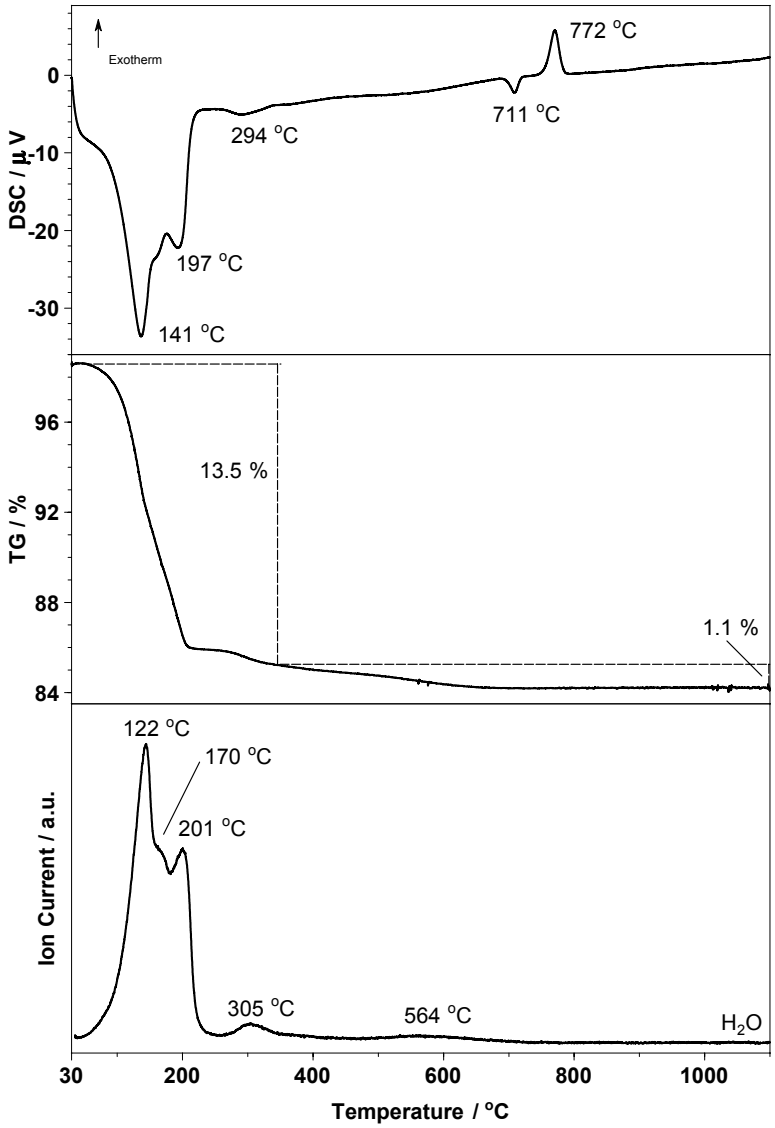

Figure 4.33 DSC, TG and MS (H_2O and CO_2) curve of the magadiite (16_Mag).

4.8. Conclusions

The materials were characterised with several mineralogical and chemical methods including XRD, STA, BET, ESEM, XRF, CEC, layer charge (ξ) ICP-OES and FTIR. The results of this characterisation were used as basis for selection of different clay minerals for the subsequent investigation of a) characterisation of layer charge reduced materials and of b) the characterisation of the edges (Chapter 5) (Figure 4.34).

Sepiolite Pangel S9 was chosen due to its small amount of impurities compared to the other two fibrous minerals. The Indian Bentonite was selected due to its higher layer charge in comparison with the other dioctahedral smectites. The Volclay was selected due to its lower layer charge compared to the Indian Bentonite and is used as standard in our institute. The vermiculite was chosen due to its swellability compared to the illite and due to its higher layer charge and its layer appearance compared to the smectite.

While several clay minerals were characterised comprehensively, special attention was paid to the cation exchange behaviour of vermiculite. After grinding and purification, which was combined with a homoionic exchange (Na^+), it was possible to exchange all interlayer cations against Cu-triethylenetetramine (Cu-trien). On the basis of these results vermiculite can be used to prepare pillared clays, which will upgrade the spectrum of the charge density, remarkably.

The raw material of all swellable and non-swellable clay minerals, except sepiolite (11_Pansil) and palygorskite (12_Palygorskite), were used for the structural modification with mineral acids to receive information on their stability and to prepare materials with a simple chemical composition, which have a similar layered morphology like the untreated materials and which still will have the ability to adsorb organic molecules.

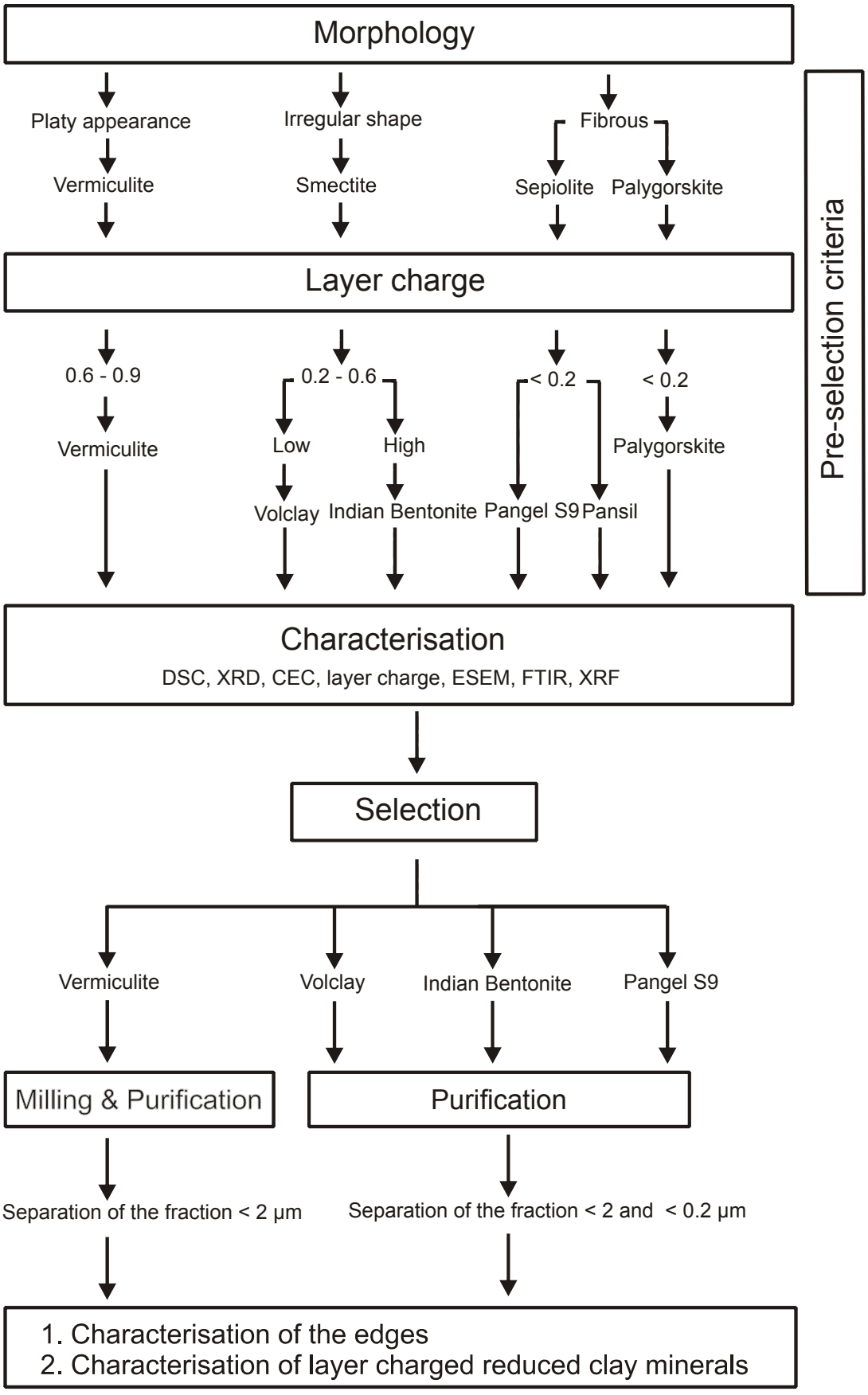

Figure 4.34 Selection scheme, sample preparation and analytical scope for the individual clay minerals.

References

Brauner K. and Preisinger A. (1956) Struktur und Entstehung des Sepioliths. Tschermaks mineralogisch petrologische Mitteilungen **6**, pp. 120-140.

Brindley G. W. (1969) Unit cell of magadiite in air, in vacuum, and under other conditions. The American Mineralogist **54**, pp. 1583-1591.

Brindley G. W. and Brown G. (1980) Crystal structures of clay minerals and their X-ray identification. Mineralogical Society, Monograph 5, London, pp. 539.

Drits V. A., Besson G. and Muller F. (1995) An improved model for structural transformations of heat-treated aluminous dioctahedral 2:1 layer silicates. Clay and Clay Minerals **43**, pp. 718-731.

Drits V. A., Lindgreen H., Salyn A. L., Ylagan R. and McCarty D. K. (1998) Semiquantitative determination of trans-vacant and cis-vacant 2:1 layers in illites and illite-smectites by thermal analysis and X-ray diffraction. American Mineralogist **83**, pp. 1188-1198.

Eugster H. P. (1967) Hydrous sodium silicates from Lake Magadi, Kenya; precursors of bedded chert. Science **157**, pp. 1177-1180.

Eypert-Blaison C., Humbert B., Michot L. J., Pelletier M., Sauzeat E. and Villieras F. (2001) Structural role of hydration water in Na- and H-Magadiite: A spectroscopy study. Chemistry of Material **13**, pp. 4439-4446.

Farmer V. C. (1974) The infrared spectra of minerals. Mineralogical Society, Monograph 4, London, pp. 539.

Frost R. L., Cash G. A. and Kloprogge J. T. (1998) 'Rocky Mountain leather', sepiolite and attapulgite – an infrared emission spectroscopic study. Vibrational Spectroscopy **16**, pp. 173-184.

Frost R. L. and Ding Z. (2003) Controlled rate thermal analysis and differential scanning calorimetry of sepiolites and palygorskites. Thermochimica Acta **397**, pp. 119-128.

Jasmund K. and Lagaly G. (1993) Tonminerale und Tone: Struktur, Eigenschaften, Anwendung und Einsatz in Industrie und Umwelt. Steinkopff Verlag, Darmstadt, pp. 490.

Jones B. F. and Galan E. (1988) Sepiolite and Palgorskite in Hydrous Phyllosilicates (exclusive of micas). Bailey S. W. (ed.), Mineralogical Society of America **19**, BookCrafters Inc., Michigan, pp. 631-674.

Komadel P., Janek M., Madejová J., Weekes A. and Breen C. (1997) Acidity and catalytic activity of mildly acid-treated Mg-rich montmorillonite and hectorite. Journal of Chemical Society, Faraday Transactions. **93**(23), pp. 4207-4210.

Komadel P., Madejová J., Janek M., Gates W. P., Kirkpatrick R. J. and Stucki J. W. (1996) Dissolution of hectorite in inorganic acids. Clays and Clay Minerals **44**(2), pp. 228-236.

Komadel P., Schmidt D., Madejová J. and Čičel B. (1990) Alteration of smectites by treatments with hydrochloric acid and sodium carbonate solutions. Applied Clay Science **5**, pp. 113-122.

Köster H. M. (1977) Die Berechnung kristallchemischer Strukturformeln von 2:1-Schichtsilikaten unter Berücksichtigung der gemessenen Zwischenschichtladungen und Kationenaustauschkapazitäten, sowie die Darstellung der Ladungsverteilung in der Struktur mittels Dreieckskoordinationen. Clay Minerals **12**, pp. 45-54.

Lagaly G. (1989) Erkennung und Identifizierung von Tonmineralen mit organischen Stoffen. Jahrestagung der deutschen Ton- und Tonmineralgruppe (DTTG), pp. 86-130.

Lagaly G. (1994) Layer charge determination by alkylammonium ions in layer charge characteristics of 2:1 silicate clay minerals. Mermut A. R. (ed.), The Clay Minerals Society **6**, Aurora, pp. 1-46.

Lagaly G. and Weiss A. (1970) Anordnung und Orientierung kationischer Tenside auf ebenen Silicatoberflächen Teil IV. Kolloid-Zeitschrift und Zeitschrift für Polymere **243**, pp. 48-55.

Liu W. (2001) Modeling description and spectroscopic evidence of surface acid-base properties of natural illites. Water Research **35**(17), pp. 4111-4125.

Madejová J., Bujdák J., Janek M. and Komadel P. (1998) Comparative FT-IR study of structural modifications during acid treatment of dioctahedral smectites and hectorite. Spectrochimica Acta **54**, pp. 1397-1406.

Makó E., Senkár Z., Kristóf J. and Vagvölgyi V. (2006) Surface modification of mechanochemically activated kaolinites by selective leaching. Journal of Colloid and Interface Science **294**, pp. 362-370.

Nagata H., Shimoda S. and Sudo T. (1974) On Dehydration of bound water of sepiolite. Clays and Clay Minerals **22**, pp. 285-293.

Niederbudde E. A., Stanjek H. and Emmerich K. (2002) Tonmineral Methodik, Handbuch der Bodenkunde.

Olis A. C., Malla P. B. and Douglas L. A. (1990) The rapid estimation of the layer charges of 2:1 expanding clays from a single alkylammonium ion expansion. Clay Minerals **25**, pp. 39-50.

Ravichandran J. and Sivasankar B. (1997) Properties and catalytic activity of acid-modified montmorillonite and vermiculite. Clays and Clay Minerals **45**(6), pp. 854-858.

Rösler H. J. (1979) Lehrbuch der Mineralogie. VEB Deutscher Verlag für Grundstoffindustrie, Leipzig, pp. 832.

Serna C., Ahlrichs J. L. and Serratosa J. M. (1975) Sepiolite anhydride and crystal folding. Clays and Clay Minerals **23**, pp. 411-412.

Smykatz-Kloss W. (1974) Differential thermal analysis: Application and results in mineralogy. Wyllie P. J. (ed.), Minerals, Rocks and Inorganic materials, Springer Verlag, Berlin, pp. 185.

Stevens R. E. (1945) A system for calculating analyses of micas and related minerals to end members. U.S. Geol. Survey Bull. **950**, pp. 101-119.

Superti G. B., Olivereira E. C. and Pastore H. O. (2007) Aluminium magadiite: An acid solid layered material. Chemistry of Material **19**, pp. 4300-4315.

Tributh H. and Lagaly G. (1986) Aufbereitung und Identifizierung von Boden- und Lagerstättentonen Teil I - Aufbereitung der Proben im Labor. GIT Fachzeitschrift für das Laboratorium **30**, pp. 524-529.

Tyagi B., Chudasama C. D. and Jasra R. V. (2006) Determination of structural modification in acid activated montmorillonite clay by FT-IR spectroscopy. Spectrochimica Acta Part A **64**, pp. 273-278.

Vicente-Rodríguez M., Bañares-Muñoz M. and Lopez-Gonzalez J. (1996) Comparative FT-IR study of the removal of octahedral cations and structural modifications during acid treatment of several silicates, Spectrochimica Acta **52**, pp. 1685-1694.

Vivaldi J. L. M. and Hach-Ali P. F. (1970) Palygorskites and Sepiolites (Hormites) in Differential Thermal Analysis. MacKenzie, R. C. (edt.), Academic Press, London, New York, pp. 554-573.

Wilson M. J. (1994) Clay mineralogy: Spectroscopic and chemical determinative methods. Chapman & Hall, Oxford, pp. 367.

Wolters F., Lagaly G., Kahr G., Nueesch R. (†) and Emmerich K. (2009) A comprehensive characterisation of dioctahedral smectites. Clays and Clay Minerals, in print

Wolters F. and Emmerich K. (2007) Thermal reactions of smectites – Relation of dehydroxylation temperature to octahedral structure. Thermochimica Acta **462**, pp. 80-88.

5 Comprehensive description of layer and edge charge and exchange properties

5.1 Introduction

The layers of a 2:1 clay mineral consist of an octahedral (O) sheet, which is surrounded by two tetrahedral (T) sheets (Figure 5.1). The TOT-layers are connected by interlayer cations (e.g., Na^+, Ca^{2+}, Mg^{2+}).

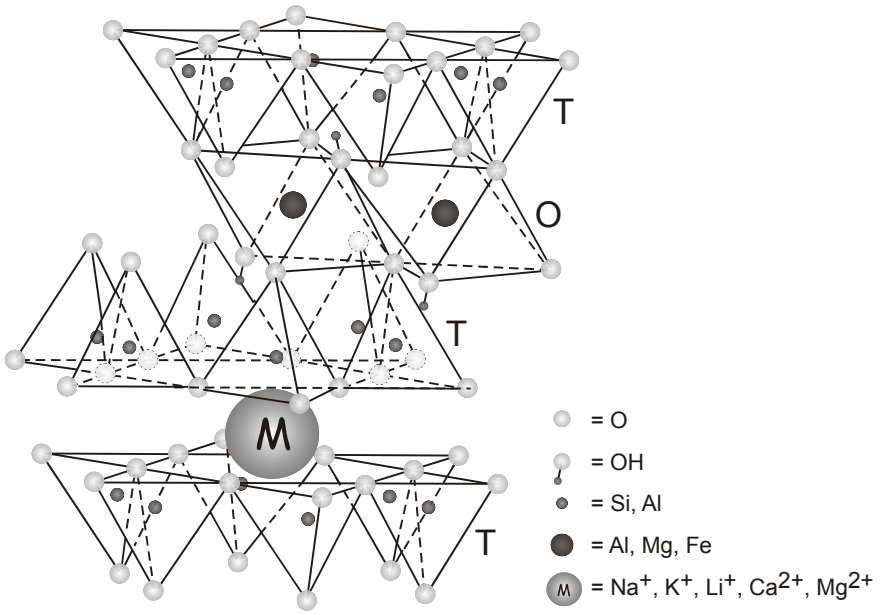

Figure 5.1 Structure model of clay minerals.

Small interlayer cations such as Li^+ and small metal cations like Cu^{2+}, Ni^{2+} leave their interlamellar position upon heating of dioctahedral clay minerals to migrate into the structure. This phenomena is well-known as Hofmann-Klemen effect (Hofmann and Klemen, 1950)

A negative surface charge is caused by substitutions of aluminium for silicon in the tetrahedral sheet and exchange of twofold charged cations like iron and magnesium for aluminium in the octahedral sheets. Thus, the charge of the basal surface is always negative and independent of pH. In contrast, the charge of the edges depends on pH. At low pH, the edges are saturated with protons. Therefore, they are positively charged. With increasing pH, the protons are released and the amount of the negative charge decreases until at high, basic pH the edges are completely negatively charged.

Resulting from layer charge and edge charge, clay minerals are characterised by their ability to exchange cations. The cation exchange capacity (CEC) is an important property of clay minerals. The total CEC of clay minerals consists of two parts: the exchange capacity of

the interlayer and that of the edges. At about pH 7, smectites can have up to 20% negative charge of the edges (Lagaly, 1981) (Figure 5.2).

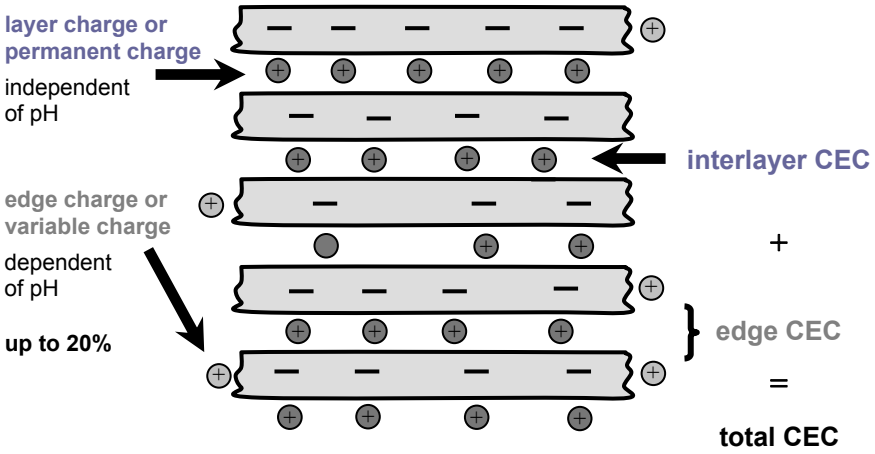

Figure 5.2 Arrangement of the positive charges in the layers of clay minerals.

At low pH, the edges are positively charged (Figure 5.3); thus edge charge does not contribute to the measured CEC at low pH. The difference between the total CEC at pH 7 and the exchange capacity in the acid range gives the charge of the edges. At high pH, the edges are negatively charged (Figure 5.3); therefore all edges contribute to CEC.

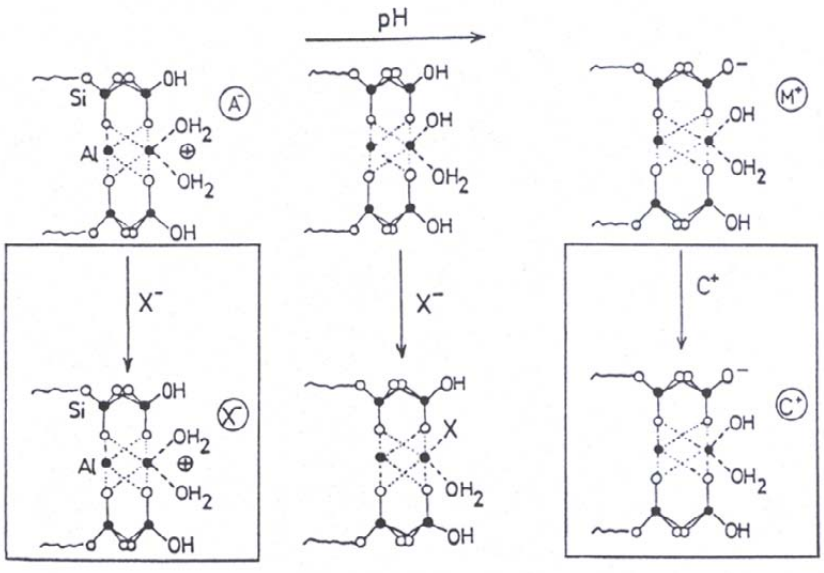

Figure 5.3 Charge and exchangeable cations on the edges of the clay minerals in dependence of pH (source: Jasmund and Lagaly, 1993).

5.2 Material

The purified and Na-exchanged bulk materials of Volclay, Indian Bentonite, sepiolite and vermiculite were fractionated and used for determination of the layer and edge charges.

Determination of the edge charge properties was performed on purified and Na-exchanged bulk materials, as well as on < 2 µm and < 0.2 µm fractions. The samples are listed in Table 5.1. The purification and the separation of the fractions are explained in Chapter 2.

Table 5.1 Purified and Na-exchanged bulk material and fractions.

Sample	Bulk material	Fraction < 2 µm	Fraction < 0.2 µm
4_Vol	X	X	X
6_IndBent	X	X	X
8_Verm	X	X	n.s.
10_PangelS9	X	X	X

n.s. not separated.

The Na^+ in the interlayer of a part of each material was exchanged against Cu^{2+} and Li^+ to create Cu- and Li-exchanged materials to this end, 10 g of Na^+-exchanged material were dispersed in 500 ml deionised water. Solid copper chloride ($CuCl_2$) or lithium chloride (LiCl) was added to the suspensions. The concentration was 20 times that of the CEC. The suspensions were shaken for 24 h. Thereafter, the suspensions were centrifuged at 4500 min^{-1} between 10 and 30 min. In some cases, it was necessary to add additional LiCl to the Li-exchanged sample for flocculation. The clear supernatant was replaced by fresh deionised water and solid $CuCl_2$ or LiCl were added again. The procedure was repeated four times, resulting in a complete exchange of Cu^{2+} or Li^+ against Na^+. After the reaction, the Cu-exchanged materials were washed with deionised water to remove chloride and surplus cations until the conductivity of the supernatant solutions were below 5 µS/cm. The Li-exchanged materials were filled in dialyse tubes to remove the excess salt. The suspensions were dialysed until the conductivity of the surrounding deionised water was below 5 µS/cm. The chloride free samples were dried at 60 °C. Afterwards the samples were milled slightly in an agate mill. For the creation of layer charge reduced materials, the Cu- and Li-exchanged materials of Volclay and Indian Bentonite were used. The samples were divided into 5 portions of 2 g each. One portion was not treated, while the others were heated for 24 h at several temperatures (110, 150, 200 and 300 °C).

5.3 Layer charge and layer charge reduction

Smectites are utilized in many industrial processes due to their high CEC, swelling ability and high surface area. Reduction of layer charge upon heating causes changes in the expansion properties of the clays. It is well known that small cations like Li^+ migrate into the structure of clay minerals like smectite (Hofmann and Klemen, 1950), but the location of their fixation is still under discussion.

In the last years, several studies about layer charged reduced smectites have been published. Mosser et al. (1997) used several methods (STA, IR, EPR, XPS, XRD, CEC) to compare a dioctahedral with a trioctahedral smectite in relation to the migration behaviour of Cu^{2+} upon heating at 100 to 500 °C. The influence of the migration of several cations on the dehydroxylation behaviour of smectites was investigated by Emmerich et al. (1999, 2001). A smectite was homoionically exchanged with Li^+, Na^+, Cu^{2+}, Zn^{2+}, Sr^{2+} and Ca^{2+} and heated at several temperatures 220 to 700 °C.

Sorption capabilities of layer charge reduced materials were researched by Hrobáriková and Komadel (2002). They used Li-saturated montmorillonite, which were heated at several temperatures (110 to 300 °C). Beside the sorption capacity, they also investigated the influence of Li-fixation on CEC and swelling ability, using raw materials of various sources, differing in layer charge and chemical composition (Hrobáriková et al., 2001). The hydration properties of layer charge reduced montmorillonite was analysed gravimetrically and with in situ XRD by Komadel et al. (2002). The samples were heated at 110 to 180 °C.

Karakassides et al. (1999) showed that FTIR and ESR spectroscopy are powerful techniques to investigate the location of Li^+, Cu^{2+} and Cd^{2+} in heated montmorillonites (130 to 300 °C). Detailed FTIR spectroscopic investigations of layer charge reduced montmorillonites were also done by Madejová et al. (1996, 1999, 2000, 2006) to determine the influencing factors of the fixation of Li^+, Cu^{2+} and Cd^{2+} in the structure of the smectites. Madejová et al. (2006) researched the possibility of infrared spectroscopy in the far-, mid- and near infrared regions to follow structural changes upon heating in Li- and Cu-saturated montmorillonites.

A comprehensive description about the preparation and properties of reduced-charge smectites were published by Komadel et al. (2003). Gates et al. (2000) investigated the changes in electronic and structural properties that are induced by Li^+ fixation by solid state ^{29}Si and ^{27}Al nuclear magnetic resonance spectroscopy.

Layer charge reduction is one method to change the properties of the clay minerals like smectite without changing the overall chemistry too much. To modify these new materials they were treated with acid (Pálková and Madejová, 2003; Pálková et al., 2003). Dissolution of layer charge reduced samples was slower and took place mainly from the particle edges

compared to unheated materials (Pálková et al., 2003). Komadel et al. (1999) used Li fixation to stabilize Fe^{2+} in reduced Fe-rich smectites.

In the present study, several layer charged reduced materials were prepared. The main focus was put on the influence of layer charge and tetrahedral charge. The results of CEC measurements were compared with the measurements of FTIR spectroscopy. The dehydration behaviour of the different layer charge reduced materials was compared with possible application of charge reduced smectites as standard material for investigation of charge related properties and behaviour.

5.3.1 Methods

The CEC of the homoionic exchanged and layer charged reduced materials were measured with 0.01 M Cu-triethylenetetramine (Cu-trien) according to Meier and Kahr (1999). The concentration of Cu-trien in the overlaying solution was determined by photometry (λ = 580 nm). The exchangeable cations were analysed by ICP-OES from the supernatant solutions. The dilution factors were 1:4 or 1:10 in dependence on the concentration.

FTIR was used to observe the migration of ions within the clay structure. A Bruker IFS 66/s spectrometer equipped with a DTGS detector was employed to obtain the IR-spectra. Sixty-four scans in the 4000 – 400 cm^{-1} spectral range were recorded with a scanner velocity of 2.2 kHz, a resolution of 4 cm^{-1} and a lens aperture of 12 mm. For the ATR measurements, a Golden Gate Mark II ATR single reflection diamond cell (Specac Limited) equipped with KRS5 lenses was used. For the ATR measurements no further sample preparation was necessary; only a small amount of powder was pressed on the diamond surface by a sapphire tipped anvil. To apply reproducible contact pressures, a torque screw driver was used. For Golden Gate ATR measurements, a torsional moment of 90 cNm is applied as standard.

The dehydration behaviour of the homoionic exchanged and layer charged reduced materials were investigated by STA. The measurement conditions are listed in Table 5.2. The short isothermal segment at the beginning of the measurement was added to redress the balance. In advance of the measurements, the samples were stored above a saturated $Mg(NO_3)_2$ solution to equilibrate at constant humidity (r.h. 53%).

Table 5.2 Experimental parameters for simultaneous thermal analysis.

Dynamic segment	Start temperature	[°C]	35
	End temperature	[°C]	1100
	Heating rate	[K/min]	10
Isothermal segment at	35 °C	[min]	10
	1100 °C	[min]	30
Atmosphere	Nitrogen as protective gas	[ml/l]	20
	Synthetic air as purging gas	[ml/l]	50
Sample holder	Pt/Rh		
Crucible	Pt/Rh with lid		
Reference material	Empty crucible with lid		
Net weight		[mg]	100

5.3.2 Results and Discussion

The influence of heat treatment on the CEC of smectites was investigated on Volclay and Indian Bentonite samples, which were saturated with Li^+ and Cu^{2+}. Both smectites are dioctahedral. The raw smectite in Indian Bentonite has a higher layer charge than the Volclay smectite, while the octahedral charges were similar. Therefore, the two samples differ in tetrahedral charge (Table 5.3). The Volclay smectite had a lower tetrahedral charge compared to the smectite of the Indian Bentonite. The CEC decrease with increasing heat treatment was dependent on the type of clay used. The CEC of the two clay fractions (< 2 µm and < 0.2 µm) did not vary significantly (Figure 5.4).

Table 5.3 Structural formula of the smectite fractions < 0.2 µm.

Sample	Structural formula
4_Vol	$Me^{+}_{0.25}(Si_{3.95}Al^{3+}_{0.05})(Al^{3+}_{1.58}Fe^{3+}_{0.20}Mg^{2+}_{0.23})[O_{10}(OH)_2]$
6_IndBent	$Me^{+}_{0.34}(Si_{3.71}Al^{3+}_{0.29})(Al^{3+}_{1.32}Fe^{3+}_{0.49}Mg^{2+}_{0.26})[O_{10}(OH)_2]$

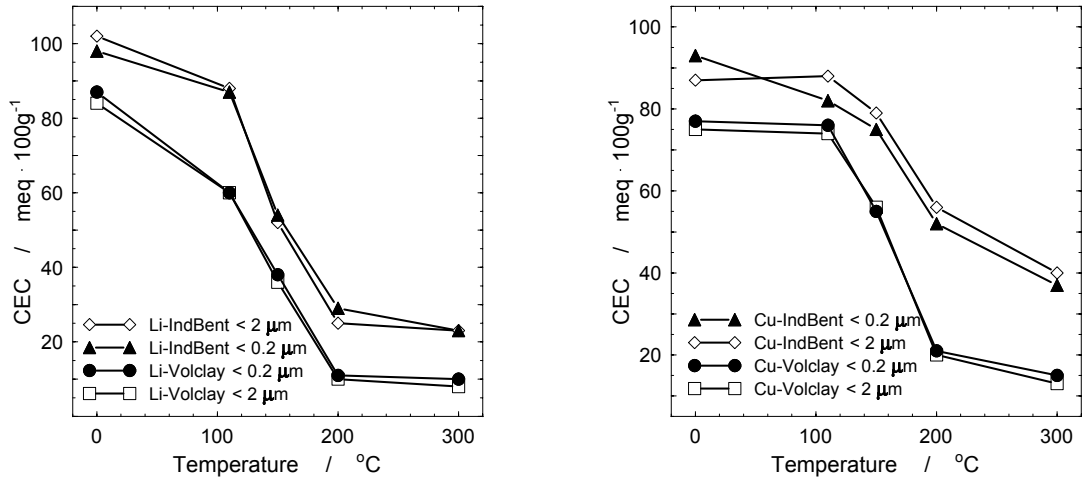

Figure 5.4 Variation with heat treatment of the CEC a) of the Li-exchanged and b) Cu-exchanged Volclay (< 2 µm / < 0.2 µm) and Indian Bentonite (< 2 µm / < 0.2 µm).

The CEC of the Li-exchanged Volclay decreased about 55% at 150 °C and up to 90% at 300 °C. The Li-saturated Indian Bentonite had a CEC of 23 mq/100g at 300 °C, which equals to a decrease of about 77% of the original CEC (Table 5.4).

Table 5.4 Percentage of the CEC decrease for different temperatures normalized to the original CEC value of the Li- and Cu-saturated Volclay < 2 µm and Indian Bentonite < 2 µm at room temperature.

Temperature [°C]	Li-Volclay < 2 µm [%]	Li-IndBent < 2 µm [%]	Cu-Volclay < 2 µm [%]	Cu-IndBent < 2 µm [%]
RT	0	0	0	0
110	19	11	1	11
150	57	45	25	19
200	88	70	73	44
300	90	77	83	60

The CEC of the Cu-saturated Volclay heated to 110 °C was nearly identical to that for the unheated Cu-exchanged Volclay. At 150 °C, the CEC decreased by 25% and at 200 °C the CEC diminished to less than half of the original CEC (75 meq/100g). The difference between the CEC at 200 °C and 300 °C averaged 10% (Figure 5.4 and Table 5.4). For the Cu- and Li-exchanged Indian Bentonite, the CEC decreased to the same level upon heating to 110 °C (Table 5.4). At 300 °C the decrease of the CEC reached 77% for the Li-exchanged Indian Bentonite and 60% for the Cu-treated material. The CEC values of the Li-saturated samples decreased with increasing temperature more than those of the Cu-exchanged materials. The CEC of the Li- and Cu-exchanged and heat treated Volclay showed a stronger decrease compared to the Indian Bentonite (Table 5.4). It is known that the CEC decreases with increasing temperature, because small exchangeable cations like Li^+ and Cu^{2+} move into the structure (Hofmann and Klemen, 1950). A decrease in CEC is combined with an apparent reduced layer charge.

The Li^+ and Cu^{2+} cations are similar in size but differ in charge. According to Madejova et al. (1999) Li^+ is fixed within the octahedral vacancies and Cu^{2+} is trapped in the hexagonal cavities of the tetrahedral sheet. The migration is combined with a reduction of the charge deficit in the structure. The content of Li^+ or Cu^{2+}, which moved into the structure of the smectite, is equivalent to the CEC reduction. These results suggest that more Li^+ or Cu^{2+} moved into the structure of the Volclay smectite than in the smectite from the Indian Bentonite. The octahedral charge of both was similar, but layer charge and tetrahedral charge varied. The higher layer charge and the higher tetrahedral charge of the smectite in the Indian Bentonite retarded the migration of Cu^{2+} and Li^+ into the structure. The higher content of iron in the octahedral sheet of the Indian Bentonite influenced the migration of

Cu^{2+} and Li^{+} in the structure, too. Therefore, the CEC reduction of the smectite was higher in the Volclay than in Indian Bentonite.

These changes in the CEC are also reflected in their FTIR spectra. Figure 5.5 displays the spectra of Li-saturated and heat treated (300 °C) material of the < 2 µm fraction of Volclay and Indian Bentonite and Figure 5.6 shows the corresponding FTIR spectra for the Cu-exchanged and heat treated material. The intensity of all vibrations in the range between 500 cm^{-1} and 1250 cm^{-1} decreased upon heating.

The unheated and homoionically exchanged material showed a sharp vibration around 990 cm^{-1}. This vibration can be assigned to a Si-O stretching vibration (in-plane) (Farmer, 1974; Komadel et al., 1996; Madejová et al., 1998). After heating, this vibration shifted to higher wavenumber. The shift is induced by the migration of Li^{+} and Cu^{2+} into the structure, which caused the deformation of the tetrahedral sheet. Another band at 512 cm^{-1} can be assigned to a Si-O-Al vibration of aluminium in the tetrahedral sheet (Farmer, 1974; Komadel et al., 1996; Madejová et al., 1998). In the spectra of the Li-exchanged material a decrease of the vibration intensity was observed. The Cu-saturated samples showed a shift of this vibration to a higher wavenumber (520 cm^{-1}). The shifts proved the structural changes of the tetrahedral sheet.

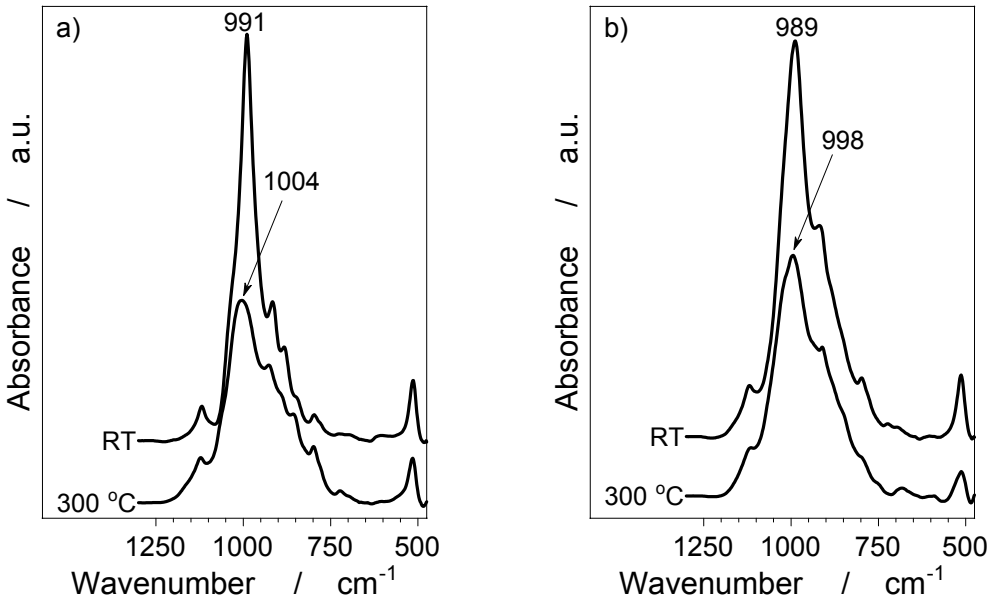

Figure 5.5 FTIR spectra of Li-exchanged and heat treated (T 300 °C) Volclay < 2 µm (a) and Indian Bentonite < 2 µm (b).

The spectra of the Li- and Cu-exchanged Volclay showed stronger shifts of the Si-O vibration near 990 cm^{-1} than the Indian Bentonite. These results of FTIR spectroscopy are in good agreement with the results of the CEC measurements. The higher layer charge and the higher tetrahedral charge of the smectite (Indian Bentonite) influenced the migration of the cations into the structure. The spectra of the Li-saturated and heated samples showed

changes in the region between 930 and 830 cm^{-1}. The vibrations in this range are connected to octahedral cations (Al^{3+}, Fe^{3+}, Mg^{2+}) (see Chapter 4 and 6). The changes reflect that Li^{+} migrate deeper into the structure (near or into the octahedral sheet) than Cu^{2+} (Madejová et al., 1999).

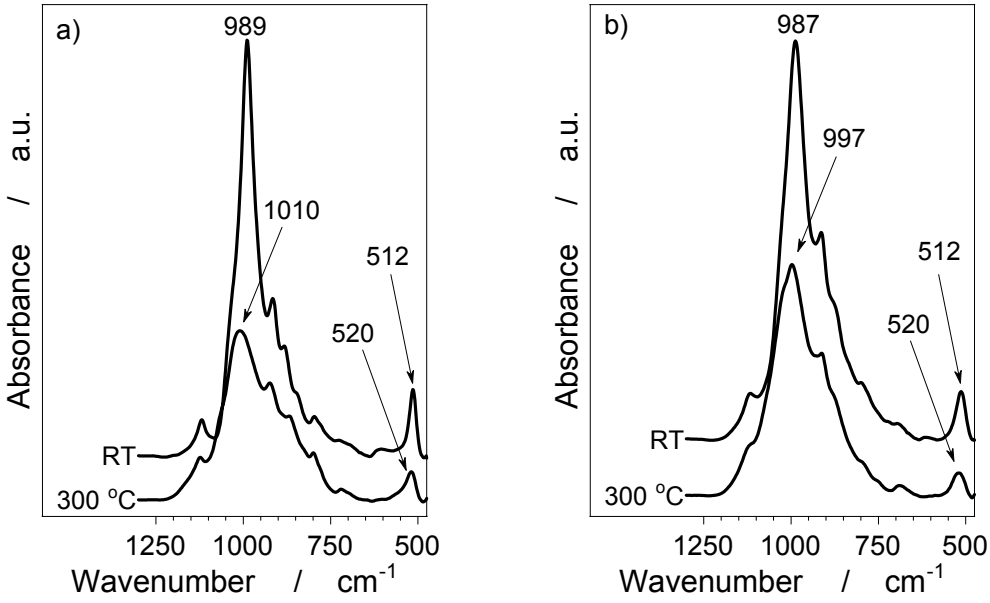

Figure 5.6 FTIR spectra of Cu-exchanged and heat treated (T 300 °C) Volclay < 2 µm (a) and Indian Bentonite < 2 µm (b).

In addition to the CEC and FTIR measurements, the dehydration behaviour of the Li- and Cu-exchanged and heat treated material was characterized. The dehydration values of the fraction < 2 µm are listed in Table 5.5.

Table 5.5 Development of the dehydration behaviour in dependence on the temperature for the Li- and Cu-saturated Volclay < 2 µm and for the Indian bentonite < 2 µm.

Temperature [°C]	Li-Volclay < 2 µm [%]	Li-IndBent < 2 µm [%]	Cu-Volclay < 2 µm [%]	Cu-IndBent < 2 µm [%]
RT	15.0	17.3	12.7	17.5
110	10.8	14.8	11.6	16.0
150	6.4	10.6	6.3	13.6
200	2.1	6.3	2.2	9.1
300	1.6	5.4	1.8	7.5

The mass loss of the < 0.2 µm fraction due to dehydration is higher (~ 1%) than the mass loss of the < 2 µm fraction. The dehydration decreased with increasing temperature. The development of the dehydration is confirmed with the CEC reduction.

It was not possible to measure the layer charge for the layer charge reduced material with dodecylamine (Olis et al., 1990). A test with a source clay (SWy-2) from the Clay Minerals

Society, saturated with Li and heated between 110 and 210 °C, showed that all samples heated up to T > 120 °C intercalated dodecylamine in a planar alignment. Therefore, the layer charge cannot be measured. The resulting layer charge after heat treatment was calculated from measured CEC values (Table 5.6). An average molecular weight of 375 g/mol was used and the CEC resulting from edge charges (see Chapter 5.4 and Table 5.7) subtracted from the total measured CEC.

Table 5.6 Reduced layer charge in dependence on the temperature for the Li- and Cu-saturated Volclay < 2 µm and for the Indian Bentonite < 2 µm.

Temperature [°C]	Li-Volclay < 2 µm [%]	Li-IndBent < 2 µm [%]	Cu-Volclay < 2 µm [%]	Cu-IndBent < 2 µm [%]
RT	0.27	0.31	0.26	0.31
110	0.18	0.27	0.26	0.27
150	0.09	0.15	0.19	0.24
200	0	0.06	0.06	0.16
300	0	0.05	0.03	0.10

Table 5.7 Edge charge of Li- and Cu-exchanged Volclay and of Indian Bentonite (subtracted from the measured CEC values).

Edge charge	Li-Volclay < 2 µm	Li-IndBent < 2 µm	Cu-Volclay < 2 µm	Cu-IndBent < 2 µm
meq/100g	12	15	5	10

The smectite in the Volclay has a lower layer charge than the smectite of the Indian Bentonite. Heat treatment can be applied to create materials with a certain layer charge. Variations in the layer charge are greater, when the raw materials have a higher layer charge at the beginning. The strength of the changes depends on the interlayer cation (Li^+, Cu^{2+}). Allowing for the error of the CEC method (± 2 meq/100g) for the Li- and Cu-saturated Indian Bentonite, as well as for the Cu-exchanged Volclay, we assumed that the edge charge stayed unchanged upon heating. The edge charge of the Li-saturated Volclay stayed unchanged only up to 150 °C. Due to the low CEC values above 200 °C, we assumed that only a small content of Cu-trien cations moved into the interlayer. The rest of the exchangeable cations are located at the edges, but part of the edges is also blocked (Table 5.6). Above 200 °C, the total measured CEC of the Li-saturated Volclay was lower than the CEC of the edges of the starting material; this means that these materials had no layer charge. With increasing temperature the CEC as well as the layer charge decreased and reached a constant limit. This limit was reached at lower temperature for Li-exchanged samples than for Cu-exchanged samples.

After heating up to 110 °C, the Cu-exchanged smectite of the Indian Bentonite had the same layer charge as the unheated Li- and Cu-exchanged smectite of the Volclay. The Cu-

exchanged Volclay heated up to 200 °C had the same layer charge as the Li-exchanged Indian Bentonite heated up to the same temperature. The Li-saturated Volclay heated at 150 °C had the same layer charge as the Li-saturated Indian Bentonite heated up to 300 °C. The Li-exchanged Volclay heated up to 150 °C had the same layer charge as the Cu-exchanged Indian Bentonite heated up to 300 °C. The materials have nearly the same layer charge, but the dehydration properties differed. This indicates that layer charge reduced materials can only find restricted use for model investigations in dependence on the layer charge.

5.4 Edge charge

The characterisation of the edges is difficult for clay minerals compared to the characterisation of their surface, because the surface area is larger than the area of the edges. Kaufhold (2001) investigated the influence of the pH on the cation exchange capacity to characterise the edges. Amman et al. (2005) studied the influence of the pH on two copper complexes. Weiss et al. (1956) used an anion exchange procedure to determine the content of the edge charge.

5.4.1 Methods

Two methods were used to characterise the edge charge of these clay minerals. First, the CEC was measured in dependence on the pH. Second, the hydroxyl groups of the edges were exchanged against fluoride.

CEC measurements with Cu-trien, as described in Chapter 3, were modified by adding of HCl or NaOH to vary the pH of the exchange solution. The modification scheme followed Kaufhold (2001). The used solutions consisted of 5 ml 0.01 M Cu-trien, 9 ml deionised water and 1 ml acid or base (Table 5.8).

Table 5.8 Concentrations of HCl and NaOH.

HCl [mol·l^{-1}]	NaOH [mol·l^{-1}]
0.1	0.1
0.01	0.01
0.001	0.001
0.0001	0.0001
0.00001	0.00001

Sodium fluoride solution, instead of an ammonium fluoride solution (Weiss et al. 1956), was used for anion exchange. The NaF solution was applied to avoid the cation exchange with the interlayer cations during the anion exchange procedure. Due to the purification, the used materials are Na^+-saturated. The purification and the homoionic exchange are

necessary, because Ca-rich and Mg-rich phases like Calcite and Dolomite can be dissolved by NaF. The released Ca and Mg form insoluble complexes with fluoride, which would have an influence on the fluoride concentration in the supernatant.

Prior to the measurements, the hydration state of the samples was equilibrated by storing the samples above magnesium nitrate between 3 and 5 d. Thereafter, 100 mg of the material is weighed in 50 ml centrifuge tubes. 50 ml of a 0.01 M sodium fluoride solution was added and the suspensions were shaken, several hours (3, 20, 48, 72 and 96 h). The hydroxyl groups of the edges were exchanged against fluoride. After the exchange, the samples were centrifuged (4500 cm^{-1}, 10 min, 21 °C) and the clear supernatant was separated from the solid. The fluoride in the solutions was analysed using ion chromatography. The difference between the amount of fluoride before and after the exchange reflects the charge of the edges.

The influence of NaF on the structure of the clays was investigated by ICP-OES. The content of Si, Al, Fe and Mg was measured in the supernatant. These four cations are in the tetrahedral and octahedral sheets. The investigations were done to control the stability of the clay minerals against the fluoride solution.

5.4.2 Results and Discussion

pH-depended CEC

The influence of the pH on the stability of Cu-trien was tested before the measurements started. The concentration of the Cu-trien solution was 0.01 M. The pH of the calibration solutions were measured and calculated (Table 5.9). The measured pH values differ from the calculated pH. The influence of Cu-trien on pH is stronger than that of HCl. Therefore, the measured pH below 7 is higher than the calculated pH values. Cu-trien has no influence on the pH at high NaOH concentration. Cu-trien can be regarded as a weak acid.

Table 5.9 Concentrations of HCl or NaOH and the measured and calculated pH of the calibration solutions.

HCl or NaOH [mol·l^{-1}]	$pH_{measured}$	$pH_{calculated}$
0.1	3.1	2.2
0.01	4.0	3.2
0.001	5.9	4.2
0.0001	6.5	5.2
0.00001	6.6	6.2
-	7.1	7
0.00001	6.9	7.8
0.0001	7.3	8.8
0.001	8.4	9.8
0.01	10.8	10.8
0.1	11.8	11.8

Cu-trien is stable from pH 4 to pH 11 (Figure 5.7). Below pH 4 and above pH 12 the stability of Cu-trien decreases. Therefore, separate calibrations are useful for acids with a molarity of 0.1 and 0.01 M and for base with a molarity of 0.1 M. The data are comparable with those of Kaufhold (2001) and Amman et al. (2005). Kaufhold (2001) used a higher volume of Cu-trien (10 ml) and a lower volume (0.5 ml) of HCl and NaOH (0.1 and 0.01 M). Amman et al. (2005) used a buffer to adjust the pH of the solution. This buffer solution (pH 8) was prepared by dissolving of 0.1 M (12.114 g) of tris(hydroxymethyl)amminomethane and 55.8 ml of 1 M HCl in water to give 100 ml of solution. 1 ml of the buffer was added to 3 ml of the separated supernatant.

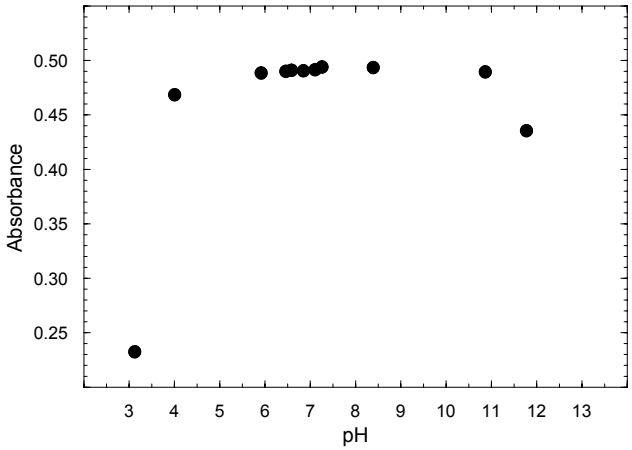

Figure 5.7 Influence of the pH (measured) on the stability of Cu-triethylenetetramine.

In all Figures (5.8 - 5.10), the measured pH of the calibration solutions is plotted on the x-axis for a better illustration because the clay materials also have an influence on the

measured pH value (Table 5.9). Clay minerals are able to buffer low concentrations of acids and bases. Clay minerals react amphoteric.

The first measurements of the pH-dependent CEC were carried out on the bulk material of Volclay (4_Vol), Indian Bentonite (6_IndBent) and sepiolite (10_PangelS9) to check the feasibility (Figure 5.8). The measurements showed that the added acid caused a decrease and the added base an increase of the CEC. At low pH, the edges did not contribute to the CEC, while the bases increased the number of negative charged edges, which lead to higher CEC values. After these measurements, purified and Na-exchanged materials were used. The results of both bentonites are shown in Figure 5.9 and for the sepiolite Pangel S9 in Figure 5.10.

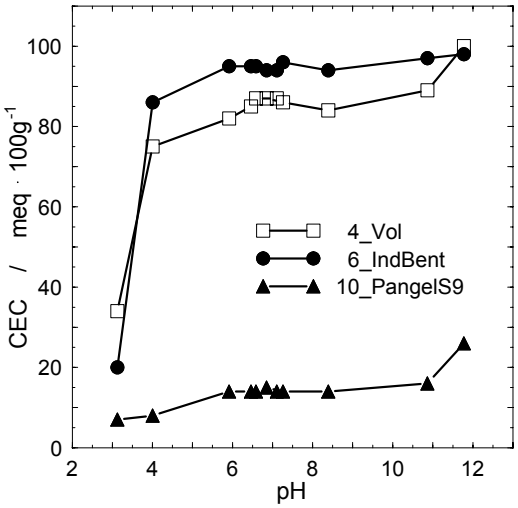

Figure 5.8 CEC of the untreated bulk material in dependence on the pH.

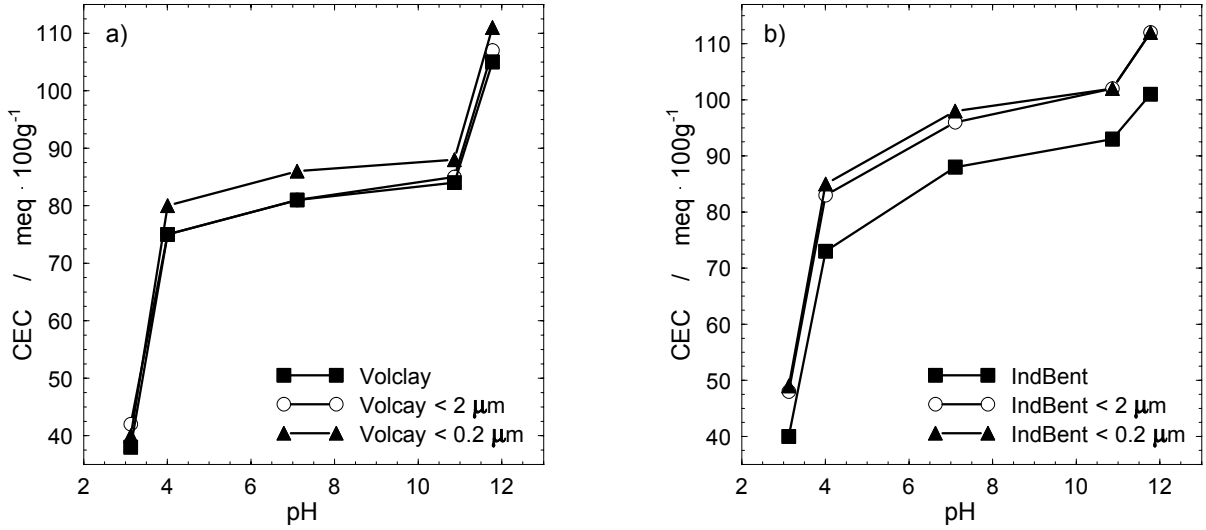

Figure 5.9 CEC in dependence on pH of the purified and fractionated materials of a) Volclay and b) Indian Bentonite compared to the purified bulk material.

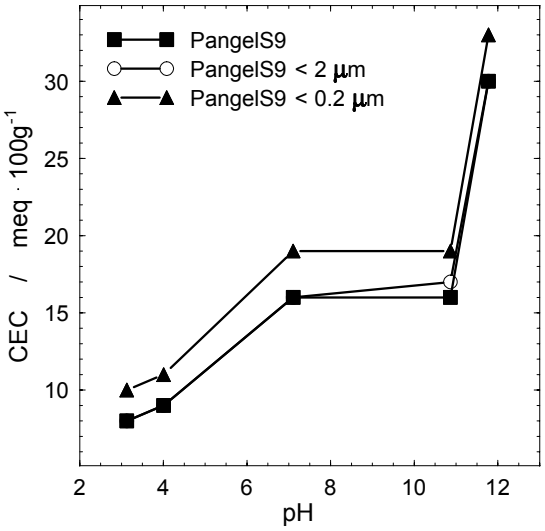

Figure 5.10 CEC in dependence on pH of the purified and fractionated material of the sepiolite Pangel S9 compared to the purified bulk material.

Table 5.9 Measured CEC and pH after the exchange experiment for the < 0.2 µm fraction of Volclay, Indian Bentonite (IndBent) and Sepiolite (Pangel S9).

Addition of 1ml	Volclay < 0.2 µm		IndBent < 0.2 µm		PangelS9 < 0.2 µm	
	pH	CEC [meq/100g]	pH	CEC [meq/100g]	pH	CEC [meq/100g]
HCl 0.1 M	2.9	40	2.9	49	3.1	10
HCl 0.01 M	4.8	80	4.3	85	5.8	11
deionised water	5.7	86	5.4	98	6.7	19
NaOH 0.01 M	6.8	88	8.8	102	7.5	19
NaOH 0.1 M	11.9	111	11.9	112	11.8	33

Following the CEC measurements, a part of the overlaying solution was analysed for released Si^{4+}, Al^{3+}, $Fe^{3+/2+}$ and Mg^{2+}. The investigations were done to control the dissolution of the clay minerals during the reaction.

Despite homoionic exchange with Na^{+} of the interlayer cations, 1 meq/100g Mg^{2+} is still present in the interlayer (Table 5.10). Around pH 7, one might expect that Mg^{2+} comes only from the interlayer sheet. The largest amount of Mg^{2+} is present in the octahedral sheet.

Table 5.10 Mg^{2+} content of the interlayer of Volclay < 2 µm (pH 7).

Volclay < 2 µm	mg/l	mmol	meq/100g
Mg (pH 7)	0.0873	0.00022	1

The concentrations of the octahedral and tetrahedral cations in the supernatant solution after the CEC measurements were very low (well below 0.0001%, Table 5.11).

Table 5.11 Si^{4+} content of the supernatant solution of Volclay < 2 µm.

Addition of 1ml	Si^{4+}	
	mmol	%
0.1 M HCl	0.00058	0.00001
0.01 M HCl	0.00026	0.000004
deionised water	0.00024	0.000004
0.01 M NaOH	0.00043	0.000007
0.1 M NaOH	0.00232	0.00004

The release occurred unbalanced, which means that the dissolution of the clay minerals by acid or base occurred incongruently. The concentration and the volume of acid or base are too low to affect dissolution of the octahedral and tetrahedral sheet of the clay minerals (Chapter 6). The results show that the release of these elements is insignificant and the clay minerals stay unaltered during the exchange reaction.

The CEC, as a function on pH, was used to estimate the charge of the edges. The difference between the total CEC measured around pH 7 and the CEC in the acid range corresponds to the charge of the edges. The value of 0.01 M HCl was used, because the Cu-trien complex is not stable with 0.1 M HCl (Figure 5.11). The value of 0.1 M NaOH was used to estimate the maximum of the charge of the edges.

The charge of the edges of the purified and fractionated Volclay, as well as of the Indian Bentonite, is listed in Table 5.12 and the maximum of the edge charge of both materials in Table 5.13.

Table 5.12 Charge of the edges of purified and fractionated Volclay and Indian Bentonite.

		bulk	< 2 µm	< 0.2 µm
Volclay	[%]	6 ± 2	7 ± 2	7 ± 2
Indian Bentonite	[%]	15 ± 2	14 ± 2	13 ± 2

Table 5.13 Maximum of the edge charge of purified and fractionated Volclay and Indian Bentonite.

		bulk	< 2 µm	< 0.2 µm
Volclay	[%]	18 ± 2	23 ± 2	23 ± 2
Indian Bentonite	[%]	12 ± 2	13 ± 2	12 ± 2

The charge of the edges did not differ significantly between the purified bulk material and the fraction of sepiolite. The values were above 40%. The maximum of the edge charge averaged above 40%, too (Table 5.14). The high value can be explained by its tube-like structure.

Table 5.14 Edge charge and maximum of the edge charge of purified and fractionated sepiolite.

Sepiolite		bulk	< 2 µm	< 0.2 µm
Edge charge	[%]	40 ± 4	44 ± 4	42 ± 4
Maximum of the edge charge	[%]	43 ± 4	47 ± 4	42 ± 4

The results for the CEC in dependence on pH for vermiculite showed large variation. Vermiculite was much less stable against acid than smectite (Chapter 7). The incorporation of Cu-trien into the vermiculite interlayer is limited to certain conditions (Chapter 4).

Fluoride exchange of hydroxyl groups

The fluoride content of the supernatant was only slightly reduced after the reaction. The pH increase of the fluoride solution after the reaction proved the release of the hydroxyl groups and is an indicator that anion exchange took place. The difference between the fluoride concentration before and after the anion exchange can be used to estimate the charge of the edges. The variation of shaking time showed that 3 h (Table 5.15) was too short for the complete exchange, because the charge of the edges was lower after 3 h than after 20 h (Tables 5.16 and 5.17).

Table 5.15 Charge of the edges after the reaction with sodium fluoride after 3 h.

Sample	Bulk material# [%]	Fraction < 2 µm# [%]	Fraction < 0.2 µm# [%]
Volclay	8 ± 2	9 ± 1	7 ± 2
Indian Bentonite	8 ± 1	7 ± 1	9 ± 2
Vermiculite	5 ± 2	5 ± 2	-

Material was purified according to Tributh and Lagaly (1986).

A shaking time between 20 h and 48 h was enough for the exchange (Tables 5.16 and 5.17). With increasing time, the results were constant within the variation limit of the error of the method (± 3%) (Table 5.17).

Table 5.16 Charge of the edges after the reaction with sodium fluoride after 20 h.

Sample	Bulk material# [%]	Fraction < 2 µm# [%]	Fraction < 0.2 µm# [%]
Volclay	14 ± 2	14 ± 3	14 ± 2
Indian Bentonite	17 ± 2	16 ± 2	-
Vermiculite	10 ± 1	10 ± 1	-

Material was purified according to Tributh and Lagaly (1986).

Table 5.17 Charge of the edges after the reaction with sodium fluoride.

Sample		3 h	20 h	48 h	72 h	96 h
Volclay#	[%]	8 ± 2	14 ± 2	11 ± 2	15 ± 2	12 ± 2
Indian Bentonite#	[%]	8 ± 2	17 ± 3	17 ± 3	13 ± 2	16 ± 2
Vermiculite#	[%]	5 ± 1	10 ± 1	9 ± 2	9 ± 1	7 ± 1

Bulk material, which was purified according to Tributh and Lagaly (1986).

Sepiolite showed unreliable results for the fluoride reaction. The method cannot be applied for this material. The reason might be the tube-like structure of sepiolite, allowing a higher content of fluoride to be adsorbed rather than exchanged at the edges.

The fluoride solution can attack cations in the tetrahedral and octahedral sheet. Therefore, the supernatant solution after the reaction was analysed for the release of Si^{4+}, Al^{3+}, $Fe^{2+/3+}$ and Mg^{2+} after 96 h. In the supernatant solution of vermiculite samples, the element concentrations of Si^{4+}, Al^{3+}, $Fe^{2+/3+}$ and Mg^{2+} were below 0.5 mg/50ml. The release of these elements is unbalanced. The release of the elements occurred in the following order: Al^{3+} > $Fe^{2+/3+}$ > Si^{4+} > Mg^{2+}. This means that the dissolution of vermiculite by NaF was incongruent. The element concentration in mg/50ml in the supernatants of the smectite samples is higher compared to the vermiculite sample. The dissolution of smectite occurred congruently, because the ratio between Si^{4+}, Al^{3+}, $Fe^{2+/3+}$ and Mg^{2+} in the structural formula is equal with that in the supernatant solution. The structural formulas are given in Chapter 4. The content of Si^{4+}, Al^{3+}, $Fe^{2+/3+}$ and Mg^{2+} in mol and the corresponding amount in % are listed in Table 5.18.

Table 5.18 Content of Si, Al, Fe and Mg of the structural formula in mol and %.

	Vermiculite < 2 µm		Volclay < 2 µm		Indian Bentonite < 2 µm	
Element	[mol]	[%]	[mol]	[%]	[mol]	[%]
Si^{4+}	3.03	50.0	3.92	65.1	3.66	60.4
Al^{3+}	0.97	16.0	1.64	27.2	1.62	26.7
$Fe^{2+/3+}$	0.31	5.1	0.19	3.2	0.52	8.6
Mg^{2+}	2.63	43.4	0.27	4.5	0.26	4.3

The values of Si^{4+}, Al^{3+}, $Fe^{2+/3+}$ and Mg^{2+} in mg/50ml were converted in mmol and the percentages of each element were calculated in relation to the structural formula. The release of Si^{4+} was nearly 0.01% and the release of Al^{3+}, $Fe^{2+/3+}$ and Mg^{2+} was well below 0.01%. These low concentrations in the supernatants are insignificant. The results show that NaF did not disintegrate the clay mineral structure.

5.4.3 Conclusions

Both methods applied for edge charge determination can be used for smectites. There are limitations for application of these methods to vermiculite and sepiolite samples, but still one method can be applied for these materials. The charge of the edges of the vermiculite was determined with the fluoride method. The charge of the edges of the sepiolite was ascertained by using the CEC measurements in dependence on pH. The vermiculite has a charge of the edges of 10% and the sepiolite of about 40%.

Both methods were applied to estimate the charge of the edges of the smectites. The values are comparable. The smectite in the Indian Bentonite had a charge of the edges of 13% and in the Volclay of 14%.

In summary, both methods can be used to determine the charge of the edges in cases where the acid-base-system of Cu-trien and of the clay minerals does not interfere. This method of characterisation of clay edges can be used as screening for modification of edges. The modification of clay edges can be performed in order to achieve their homogenous and oriented arrangement by edge-to-edge or surface-to-edge connections (e.g., in clay polymer-nanocomposites).

References

Amman L., Bergaya F. and Lagaly G. (2005) Determination of the cation exchange capacity of clays with copper complexes revisited. Clay Minerals **40**, pp. 441-453.

Emmerich K., Madsen F. T. and Kahr G. (1999) Dehydroxylation behaviour of heat-treated and steam-treated homoionic cis-vacant montmorillonites. Clays and Clay Minerals **47**(5), pp. 591-604.

Emmerich K., Plötze M. and Kahr G. (2001) Reversible collapse and Mg^{2+} release of de- and rehydroxylated homoionic cis-vacant montmorillonites. Applied Clay Science **19**, pp. 143-154.

Farmer V. C. (1974) The infrared spectra of minerals. Mineralogical Society, Monograph 4, London, pp. 539.

Gates W. P., Komadel P., Madejová J., Bujdák J., Stucki J. W. and Kirkpatrick R. J. (2000) Electronic and structural properties of reduced-charge montmorillonites. Applied Clay Science **16**, pp. 257-271.

Hofmann U. and Klemen R. (1950) Verlust der Austauschfähigkeit von Lithium-Ionen an Bentonit durch Erhitzung. Zeitschrift für Anorganische und Allgemeine Chemie **262**, pp. 95-99.

Hrobáriková J., Madejová J. and Komadel P. (2001) Effect of heating temperature on Li-fixation, layer charge and properties of fine fractions of bentonites. Journal of Materials Chemistry **11**, pp. 1452-1457.

Hrobáriková J. and Komadel P. (2002) Sorption properties of reduced-charge montmorillonites. Geologica Carpathica **53**(2), pp. 93-98.

Jasmund K. and Lagaly G. (1993) Tonminerale und Tone: Struktur, Eigenschaften, Anwendung und Einsatz in Industrie und Umwelt. Steinkopff Verlag, pp. 490.

Lagaly G. (1981) Characterization of clays by organic compounds. Clay Minerals **12**, pp. 45-54.

Karakassides M. A., Madejová J., Arvaiová B., Bourlinos A., Petridis D. and Komadel P. (1999) Location of Li(I), Cu(II) and Cd(II) in heated montmorillonite: evidence from specular reflectance infrared and electron spin resonance spectroscopies. Journal of Materials Chemistry **9**, pp. 1553-1558.

Kaufhold S. (2001) Untersuchungen zur Eignung von natürlich alterierten sowie mit Oxalsäure aktivierten Bentoniten als Bleicherde für Pflanzenöle. Dissertation, Fakultät für Bergbau, Hüttenwesen und Geowissenschaften der Rheinisch-Westfälischen Technischen Hochschule Aachen, pp. 178.

Komadel P., Madejová J., Janek M., Gates W. P., Kirkpatrick R. J. and Stucki J. W. (1996) Dissolution of hectorite in inorganic acids. Clays and Clay Minerals **44**(2), pp. 228-236.

Komadel P., Hrobáriková J., Smrcok L. and Kuppelhuper-Bitschnau B. (2002) Hydration of reduced charge montmorillonite. Clay Minerals **37**(3), pp. 543-550.

Komadel P., Madejová J. and Bujdák J. (2003) Preparation and properties of reduced-charge smectites - a review. Clays and Clay Minerals **53**(4), pp. 313-334.

Komadel P., Madejová J. and Stucki J. W. (1999) Partial stabilization of Fe(II) in reduced ferruginous smectite by Li fixation. Clays and Clay Minerals **47**(4), pp. 458-465.

Madejová J., Arvaiová B. and Komadel P. (1999) FTIR spectroscopic characterisation of thermally treated Cu^{2+}, Cd^{2+} and Li^{+} montmorillonites. Spectrochimica Acta Part A **55**, pp. 2467-2476.

Madejová J., Bujdák J., Gates W. P. and Komadel P. (2000) Preparation and infrared spectroscopic characterization of reduced-charge montmorillonite with various Li contents. Clay Minerals **31**(2), pp. 233-241.

Madejová J., Bujdák J., Janek M. and Komadel P. (1998) Comparative FT-IR study of structural modifications during acid treatment of dioctahedral smectites and hectorite. Spectrochimica Acta **54**, pp. 1397-1406.

Madejová J., Bujdák J., Petit S. and Komadel P. (1996) Effects of chemical composition and temperature of heating on the infrared spectra of Li-saturated dioctahedral smectites - (II) Near-infrared region. Clay Minerals **35**(5), pp. 753-761.

Madejová J., Pálková H. and Komadel P. (2006) Behaviour of Li^{+} and Cu^{2+} in heated montmorillonite: Evidence from far-, mid-, and near-IR regions. Vibrational Spectroscopy **40**, pp. 80-88.

Meier L. P. and Kahr G. (1999) Determination of the cation exchange capacity (CEC) of clay minerals using the complexes of copper(II) ion with triethylenetetramine and tetraethylenepentamine. Clays and Clay Minerals **47**(3), pp. 386-388.

Mosser C., Michot L. J., Villieras F. and Romeo M. (1997) Migration of cations in copper(II)-exchanged montmorillonite and laponite upon heating. Clays and Clay Minerals **45**(6), pp. 789-802.

Olis A. C., Malla P. B. and Douglas L. A. (1990) The rapid estimation of the layer charges of 2:1 expanding clays from a single alkylammonium ion expansion. Clay Minerals **25**, pp. 39-50.

Pálková H. and Madejová J. (2003) FTIR study of structural modifications of Li-montmorillonites. Solid State Chemistry V **90-91**, pp. 503-508.

Pálková H., Madejová J. and Righi D. (2003) Acid dissolution of reduced-charge Li- and Ni-montmorillonites. Clays and Clay Minerals **51**(2), pp. 133-142.

Tributh H. and Lagaly G. (1986) Aufbereitung und Identifizierung von Boden- und Lagerstättentonen Teil I - Aufbereitung der Proben im Labor. GIT Fachzeitschrift für das Laboratorium **30**, pp. 524-529.

Weiss A., Mehler A., Koch G. and Hofmann U. (1956) Über das Anionenaustauschvermögen der Tonmineralien. Zeitschrift für anorganische und allgemeine Chemie **284**, pp. 247-271.

6 Structural modifications during acid treatment of several clay minerals

The results of Chapter 6 are submitted to Applied Clay Science in the form of two publications:

Steudel A., Batenburg L. F., Fischer H. and Emmerich K. (2009) Alteration of swelling clay minerals by acid activation. Applied Clay Science, in print.

Steudel A., Batenburg L. F., Fischer H. and Emmerich K. (2009) Alteration of non-swelling clay minerals and magadiite by acid activation. Applied Clay Science, in print.

6.1 Introduction

Clay minerals like smectite, vermiculite, illite, sepiolite and even kaolinite vary in their chemical composition, which causes different mineralogical properties such as layer charge, cation exchange capacity, adsorption capacity and morphology. Therefore, a detailed description of the clay minerals is very important (Wolters et al., 2008). Because of their large variability (e.g., in chemical composition), clay minerals are widely used for many industrial applications including ceramic industries, food industries, chemical industries and paper industries. They are applied in their natural form or after specific modification (Komadel, 2003). One type of modification is acid treatment. Diluted sulphuric acid and other inorganic acids (e.g., hydrochloric acid, nitric acid, oxalic acid) find use for the preparation of acidic activated clay minerals to enhance the catalytic activity of these minerals (Komadel et al., 1997) and to obtain bleaching earth (Kaufhold, 2001), which is used e.g., for the purification of beverages and cooking oil.

There are several studies dealing with acid treatment. A number of workers have investigated the influence of hydrochloric acid on the structure of smectite (Novák and Číčel, 1978; Komadel et al., 1990; Ravichandran and Sivasankar, 1997; Madejová et al., 1998; Pálková et al., 2003; Klinke 2007). Abdul-Latif and Weaver (1969), Vicente-Rodríquez et al. (1995) and Yebra-Rodríquez et al. (2003) treated sepiolite and palygorskite with hydrochloric acid. Jozefaciuk and Bowanko (2002) and Caroll and Starkey (1971) investigated the influence of acid treatment on clay minerals like montmorillonite, biotite, illite, kaolinite, halloysite, vermiculite. Snäll and Liljefors (2000) treated mica- and chlorite-rich bulk clays and other minerals like amphibole, titanite, epidote and plagioclase with hydrochloric acid.

Only a few workers used sulphuric acid for the treatment of minerals of the smectite or kaolinite group (Breen et al., 1995; Komadel et al., 1997; Hradil et al., 2002; Makó et al.,

2006; Tyagi et al., 2006; Önal and Sarikaya, 2007). Two studies (Komadel et al., 1990; Hradil et al., 2002) used both acids but in different concentrations.

From these studies, it is well known that acid treatment of clay minerals causes corrosion of the octahedral sheet. It is still a matter of debate if this process is complete or incomplete. Furthermore, only a few of these earlier studies compared differences in the influence of sulphuric and hydrochloric acid on clay minerals (e.g., Komadel et al., 1996).

The aim of this study was to prepare materials with a simple chemical composition, which have a similar layered morphology like the untreated materials and which still have the ability to adsorb organic molecules. We selected samples from five clay mineral groups and two acids (HCl, H_2SO_4). Special attention was given to the dissolution kinetics of the octahedral sheet with respect to aluminium, magnesium and iron. Furthermore, we obtained information on the stability of several clay minerals by using two several acids with the same concentration at different reaction times.

6.2 Materials and acid treatment

Seven bentonites with a high content of smectite, one vermiculite, one illite, one sepiolite, three kaolin samples and one magadiite were used. Although, most of the sample data are already given in Chapter 2 all samples, except 11_Pansil and 12_Palygorskite, are listed again in Table 6.1 for a better readability of Chapter 6.

Table 6.1 Sample data.

Sample	Name	Provenance	Supplier
1_Calci	Bentonite (Calcigel)	Germany	Südchemie
2_EXM757	Montmorillonite	Germany	Südchemie
3_SWy-2	Bentonite	USA	Source Clay Repository of the Clay Mineral Society
4_Vol	Bentonite (Volclay)	USA	Südchemie
5_WYO	Bentonite	USA	Wyoming
6_IndBent	Bentonite (Indian)	India	F. Wolters / IFG
7_NHec	Hectorite (natural)	USA	Elementis
8_Verm	Vermiculite	Russia	S. Dultz / Uni Hannover
9_Illite	Mica (Illite)	France	Commercial product of B+M
10_PangelS9	Sepiolite (Pangel S9)	Spain	Tolsa
13_Pol	Kaolin (Polwhite)	GB	IMERYS
14_Kaolex	Kaolin (Kaolex)	USA	Kentucky-Tennessee Clay Company
15_Rogers	Kaolin (Rogers)	USA	Kentucky-Tennessee Clay Company
16_Mag	Magadiite (synthetic)	---	TNO (NL)

In contrast to the other raw materials, the natural vermiculite has a low < 2 µm fraction content; particle size separation revealed an amount of less than 10 %. Therefore, particle size had to be reduced by grinding without affecting the vermiculite structure. Best results were obtained with a CGS 10 mill (Netzsch). More detailed descriptions were given in Chapter 4.

The acid treatment was performed with untreated bulk materials, because for most of the industrial applications purification and separation of clay < 2 µm fraction is too time consuming and too expensive.

For the experiments, 4 g of each bulk material were treated with H_2SO_4 and HCl at concentrations of 1, 5 and 10 M at 80 °C for several hours. The volume of the suspensions was 400 ml. This resulted in a suspension of 1 % solid in an acidic liquid. 100 ml deionised water (VE-water) were used to disperse the clay. The reaction between pure water and H_2SO_4 is very strong. Therefore, heat development was inhibited by cooling with ice. The chilled acid (300 ml) was mixed with the clay suspension by mechanical stirring. Subsequently, the suspensions were heated to 80 °C in an oil bath. Reaction time varied between 1.5 and 96 h. Table 6.2 shows the applied reaction times of the bulk material for H_2SO_4 at a concentration of 5 M at 80 °C.

Table 6.2 Reaction times of clay suspensions with 5 M H_2SO_4 at 80 °C.

Time [h] / Sample	1.5	5	20	72	96
1_Calci	X	X	X	X	X
2_EXM757	X	X	X	X	X
3_SWy-2			X		X
4_Vol	X	X	X	X	X
5_WYO			X		X
6_IndBent	X	X	X		X
7_NHec	X	X	X		X
8_Verm	X	X	X	X	
9_Illite			X		X
10_PangelS9	X	X	X	X	
13_Pol	X	X	X	X	X
14_Kaolex			X		X
15_Rogers			X		X
16_Mag				X	

One bentonite (4_Vol), one kaolin (13_Pol), the sepiolite (10_PangelS9) and the vermiculite (8_Verm) were also treated with HCl under the same reaction conditions to show the influence of various kinds of acid.

The same 4 materials were treated with H_2SO_4 and HCl to investigate the influence of the acid concentration, using several concentrations (1, 5 and 10 M) at constant reaction time and constant temperature (80 °C). The bentonite and the kaolin were treated for 96 h and the other two materials (sepiolite, vermiculite) were treated for 20 h, because of their lower stability in the presence of acids (Table 6.3).

Table 6.3 Variation of the acid concentration, using HCl and H_2SO_4 at 80 °C.

Sample	Time [h]	Molarity 1 M	Molarity 5 M	Molarity 10 M
4_Vol	96	X	X	X
8_Verm	20	X	X	X
10_PangelS9	20	X	X	X
13_Pol	96	X	X	X

At the end of the reaction interval, the suspensions were cooled down with ice for 5 to 10 min. The samples were then centrifuged to separate the acid from the residual clay fragments. The acidic supernatant was removed and the remaining solid washed with deionised water and repeatedly centrifuged until the conductivity of the supernatant solution was below 5 µS/cm. Then the suspensions were freeze-dried.

6.3 Methods

The chemical composition of the natural and acid treated materials was determined by X-ray fluorescence analysis (XRF). The analysis were performed on a MagiXPRO spectrometer from Phillips equipped with a rhodium X-ray tube (stimulation power: 3.2 KW) using molten pellets. For these pellets, powdered samples were mixed with lithium tetraborate in the ratio of 1 to 7 and molten in a platinum crucible at a smelting apparatus. The loss of ignition was determined separately by storing a sample in an oven at 1000 °C for 2 h.

The content of lithium in the octahedral sheet of the hectorite was estimated by inductively coupled plasma optical emission spectroscopy (ICP-OES). Therefore, the material was diluted with nitrohydrochloric acid and with a mixture of hydrofluoric and nitric acid, using a microwave.

The composition of the supernatant solutions, which were separated from the residual clay fragments after reaction, were analysed by ICP-OES. The dilution factors were 1:20, 1:50 or 1:100 in dependence on concentration due to the reaction time. A certain amount of solution (20 ml) was used to determine Si^{4+}, Al^{3+}, $Fe^{2+/3+}$, Mg^{2+}, Na^{+}, Ca^{2+} and K^{+}.

Examination of the changes in particle morphology was carried out with an Environmental Scanning Electron Microscope (ESEM) using a Philips ESEM XL 30 FEG. This kind of SEM uses a chamber atmosphere of 1 to 3 Torr water vapour instead of high vacuum. The

microscope is equipped with a special gaseous secondary electron detector (GSE-detector); therefore sputtering of the samples with conductive material (gold, carbon) is not necessary. Thus, it can be used for the investigation of moisture sensitive samples like clay minerals. A chamber atmosphere of 1 Torr and an acceleration voltage of 20 kV were applied. The used holder consists of aluminium, which was laminated with an adhesive carbon foil. Very small amounts of the clay powder were dispensed onto the foil.

Nitrogen adsorption, using a Quantochrome Autosorb-1MP and BET evaluation, was used to measure specific surface area (A_S or SSA in most literature) (Brunauer et al., 1932; Gregg and Sing, 1991). Eleven adsorption points in the range of p/p_0 from 0.05 to 0.32 were used for BET evaluation. The outgassing conditions were 24 h under vacuum at 95 °C. The t-plot according to De Boer et al. (1966) was applied to estimate the external specific surface area (A_E) and the micro-pore area (A_{MP}).

X-ray diffraction analysis (XRD) was used to determine the mineralogical composition of the natural and acid treated materials, as well as the changes in the long range order. Powdered samples were used. The measurements were performed on a Siemens D5000 diffractometer (CuKα radiation) equipped with a graphite secondary monochromator. The patterns were recorded between 5 and 80° 2θ (step size: 0.02° 2 θ / 5 s). Fix slit (primary and secondary) were used with a size of 1 mm and a detector slit (secondary) of 0.1 mm. Qualitative phase analysis was done using Brindley and Brown (1980) and the Diffrac Plus Evaluation software (Version 10.0) by Bruker. Quantification of the samples was done with the Rietveld program “Autoquan” (Agfa NDT Pantak Seifert GmbH_CO.KG, Version 2.7.0.0). The Rietveld method is based on a mathematical method, which calculates a pattern by the optimisation of crystal structure parameters, profile form functions and background functions (Kleeberg and Bergmann, 2002). This calculated diffractogram is adjusted by increment match to the measured pattern until the best match within defined limits is achieved. An internal standard (ZnO) was used to quantify the content of amorphous SiO_2 in the acid treated samples. For these measurements, the powdered samples were mixed with ZnO in the ratio of 9:1.

The Fourier Transform Infrared Spectroscopy (FTIR, DRIFT) of the natural and acid treated materials was used to investigate the short range of structural changes, which were caused by the acid treatment. For a better discrimination of the bands in the Si-O stretching region (1200 - 800 cm^{-1}), a diffuse reflectance accessory from Spectra-Tech Inc. (DRIFT) was used. For the measurements, 2.5 mg of a sample was mixed with 500 mg KBr. The powder was filled loosely into a sample cup to obtain a random orientation. The FTIR spectra were recorded on a Bruker IFS66/S spectrometer equipped with a deuterated triglycinesulfonate detector (DTGS). Sixty-four scans were recorded in the 4000 - 400 cm^{-1}

spectral range with a resolution of 4 cm^{-1} using a scanner velocity of 4 kHz and a lens aperture of 12 mm. After preparation and prior to the measurement, each sample was flushed with nitrogen for 2 min. Pure KBr was used for the background measurements.

The raw DRIFT data were transformed using Kubelka-Munk-Function (Kubelka and Munk, 1931; Petrick, 2007). The interpretation of the FTIR spectra was made by description of changes in band position and shape. In addition, PeakFit program 4.0 from Jandel Scientific was used to determine peak areas of selected peaks. According to Petrick (2007), the percentages of the area from vibration bands, which are connected to octahedral cations, were determined by curve fitting. Details of the peak fit program are described in the appendix. The data obtained from calculated band areas were compared with the adjusted amount of the unreacted octahedral cations like aluminium, magnesium and iron, which were measured by XRF.

The cation exchange capacity (CEC) of the starting materials, except of vermiculite, was measured with 0.01 M copper triethylenetetramine (Meier and Kahr, 1999). The CEC of the acid-treated bentonites, kaolins and sepiolites was also determined with copper triethylenetetramine solution to check how far the acid treatment has affected the initial CEC. The concentration of copper triethylenetetramine in the overlaying solution was measured by photometry (λ = 580 nm).

Due to its size, the Cu-triethylenetetramine molecule can not be exchanged completely into natural vermiculites. Therefore, the CEC of the vermiculite and acid treated vermiculite was determined with the ammonium acetate method according to MacKenzie (1951) and Emmerich (2000).

More detailed descriptions of the methods are given in Chapter 3.

6.4 Results and Discussion

6.4.1 Bentonites and Smectites

Composition, colour, morphology and surface

Smectites are Al-bearing layer silicates and the main phases in the < 2 µm fraction of bentonites. The chemical composition of the crude samples is given in Table 6.4.

Table 6.4 XRF-analysis of the natural bentonites.

Oxides		1_Calci	2_EXM757	3_SWy-2	4_Vol	5_WYO	6_IndBent	7_NHec
SiO_2	[%]	49.35	61.01	61.26	56.50	59.85	43.08	55.03
Al_2O_3	[%]	16.61	17.15	17.98	18.56	15.21	15.59	1.99
MgO	[%]	4.15	2.08	2.41	2.26	5.41	2.40	22.84
Fe_2O_3	[%]	5.09	3.76	3.79	3.56	1.61	13.74	0.81
TiO_2	[%]	0.38	0.16	0.15	0.15	0.17	0.94	0.08
MnO	[%]	0.05	0.01	0.03	0.01	0.33	0.12	0.02
Na_2O	[%]	0.26	2.95	1.34	1.88	2.17	3.29	3.31
CaO	[%]	4.26	0.74	1.54	1.14	2.37	1.23	1.88
K_2O	[%]	1.52	0.17	0.59	0.52	0.52	0.10	0.42
P_2O_5	[%]	0.06	0.52	0.04	0.04	0.07	0.06	0.87
LOI	[%]	17.7	11.4	10.3	15.4	12.3	18.8	12.7

The dioctahedral smectites differ in the composition of their interlayers and octahedral sheets. Especially, the Fe- and Mg-contents vary strongly. The cation contents of the smectite interlayers and the Al, Fe and Mg content of the octahedral sheet are listed in Tables 6.5 and 6.6, respectively. The smectite in bentonite EXM757 (2_EXM757) consists of a Na-rich smectite, while the bentonite Calcigel (1_Calci) consists of a Ca-rich smectite with a high content of Mg^{2+} (28%) in the interlayer. In comparison to the other dioctahedral smectites, this smectite has a higher content of Fe^{3+} and Mg^{2+} in the octahedral sheet. In the Wyoming bentonites (3_SWy-2, 4_Vol, 5_WYO) Na^+ and Ca^{2+} are the main interlayer cations. The Indian Bentonite (6_IndBent) consists of a Na-rich smectite. Furthermore, one third of Al^{3+} in the octahedral sheet is substituted by Fe^{3+}; therefore this dioctahedral smectite (6_IndBent) belongs to the Fe-rich smectites.

The main cation in the octahedral sheet of the hectorite is Mg^{2+}. It can partly be substituted by Li^+. The amount of Li^+ has been determined by ICP-OES to be 1.1%.

Table 6.5 Content of interlayer cations [%] of the smectites.

Sample	Na^+ [%]	Ca^{2+} [%]	Mg^{2+} [%]	K^+ [%]	M^{2+} (Ca, Mg) : M^+ (Na) ratio
1_Calci	11	58	28	2	8:1
2_EXM757	83	14	2	1	1:6
3_SWy-2	48	31	19	2	1:1
4_Vol	61	31	6	2	1:2
5_WYO	67	29	4	-	1:2
6_IndBent	90	8	1	1	1:11
7_NHec	90	7	3	-	1:13

Table 6.6 Content of aluminium, iron and magnesium in the octahedral sheet [%] and the amount of the tetrahedral charge.

Sample	Al^{3+} [%]	Fe^{3+} [%]	Mg^{2+} [%]	Li^+ [%]	$\Sigma(Mg^{2+}, Fe^{3+})$ [%]	tetrahedral charge [%]
1_Calci	65	15	20	-	35	62
2_EXM757	77	11	12	-	23	16
3_SWy-2	74	11	15	-	26	72
4_Vol	79	10	11	-	21	20
5_WYO	76	13	11	-	24	39
6_IndBent	64	24	13	-	37	85
7_NHec	2	1	87	10	88	38

Figure 6.1 depicts the Al_2O_3 content of the residual solid of the acid treated dioctahedral bentonites in dependence of the time. Figure 6.1 (left) presents the unreacted Al_2O_3 in %, while Figure 6.1 (right) the amount of unreacted Al_2O_3 as expressed as [$g \cdot mol^{-1}$] related to the molecular weight of the formula unit (half unit cell).

The Al_2O_3 content was adjusted, because other Al_2O_3 containing phases occur in the bulk material (Table 6.10). For this reason, the Al_2O_3 content of the impurities was subtracted from the total amount of Al_2O_3 (Table 6.4). The resulting "corrected" Al_2O_3 content gives information on the stability of the residual solid of the smectites. The corresponding curves of the other octahedral cations (Mg^{2+}, Fe^{3+}) are found in the appendix. The adjustment of the Mg^{2+} and Fe^{3+} content was not necessary, because the main part of the measured Mg^{2+} and Fe^{3+} stems from the smectite.

Both graphs in Figure 6.1 reveal that the Al_2O_3 content of the smectite in the Indian Bentonite and in the Calcigel decreased faster than the Al_2O_3 content of the other dioctahedral smectites like Wyoming bentonites (4_Vol, 5_WYO, 3_SWy-2).

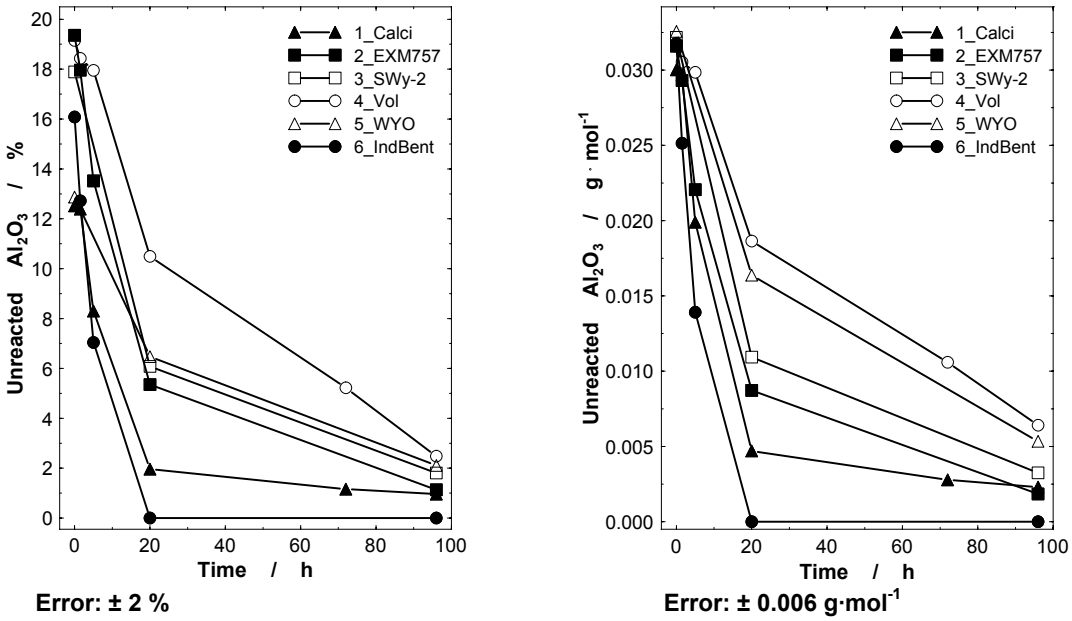

Figure 6.1 Both graphs show the chemical composition of the residual solid with unreacted oxides in % determined by XRF (left) and with unreacted oxides [g·mol^{-1}] related to the molecular weight of the formula unit (half unit cell) (right). The material was treated with 5 M H_2SO_4 for 0, 1.5, 5, 20, 72 and 96 h at 80 °C.

The chemical composition of the residual solid for the hectorite sample in comparison to the raw material is displayed in Table 6.7. After 1.5 h the Al_2O_3 and especially the MgO content were below 1%.

Table 6.7 Chemical composition of the crude and residual hectorite.

Oxides		Hectorite (7_NHec)	
		untreated	1.5h
SiO_2	[%]	63.04	99.06
Al_2O_3	[%]	2.28	0.42
MgO	[%]	26.16	0.00
Fe_2O_3	[%]	0.93	0.16
TiO_2	[%]	0.09	0.08
MnO	[%]	0.02	0.00
Na_2O	[%]	3.80	0.02
CaO	[%]	2.16	0.08
K_2O	[%]	0.53	0.13
P_2O_5	[%]	1.00	0.00

The data of the chemical composition reveal that acid treatment caused the leaching of the octahedral cations. This was proved by the decreasing Mg^{2+}, Fe^{3+} and Al^{3+} content in all bentonite samples investigated. The composition of the octahedral sheet played an important role for the different dissolution rates. Additionally, the data confirm that the dioctahedral smectites are more stable than the trioctahedral smectites.

For the experiment, 4 g of each sample was used. After 1.5 h acid treatment, the total weight of solid was significantly reduced for all bentonite samples. In dependence on the material composition, only 40 to 60% of the material remained. The decrease of weight proved the partial dissolution of the materials.

The bentonite samples are coloured (Figure 6.2), due to the presence of the octahedral cations, especially of iron. The Indian Bentonite was dark brown, whereas the Volclay and the Calcigel were greyish. The other bentonites and the hectorite were lightly coloured. After acid treatment, the materials were significantly lighter in colour (Figure 6.2). The hectorite was completely white after 1.5 h. The Indian Bentonite and the bentonite EXM757 were white after 20 h. The other bentonites were light brown or grey after 96 h. The lightening of the material is proof of the partial release of the octahedral cations.

Figure 6.2 Colour of the material before (left side) and after (right side) acid treatment (5 M H_2SO_4 at 80 °C).

All crude bentonites consist of thick agglomerates of smectites with irregular shape and partly sharp grain boundaries. For examples, Figures 6.3a and 6.4a show the morphology of smectite particles in the natural Indian Bentonite and hectorite. After acid treatment, their morphologies have remarkably changed (Figure 6.3b and 6.4b). The particles of the treated Indian Bentonite and hectorite are smaller and thinner compared to the raw material; however they are still agglomerated. The ESEM images of the other bentonites show similar changes. These images are given in the appendix.

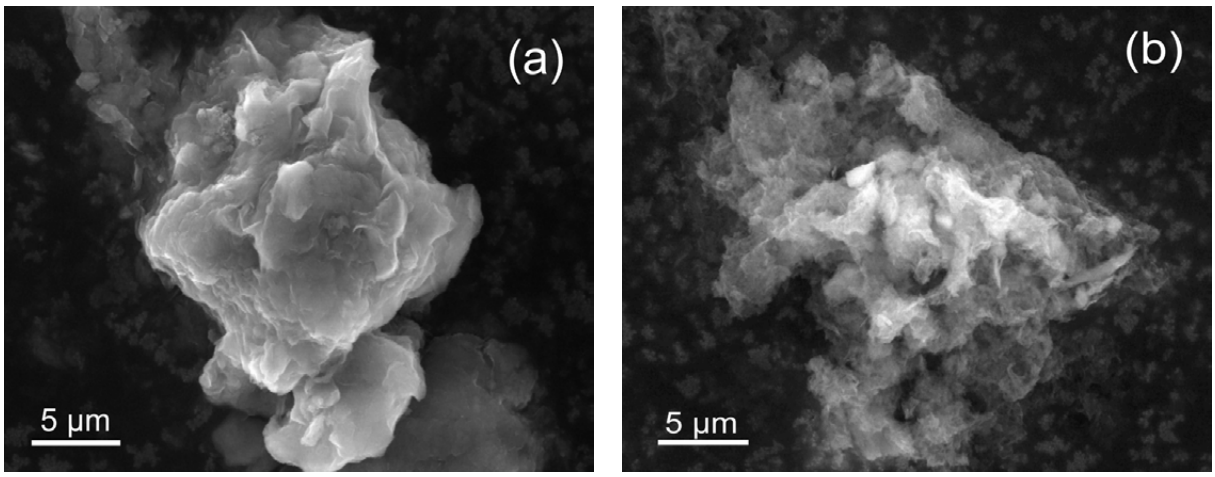

Figure 6.3 ESEM image of the a) raw and b) acid treated Indian Bentonite (6_IndBent). The material was treated with 5 M H_2SO_4 at 80 °C for 96 h.

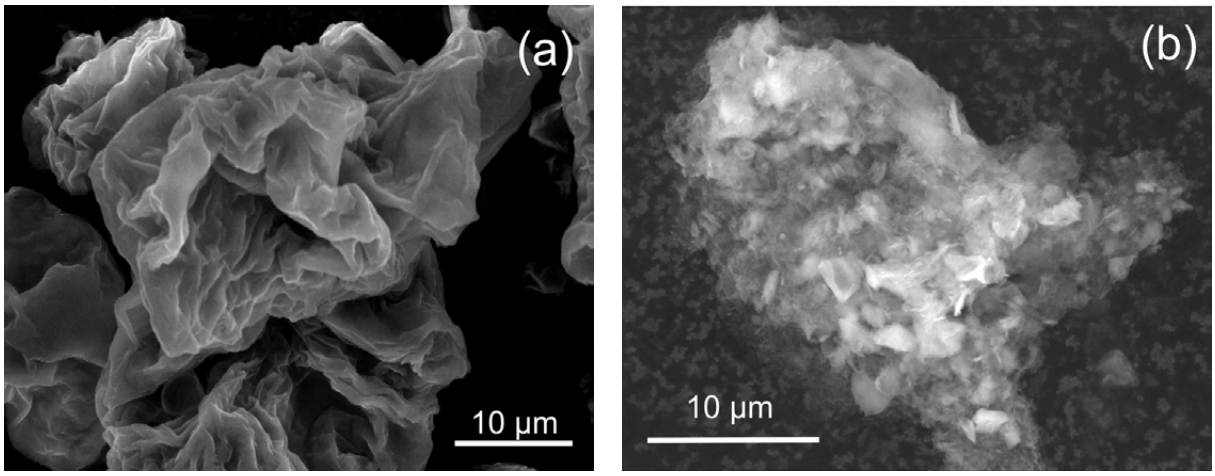

Figure 6.4 ESEM image of the a) raw and b) acid treated hectorite (7_NHec). The material was treated with 5 M H_2SO_4 at 80 °C for 96 h.

The smectites are the main phase in the fraction < 2 µm of the bentonites. Due to their small particle size, the specific surface area (A_S) ranged from 20 to 65 m^2/g.

Two different behaviours for the development of A_S with ongoing acid treatment was observed. For some clays, A_S increased and reached a constant value (4_Vol, SWy-2, 5_WYO); for others, A_S increased and then decreased (1_Calci, 2_EXM757, 6_IndBent, 7_NHec) with further acid treatment (Figure 6.5a). The Indian Bentonite (6_IndBent) displayed the highest A_S after acid treatment of all dioctahedral smectites. After 90 min, the A_S of the hectorite reached a value of 280 m^2/g and with further acid treatment the A_S decreased, but it is still remarkably higher than that of the untreated material (Figure 6.5b). After 96 h, the acid treated hectorite still had a A_s of 122 m^2/g. This trioctahedral smectite showed the same behaviour as vermiculite. The progression of both curves is similar (Figure

6.5b and 6.17). After 96 h, the A_S of the dioctahedral smectites ranged from 80 to 315 m^2/g and is still higher than that of the untreated materials.

The values of the micropore area and the external area, as a function of acid treatment, are given in the appendix. The development of the micropore area reveals that acid treatment caused at first a delamination of the particles. In this case, the delamination of the particles caused a decreasing number of layers per stack. The high values of the A_S of some bentonites (1_Calci, 6_IndBent, 7_NHec) indicate a reduction of layers per stack, too. The maximum of the theoretical A_S was calculated according to Müller-Vonmoos and Kahr (1983) (Table 6.8). These values, which are related to the calculated smectite content (Table 6.10), indicate a complete delamination of the particle into single layers.

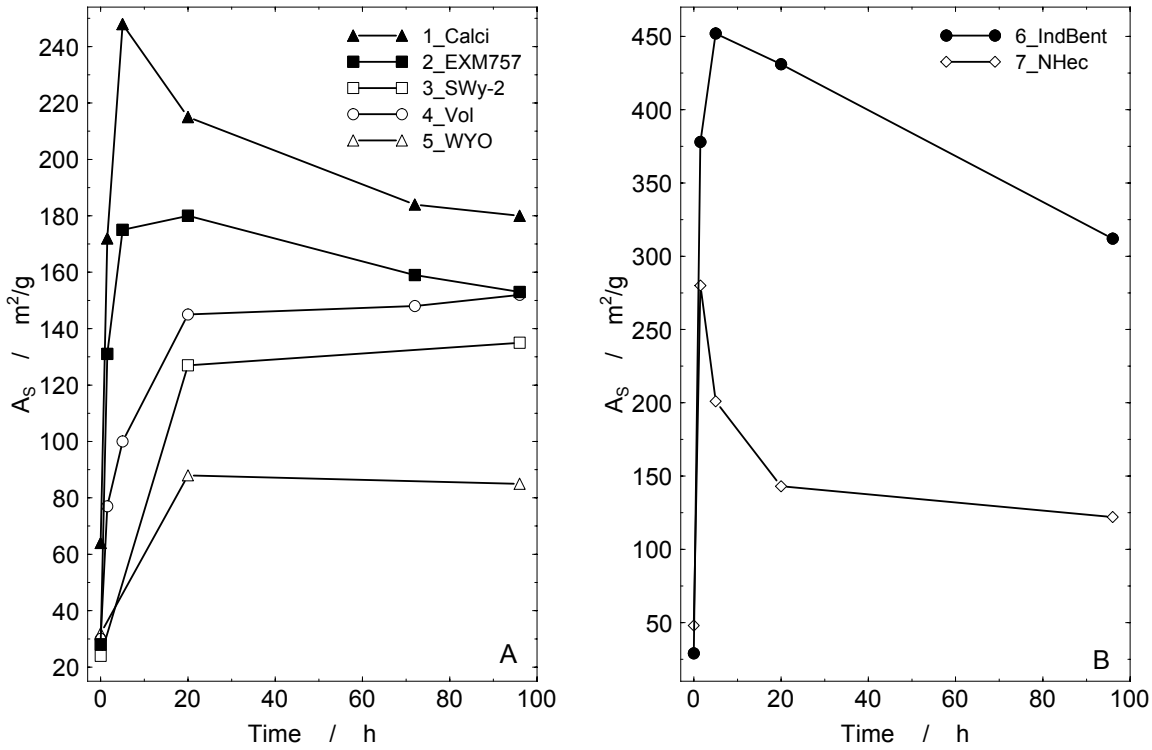

Figure 6.5 Influence of acid treatment with 5 M H_2SO_4 at 80 °C on the specific surface area. Part a) displayed results for bentonite samples that reached a maximum below 250 m^2/g and b) for bentonite samples that attained more than 250 m^2/g as values.

Table 6.8 Calculation of the theoretical surface area in relation to the smectite content.

Sample	d_{060} [nm]	d_{400} [nm]	a [nm]	b [nm]	A* [nm^2]	M** [g/mol]	A_S(max)*** [m^2/g]	$m_{smectite}$ # [%]	A_S ## [m^2/g]
1_Calci	0.12914	0.14988	0.51657	0.89929	0.4645	743.90	749	64	480
2_EXM757	0.12899	0.14978	0.51598	0.89865	0.4637	734.90	757	87	659
3_SWy-2	0.12884	0.14967	0.51536	0.89801	0.4628	733.86	757	79	598
4_Vol	0.12889	0.14965	0.51557	0.89794	0.4629	731.78	759	80	607
5-WYO	0.12881	0.14984	0.51523	0.89906	0.4632	736.92	754	67	505
6_IndBent	0.12911	0.15005	0.51644	0.90033	0.4650	753.88	740	89	659
7_NHec	0.13055	0.15177	0.52221	0.91065	0.4755	750.82	760	94	714

* Area of the base plane of the unit cell.

** Molecular weight per unit cell.

*** Calculated specific surface area, assuming a smectite content of 100%.

\# Smectite content obtained from Rietveld quantification (of Table 6.10).

\## Specific surface area calculated based on smectite content.

Table 6.9 shows the calculated A_S in comparison to the A_S of natural material and to the maximum of A_s after acid treatment. The maximum value of A_S was reached after different times (e.g., for the Calcigel after 5 h acid treatment) for the various bentonites. The calculation of layers per stack does not indicate the thickness of the coherently scattering domains for XRD.

Table 6.9 Comparison between the theoretical and measured A_s and rate of delamination, as well as the number of layers per stack.

Sample	Maximum of A_s [m^2/g]		A_s of the crude material [m^2/g]	Number of layers per stack	Degree of Delamination [%]
	theoretical	Measured			
1_Calci	480	248	65	7-8	52
2_EXM757	659	141	28	23-24	21
3_SWy-2	598	135	24	25	23
4_Vol	607	152	30	20	25
5_WYO	505	88	32	15-16	17
6_IndBent	659	452	29	22-23	69
7_NHec	714	280	48	14-15	39

The maximum of the measured A_S of the Calcigel (1_Calci) is 248 m^2/g after 5 h. This value is slightly higher than half of the theoretical A_S (480 m^2/g). This implies that the number of layers per stack is reduced from 8 to 4 by acid treatment. With further acid treatment (20 h), A_S decreased, while the number of micropores did not increase. This means that with ongoing acid treatment, small particles were completely dissolved. Nearly 70% of the particles from the Indian Bentonite (6_IndBent) and nearly 40% of particles from the hectorite were delaminated by acid treatment. The smectite particles of the Indian Bentonite consist of

22 to 23 layers and the hectorite particle consist of 14 to 15 layers per stack. Thus they are reduced to 6 to 7 layers (6_IndBent) and to 8 to 9 layers (7_NHec) per stack by acid treatment. The delamination of the Wyoming bentonites (3_SWy-2, 4_Vol, 5_WYO) occurred more slowly compared to the other bentonites (1_Calci, 6_IndBent, 7_NHec). Between 15 and 25% of the particles are delaminated. The layers per stack ranged from 12 to 20 after acid treatment.

The delamination of smectites proceeded in different ways. One reason may be the differences in charge distribution in the octahedral and tetrahedral sheets. High contents of substitutions in the tetrahedral sheet cause distortions within the crystal structure and a weakening of the linkage between the layers. Indian Bentonite and Calcigel have the highest content of tetrahedral charge compared to the other smectites, which have nearly the same amount of tetrahedral charge (Table 6.7). Another reason is the exchange of the interlayer cations during acid treatment and the protonation of the SiO-groups of the tetrahedral sheet at low pH (< 2). The interlayer cations like Na^+, Ca^{2+} and Mg^{2+} were exchanged by H^+ ions. The protons cause a positive surface charge of the layers, which tend to repulse each other, thereby enhancing delamination of the layers.

Long range order

The mineralogy of the samples is shown in Table 6.10. All bentonites have similar impurities like quartz, feldspars, mica and calcite. The smectite content of the raw materials ranged from 64 to 94%. One of the smectites is a trioctahedral (d_{060} = 0.152 nm; Brindley and Brown, 1980) natural hectorite (7_NHec). All the other smectites are dioctahedral (d_{060} between 0.149 and 0.150 nm; Brindley and Brown, 1980).

The changes in the long range order with acid treatment were observed by X-ray diffraction. In the XRD pattern, the intensity of the basal reflection (d_{001}) and of the peaks ($d_{020,\ 110,\ 021}$ and d_{060}) decreased with increasing acid treatment. The peaks of the impurities (quartz, cristobalite, feldspar, mica) were still partly detected, because their dissolution is much slower (Carroll and Starkey, 1971; Snäll and Liljefors, 2000; Jozefaciuk and Bowanko, 2002). Additionally the background increased with increasing acid treatment, which can be interpreted as increasing content of X-ray amorphous silica phases.

The X-ray patterns (Figure 6.6 and 6.7) of the acid treated and natural Indian Bentonite (6_IndBent) and hectorite (7_NHec) show that the octahedral sheet of the Indian Bentonite (Figure 6.1) was completely dissolved after 20 h, whereas the octahedral sheet of the hectorite was already dissolved after 1.5 h. In comparison, the Volclay still exhibited a very small and broad peak after 96 h. Its octahedral sheet was not completely dissolved. The X-ray patterns of the other bentonites are displayed in the appendix.

Table 6.10 Quantification of the natural bentonites from Rietveld analysis of XRD patterns.

Phases[#] \ Sample	1_Calci [%]	2_EXM757 [%]	3_SWy-2 [%]	4_Vol [%]	5_WYO [%]	6_IndBent [%]	7_NHec [%]
Smectite (Na-rich, di)*	-	86.5 ± 1.3	79.4 ± 2.1	60.0 ± 4.2	67.2 ± 2.2	82.2 ± 3.6	-
Smectite (Na-rich, tri)*	-	-	-	-	-	-	93.9 ± 1.3
Smectite (Ca-rich, di)*	24.6 ± 10.8	-	-	19.8 ± 3.6	-	6.7 ± 3.0	-
Smectite (Mg-rich, di)*	38.9 ± 10.2	-	-	-	-	-	-
Kaolinite*	3.8 ± 0.8	-	-	-	-	4.4 ± 0.8	-
Muscovite / Illite*	13.7 ± 1.5	-	3.7 ± 1.4	2.8 ± 0.9	5.4 ± 1.4	-	-
Quartz	5.9 ± 0.7	2.3 ± 0.3	10.5 ± 1.0	4.4 ± 0.5	6.6 ± 0.8	1.1 ± 0.3	-
Cristobalite	-	11.2 ± 1.3	-	-	3.6 ± 0.6	-	-
K-Feldspars (Orthoclase)*	-	-	4.2 ± 1.4	4.0 ± 0.9	-	-	-
K-Feldspars (MicroclineInt1)*	-	-	-	-	3.9 ± 0.7		-
Plagioclase (Albite)*	2.5 ± 0.7	-	-	4.1 ± 0.8	-	-	-
Plagioclase (Oligoclase)*	-	-	-	-	8.0 ± 1.8	-	-
Plagioclase (Anorthite)*	-	-	-	-	-	3.9 ± 1.2	-
Calcite	3.3 ± 0.5	-	2.2 ± 0.4	1.3 ± 0.4	3.5 ± 0.6	-	3.1 ± 0.8
Dolomite	7.3 ± 0.5	-	-	-	-	-	-
Ankerite (Fe 0.54)	-	-	-	-	-	-	0.7 ± 0.6
Maghemite	-	-	-	-	-	0.9 ± 0.3	-
Hematite	-	-	-	-	-	0.8 ± 0.3	-
Gypsum	-	-	-	3.6 ± 0.6	0.9 ± 0.4	-	-
Clinoptilolite*	-	-	-	-	1.0 ± 0.5	-	-
Analcime (cubic)*	-	-	-	-	-	-	1.2 ± 0.8

In parenthesis the structure model used for Rietveld analysis is given.

* Al_2O_3 containing phases.

Obviously, the dissolution of the smectite phase resulted in a dissolution of the octahedral sheet and the release of aluminium, iron and magnesium. In addition, aluminium was removed from the tetrahedral sheet, which changed the electron density in the crystal structure and this affected peak intensities. Furthermore, acid treatment caused reduction of the crystallite size of the particles, which also affects peak intensities. The long range order was lastingly disturbed by acid treatment.

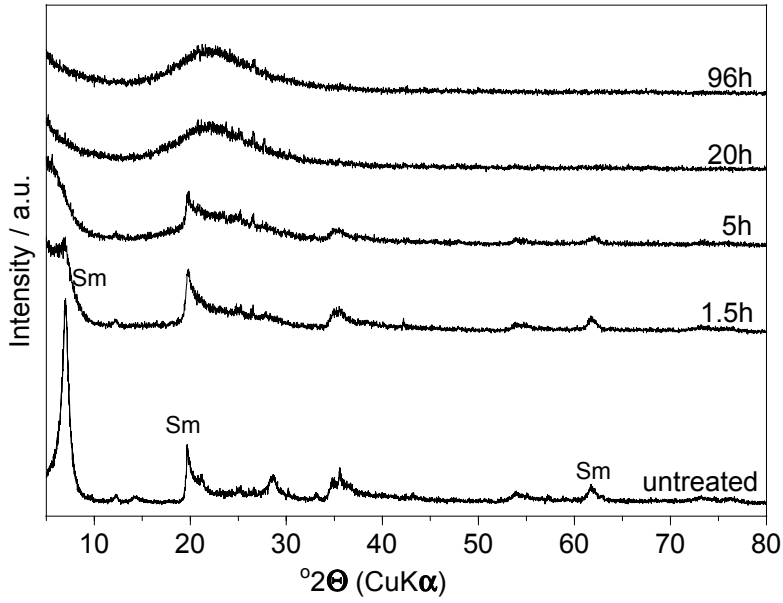

Figure 6.6 X-ray pattern (powder sample) of the raw and acid treated Indian Bentonite (5 M H_2SO_4 at 80 °C);
Sm: characteristic Smectite peaks with increasing 2θ (001), (020,110,021), (060).

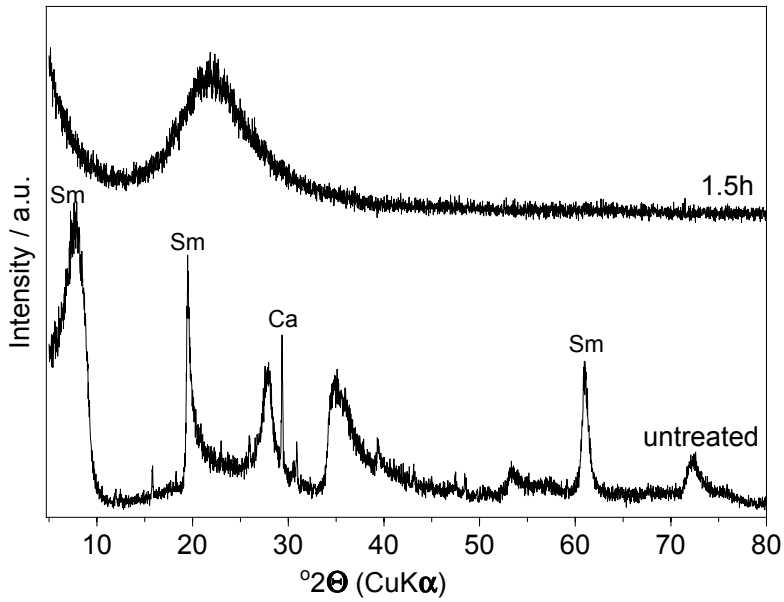

Figure 6.7 X-ray pattern (powder sample) of the raw and acid treated hectorite (5 M H_2SO_4 at 80 °C);
Sm: characteristic Smectite peaks with increasing 2θ (001), (020,110,021), (060); Ca: Calcite.

Short range order

Changes in the short range order, caused by the successive dissolution of octahedral cations, can be observed in the FTIR-spectra. Figure 6.8 and 6.9 displays the FTIR spectra of the raw and acid treated dioctahedral smectites a) Indian Bentonite, b) EXM757, c) Calcigel and d) Volclay and Figure 6.13 depicts the FTIR spectra of natural and acid treated

hectorite (trioctahedral). The spectra of the other two bentonites (3_SWy-2 and 5_WYO) are given in the appendix.

In general, dioctahedral smectites show sharp vibration bands in the region between 400 and 1200 cm^{-1}. Their assignments are listed in Table 6.11 (Farmer, 1974; Komadel et al., 1990; Komadel et al., 1996; Madejová et al., 1998; Tyagi et al., 2006).

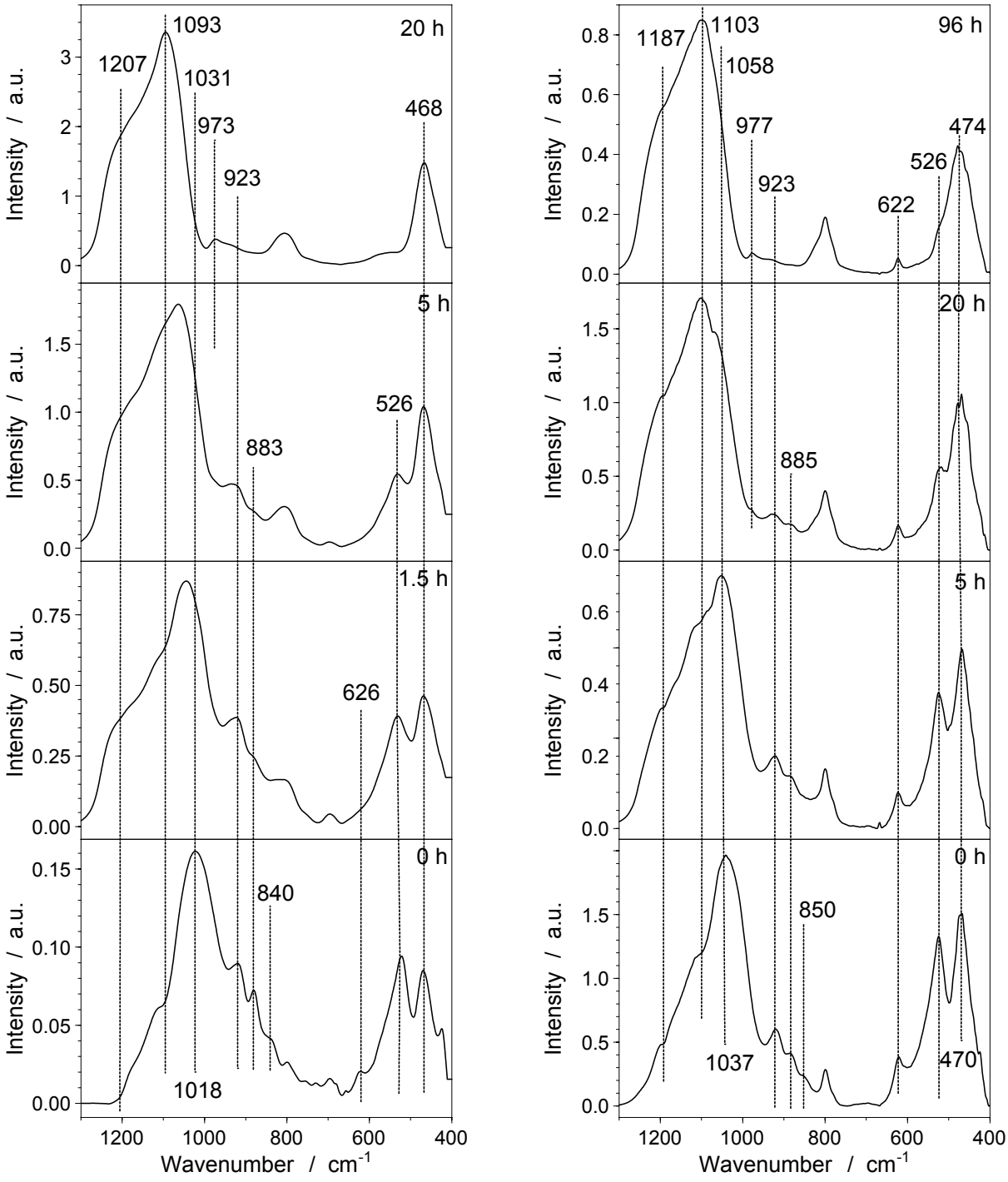

a) Indian Bentonite (6_IndBent) b) EXM757 (2_EXM757)

Figure 6.8 FTIR spectra of the raw and acid treated a) Indian Bentonite (6_IndBent) and b) EXM757 (2_EXM757), which were treated with 5 M H_2SO_4 at 80 °C for several hours.

In this region, Si-O bending vibrations (400 – 600 cm^{-1}), OH bending vibrations or interactions with octahedral cations (600 – 950 cm^{-1}) and Si-O stretching vibrations (700 - 1200 cm^{-1}) occur (Farmer, 1974; Friedrich, 2004). Most of these bands are remarkably affected by acid treatment.

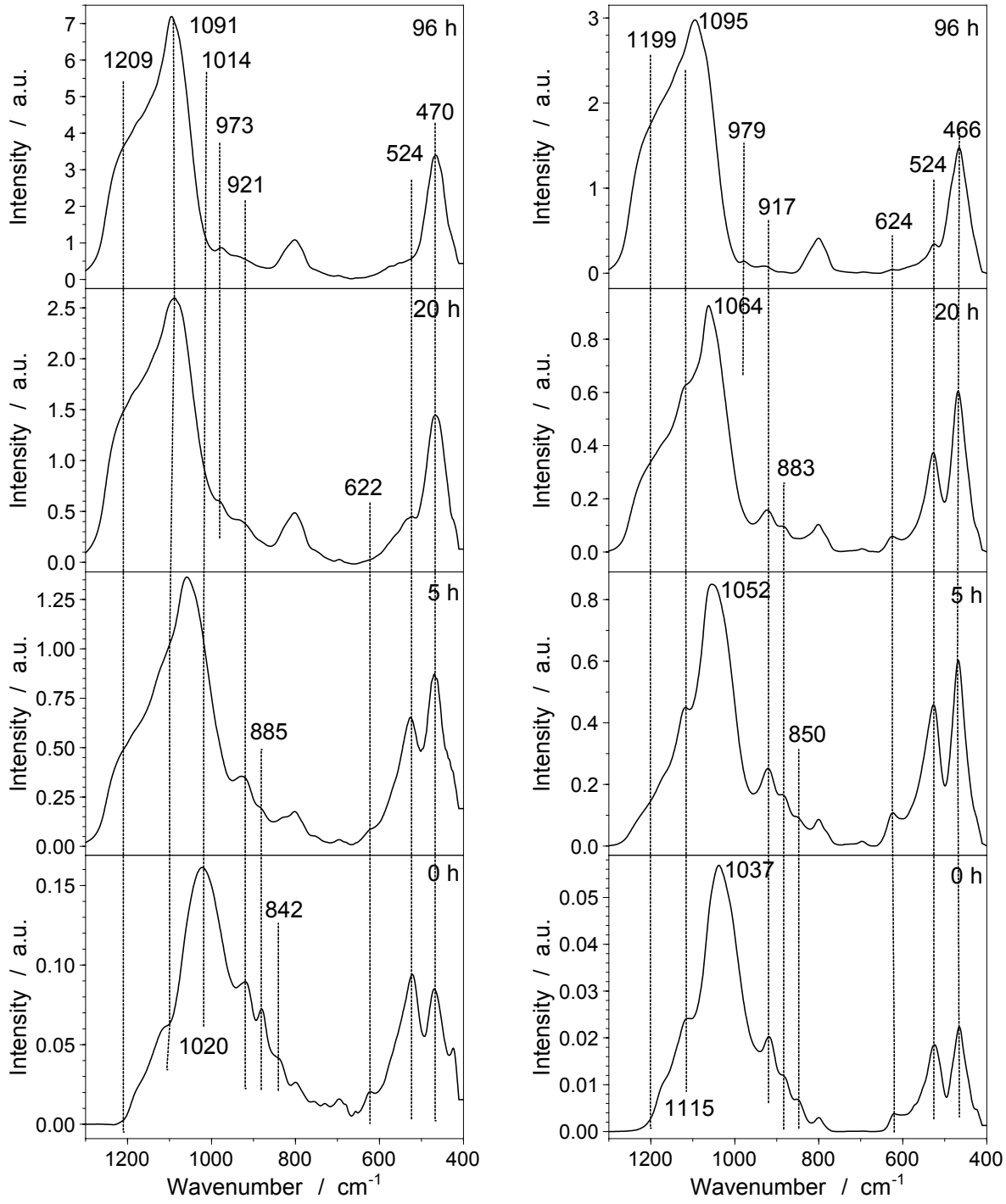

Figure 6.9 FTIR spectra of the raw and acid treated c) Calcigel (1_Calci) and d) Volclay (4_Vol), which were treated with 5 M H_2SO_4 at 80 °C for several hours.

Especially, the intensities of the bands related to aluminium in the octahedral sheet (920, 883, 850, 624 and 524 cm^{-1}) change. The band near 920 cm^{-1} can be assigned to an AlAlOH bending vibration and gives information on the content of aluminium in the octahedral sheet. Both vibrations at lower wavenumbers (883 and 850 cm^{-1}) reflect a partial substitution of aluminium by iron (AlFeOH bending vibration) and magnesium (AlMgOH bending vibration). The absorption band around 624 cm^{-1} can be attributed to a R-O-Si (R = Al, Fe, Mg) vibration and indicates a perpendicular vibration of the octahedral cations. The band near 524 cm^{-1} can be assigned to a Si-O-Al vibration of aluminium in the octahedral sheet. All the other bands near 1115 (shoulder), 1037 and 466 cm^{-1} are strong Si-O vibrations in the bending and stretching region.

Table 6.11 Positions and assignments of the vibrational bands of the dioctahedral smectites.

Wavenumbers [cm^{-1}]				Assignment*
a) 6_IndBent	b) 2_EXM757	c) 1_Calci	d) 4_Vol	
1115	1103	1091	1115	Si-O stretching vibration (out-of-plane)
1018	1037	1020	1037	Si-O stretching vibration (in-plane)
923	923	921	917	AlAlOH bending
883	885	885	883	AlFeOH bending
840	850	842	850	AlMgOH bending
626	622	622	624	R-O-Si with R = Al, Mg, Fe
526	526	524	524	Si-O-Al vibration (Al octahedral cation)
468	470	470	466	Si-O-Si bending vibration

* Komadel et al., 1990; Madejová et al., 1998; Tyagi et al., 2006.

Acid treatment caused changes in the intensity of all bands, which are related to octahedral cations. The intensity of the bands near 624 and 524 cm^{-1} decreased with increasing acid treatment. The band near 624 cm^{-1} completely disappeared for the Indian Bentonite after 1.5 h, for the Calcigel after 5 h and for the Volclay after 96 h. In contrast, a small band still existed for the EXM757 after 96 h. The band near 524 cm^{-1} completely disappeared after 96 h for the Calcigel and for the EXM757 and after 20 h for the Indian Bentonite. In the FTIR spectra of the Volclay, a small band near 524 cm^{-1} remained.

The intensities of the OH bending vibrations near 920, 883 and 850 cm^{-1} decreased with increasing acid treatment (Figure 6.8a - b and 6.9c - d). All FTIR spectra of the dioctahedral smectites show that the AlMgOH vibrations disappeared after a short treatment time. The AlMgOH band disappeared after 1.5 h for the Indian Bentonite (Figure 6.8a) and after 5 h for the Calcigel (Figure 6.9c). In the spectra of EXM757 (Figure 6.8b) and Volclay (Figure 6.9d), a small AlMgOH band still existed after 5h, which disappeared completely after 20 h.

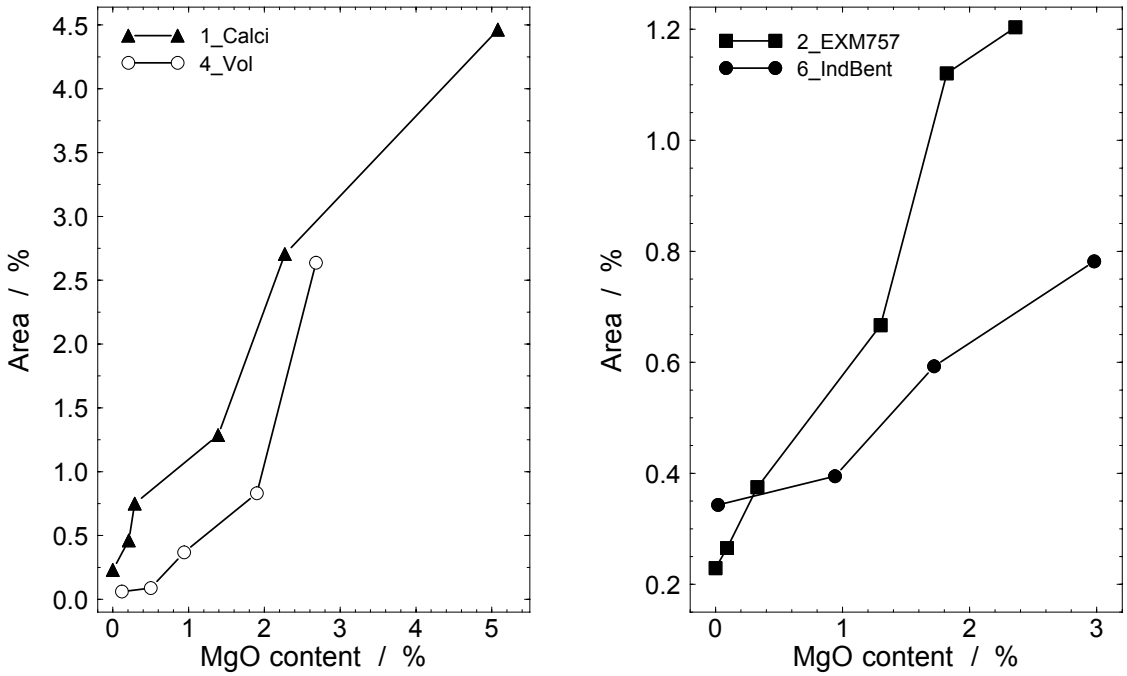

Figure 6.10 Comparison between the unreacted Mg content and the area of the AlMgOH vibration near 850 cm^{-1}. Dioctahedral smectites were treated with 5 M H_2SO_4 at 80 °C at 1.5, 5, 20, 72 and 96 h.

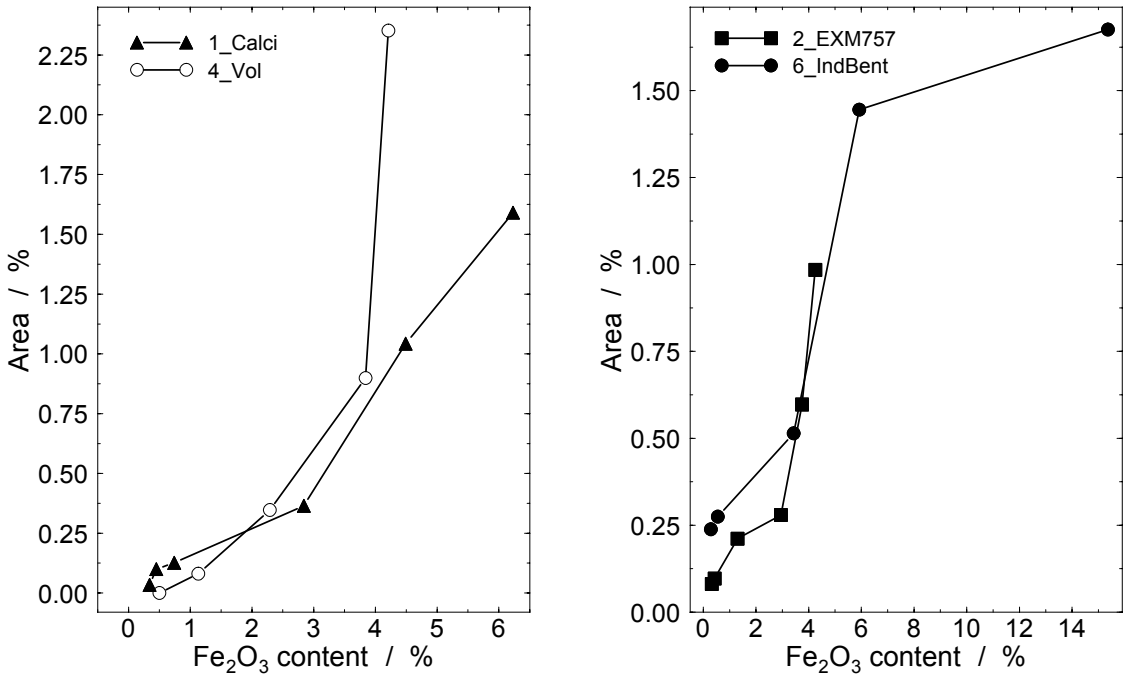

Figure 6.11 Comparison between the unreacted Fe content and the area of the AlFeOH vibration near 885 cm^{-1}. Dioctahedral smectites were treated with 5 M H_2SO_4 at 80 °C at 1.5, 5, 20, 72 and 96 h.

Figures 6.10 and 6.11 show the content of undissolved magnesium and unreacted iron compared to the area of the AMgOH band and of the AlFeOH band of Calcigel (1-Calci), Volclay (4_Vol); Indian Bentonite (6_IndBent) and EXM757 (2_EXM757). In comparison to

the AlMgOH band, the intensity of the AlFeOH band decreased more slowly. The AlFeOH vibration disappeared after 5 h for the Indian Bentonite and after 20 h for the Calcigel. In the spectra of EXM757 and Volclay, a small AlFeOH band still existed after 20 h, which disappeared completely after 96 h.

The release of aluminium occurred continuously (Figure 6.12). They display the content of unreacted aluminium in comparison to the area of the AlAlOH band for the Calcigel (1_Calci), Volclay (4_Vol), Indian Bentonite (6_IndBent) and for smectite in the bentonite EXM757 (2_EXM757). The AlAlOH band disappeared completely for the Indian Bentonite after 20 h and for the two dioctahedral smectites (Calcigel, EXM757) between 20 and 96 h; while in the Volclay spectra, a small AlAlOH vibration still existed. The decrease of intensity shows the release of octahedral cations. The dissolution of the octahedral cations occurred in the following order: Mg^{2+} > Fe^{3+} > Al^{3+}. The occurrence of a small AlAlOH band after 96 h indicates that the smectite was not fully dissolved.

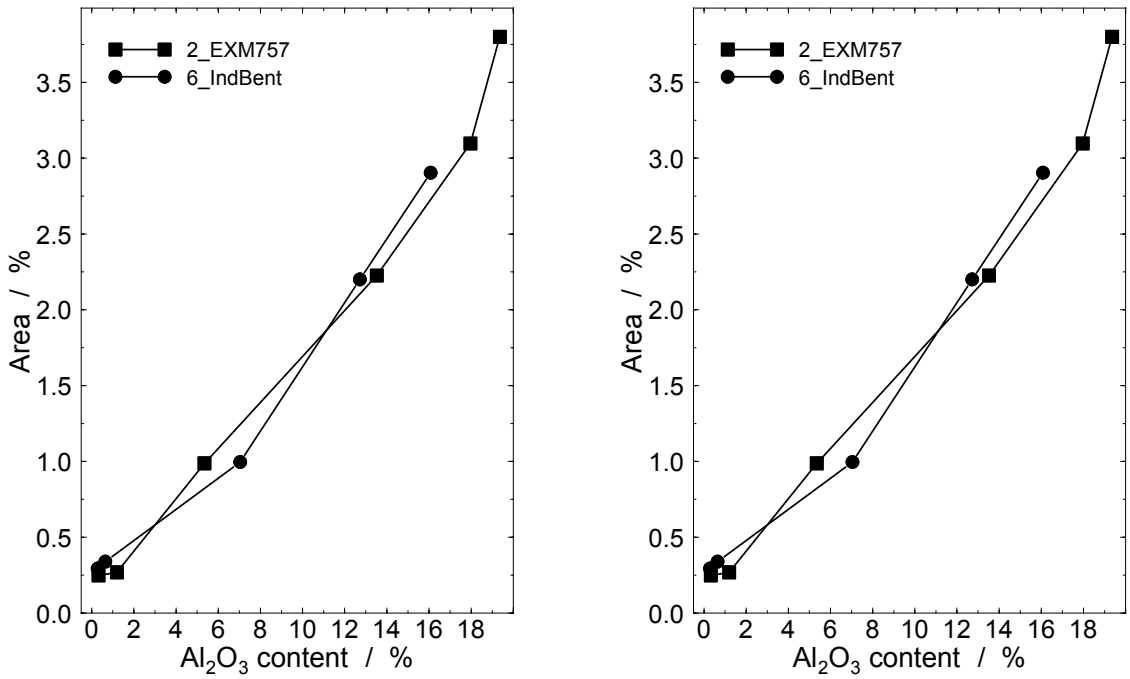

Figure 6.12 Comparison between the unreacted aluminium content and the area of the AlAlOH vibration near 920 cm^{-1}. Dioctahedral smectites were treated with 5 M H_2SO_4 at 80 °C at 1.5, 5, 20, 72 and 96 h.

The leaching of the octahedral cations caused a relative increase in the intensity of Si-O vibrations. The strong Si-O band near 466 cm^{-1} increased with increasing treatment and after 96 h a broad vibration still exists. This absorption band is characteristic for amorphous silica. Another vibration near 800 cm^{-1}, which overlapped the Si-O vibration of quartz, indicates the formation of amorphous silica with a three-dimensional framework (Komadel et al., 1990; Madejová et al., 1998). Between 20 h and 96 h a broad vibration near 979 cm^{-1} appeared in the spectra of the dioctahedral smectites. This band can be assigned to Si-O stretching of

SiOH groups, which are present in the three dimensional product formed, while the octahedral sheet in the smectite layers becomes substantially dissolved (Madejová et al., 1998). The bands in the SiO stretching region (700 – 1200 cm^{-1}) disappeared and a strong and broad vibration around 1091 cm^{-1} with a broad shoulder at higher wavenumber arose. Both bands are typical for the presence of amorphous silica (Friedrich, 2004). The changes in the SiO stretching region show the partial transformation of the layered tetrahedral sheet to a three dimensional framework of protonated amorphous silica (Madejová et al., 1998).

The FTIR spectra (Figure 6.13) of the trioctahedral smectites generally show broad and rounded absorption bands (Wilson, 1994). Their assignments are listed in Table 6.12 (Farmer, 1974; Komadel et al., 1990; Komadel et al., 1996; Madejová et al., 1998; Tyagi et al., 2006).

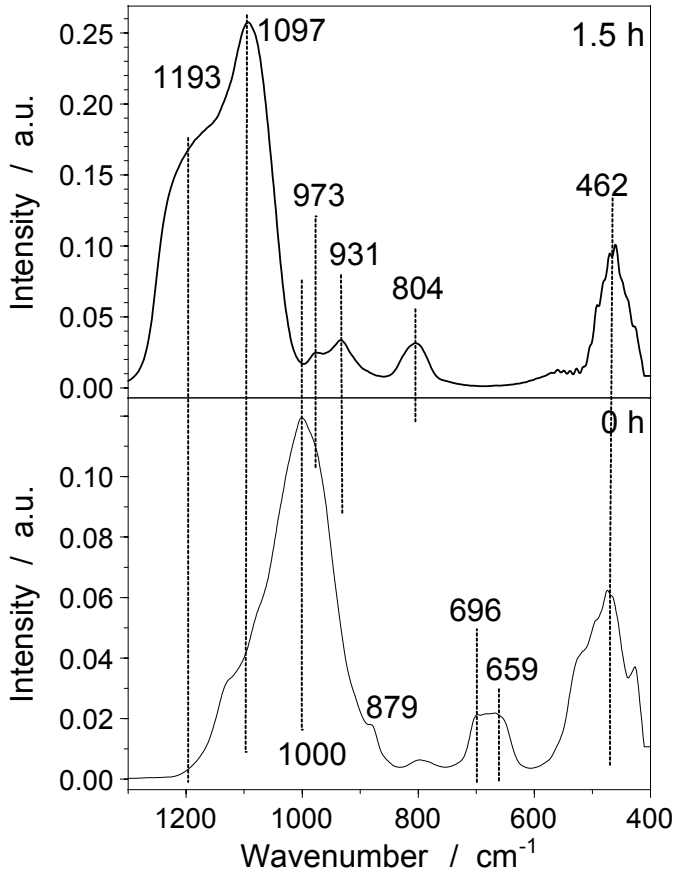

Figure 6.13 FTIR spectra of the raw and acid treated hectorite (1.5 h).
The natural hectorite (7_NHec) was treated with 5 M H_2SO_4 at 80 °C.

In the OH bending region from 550 – 900 cm^{-1}, a broad band occurred with two maxima (696 and 659cm^{-1}). The band at lower wavenumbers can be assigned to a OH bending vibration (Komadel et al. 1990; Madejová et al., 1996). The vibration at 696 cm^{-1} can be attributed to a Si-O (out of plane) bending vibration. The strong band at 462 cm^{-1} can be assigned to a Si-O (in plane) bending vibration and to a Si-O-Mg band. The Si-O-Mg band is

overlapped by the strong Si-O-Si vibration (462 cm^{-1}). In the stretching region, one sharp band with a shoulder to higher wavenumbers existed. This band near 1000 cm^{-1} is attributed to a SiO stretching vibration. The band at 879 cm^{-1} supports the presence of calcite in the sample.

Table 6.12 Positions and assignment of the vibrational bands of the trioctahedral smectite.

Wavenumber [cm^{-1}]	Assignment
1124	Si-O stretching vibration (out-of-plane)
1000	Si-O stretching vibration (in-plane)
696	SiO bending vibration (out of plane)
659	OH bending vibration
526	MgO
460	SiO bending vibration (in plane)
463	Si-O-Mg vibration

* Farmer, 1974; Komadel et al., 1996; Madejová et al., 1998.

The vibrations at 696 and 659 cm^{-1} disappeared completely after 1.5 h in 5 M H_2SO_4 at 80 °C (Figure 6.13). This implies that the cations from the octahedral sheet were dissolved completely. The strong OH stretching vibration at 1000 cm^{-1} disappeared completely and five new absorption bands at 1193, 1087, 973, 931 and 804 cm^{-1} appeared after acid treatment. Similar to dioctahedral smectites, the new vibrations are characteristic for amorphous silica (Komadel et al., 1990; Madejová et al., 1998; Makó et al., 2006). The vibration at 931 cm^{-1} can be assigned to SiO-stretching of SiOH groups (Farmer, 1974; Komadel et al., 1996). The intensity of the broad Si-O band at 460 cm^{-1} increased with acid treatment and the band width narrowed. The Si-O-Mg band, which was overlapped by the strong Si-O band, completely disappeared. The overlapping of these both bands was detected by band fitting using PeakFit program 4.0 from Jandel Scientific. The disappearance of the Si-O-Mg band implies that the cations were dissolved from the octahedral sheet. The band at 460 cm^{-1} is also characteristic for the presence of amorphous silica. With further acid treatment, the intensity of SiO vibrations characteristic for amorphous silica increased even more, but no other changes in the FTIR spectra were observed.

According to these spectroscopic results, we conclude that trioctahedral smectites dissolve in acids much faster than dioctahedral smectites. The dissolution of dioctahedral smectites was not complete, because vibrations attributed to octahedral cations were observed in the FTIR spectra of the residue. The acid treatment of both dioctahedral and trioctahedral smectites leads to the formation of a hydrous amorphous silica phase (Komadel et al., 1990; Komadel et al., 1996; Madejová et al., 1998).

Layer charge and exchange reactions

The raw bentonites have a CEC between 60 and 95 meq/100g. The measured CEC is only caused by the existence of the smectite phase. The CEC decreased with increasing acid treatment (Figure 6.14), but after 96 h some dioctahedral bentonites like Volclay and SWy-2 still exhibited a CEC. The natural hectorite (7_NHec) has a CEC of 90 meq/100g. This CEC decreased faster than that of the dioctahedral bentonites. After 90 min the measured CEC is about 20 meq/100g. The CEC of the Indian Bentonite (6_IndBent) and of Calcigel decreased faster than those of the Wyoming bentonites like Volclay, SWy-2 and WYO-Bentonite. After 20 h, both had a CEC below 10 meq/100g. The Wyoming bentonites have a CEC near 10 meq/100g after 96 h.

The low CEC and the high A_S caused a lower charge density. The decrease of the charge density was corroborated by the exchange with large molecules like alkylammonium ions while measuring layer charge (Lagaly and Weiss, 1970; Lagaly, 1989 and 1994; Wolters et al., 2008). The raw and acid treated smectites were intercalated with alkylammonium ions such as dodecylamine (C_{12} chain). The intercalation of the alkylammonium ions resulted in an expansion of the interlayer and a shift of the characteristic basal XRD peaks.

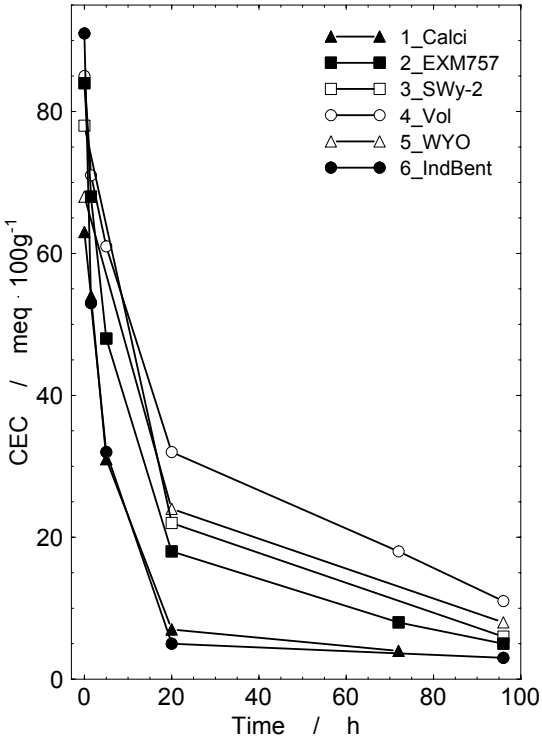

Figure 6.14 Changes in measured CEC with time of acid treatment for the bentonites investigated (5M H_2SO_4).

Low to medium charged smectites show monolayer (1.36 nm) and bilayer (1.77 nm), as well as the transition from monolayer to bilayer after the intercalation with alkylammonium ions. Higher charged samples produced pseudotrimolecular layer (2.17 nm) and paraffin-type

configurations (> 2.2 nm) (Lagaly, 1994). Most of the crude smectites had a basal reflection around 1.5 nm after the intercalation with dodecylamine (Table 6.13). Thus, these intercalated smectites can be regarded as mixed layers with monolayers and bilayers. Only the montmorillonite of the Indian bentonite produced bilayer due to its higher layer charge. After acid treatment, most of the smectite residuals intercalated dodecylamine in a planar alignment. The portion of bilayers was reduced.

Table 6.13 Basal reflection (d_{001}) of the raw and acid treated smectites after the intercalation with dodecylamine.

Sample	Crude [nm]	1.5 h [nm]	20 h [nm]	96 h [nm]
1_Calci	1.53	n.m.	n.m.	n.m.
2_EXM757	1.54	1.38	1,36	n.m.
3_SWy-2	1.51	n.m.	1.36	n.m.
4_Vol	1.51	1.38	1.36	1.36
5-WYO	1.54	n.m.	1.36	n.m.
6_IndBent	1.79	1.37	n.m.	n.m.

n.m. not measured.

The raw Calcigel had predominantly mono- and bilayer, but also small amounts of pseudotrilayer were observed. The acid treated Calcigel showed ordered pseudotrilayer (1.16 and 2.34 nm) after the intercalation.

The CEC and the adjusted Al_2O_3 content was used to estimate the residual smectite content after acid treatment. The values of the residual smectite content after 96 h are shown in Table 6.14.

Table 6.14 Smectite content estimated from CEC and from the adjusted Al_2O_3 content after 5 M H_2SO_4 at 80 °C for 96 h.

Sample	Smectite content from [%]	
	CEC	Al_2O_3
1_Calci	5	5
2_EXM757	5	5
3_SWy-2	7	8
4_Vol	10	10
5_WYO	12	11

These smectite contents were compared with the calculated contents from quantitative XRD analysis. An internal standard (ZnO) was used to quantify the amorphous SiO_2. For the sample 4_Vol after 96 h (5 M H_2SO_4, 80 °C), Rietveld calculation yielded a smectite content of 24%. The reason for the deviation in smectite content is the correlation between the

smectite model (Ufer et al., 2004) and the high content of amorphous silica phase. This correlation led to a reduced dimensioning of the smectite content.

The exchange of interlayer cations against H^+ ions occurred upon acid treatment, which was proved by the determination of the sum of the exchangeable cations. The sum of the exchangeable cations was lower than the CEC value. This difference can be explained by the existence of H^+, which were exchanged against Cu-trien, but cannot be measured by ICP-OES. Further acid treatment caused the release of octahedral cations and the protonation of the SiO groups, which showed a weak cross-linking. These factors resulted in a decrease of the layer charge, which led to a reduction of the CEC.

6.4.2 Vermiculite

The vermiculite (8_Verm) is a trioctahedral mineral, with high magnesium content in the octahedral sheet. In comparison to the smectites in bentonites, the vermiculite has a higher layer charge due to substitutions in the octahedral and tetrahedral sheets.

Composition, colour, morphology and surface

The chemical composition of the natural and residual vermiculite is shown in Table 6.15. After 1.5 h of acid treatment, the chemical composition strongly changed. All elements except Si were nearly completely dissolved and their concentrations were below 0.5%.

Table 6.15 Chemical composition (XRF) of the raw and residual vermiculite (5 M H_2SO_4, 80 °C).

Oxides		Vermiculite (8_Verm)	
		Untreated	1.5h
SiO_2	[%]	46.23	99.50
Al_2O_3	[%]	12.81	0.28
MgO	[%]	32.68	0.01
Fe_2O_3	[%]	6.45	0.11
TiO_2	[%]	0.69	0.02
MnO	[%]	0.08	0.01
Na_2O	[%]	0.00	0.00
CaO	[%]	0.71	0.05
K_2O	[%]	0.33	0.01
P_2O_5	[%]	0.02	0.00

The total weight of solid vermiculite was significantly reduced after 1.5 h acid treatment. Only 35% of the material remained. With increasing treatment time, the weight of the residual material was the same. The decrease of weight proved the partial dissolution of the materials. The same weight after 1.5 h and after 96 h showed that a part of the material is stable against acid. According to the chemical data, the residual material consisted of silicon.

The vermiculite sample is light brown (Figure 6.15), which was caused by the octahedral cations, especially by the content of iron. The vermiculite was completely white after 1.5 h (Figure 6.15). The lightening of the material proved the partial release of the octahedral cations.

Figure 6.15 Colour of the material before (left) and after (right) acid treatment (5 M H_2SO_4, 80 °C).

The raw vermiculite consisted of thick agglomerates with a layered appearance and with irregular shape (Figure 6.16a). After acid treatment, the layered appearance is still present (Figure 6.16b).

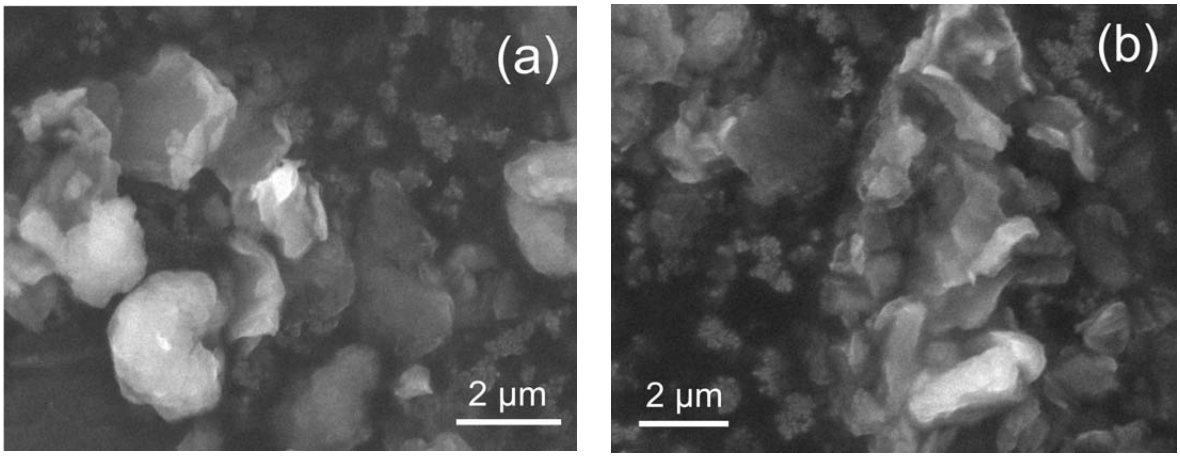

Figure 6.16 ESEM images of the a) raw and b) acid treated vermiculite (8_Verm). The material was treated with 5 M H_2SO_4 at 80 °C for 20 h.

The vermiculite had an A_S value of 36 m^2/g. This value is similar to that of the bentonites. Acid treatment caused an increase in A_s (Figure 6.17). After 90 min of treatment, the vermiculite had an A_S of 615 m^2/g. With further acid treatment, the A_S decreased but remained higher than that of the untreated material (Figure 6.17). After 20 h, the acid treated vermiculite had an A_S of 387 m^2/g. The A_S of vermiculite was higher than that of smectite.

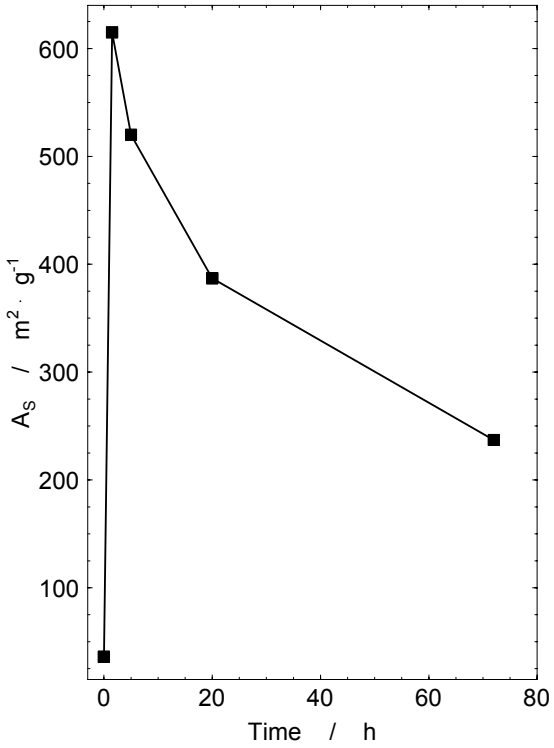

Figure 6.17 The influence of the acid treatment on the specific surface area of the vermiculite. The material was treated with 5 M H_2SO_4 at 80 °C.

From the gas adsorption data (N_2), the external specific surface area (A_E) and the micropore area (A_{MP}) can be estimated by using the t-plot according to De Boer et al. (1966). In Table 6.16, the percentages of the A_{MP} relative to the A_S for the starting vermiculite material and for the acid treated vermiculite are presented.

Table 6.16 Specific surface area (A_S), external specific surface area (A_E) and micro-pore area (A_{MP}) of the starting (8_Verm) and acid treated vermiculite (5 M H_2SO_4, 80 °C).

	Vermiculite (8_Verm)			
Time [h]	A_S [m^2/g]	A_E [m^2/g]	A_{MP} [m^2/g]	A_{MP} / A_S [%]
0	36	12	24	67
1.5	615	503	111	18
5	520	442	76	15
20	387	366	21	5
72	236	218	18	7

The starting material has a high content of micropores (< 2 nm) and a small specific surface area (Figure 6.18a) due to the grinding procedure (see Chapter 4.3.2). The percentage of micropores decreased with increasing acid treatment (Table 6.16).

The starting material had more macropores (> 50 nm) than the 90 min acid treated material (Table 6.17). With further acid treatment, the content of macropores increased.

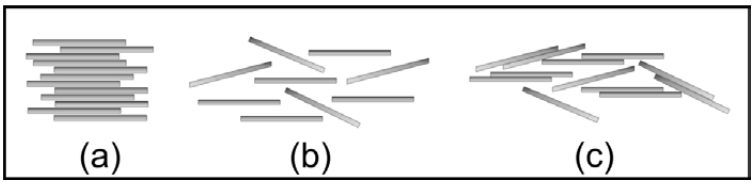

Figure 6.18 Schematic representation of the particle arrangement a) of the starting, b) of the 1.5 h acid treated and c) of the 20 h acid treated material.

Table 6.17 Amount of macropores of the starting (8_Verm) and acid treated vermiculite (5 M H_2SO_4, 80 °C) for varying treatment times.

Vermiculite (8_Verm)	
Time [h]	Macro-pores [%]
0	9
1.5	3
5	4
20	5
72	7

The A_S maximum was calculated according to Müller-Vonmoos & Kahr (1983). This value represented the complete delamination of the particles. The calculated A_S was 647 m^2/g and agreed well with the measured specific surface area (615 m^2/g) after 1.5 h acid treatment. The agreement of both values, as well as the low content of micro and macropores, implied that the vermiculite particles were delaminated almost completely by acid treatment (Figure 6.18b). With ongoing acid treatment, the external specific surface area and the micro-porosity decreased. This means that the particles were still delaminated, but some particles started to accumulate again (Figure 6.18c). This was supported by the associated observed increase in macropore content (Table 6.17).

Long range order

The vermiculite sample (8_Verm) consisted of 84% vermiculite and contained the following impurities: calcite (2%) and phlogopite (14%). Phlogopite is a trioctahedral mica, which also has a high content of magnesium in the octahedral sheet.

The X-ray pattern (Figure 6.19) showed the changes in the long range order of the acid treated vermiculite and of the impurities. Already, after 1.5 h, the X-ray pattern showed no longer any significant peak. In this case, the vermiculite and all impurities are completely dissolved. A hydrous X-ray amorphous silica phase was formed.

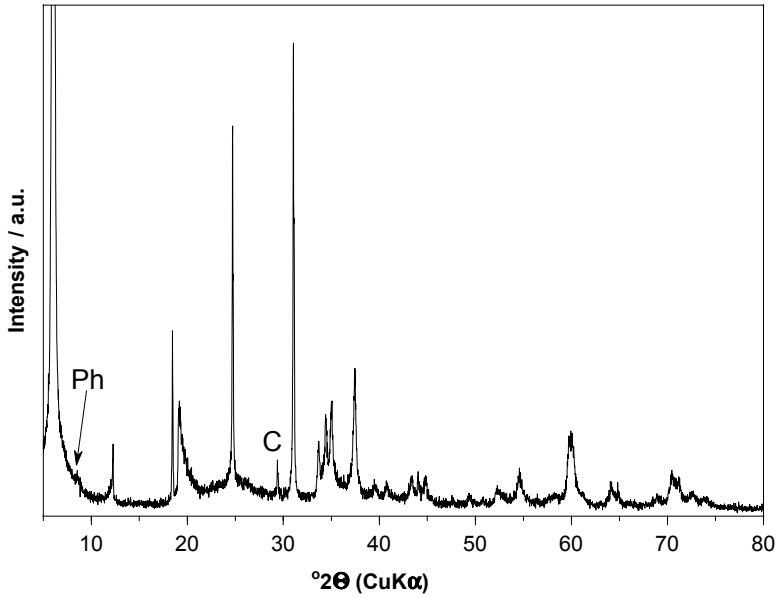

Figure 6.19 X-ray pattern (powder sample) of the raw and acid treated vermiculite (5 M H_2SO_4, 80 °C);
Ph: Phlogopite; Ca: Calcite; all not indexed peaks originated from vermiculite.

Short range order

The influence of acid on the structure of vermiculite is also shown in the FTIR spectrum (Figure 6.20). All trioctahedral clay minerals like vermiculite show broad and rounded absorption bands (Wilson, 1994). They had a distinctive OH-band, which is broad, strong and at lower frequency (995 cm^{-1}) compared to dioctahedral clay minerals like montmorillonite. In the region from 550 – 900 cm^{-1}, very small (823 cm^{-1}) and very broad bands (736 and 665 cm^{-1}) are observed, which can be assigned to OH bending vibrations, whose band positions are influenced by the kind of octahedral cation (Farmer, 1974; Wilson, 1994; Ravichandran and Sivasankar, 1997). Thus, these vibrations give information on the amount of the various octahedral cations. The other strong band at 466 cm^{-1} can be attributed to a Si-O bending vibration.

The OH vibrations, which are associated with octahedral cations, disappeared completely (Figure 6.20) during acid treatment of vermiculite. This implies that the octahedral cations were completely dissolved from the octahedral sheet. The strong OH stretching vibration at 995 cm^{-1} disappeared completely and four new absorption bands at 1176, 1089, 944 and 806 cm^{-1} appeared after acid treatment. The intensity of the Si-O band at 466 cm^{-1} increased with acid treatment. The increase of these vibrations is characteristic for the presence of amorphous silica (Komadel et al., 1990; Madejová et al., 1998; Makó et al., 2006). The vibration at 944 cm^{-1} can be assigned to SiO-stretching of SiOH groups (Farmer, 1974; Komadel et al., 1996).

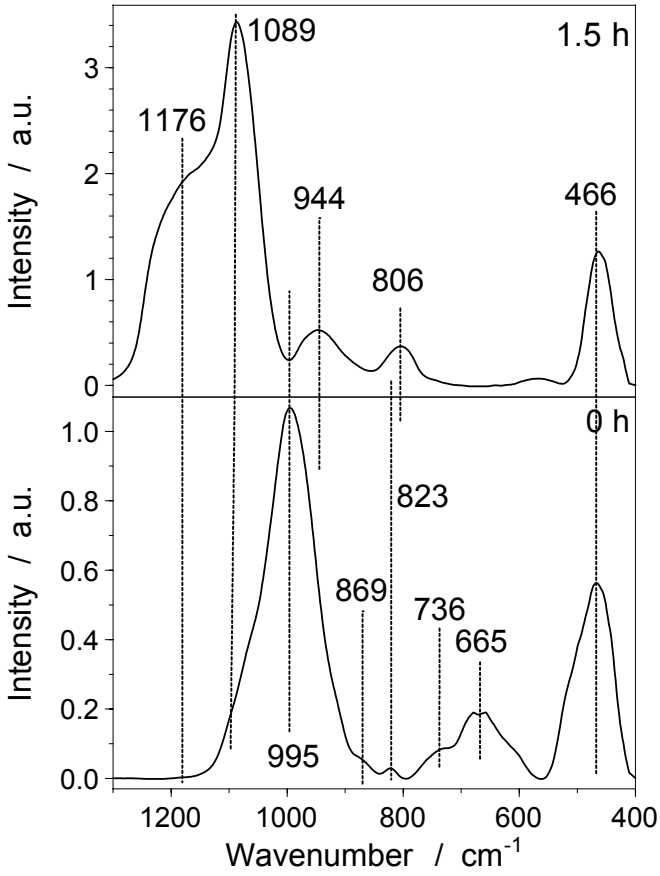

Figure 6.20 FTIR spectra of the raw and acid treated vermiculite (1.5 h). Vermiculite (8_Verm) was treated with 5 M H_2SO_4 at 80 °C.

Layer charge and exchange reactions

The CEC of the vermiculite was measured with ammonium acetate because the molecules of Cu-triethylenetetramine cannot be exchanged due to their size (4.0 to 4.5 nm^2) and the influence of the interlayer cations (see Chapter 4.3.2). The raw vermiculite had a CEC of 160 meq/100g and it was remarkably reduced by acid treatment to about 16% of the starting value (25 meq/100g).

6.4.3 Illite

Illite is a dioctahedral 2:1 layer silicate with a small particle size (< 2 µm). Illite is characterised by a layer charge between 0.6 and 0.9 eq/FU, which is higher than that of smectites but lower than that of muscovite. Illite has lower potassium contents in the interlayer than muscovite, because the potassium is partly substituted by H_3O^+ ions. Its layer charge is in the same range as vermiculite. The difference between illite and vermiculite are the different interlayer cations and the content of octahedral cations. Illite has only potassium cations in its interlayer sheets and is not swellable, while vermiculite is swellable. The negative charge of both is caused by substitutions in the octahedral and tetrahedral sheets.

Composition, colour, morphology and surface

The chemical composition of the natural and two acid treated illite samples is given in Table 6.18. After 20 h, the magnesium and iron content decreased down to 0.5%. The data reveal that magnesium and iron were removed faster than aluminium.

Table 6.18 Chemical composition of the raw and residual illite (5 M H_2SO_4, 80 °C).

Oxides		Illite (9_Illite)		
		Untreated	20 h	96 h
SiO_2	[%]	53.09	92.30	95.88
Al_2O_3	[%]	24.58	4.86	2.10
MgO	[%]	3.65	0.00	0.00
Fe_2O_3	[%]	8.85	0.21	0.16
TiO_2	[%]	0.89	0.52	0.27
MnO	[%]	0.01	0.01	0.00
Na_2O	[%]	0.00	0.00	0.00
CaO	[%]	0.05	0.00	0.00
K_2O	[%]	6.82	2.08	1.35
P_2O_5	[%]	0.41	0.01	0.01

Magnesium and iron were dissolved from the octahedral sheet of illite and phlogopite (Table 6.24). 76% of the total iron is associated with illite. 24% of iron belongs to phlogopite. 70% of the total magnesium comes from illite and 30% from phlogopite. These values were calculated from the oxide composition of each mineral and the total oxide composition relating to the quantification. The adjustment of both values was not necessary, because no other magnesium and iron containing phases occurred in the bulk material (Table 6.24) and after 20 h both elements had completely disappeared.

The Al_2O_3 content was adjusted because several other Al-containing minerals are present in the bulk material (kaolinite and feldspars, Table 6.24). After 20 h, the aluminium content is about 5%. After 96 h, the aluminium content still is higher than 2%. For this reason, the Al_2O_3 content was subtracted from the total amount of Al_2O_3 (Table 6.18). The adjusted Al_2O_3 value (Table 6.19) was used to estimate the content of residual illite.

Table 6.19 Adjusted Al_2O_3 contents of the natural and residual illite.

Elements		Illite (9_Illite)		
		Untreated	20 h	96 h
Al_2O_3	[%]	19.76	2.81	1.04

The total weight of the solid illite was significantly reduced after 20 h. Only 40% of the illite sample remained. The illite was dark brown, which was caused by iron in the octahedral sheet. After 20 h, the residual solid was completely white (Figure 6.21).

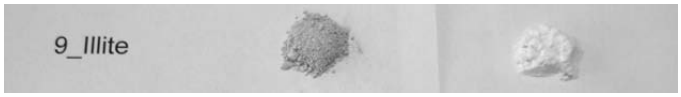

Figure 6.21 Colour of the material before and after acid treatment (5 M H_2SO_4 at 80 °C).

The raw illite consisted of small agglomerates with slat-shaped crystals (Figure 6.22a). After acid treatment, the particles are agglomerated (Figure 6.22b) and the slat-like appearance is still observable.

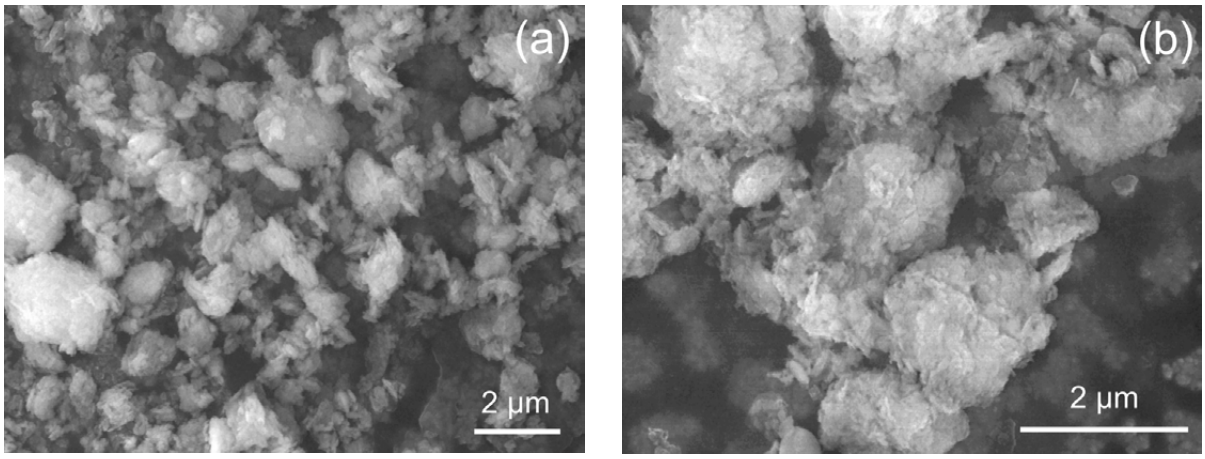

Figure 6.22 ESEM image of the a) raw and b) acid treated illite (9_Illite).
The material was treated with 5 M H_2SO_4 at 80 °C for 96 h.

The untreated illite had a larger specific surface area (95 m^2/g) than vermiculite (36 m^2/g) and smectite (nearly 30 m^2/g) due to its small particle size (Table 6.20).

Table 6.20 Grain size distribution of the natural illite.

Sample		d_{10}	d_{50}	d_{90}
9_Illite	[nm]	51	144	420

The A_S was affected by the acid treatment (Table 6.21). After 20 h, an A_S of 193 m^2/g was measured. After 96 h, the treated illite had an A_S of 161 m^2/g, which was higher than the A_S of the raw material. The high specific surface area and the content of micropores implied the delamination of the particles until 20 h (Table 6.21).

Table 6.21 Specific surface area (A_S), external specific surface area (A_E) and micro-pore area (A_{MP}) of the starting (9_Illite) and acid treated illite (5 M H_2SO_4, 80 °C).

	Illite (9_Illite)			
Time [h]	A_S [m^2/g]	A_E [m^2/g]	A_{MP} [m^2/g]	A_{MP} / A_S [%]
0	94	81	13	14
20	193	169	24	12
96	161	132	29	18

In this case the delamination of the particles caused a decreasing number of layers per stack. The maximum of the theoretical A_S, which was related to the calculated illite content, was calculated according to Müller-Vonmoos and Kahr (1983) (Table 6.22). The value indicates the complete delamination of the particles into single layers, but the calculation of the layers per stack does not indicate the thickness of the coherently scattering domains for XRD. The maximum of the measured A_S for the illite is reached until 20 h and is approximately 35% of the theoretical A_S (541 m^2/g) (Table 6.23). The number of layers per stack is reduced from 6 to 4 by acid treatment.

Table 6.22 Calculation of the theoretical surface area in relation to the illite content.

Sample	a [nm]	b [nm]	A* [nm^2]	M** [g/mol]	A_s(max)*** [m^2/g]	m_{illite}# [%]	A_S## [m^2/g]
9_Illite	0.5208	0.8995	0.4685	395.05	790	76	541

* Area of the base plane of the unit cell.

** Molecular weight per unit cell.

*** Calculated specific surface area, if the illite content is 100%.

\# Smectite content obtained from Rietveld quantification.

\## Calculated specific surface area referring to the illite content.

Table 6.23 Comparison between the theoretical and measured A_S and rate of delamination, as well as the number of layers per stack.

Sample	Maximum of A_s [m^2/g]		A_s of the crude material [m^2/g]	Number of layers per stack	Degree of Delamination [%]
	theoretical	measured			
9_Illite	541	194	94	6	35

With ongoing acid treatment, A_E and A_S decreased; the content of micropores, as well as the ratio between micropores and specific surface area increased. After 96 h, the delaminated particles started to reaccumulate.

Long range order

Rietveld quantification showed that the illite sample revealed 76% illite (Table 6.24). The main impurity is phlogopite (7.8%); further minerals are kaolinite (5.4%), feldspars (5.5%) and calcite (2.4%).

Table 6.24 Phase content of the illite sample.

Sample	9_Illite [%]
Illite	76.4 ± 2.0
Phlogopite	7.8 ± 1.2
Kaolinite	5.4 ± 0.7
K-feldspar (Orthoclase)	4.4 ± 0.6
Plagioclase (Anorthite)	1.1 ± 0.9
Calcite	2.4 ± 0.4
Anhydrite	1.4 ± 0.3
Apatite	0.7 ± 0.4
Quartz	0.4 ± 0.3

Due to the acid treatment, the intensity of the basal reflection (d_{001}) of the illite (1.01 nm) and its d_{060} peak at 0.1498 nm decreased with increasing time (Figure 6.23).

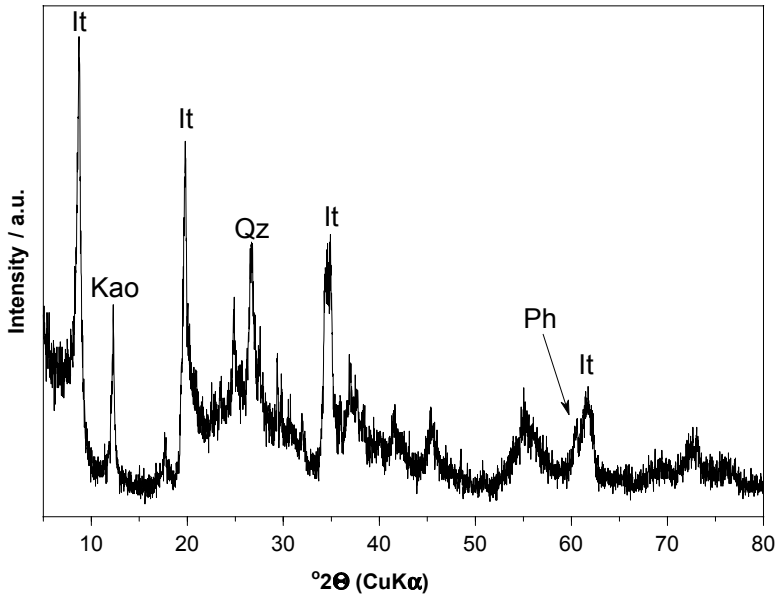

Figure 6.23 X-ray pattern (powder sample) of the raw and acid treated illite (5 M H_2SO_4, 80 °C); It: characteristic illite peaks with increasing 2θ (001), (002), (130), (060); Qz: Quartz; Kao: Kaolinite; Ph: Phlogopite (060).

But after 20 h, a small d_{001} reflection still remained, i.e. the illite was not completely dissolved. Similar to the smectite and vermiculite samples, the accessory minerals phlogopite and calcite were dissolved, because their diffraction peaks, e.g., the d_{060} peak of

the phlogopite at 0.1538 nm (~ 60° 2θ) disappeared. As for the smectites and vermiculite, the background increased with increasing acid treatment because of the increasing content of X-ray amorphous silica phases (Opal-A).

Short range order

The dissolution of aluminium and iron was observed with FTIR. Figure 6.24 illustrates the FTIR spectra of the raw illite (9_illite) and of the acid treated samples after 20 and 96 h. The spectra show distinctive changes, especially in the region between 400 and 1200 cm^{-1}.

The FTIR spectrum of the raw illite showed a number of sharp bands in the region between 400 and 1200 cm^{-1}. Their assignments are listed in Table 6.25 (Farmer, 1974; Komadel et al., 1996; Liu, 2001).

Table 6.25 Positions and assignments of the vibrational bands of the illite.

Wavenumber [cm^{-1}]	Assignment*
1101	Si-O stretching vibration (out-of-plane)
1031	Si-O stretching vibration (in-plane)
912	AlAlOH bending
877	AlFeOH bending
823	AlMgOH vibration
750	Al-O-Si vibration
700	OH bending
538	Si-O bending
472	Si-O-Si vibration
431	Si-O bending

* Farmer, 1974; Wilson, 1994; Liu, 2001.

Especially, the bands at 912, 877 and the weak absorption bands near 825 and 750 cm^{-1} were remarkably affected upon acid treatment. Acid treatment caused the loss and the formation of bands and changes in the intensity of vibrations. The intensity of the OH bands at 912 and 877 cm^{-1} decreased with increasing acid treatment (Figure 6.24) and after 96 h the bands nearly disappeared. This implies the dissolution of the octahedral sheet by acid treatment. All these bands are connected to cations (aluminium, magnesium, iron) in octahedral positions. The band at 912 cm^{-1} is assigned to OH deformation vibration, which gives information on the content of aluminium in the octahedral sheet. The absorption bands at 825 and 750 cm^{-1} originate from AlMgOH deformations or, by analogy with muscovite, from Al-O-Si vibrations (Famer, 1974; Wilson, 1994).

The weak band in the raw illite spectrum at 700 cm^{-1} can be assigned to an OH bending vibration. The vibration at 538 cm^{-1} is attributed to a Si-O-Al bending vibration of aluminium

within the tetrahedral sheet. All the other bands at 1031, 472 and 431 cm^{-1} are strong Si-O vibrations. The vibration at 1031 cm^{-1} had a weak shoulder at 1101 cm^{-1}, which also is a Si-O stretching vibration. The intensity of the tetrahedral Si-O-Al vibrations at 538 cm^{-1} decreased with increasing acid treatment. After 96 h, a small and broad band at 538 cm^{-1} still existed. This weak band implies that small amounts of aluminium still remain, whereas most of the octahedral aluminium is dissolved. All the changes indicate the modification of the tetrahedral and octahedral sheet. The intensity of the Si-O bands increased with increasing acid treatment. New absorption bands appeared at 802, 1101 and 1220 cm^{-1}, which are characteristic for amorphous silica (Komadel et al., 1990; Madejová et al., 1998; Makó et al., 2006).

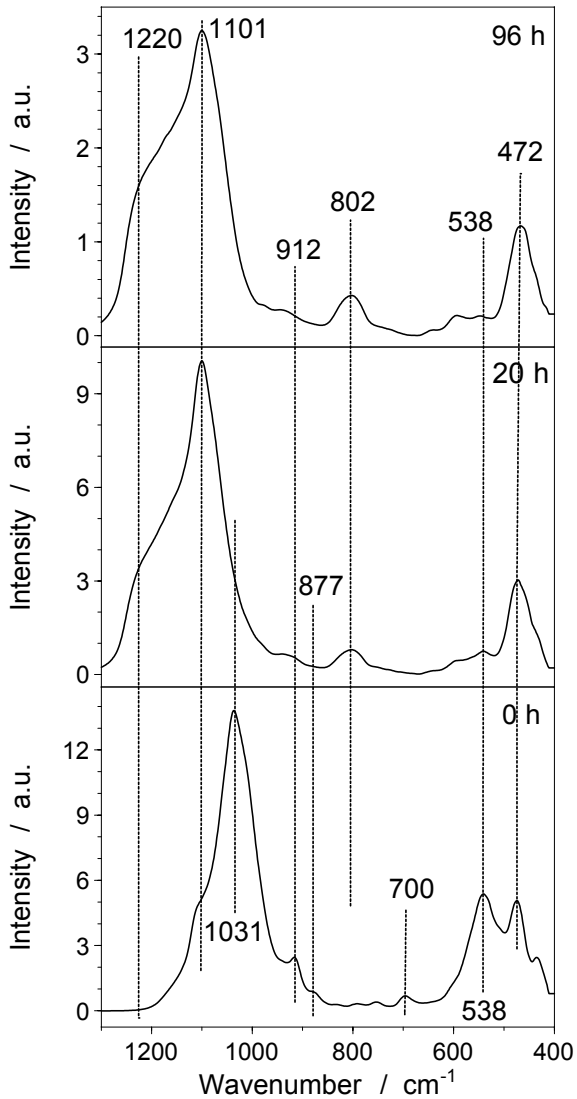

Figure 6.24 FTIR spectra of the raw and acid treated illite (20 h, 96 h). Illite (9_Illite) was treated with 5 M H_2SO_4 at 80 °C.

6.4.4 Sepiolite

Sepiolite is a hydrous Mg-bearing silicate with a fibrous morphology and distinctive layered appearance. Sepiolite belongs to the layer silicates, but has also structural affinities with inosilicates (Vivaldi and Hach-Ali, 1970). The sepiolite contains a high content of magnesium in the octahedral sheet. In comparison to the other clay mineral groups like smectites, vermiculite, and micas, sepiolite has only few substitutions in the octahedral and tetrahedral sheet. Therefore, layer charge and cation exchange capacity are relatively low (15 meq/100g).

Composition, colour, morphology and surface

The chemical composition of the natural and acid treated sepiolite sample is shown in Table 6.26. After 1.5 h treatment with 5 M H_2SO_4 at 80 °C, the content of magnesium and iron decreased below 0.5%. At the same time 14% of the total Al_2O_3 content was dissolved. The aluminium mainly comes from the octahedral and tetrahedral sheet of the muscovite, while magnesium is dissolved only from the octahedral sheet of the sepiolite. The low iron content is associated with the muscovite and sepiolite in the sample (10_PangelS9) (Figure 6.27), because both minerals can contain up to 8% iron in the structure.

Adjustment of both values was not necessary, because no other phases in the bulk material contained magnesium and iron. The Al_2O_3 content was not adjusted, because nearly all the aluminium is associated with muscovite.

Table 6.26 Chemical composition (XRF) of the raw and residual sepiolite after 1.5 h (5 M H_2SO_4, 80 °C).

Oxides		Sepiolite (10_PangelS9)	
		Untreated	1.5 h
SiO_2	[%]	66.07	95.97
Al_2O_3	[%]	3.09	2.66
MgO	[%]	28.28	0.00
Fe_2O_3	[%]	1.00	0.19
TiO_2	[%]	0.15	0.11
MnO	[%]	0.04	0.01
Na_2O	[%]	0.12	0.00
CaO	[%]	0.42	0.01
K_2O	[%]	0.77	0.97
P_2O_5	[%]	0.06	0.00

The weight of the sepiolite sample was significantly reduced after 1.5 h acid treatment. Approximately, 50% of the material was dissolved. The sepiolite sample had a creamy colour. After 1.5 h of acid treatment, the residual material was completely white (Figure 6.25).

Figure 6.25 Colour of the material before (left) and after (right) acid treatment (5 M H_2SO_4, 80 °C).

The raw sepiolite consisted of thin agglomerates with a fibrous morphology (Figure 6.26a). After acid treatment the fibrous morphology was still present (Figure 6.26b).

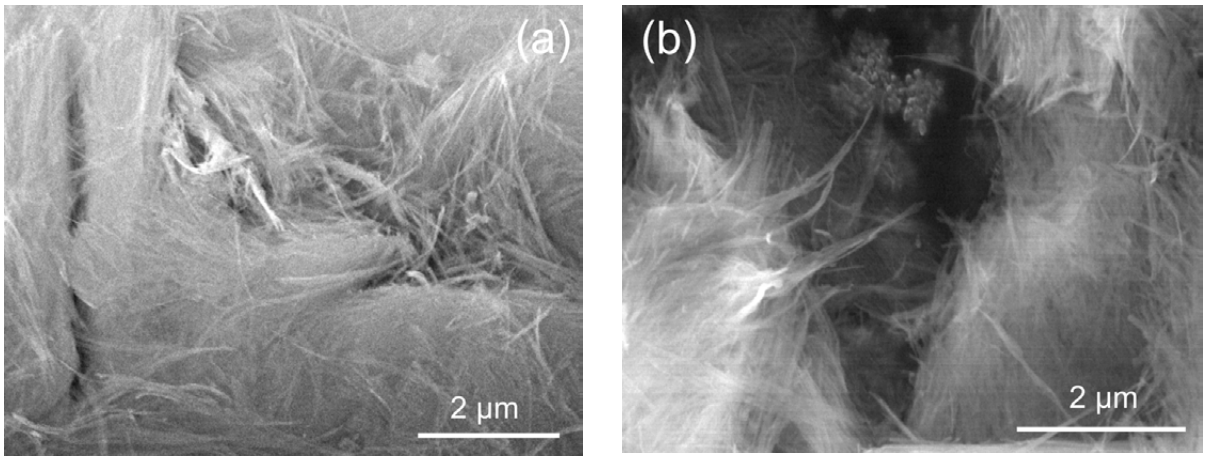

Figure 6.26 ESEM image of the a) raw and b) acid treated sepiolite (10_PangelS9). The material was treated with 5 M H_2SO_4 at 80 °C for 20 h.

In contrast to the other clay minerals (smectite, vermiculite, illite), sepiolite had a very high specific surface area (300 m^2/g) and a high content of micropores (167 m^2/g) due to its channel-like structure. The acid treatment caused a decrease of the A_S (138 m^2/g), as well as a strong reduction of the micropores (18 m^2/g). This decrease is associated with a decrease of the surface roughness (described by the number of micropores). With further acid treatment, both values increased again, but did not attain starting values (Table 6.27). This increase was caused by the formation of new pores increasing the roughness of the surface.

Table 6.27 Specific surface area (A_S), external specific surface area (A_E) and micro-pore area (A_{MP}) of the starting (10_PangelS9) and acid treated sepiolite (5 M H_2SO_4, 80 °C).

Sepiolite (10_PangelS9)				
Time [h]	A_S [m^2/g]	A_E [m^2/g]	A_{MP} [m^2/g]	A_{MP} / A_S [%]
300	300	133	167	56
138	138	120	18	13
154	154	138	16	10
166	166	110	56	34
185	185	148	36	19

Long range order

The sepiolite sample consisted of 91% sepiolite and the following impurities: calcite (1%) and muscovite/illite (8%). The X-ray patterns (Figure 6.27) revealed the strong influence of the acid treatment on the structure of sepiolite. After 1.5 h the sepiolite is completely dissolved. In contrast, the basal spacing d_{001} of the muscovite is still present after 1.5 h treatment with 5 M H_2SO_4 at 80 °C. Furthermore a hydrous amorphous X-ray silica phase is formed. The formation of the silica phases was indicated by the increasing background.

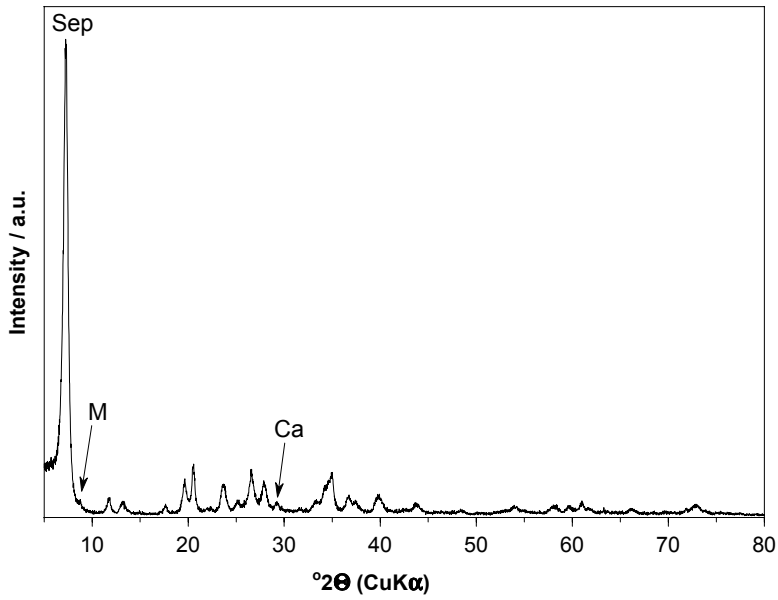

Figure 6.27 X-ray pattern (powder sample) of the raw and acid treated sepiolite (5 M H_2SO_4, 80 °C);
M: Muscovite; Qz: Quartz; Fsp: Feldspars;
all not indexed peaks originated from sepiolite.

Short range order

The dissolution of sepiolite can be observed in the FTIR spectra as well. The spectral changes occurred especially around 1200 and 400 cm^{-1} (Figure 6.28).

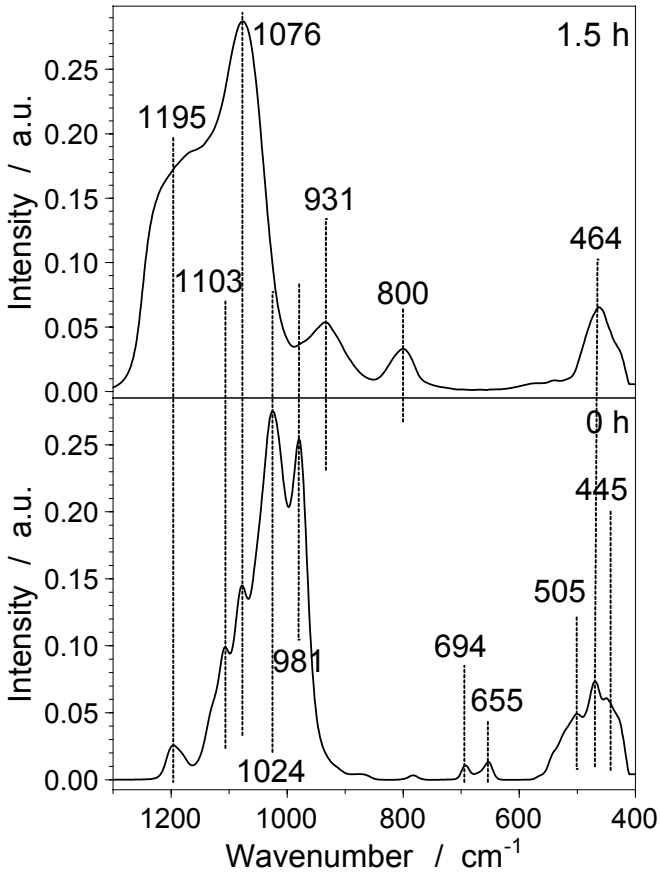

Figure 6.28 FTIR spectra of the raw and acid treated sepiolite (5 M H_2SO_4, 1.5 h, 80 °C).

The vibrations of the raw sepiolite sample (10_PangelS9) at 694 and 655 cm^{-1} can be assigned to OH translations reflecting the water molecules bonded to the Mg-O sites (Table 6.28). The band at 445 cm^{-1} is attributed to a Si-O-Mg bending vibration, which showed the linkage between the octahedral and tetrahedral sheet. This band is superimposed with the strong Si-O-Si vibrations at 505 and 464 cm^{-1}. The other bands at 1195, 1103, 1076, 1024 and 981 cm^{-1} are strong Si-O vibrations (Table 6.28) (Wilson, 1994; Vicente-Rodríquez et al., 1996; Frost et al., 2001).

Acid treatment caused changes in the intensity of all vibrations. The OH bands at 694 and 655 cm^{-1} disappeared after 1.5 h (Figure 6.23). This implies the release of magnesium from the octahedral sheet. Furthermore, the vibration at 445 cm^{-1} disappeared after 1.5 h, which can be associated with distortions and weakening of the Si-O-Mg bonds between the tetrahedral and octahedral sheets.

Table 6.28 Positions and assignment of the vibrational bands of the raw sepiolite.

Wavenumber [cm^{-1}]	Assignment*
1195	Si-O stretching vibration
1103	Si-O stretching vibration
1076	Si-O stretching vibration
1024	Si-O stretching vibration
981	Si-O stretching vibration
694	OH translation
655	OH translation
505	O-Si-O bending vibration
464	Si-O bending vibration
445	Si-O-Mg bending vibration

* Wilson, 1994; Vicente-Rodríquez et al., 1996; Frost et al., 2001.

The Si-O vibrations at 1103 and 1024 cm^{-1} disappeared in the asymmetric Si-O band at 1076 cm^{-1}, which has a broad shoulder at higher wavenumbers (1195 cm^{-1}). Also the Si-O band at 505 cm^{-1} disappeared into the broad band at 464 cm^{-1}. The results reveal that the Si-O stretching vibrations are very sensitive to acid attack. The dissolution of the octahedral sheet in acid treated sepiolite also caused changes in the Si-O vibration bands. The changes can be related to the conversion of the tetrahedral sheets into silanol groups (McKeown et al., 2002).

Besides the Si-O bands at 1195, 1076 and 464 cm^{-1}, two new vibrations at 931 and 800 cm^{-1} existed after acid treatment (1.5 h). These five bands are characteristic for amorphous silica (Komadel et al., 1990; Vicente-Rodríquez et al., 1996; Madejová et al., 1998; Myriam et al., 1998).

6.4.5 Kaolin and Kaolinite

Three kaolin samples were used for the investigations. The samples varied in their composition and particle sizes. Polwhite had 40% < 2 µm fraction, whereas the other two kaolin samples had about 80% < 2 µm fraction. The d_{10}, d_{50} and d_{90} values of the three kaolin samples are given in Table 6.29.

Table 6.29 Grain size distribution of the natural kaolin samples.

Sample		d_{10}	d_{50}	d_{90}
13_Pol	[nm]	244	1109	2022
14_Kaolex	[nm]	104	314	1317
15_Rogers	[nm]	97	390	1377

Composition, colour, morphology and surface

The chemical composition of the kaolin samples is listed in Table 6.30. Figure 6.29 reveals the Al_2O_3 content (XRF) of the residual solid of the used kaolinites in dependence on acid reaction time. The graph on the left side shows the part of unreacted Al_2O_3 in %, while the graph on the right side presents the part of unreacted Al_2O_3 in [$g \cdot mol^{-1}$] related to the molecular weight of the formula unit (half unit cell).

Table 6.30 Chemical composition (XRF) of the kaolin samples.

Oxides		13_Pol	14_Kaolex	15_Rogers
SiO_2	[%]	49.72	44.72	45.69
Al_2O_3	[%]	33.85	36.34	35.98
MgO	[%]	0.30	0.08	0.33
Fe_2O_3	[%]	0.96	1.58	0.97
TiO_2	[%]	0.04	1.58	1.39
MnO	[%]	0.02	0.00	0.00
Na_2O	[%]	0.00	0.00	0.00
CaO	[%]	0.03	0.00	0.16
K_2O	[%]	3.02	0.47	0.27
P_2O_5	[%]	0.16	0.10	0.07
LOI	[%]	11.9	14.2	15.1

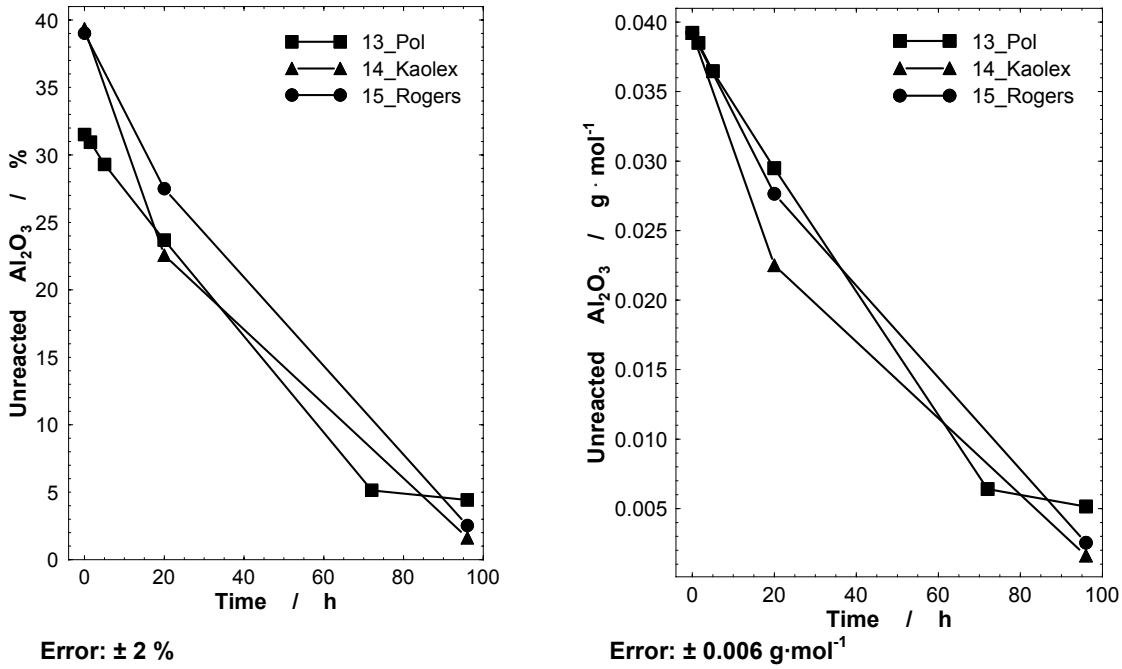

Figure 6.29 Chemical composition of the residual solid with unreacted oxides in % determined by XRF (left) and in [$g \cdot mol^{-1}$] related to the molecular weight of the formula unit (half unit cell) (right). The material was treated with 5 M H_2SO_4 for 0, 1.5, 5, 20, 72 and 96 h at 80 °C.

The Al_2O_3 content was adjusted, because other Al_2O_3 containing phases were in the bulk material (Table 6.35). For this reason, the Al_2O_3 content of the impurities was subtracted from the total amount of Al_2O_3 (Table 6.30). This Al_2O_3 content gives information on the stability of the kaolinites against acid attack.

After 96 h, the kaolinite (13_Pol) is more resistant to acid, as it has a higher Al_2O_3 content compared to the other two kaolinites. Kaolex and Rogers have a similar Al_2O_3 content after 96 h.

The value of the adjusted Al_2O_3 content can be used to estimate the residual kaolinite. This kaolinite content can be compared with the calculated content of the X-ray diffraction analysis. An internal standard (ZnO) was used to quantify the amorphous SiO_2. In contrast to the smectite samples, there was no correlation between the kaolinite model and the amorphous silica content observed during Rietveld analysis (Table 6.31).

Table 6.31 Kaolinite content estimated by XRD analysis and by the adjusted Al_2O_3 content.

Samples	Kaolinite content estimated by			
	20 h		96 h	
	XRD	Al_2O_3	XRD	Al_2O_3
13_Pol [%]	55	54	12	10
14_Kaolex [%]	51	49	8	4
15_Rogers [%]	60	61	6	6

The kaolin Polwhite (13_Pol) was creamy. The kaolin Kaolex (14_Kaolex) was yellowish and the kaolin Rogers (15_Rogers) was reddish. After acid treatment the residual kaolin were white (Figure 6.30).

Figure 6.30 Colour of the material before (left) and after (right) acid treatment (5 M H_2SO_4, 80 °C).

The weights of the solid kaolin were significantly reduced after 20 h acid treatment. Only 65 to 80% of the kaolin samples remained. After 96 h, the weight averaged between 45 and 55% of the net weight.

All crude kaolinites consist of platy particles with a pseudohexagonal habit (Figure 6.31a, 13_Pol). The agglomerates after acid treatment have the same pseudohexagonal habit

(Figure 6.31b). The ESEM images of the other kaolinites (14_Kaolex, 15_Rogers) are given in the appendix.

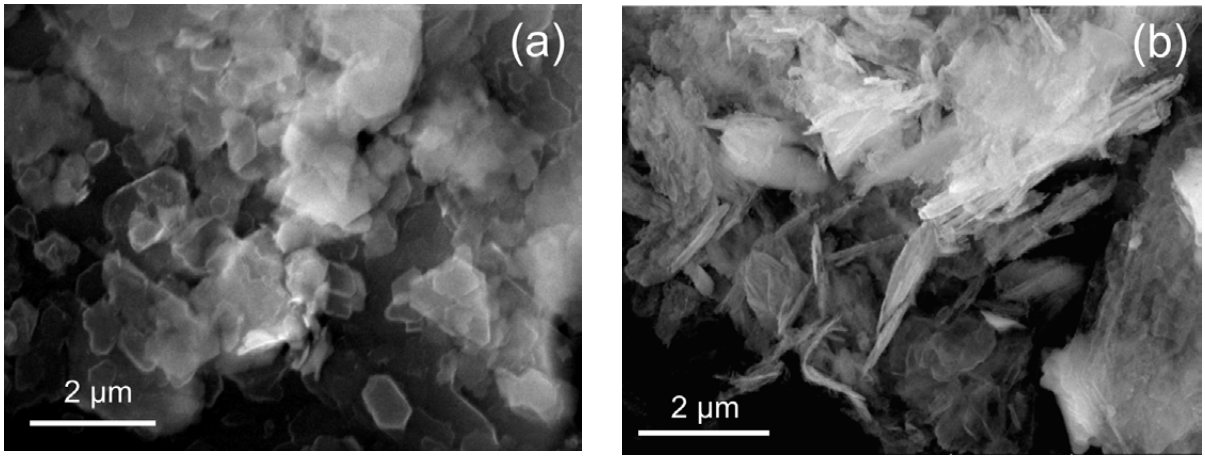

Figure 6.31 ESEM image of the a) raw and b) acid treated kaolin Polwhite (13_Pol). The material was treated with 5 M H_2SO_4 at 80 °C for 96 h.

The specific surface area (A_S) of the raw kaolin ranged from 10 to 25 m^2/g. Due to the acid treatment, the A_S increased and reached a constant value (Figure 6.32). After 96 h, the specific surface area ranged from 55 to 125 m^2/g. Both kaolin samples Kaolex (14_Kaolex) and Rogers (15_Rogers) had a higher A_S than the Polwhite (13_Pol), which can be explained by their different particle size. The A_S increased with decreasing particle size.

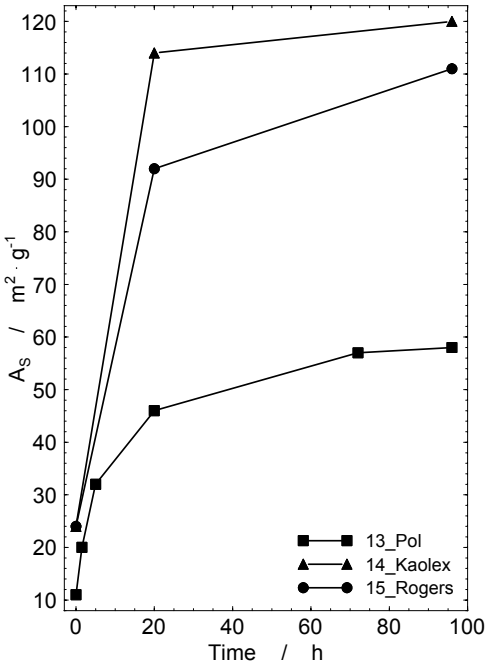

Figure 6.32 The influence of the acid treatment on the specific surface area of the used kaolinits. The material was treated with 5 M H_2SO_4 for 0, 1.5, 5, 20, 72 and 96 h at 80 °C.

The ratio between A_{MP} and A_S increased slowly with increasing acid treatment (Table 6.32, appendix). These observations imply that the particles were delaminated and the porosity did not increase.

Table 6.32 Specific surface area (A_S), external specific surface area (A_E) and micro-pore area (A_{MP}) of the starting and acid treated kaolinite Polwhite (13_Pol) (5 M H_2SO_4, 80 °C).

Kaolinite Polwhite (13_Pol)				
Time [h]	A_S [m^2/g]	A_E [m^2/g]	A_{MP} [m^2/g]	A_{MP} / A_S [%]
0	11	11	0	0
1.5	21	17	3	14
5	31	26	5	15
20	46	40	6	13
72	57	42	15	26
96	58	42	16	31

The delamination of the particles results in a reduction of the layers per stack. The theoretical A_S related to the calculated kaolinite content ranged between 804 and 965 m^2/g (Müller-Vonmoos and Kahr, 1983) (Table 6.33). Delamination of kaolinite particles occurred more slowly compared to smectites in bentonites. Between 15 and 27% of the particles are delaminated (Table 6.34). The layers per stack are reduced from 33 to 28 (13_Pol), from 18 to 13 (14_Kaolex) and from 19 to 14 (15_Rogers) by acid treatment (up to 20 h). The reason for the delamination of the kaolinite particles may be the protonation of the SiO-groups of the tetrahedral sheet at low pH (< 2). The protons cause a positive charge of the layers, which tend to reject each other

Table 6.33 Calculation of the theoretical surface area in relation to the kaolinite content.

Sample	a [nm]	b [nm]	A* [nm^2]	M** [g/mol]	A_S(max)*** [m^2/g]	$M_{kaolinite}$# [%]	A_S## [m^2/g]
13_Pol	0.5160	0.8940	0.4613	258.20	516	71	368
14_Kaolex	0.5160	0.8940	0.4613	258.20	516	85	440
15_Rogers	0.5160	0.8940	0.4613	258.20	516	86	444

* Area of the base plane of the unit cell.
** Molecular weight per unit cell.
*** Calculated specific surface area, if the kaolinite content is 100%.
# Kaolinite content obtained from Rietveld quantification (of Table 6.35).
Calculated specific surface area referring to the kaolinite content.

Table 6.34 Comparison between the theoretical and measured A_S and rate of delamination, as well as the number of layers per stack.

Sample	Maximum of A_S [m^2/g]		A_S of the crude material [m^2/g]	Number of layers per stack	Degree of Delamination [%]
	theoretical	measured			
13_Pol	368	58	11	33	15
14_Kaolex	440	120	24	18	27
15_Rogers	444	111	24	19	27

Long range order

The mineralogy of the kaoline is shown in Table 6.35. The kaolinite content of the raw materials ranged from 71 to 87%. Beside kaolinite, there were further phases, which contained Al_2O_3 in the structure (Table 6.35).

Table 6.35 Quantification of the natural kaolin samples from Rietveld analysis of XRD patterns.

Sample	13_Pol [%]	14_Kaolex [%]	15_Rogers [%]
Kaolinite	71.4 ± 1.4	85.3 ± 1.3	86.1 ± 2.6
Muscovite \ Illite	9.2 ± 0.7	-	-
Fe-rich Muscovite \ Illite	-	6.6 ± 1.1	3.3 ± 1.0
Smectite	6.9 ± 1.1	5.1 ± 1.0	9.1 ± 2.9
Orthoclase	10.8 ± 0.6	-	-
Quartz	1.7 ± 0.4	1.5 ± 0.3	-

* Al_2O_3 containing phases.

All kaoline had similar impurities including quartz, mica, smectite and anatase. The existence of smectite was verified by the measured CEC (Table 6.36) using a CEC of 82 meq/100g for the calculation.

Table 6.36 CEC of kaolin samples.

Sample	13_Pol	14_Kaolex	15_Rogers
CEC [meq/100g]	6	4	10
Smectite [%]	7	5	12

In the X-ray pattern the intensity of the basal reflections decreased with increasing acid treatment (Figure 6.33). After 96 h, all three kaolin samples still had a small d_{001} peak, which indicated that the kaolinite was not completely dissolved. In the X-ray pattern, the peaks of the impurities (quartz, feldspar, mica) were also still partly detected following acid treatment. The dissolution of some impurities was much slower than that of the kaolinite itself. Additionally, the background increased with increasing acid treatment, which means that the content of X-ray amorphous silica phases increased.

Acid treatment caused a decrease of the octahedral cation amount like aluminium and the removal of aluminium from the tetrahedral sheet and the decrement of the crystallite size of the particles, which changed the electron density in the crystal structure and this affected the peak intensities. The long range order was permanently changed by acid treatment.

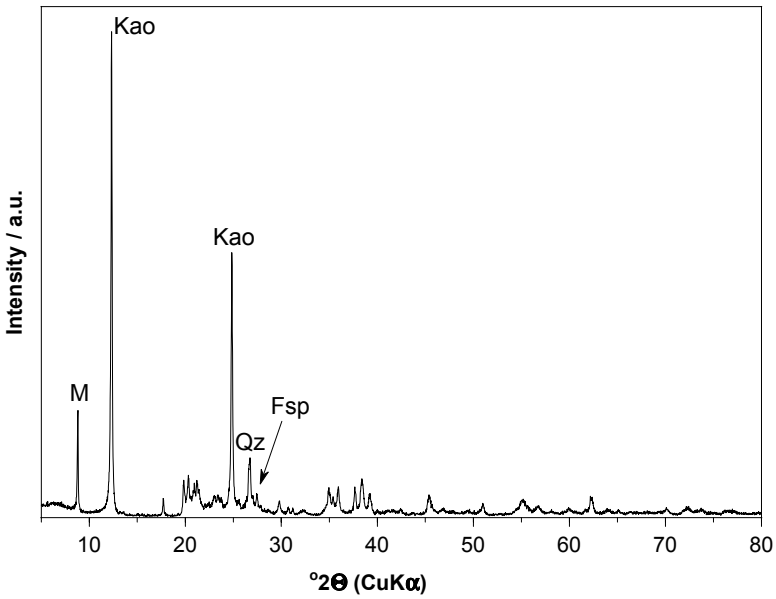

Figure 6.33 X-ray pattern (powder sample) of the raw and acid treated kaolin Polwhite (13_Pol) (5 M H_2SO_4, 80 °C);
Kao: characteristic kaolinite peaks with increasing 2θ (001), (002);
Qz: Quartz; M: Muscovite.

Short range order

The successive dissolution of aluminium can be observed in the FTIR spectra of the kaolin samples. Figure 6.34 illustrates the FTIR spectra of the raw kaolin (Polwhite, 13_Pol) and the acid treated samples after 5, 20 and 96 h. The spectra of the other two kaolin samples (14_Kaolex, 15_Rogers) are given in the appendix. The spectrum of the raw kaolinite presented sharp vibration bands in the region between 400 and 1200 cm^{-1}. Their assignments are listed in Table 6.37 (Farmer, 1974; Makó et al., 2006).

Especially, the bands at 939, 917, 792, 754 and 539 cm^{-1} are remarkably affected by acid treatment. All these bands are connected to aluminium in the octahedral and tetrahedral position. The vibrations at 939 and 917 cm^{-1} can be assigned to OH deformations, which also give information on the content of aluminium in the octahedral sheet.

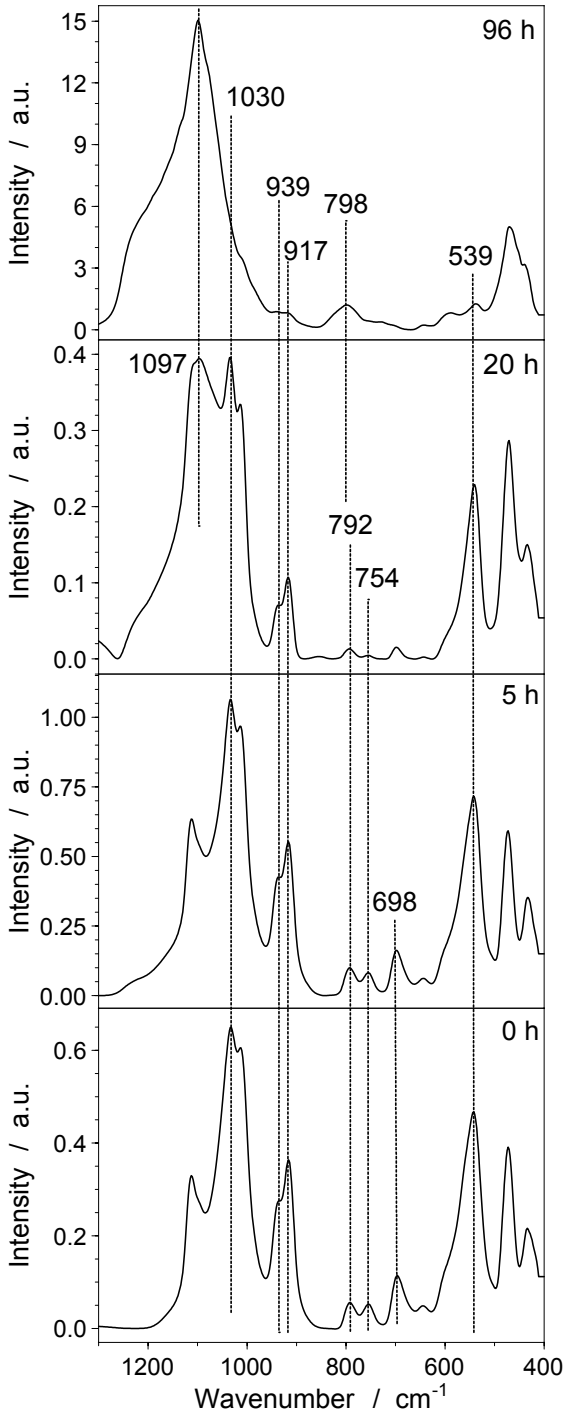

Figure 6.34 FTIR spectra of the raw and acid treated kaolin (5, 20 and 96 h). Kaolin sample Polwhite (13_Pol) was treated with 5 M H_2SO_4 at 80 °C.

Table 6.37 Positions and assignments of the vibrational bands in the lattice region of the raw kaolinite.

Wavenumber [cm^{-1}]	Assignment*
1110	(apical) Si-O out-of-plane
1030	Si-O in-plane
939	inner surface OH deformation
917	inner OH deformation
792	Si-O-Al vibrations
754	Si-O-Al vibrations
698	OH translation
644	inner surface OH vibration
539	Si-O-Al (out-of-plane) bending (Al in the tetrahedral sheet)
472	Si-O (in-plane) bending associate with OH
431	Si-O bending

* Farmer, 1974; Makó et al., 2006.

The lower bands at 792 and 754 cm^{-1} are assigned to Si-O-Al vibrations. The bands mirrored the linkage of octahedral aluminium with tetrahedral silicon via an oxygen atom. The vibration at 539 cm^{-1} is attributed to a Si-O-Al bending vibration within the tetrahedral sheet. All the other bands at 1110, 1030, 472 and 431 cm^{-1} are strong Si-O vibrations.

Acid treatment caused changes in the intensity of the Si-O-Al bands and the OH vibrations. The intensity of the OH bands at 939 and 917 cm^{-1}, as well as the area of the vibrations, decreased with increasing acid treatment (Figure 6.35) and after 96 h, the bands nearly disappeared. This implied that the release of aluminium from the octahedral sheet occurred continuously.

Figure 6.35 shows the content of unreacted aluminium compared to the area of the OH deformation bands at 939 and 917 cm^{-1}. The diagrams of the other used kaolin samples (14_Kaolex, 15_Rogers) are given in the appendix. These data support the continuous release of aluminium from the octahedral sheet. After 96 h small amounts of aluminium are still present in the structure of the (13_Pol). The kaolinite was not completely dissolved as indicated by XRD.

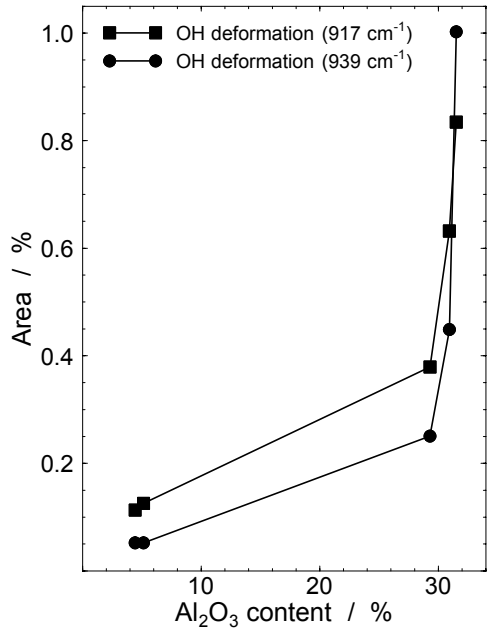

Figure 6.35 Comparison between the unreacted aluminium content and the area of the OH vibrations at 939 and 917 cm^{-1}. Kaolin Polwhite (13_Pol) treated with 5 M H_2SO_4 at 80 °C at 0, 5, 20, 72 and 96 h.

The intensities of the bridging Si-O-Al vibrations at 792 and 754 cm^{-1}, as well as the intensity of the tetrahedral Si-O-Al vibration at 539 cm^{-1} decreased with increasing acid treatment. The vibration at 792 cm^{-1} disappeared into the new absorption band at 798 cm^{-1}, while the band at 754 cm^{-1} disappeared completely. Only a small band at 539 cm^{-1} still existed after 96 h. All these changes indicate the modification of both, the tetrahedral and the octahedral sheet. The weak band at 539 cm^{-1} implies that small amounts of aluminium still remain in the tetrahedral sheet, whereas most of the octahedral aluminium is dissolved.

The intensity of the Si-O bands increased with increasing acid treatment. New absorption bands appeared at 798 and 1097 cm^{-1}, which are characteristic for amorphous silica (Komadel et al., 1990; Madejová et al., 1998; Makó et al., 2006).

6.4.6 Magadiite

The Magadiite (16_Mag) in this work is a synthesised silicic acid with a layered appearance. This sample was used to elucidate the behaviour of silicic acid against acid treatment.

Composition, colour, morphology and surface

The chemical composition of the natural and acid treated magadiite is given in Table 6.38. Magadiite had high contents of sodium and low amounts of aluminium and iron. Its formula is $NaSi_7O_{13}(OH)_3 \cdot 3H_2O$ (Eugster, 1967) or $NaSi_7O_{13}(OH)_3 \cdot 4H_2O$ (Brindley, 1969). After 72 h treatment with 5 M H_2SO_4 at 80 °C, sodium was completely dissolved. The impurities like iron and aluminium are partly dissolved, but more iron than aluminium was dissolved.

Table 6.38 Chemical composition (XRF) of the crude and residual magadiite (5 M H_2SO_4, 72 h, 80 °C)

Oxides		Magadiite (16_Mag)	
		Untreated	72h
SiO_2	[%]	92.10	99.46
Al_2O_3	[%]	0.42	0.40
MgO	[%]	0.00	0.00
Fe_2O_3	[%]	0.24	0.12
TiO_2	[%]	0.03	0.02
MnO	[%]	0.00	0.00
Na_2O	[%]	7.19	0.00
CaO	[%]	0.00	0.00
K_2O	[%]	0.02	0.00
P_2O_5	[%]	0.00	0.00

In contrast to the other materials, the total weight of the magadiite sample was not significantly reduced (20%) after 72 h treatment. This 80% remaining material is equivalent to the SiO_2 content (78%, in consideration of the loss of ignition) of the untreated magadiite. This implies that silicate hydroxide is stable against acid. The colour of magadiite was white before and after acid treatment.

The magadiite consists of thick agglomerates with an irregular shape and partly sharp grain boundaries (Figure 6.36a). The morphology of the magadiite is similar to that of smectite in bentonites. The particle agglomerates after acid treatment still had an irregular shape, but the grain boundaries are blurred compared to those of the raw particles (Figure 6.36b).

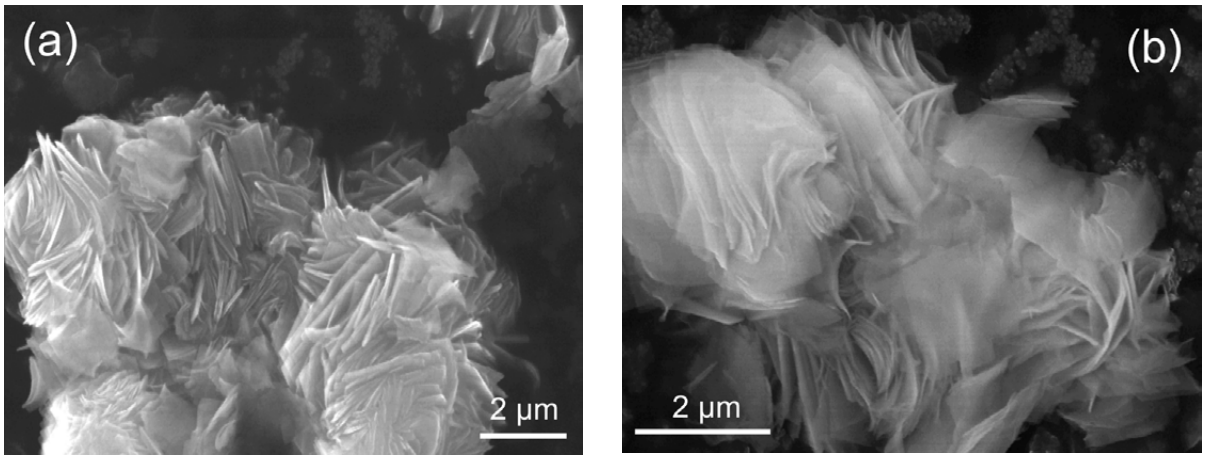

Figure 6.36 ESEM image of the a) raw and b) acid treated magadiite (16_Mag). The material was treated with 5 M H_2SO_4 at 80 °C for 72 h.

The raw magadiite had an A_S of 30 m^2/g, which is similar to that of smectites, but magadiite had a higher rate of A_{MP} (Table 6.39). The A_S and the amount of A_{MP} increased after acid treatment.

Table 6.39 Specific surface area (A_S), external specific surface area (A_E) and micro-pore area (A_{MP}) of the starting (16_Mag) and acid treated magadiite (5 M H_2SO_4, 80 °C).

Magadiite (16_Mag)				
Time [h]	A_S [m^2/g]	A_E [m^2/g]	A_{MP} [m^2/g]	A_{MP} / A_S [%]
0	30	16	14	47
72h	64	29	35	55

Figure 6.37 demonstrates the XRD pattern of the natural and acid treated magadiite under air dry conditions. The XRD powder data of a sodium silicate hydroxide hydrate were published by Brindley (1969); they correspond to the data of this work. The d_{001} peak is the strongest line in the XRD pattern with a basal spacing of 0.156 nm. After acid treatment this basal spacing collapsed to 0.132 nm. These XRD data are identical with that of Lagaly et al. (1973). The acid treated magadiite has the following structural formula $H_2Si_{14}O_{29}{\cdot}5.4H_2O$, which was published by Lagaly et al. (1973). The acid treatment caused the formation of a hydrogen silicate hydrate, which can be also described as H-Magadiite. The XRD measurements proved that magadiite is crystalline before and after acid treatment, but the basal reflections shifted, indicating that the linking of SiO_4 tetrahedral has changed.

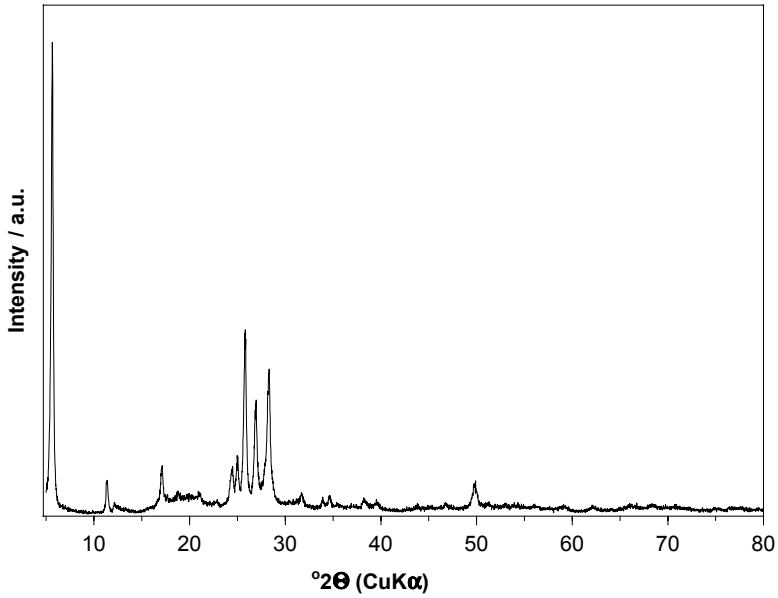

Figure 6.37 X-ray pattern (powder sample) of the raw and acid treated (5 M H_2SO_4 at 80 °C) magadiite (16_Mag). All peaks originated from magadiite.

Short range order

The FTIR spectra in the region from 400 – 1300 $cm^{-1}$of the untreated and treated magadiite are shown in Figure 6.38. According to previous studies (Eypert-Blaison et al., 2001; Superti et al., 2007), the infrared spectra of magadiite can be divided into three parts. In the first region (1000 – 1300 cm^{-1}), four absorption bands at 1236, 1201, 1172 and 1081 cm^{-1} are observed, which are assigned to antisymmetric stretching vibrations of Si-O-Si bridges. In the second region 700 – 1000 cm^{-1}, four vibrations at 941, 817, 788 and 705 cm^{-1} occur. These bands can be attributed to symmetric stretching vibrations of the Si-O-Si bridges. In the third region (400 – 700 cm^{-1}), Si-O-Si and O-Si-O bending vibrations at 617, 578 and 541 cm^{-1} can be observed.

In contrast to the other clay minerals, the acid treatment of magadiite caused only a few changes in the FTIR spectra. The positions of most of the absorption bands did not shift. The intensity of the bands in the second and third region decreased after acid treatment. Furthermore, the acid treatment caused the break of Si-O bonds. This implies that the number of symmetric stretching vibrations of the Si-O-Si bridges and Si-O-Si and O-Si-O bending vibrations decreased. The broad absorption band at 1081 cm^{-1} was sharper after acid treatment, but no shift was observed. This means that more antisymmetric stretching vibrations of Si-O-Si bridges existed. One new vibration appeared in the FTIR spectra after acid treatment. The band is located at 979 cm^{-1}. The shoulder at 1193 cm^{-1} increased with acid treatment.

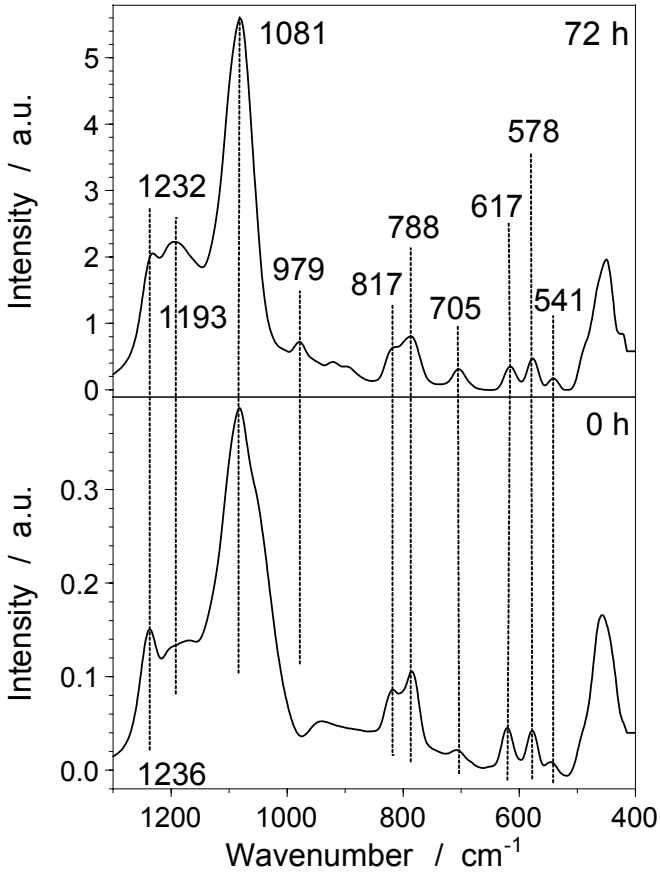

Figure 6.38 FTIR spectra of the raw and acid treated magadiite.
Magadiite (16_Mag) was treated with 5 M H_2SO_4 at 80 °C for 72 h.

6.5 Effects of H_2SO_4 compared to HCl

The results of the XRF analysis were used to compare the effects on the clays that different kinds of acid have at varying concentrations and several reaction times.

The sepiolite and the vermiculite treated with 5 M sulphuric acid or HCl for 20 h at 80 °C showed the same results. Different effects of H_2SO_4 and HCl were observed for the smectites in the bentonite (Volclay) and for the kaolin sample (Polwhite).

The dissolution of the octahedral cations like aluminium, magnesium and iron was more effective with 5 M H_2SO_4 than with HCl. In Figure 6.39, the differences are displayed for the Volclay sample.

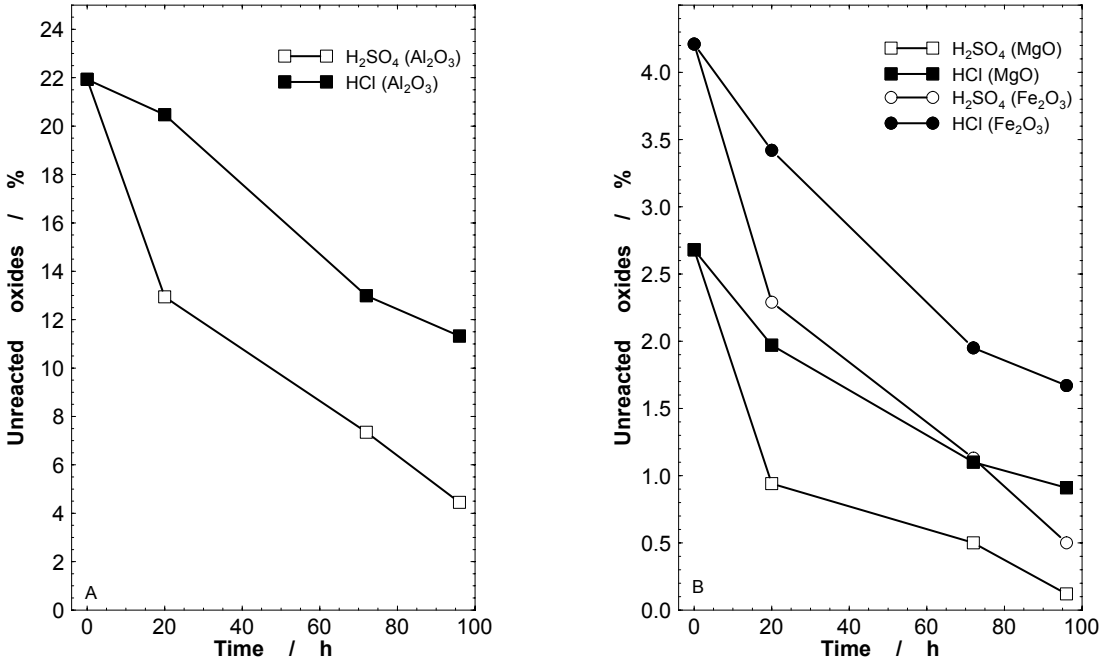

Figure 6.39 Total content of unreacted oxides of the residual solid in % determined with XRF for Al_2O_3 of the Volclay (left) and for MgO and Fe_2O_3 of the Volclay (right) after treatment with 5 M H_2SO_4 and 5 M HCl for 0, 1.5, 5, 20, 72 and 96 h at 80 °C.

The kaolin Polwhite shows the same differences in reaction with H_2SO_4 and HCl. After 72 h, the Al_2O_3 content of the residual kaolinite averages 25.98% for treatment with 5 M HCl and 10.15% for treatment with 5 M H_2SO_4.

In Table 6.40, the values of the unreacted aluminium, magnesium and iron after the treatment with 1, 5, and 10 M H_2SO_4 and HCl for 96 h at 80 °C are given. Most of the octahedral cations were dissolved by the treatment with 5 M H_2SO_4. Similar results were achieved with 10 M HCl and 1 M H_2SO_4. 1 and 5 M HCl can also be used to dissolve cations from the octahedral sheet, but the concentration was to low for a complete dissolution.

Table 6.40 Content of unreacted Al_2O_3, MgO and Fe_2O_3 of the residual Volclay after treatment with 1, 5 and 10 M H_2SO_4 and HCl for 96 h at 80 °C.

Concentration	Unreacted Al_2O_3 [%]		Unreacted MgO [%]		Unreacted Fe_2O_3 [%]	
M	H_2SO_4	HCl	H_2SO_4	HCl	H_2SO_4	HCl
1	6.57	20.32	0.29	1.99	1.03	3.29
5	**4.45**	11.32	**0.12**	0.91	**0.50**	1.67
10	22.08	**6.75**	2.20	**0.46**	3.85	**0.90**

Bold value: H^+ concentration of the H_2SO_4 and HCl solution is equal during the reaction.

The investigations show that 1 M and 5 M H_2SO_4 and 10 M HCl gave the best results, but 5 M H_2SO_4 was more effective than either 10 M HCl or 1 M H_2SO_4. 10 M H_2SO_4 and 1 M HCl were too weak to dissolve the cations from the octahedral sheet. The reason for the lower reactivity of 10 M H_2SO_4 is the lower water content with increasing acid concentration. In comparison to H_2SO_4, the reactivity of HCl is weaker because of the lower concentration of protons (1 mol HCl contains 1 mol H^+ and 1 mol H_2SO_4 contains 2 mol H^+). Therefore, 5 M H_2SO_4 have the same H^+ concentration as 10 M HCl; only these values are comparable. However, with 5 M H_2SO_4 more cations were dissolved from the octahedral sheet than with 10 M HCl (bold value in Table 6.40).

6.6 Summary and conclusions

The effects of acid treatment on bulk material of seven bentonites with a high content of smectites, one vermiculite, one illite, one sepiolite, three kaolin samples and of one magadiite were studied. Bulk material was used for most of the industrial applications purification and separation of the clay fraction (< 2 µm) is too time consuming and too expensive. The bulk materials contain other Al_2O_3 containing phases than clays; therefore the Al_2O_3 content of the impurities was subtracted from the total amount of Al_2O_3. For the adjustment of the Al_2O_3 content, four assumptions were made from the results of this chapter.

1) Feldspars like orthoclase and plagioclase albite were stable over the whole period of acid treatment studied. Only Ca-rich feldspars like anorthite started to dissolve after 20 h.

2) The dissolution of kaoline impurities was constant and independent of the matrix. This was corroborated by the investigated pure kaolin samples. After 20 h, between 25 and 50% of kaolinite was dissolved that equals between 1 and 2 g kaolinite if the total weight of the sample was 4 g and the kaolinite content averaged 90%. In a sample with 3.2 g (80%) kaolinite (main phase), between 1.2 and 2.2 g kaolinite remained, while in a sample with 0.4 g (10%) kaolinite (impurity) the kaolinite was completely dissolved.

3) The dissolution of mica depends on its chemical composition such as iron and magnesium content (up to 8.5% iron can be incorporated into the mica structure (Rösler, 1979)). Dioctahedral micas with low iron content were stable up to 96 h. The kaoline samples Kaolex and Rogers contained iron-rich dioctahedral micas, which were identified by XRD. After 96 h, up to 50% of this mica was dissolved. In the samples with smectite as main phase, the dioctahedral micas started to dissolve so that after 20 h 20%, after 72 h 50% and after 96 h 65% mica dissolved.

4) The dissolution of smectite also depends on its chemical composition. Therefore the following assumption was dissipated for samples with smectite as impurity. After 5 h 20% smectite and after 20 h up to 80% are dissolved.

The solubility of aluminium in H_2SO_4 and HCl at concentrations of 1, 5 and 10 M was checked with aluminium sulphate ($Al_2(SO_4)_3 \cdot 18H_2O$, M = 666.3 $g \cdot mol^{-1}$). The test was performed to check the saturation level under the selected conditions. Kaolinite has the highest concentration of aluminium in the structure compared to the other clay minerals smectite, vermiculite and sepiolite. A portion of 4 g kaolin Polwhite contain 38.5% Al_2O_3 that is 0.815 g Al^{3+} (M = 27 $g \cdot mol^{-1}$); 12.4 g of $Al_2(SO_4)_3 \cdot 18H_2O$ in 400 ml acid and 6.2 g in 200 ml acid were used to achieve an aluminium concentration of 0.81 g in the solution. This amount of aluminium sulphate was completely dissolved in 1, 5 and 10 M HCl, before the reaction

temperature of 80 °C was reached. In 1 and 5 M H_2SO_4, the calculated amount of aluminium sulphate was completely dissolved, too. Only in 10 M H_2SO_4, the used aluminium sulphate was not completely dissolved. In this case, the saturation of the solution was reached. The reason was the low water content.

The results of these investigations show that the dissolution of the octahedral cations occurs in the following order: $Mg^{2+} > Fe^{3+} > Al^{3+}$. The investigations of several clay mineral groups show that independent of the clay mineral group trioctahedral clay minerals such as hectorite, vermiculite, phlogopite and sepiolite, which have a high content of magnesium, are less stable than dioctahedral clay minerals with a high content of iron. The reason is that the bond between trivalent aluminium and oxygen is stronger than between divalent magnesium and oxygen. Aluminium is also more electropositive than magnesium, which also strengthen its bond to oxygen. As a result, the oxygen atoms bound to magnesium have a comparatively higher negative charge and, hence, are more easily protonated. The protonation causes a weakening of the Mg-O bond and finally a break of the linkage. Another reason is the smaller crystal radius (Bloss, 1994) of aluminium (0.675 Å) than those of magnesium (0.860 Å) and iron (0.69 Å low spin and 0.785 Å high spin) in the same coordination (6-fold), which leads to a shorter, more stable bond to oxygen.

The stability of the dioctahedral clay minerals like montmorillonite was also found to be dependent on number of substitutions in the octahedral and tetrahedral sheet. These substitutions cause deformations and distortions within the crystal structure resulting in a better solubility.

The investigations reveal that the acid treated smectites retain the capability to exchange cations. The value of the measured cation exchange capacity and the adjusted value of the measured Al_2O_3 content can be used to obtain a reliable estimation of the residual smectite content (see Chapter 6.4.1). The adjusted value of the measured Al_2O_3 content can be used to estimate the residual kaolinite (see Chapter 6.4.5). These contents can be compared with the calculated values of the X-ray diffraction analysis. The results indicate, there are two independent methods to estimate the residual smectite and kaolinite content.

The results show that acid treatment of layer silicates can be used to produce materials with a simple chemical composition that retained their layered structure. These materials have a low cation exchange capacity and a high specific surface area resulting in a lower charge density compared to the raw materials. Thus, these materials possess the ability to adsorb very large organic molecules (e.g., dodecylamine), which can be used as precursor for clay-polymer nanocomposites. Polymer incorporation will be investigated in the near future.

References

Abdul-Latif S. and Weaver C. E. (1969) Kinetics of acid-dissolution of palygorskite (attapulgite) and sepiolite. Clays and Clay Minerals **17**, pp. 169-178.

Bloss F. D. (1994) Crystallography and crystal chemistry: An introduction. Mineralogical Society of America, Washington D.C., pp. 545.

Breen C., Madejová J. and Komadel P. (1995) Characterisation of moderately acid-treated, size-fractionated montmorillonites using IR and MAS NMR spectroscopy and thermal analysis. Journal of Materials Chemistry **5**(3), pp. 469-474.

Brindley G. W. (1969) Unit cell of magadiite in air, in vacuo, and under other conditions. The American Mineralogist **54**, pp. 1583-1591.

Brindley G.W. and Brown G. (1980) Crystal structures of clay minerals and their X-ray identification. Mineralogical Society, Monograph 5, London, pp. 539.

Brunauer S., Emmett P. H. and Teller E. (1932) Adsorption of gases in multimolecular layers. Journal of the American Chemical Society **60**, pp. 309-319.

Carroll D. and Starkey H. C. (1971) Reactivity of clay minerals with acids and alkalies. Clays and Clay Minerals **19**, pp. 321-333.

De Boer J. H., Lippens B. C., Linsen B. G., Broekhoff J. C. P., Van den Heuvel A. and Osinga Th. J. (1966) The t-curve of multimolecular N_2-adsorption. Journal of Colloid and Interface Science **21**, pp. 405-414.

Emmerich K. (2000) Die geotechnische Bedeutung des Dehydroxylierungsverhaltens quellfähiger Tonminerale. Dissertation, Veröffentlichungen des Instituts für Geotechnik (IGT) der ETH Zürich, pp. 143.

Eypert-Blaison C., Humbert B., Michot L. J., Pelletier M., Sauzéat E. and Villiéras F. (2001) Structural role of hydration water in Na- and H-Magadiite: A spectroscopy study. Chemistry of Material **13**, pp. 4439-4446.

Farmer V. C. (1974) The infrared spectra of minerals. Mineralogical Society, Monograph 4, London, pp. 539.

Frost R. L., Locos O. B., Ruan H. and Kloprogge J. T. (2001) Near-infrared and mid-infrared spectroscopic study of sepiolites and palygorskites. Vibrational Spectroscopy **27**, pp. 1-13.

Friedrich F. (2004) Spectroscopic investigations of delaminated and intercalated phyllosilicates. Dissertation, Fakultät für Bauingenieur-, Geo- und Umweltwissenschaften der Universität Karlsruhe, pp. 150.

Gregg S. J. and Sing K. S. W. (1991) Adsorption, surface area and porosity. Academic Press.

Hradil D., Hostomský J. and Soukupová J. (2002) Aluminium release rates from acidified clay structures: Comparative kinetic study. Geologica Carpathica **53**(2), pp. 117-121.

Jozefaciuk G. and Bowanko G. (2002) Effect of acid and alkali treatments on surface areas and adsorption energies of selected minerals. Clays and Clay Minerals **50**(6), pp. 771-783.

Kaufhold S. (2001) Untersuchungen zur Eignung von natürlich alterierten sowie mit Oxalsäure aktivierten Bentoniten als Bleicherde für Pflanzenöle. Dissertation, Fakultät für Bergbau, Hüttenwesen und Geowissenschaften der Rheinisch-Westfälischen Technischen Hochschule Aachen, pp. 178.

Kleeberg R. and Bergmann J. (2002) Quantitative phase analysis using the Rietveld method and a fundamental parameter approach. Proceedings of the II International School on Powder diffraction, pp. 63-76.

Klinke W. (2007) Mineralogische und geochemische Untersuchungen zur Wechselwirkung zwischen Tonen und neutralen, basischen und sauren Kontaktwässern. Dissertation, Fakultät für Bauingenieur-, Geo- und Umweltwissenschaften der Universität Karlsruhe, pp. 135.

Komadel P. (2003) Chemically modified smectites. Clay Minerals **38**(1), pp. 127-138.

Komadel P., Janek M., Madejová J., Weekes A. and Breen C. (1997) Acidity and catalytic activity of mildly acid-treated Mg-rich montmorillonite and hectorite. Journal of Chemical Society, Faraday Transactions **93**(23), pp. 4207-4210.

Komadel P., Madejová J., Janek M., Gates W. P., Kirkpatrick R. J. and Stucki J. W. (1996) Dissolution of hectorite in inorganic acids. Clays and Clay Minerals **44**(2), pp. 228-236.

Komadel P., Schmidt D., Madejová J. and Čičel B. (1990) Alteration of smectites by treatments with hydrochloric acid and sodium carbonate solutions. Applied Cay Science **5**, pp. 113-122.

Kubelka P. and Munk F. (1931) Ein Beitrag zur Optik von Farbanstrichen. Zeitschrift für technische Physik **12**, pp. 593-601.

Lagaly G. (1989) Erkennung und Identifizierung von Tonmineralen mit organischen Stoffen. Jahrestagung der deutschen Ton- und Tonmineralgruppe (DTTG), pp. 86-130.

Lagaly G. (1994) Layer charge determination by alkylammonium ions in layer charge characteristics of 2:1 silicate clay minerals. Mermut A. R. (ed.), The Clay Minerals Society **6**, Aurora, pp. 1-46.

Lagaly G., Beneke K. and Weiss A. (1973) Über eine neue kristalline Kieselsäure der Zusammensetzung $H_2Si_{14}O_{29}\cdot 5H_2O$ mit Schichtstruktur und Befähigung zur Bildung von Intercalationsverbindungen. Zeitschrift für Naturforschung, B: Anorganische und Organische Chemie **28**, pp. 234-238.

Lagaly G. and Weiss A. (1970) Anordnung und Orientierung kationischer Tenside auf ebenen Silicatoberflächen Teil IV. Kolloid-Zeitschrift und Zeitschrift für Polymere **243**, pp. 48-55.

Liu W. (2001) Modeling description and spectroscopic evidence of surface acid-base properties of natural illites. Water Research **35**(17), pp. 4111-4125.

Madejová J., Bujdák J., Janek M. and Komadel P. (1998) Comparative FT-IR study of structural modifications during acid treatment of dioctahedral smectites and hectorite. Spectrochimica Acta **54**, pp. 1397-1406.

Makó E., Senkár Z., Kristóf J. and Vágvölgyi V. (2006) Surface modification of mechanochemically activated kaolinites by selective leaching. Journal of Colloid and Interface Science **294**, pp. 362-370.

Mackenzie R. C. (1951) A micromethod for determination of cation-exchange capacity of clay. Journal of Colloid Science **6**, pp. 219-222.

McKeown D. A., Post J. E. and Etz E. S. (2002) Vibrational analysis of palygorskite and sepiolite. Clays and Clay Minerals **50**, pp. 667-680.

Meier L. P. and Kahr G. (1999) Determination of the cation exchange capacity (CEC) of clay minerals using the complexes of copper(II) ion with triethylenetetramine and tetraethylenepentamine. Clays and Clay Minerals **47**(3), pp. 386-388.

Myriam M., Suárez M. and Martin-Pozas M. J. (1998). Structural and textural modifications of palygorskite and sepiolite under acid treatment. Clays and Clay Minerals **46,** pp. 225-231.

Müller-Vonmoos M. and Kahr G. (1983) Mineralogische Untersuchungen von Wyoming Bentonit MX-80 und Montigel. Technischer Bericht der Nationalen Genossenschaft für die Lagerung radioaktiver Abfälle (Nagra) **83**(12), pp. 23.

Novák I. and Číčel B. (1978) Dissolution of smectites in hydrochloric acid: II Dissolution rate as a function of crystallochemical composition. Clays and Clay Minerals **26**(5), pp. 341-344.

Önal M. and Sarikaya Y. (2007) Preparation and characterization of acid-activated bentonite powders. Powder Technology **172**, pp. 14-18.

Pálková H., Madejová J. and Righi D. (2003) Acid dissolution of reduced-charge Li- and Ni-montmorillonites. Clays and Clay Minerals **51**(2), pp. 133-142.

Petrick K. (2007) Vergleich von STA-Messungen und FTIR-spektroskopischen Messungen zur Strukturbestimmung der Oktaederschicht von Montmorillonit. Diplomarbeit, Fakultät für Bauingenieur-, Geo- und Umweltwissenschaften der Universität Karlsruhe, pp. 175.

Ravichandran J. and Sivasankar B. (1997) Properties and catalytic activity of acid-modified montmorillonite and vermiculite. Clays and Clay Minerals **45**(6), pp. 854-858.

Rösler H. J. (1979) Lehrbuch der Mineralogie. VEB Deutscher Verlag für Grundstoffindustrie, Leipzig, pp. 832.

Snäll S. and Liljefors T. (2000) Leachability of major elements from minerals in strong acids. Journal of Geochemical Exploration **71**, pp. 1-12.

Superti G. B., Olivereira E. C. and Pastore H. O. (2007) Aluminium magadiite: An acid solid layered material. Chemistry of Material **19**, pp. 4300-4315.

Tyagi B., Chudasama C. D. and Jasra R. V. (2006) Determination of structural modification in acid activated montmorillonite clay by FT-IR spectroscopy. Spectrochimica Acta Part A **64**, pp. 273-278.

Ufer K., Roth G., Kleeberg R., Stanjek H., Dohrmann R. and Bergmann J. (2004) Description of X-ray powder pattern of turbostratically disordered layer structures with a Rietveld compatible approach. Zeitschrift für Kristallographie **219**, pp. 519-527.

Vicente-Rodríguez M., Lopez-Gonzalez J. and Bañares-Muñoz M. (1995) Influence of the free silica generated during acid activation of a sepiolite on the adsorbent and textural properties of the resulting solids. Journal of Materials Chemistry **5**(1), pp. 127-132.

Vivaldi J. L. M. and Hach-Ali P. F. (1970) Palygorskites and Sepiolites (Hormites). Mackenzie R. C. (ed.), Differential Thermal Analysis, Academic Press, London, New York, pp. 554-573.

Wilson M. J. (1994) Clay mineralogy: Spectroscopic and chemical determinative methods. Chapman and Hall, Oxford, pp. 367.

Wolters F., Lagaly G., Kahr G., Nueesch R. (†) and Emmerich K. (2009) A comprehensive characterisation of dioctahedral smectites. Clays and Clay Minerals, in print.

Yebra-Rodríquez A., Martín-Ramos J. D., Del Rey F., Viseras C. and López-Galindo A. (2003) Effect of acid treatment on the structure of sepiolite. Clay Minerals **38**, pp. 353-360.

Appendix

Appendix

1 Instructions to the program “PeakFit”

Instructions to the “PeakFit” program 4.0 from Jandel Scientific

The “PeakFit” program can be applied to determine the peak area in a certain range of FTIR spectra or STA curves, especially MS curve (H_2O).

FTIR spectroscopy

The program “PeakFit” was used to determine the peak areas of selected vibrations to approve the release of the octahedral cations (Al^{3+}, Fe^{3+}, Mg^{2+}). Certain vibrations like AlAlOH, AlFeOH and AlMgOH give information about the content of octahedral cations. The release of these cations is combined with a reduction of the peak intensity and peak area. The calculated peak areas were displayed in dependency of the chemical composition after a certain reaction time (Petrick, 2007).

Simultaneous thermal analysis

The program “PeakFit” was applied to determine the peak areas in a selected temperature range to estimate the cis- and trans-vacant character of the dioctahedral smectites. The border between both varieties was defined by 600 °C. All peak areas below 600 °C were added together and all peak areas above 600 °C. The two results reflected the content of cis- and trans-vacant portions (Wolters and Emmerich, 2007).

For the application of “PeakFit”, the original data have to be transformed in a “TXT” format.

Approach of the “PeakFit” program

1. Load file

   File → Import

2. Define the “PeakFit” range

   Prepare → Section (Section Data)

“PeakFit” range:	Simultaneous thermal analysis:	from 350 to 900 °C
	FTIR spectroscopy:	from 400 to 1100 cm^{-1}

3. Adjustment of the background

   AutoFit → AutoFit and Subtract baseline (Automatic baseline subtraction)

   Several background corrections can be choosing.

4. Select the fitting mode (Automatic peak detection and fitting)

AutoFit → AutoFit Peaks I Residuals
AutoFit Peaks II Second derivative
AutoFit Peaks III Deconvolution

It is important that the function “vary widths” was selected. Consequently, the broadness of the peaks was varied. In the fitting mode, the several peaks can be superimposed, deleted or shifted according to the measured curve. The realisation of the fit was done by the button “Full Peak Fit with Graphical Update”.

5. Presentation of the calculation

Select the following button:

1. “Review Fit”
2. “Numeric”

→ Graphical presentation and designation of r^2 as well as the number of peaks

→ Peak Summary (Description of the fitting parameter)

In the peak summary, there are listed the maxima of the selected peaks and the calculated peak area in % of the several peaks. For the modulation, the number of selected peaks should not vary extremely.

References

Petrick K. (2007) Vergleich von STA-Messungen und FTIR-spektroskopischen Messungen zur Strukturbestimmung der Oktaederschicht von Montmorillonit. Diplomarbeit, Fakultät für Bauingenieur-, Geo- und Umweltwissenschaften der Universität Karlsruhe, pp. 175.

Wolters F. and Emmerich K. (2007) Thermal reactions of smectites – Relation of dehydroxylation temperature to octahedral structure. Thermochimica Acta **462**, pp. 80-88.

Appendix

2. Data sheets “Mineralogical characterisation”

2.1 Bulk material

Sample: Bentonite Calcigel (1_Calci)

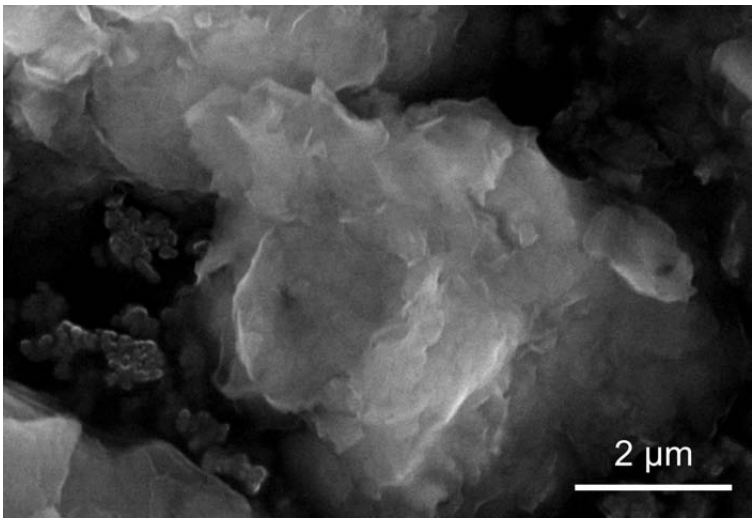

Figure 1 ESEM image.

XRF-Analysis

SiO_2	[%]	49.35
Al_2O_3	[%]	16.61
MgO	[%]	4.15
Fe_2O_3	[%]	5.09
TiO_2	[%]	0.38
MnO	[%]	0.05
Na_2O	[%]	0.26
CaO	[%]	4.26
K_2O	[%]	1.52
P_2O_5	[%]	0.06
LOI	[%]	17.7

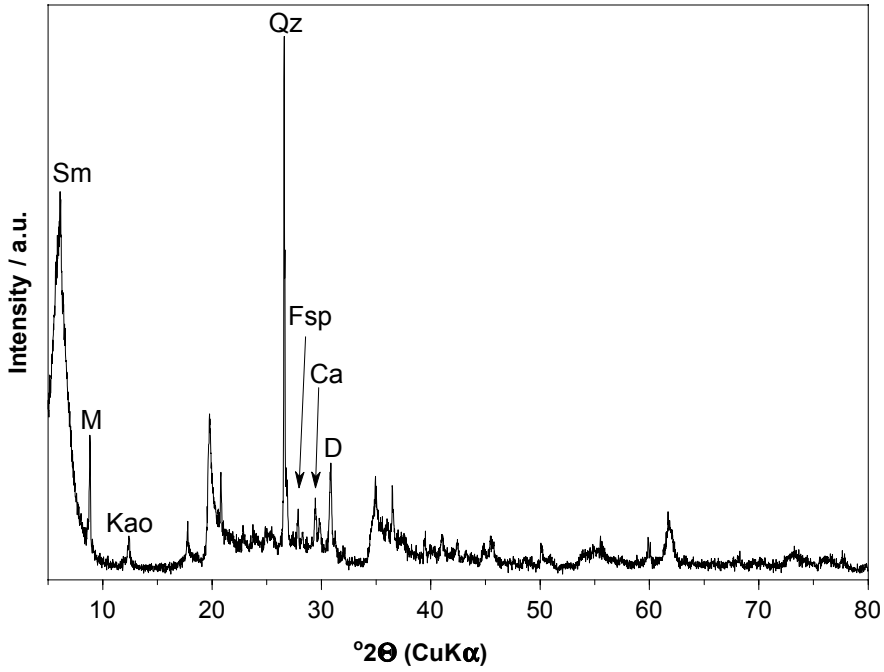

Phase	%
Smectite	63.5
Kaolinite	3.8
Muscovite	13.7
Quartz	5.9
Plagioclase (Albite)	2.5
Calcite	3.3
Dolomite	7.3

Figure 2 X-ray diffraction analysis (powder sample).
Sm: Smectite (001); Qz: Quartz; Fsp: Feldspar;
Ca: Calcite; M: Muscovite; D: Dolomite.

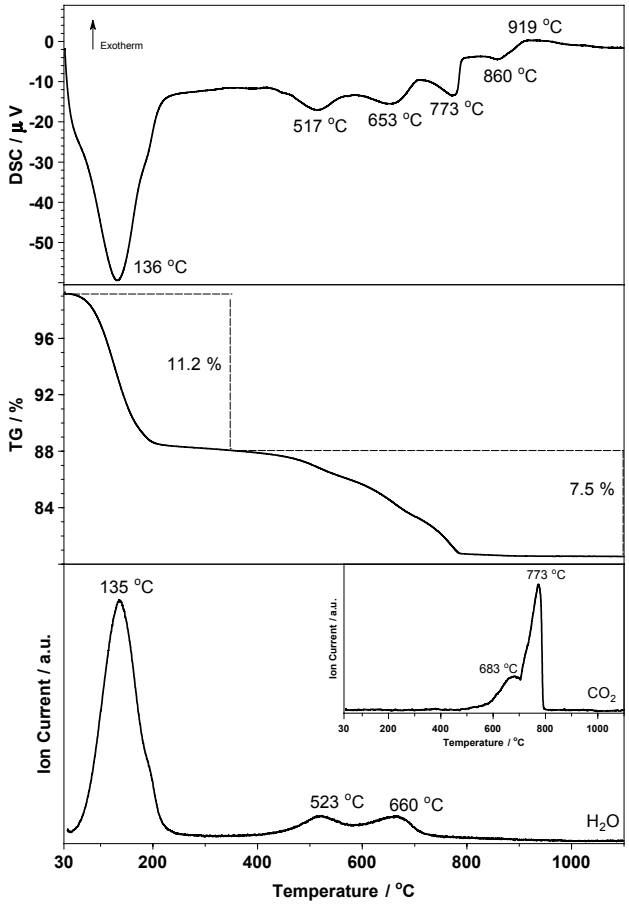

Figure 3 Simultaneous thermal analysis; starting mass of TG: 99.29%.

Grain size distribution

Fraction	%
> 63 µm	2
63 – 20 µm	14
20 – 2 µm	22
< 2 µm	61

Chemical and physical parameters

Method	Value
CEC	63 meq / 100g
ξ (n_c=12)	0.30 eq/FU
BET	64 m^2/g

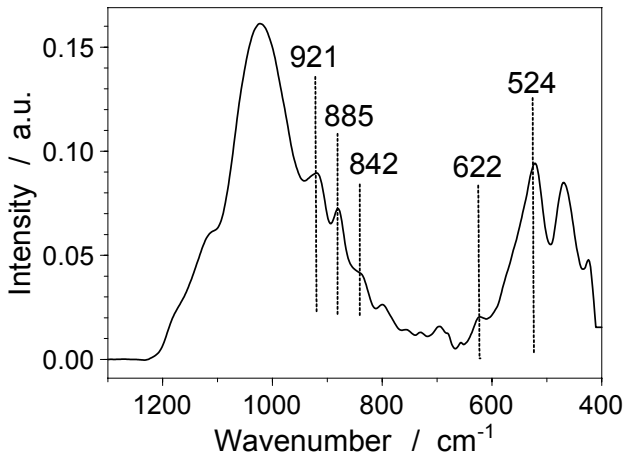

Figure 4 FTIR-spectrum.

Composition of the interlayer

Interlayer composition / FU	Na^+	Ca^{2+}	Mg^{2+}	K^+
[mol]	0.03	0.09	0.045	0.01

Sample: Bentonite EXM757 (2_EXM757)

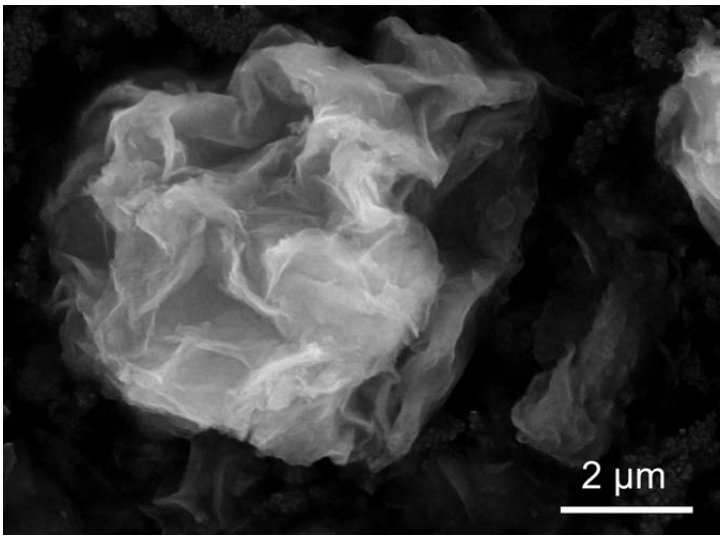

Figure 1 ESEM image.

XRF-Analysis

SiO_2	[%]	61.01
Al_2O_3	[%]	17.15
MgO	[%]	2.08
Fe_2O_3	[%]	3.76
TiO_2	[%]	0.16
MnO	[%]	0.01
Na_2O	[%]	2.95
CaO	[%]	0.74
K_2O	[%]	0.17
P_2O_5	[%]	0.52
LOI	[%]	11.4

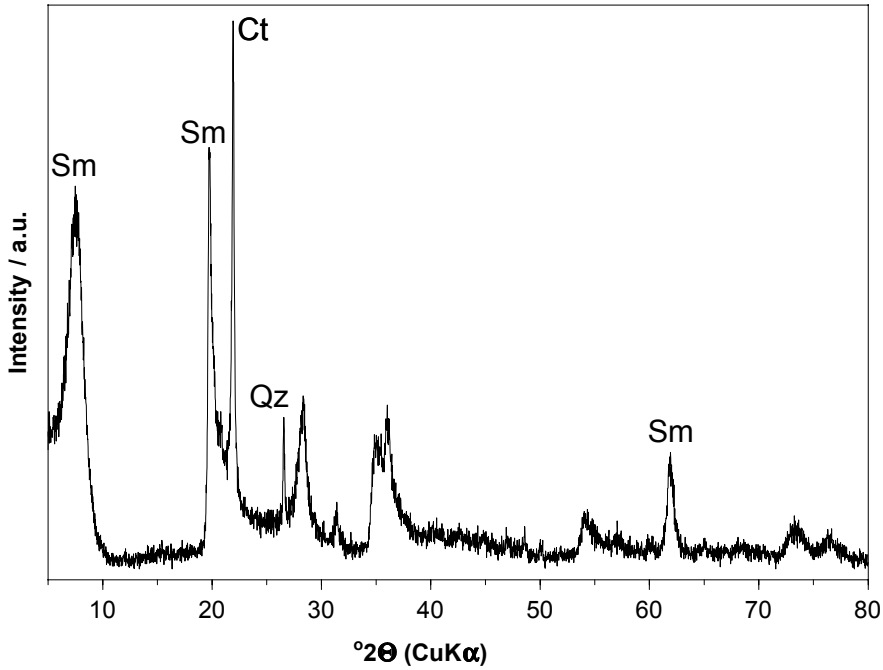

Phase	%
Smectite	86.5
Cristobalite	11.2
Quartz	2.3

Figure 2 X-ray diffraction analysis (powder sample).
Sm: characteristic smectite peaks with increasing 2θ (001), (020,110,021), (060);
Qz: Quartz; Ct: Cristobalite.

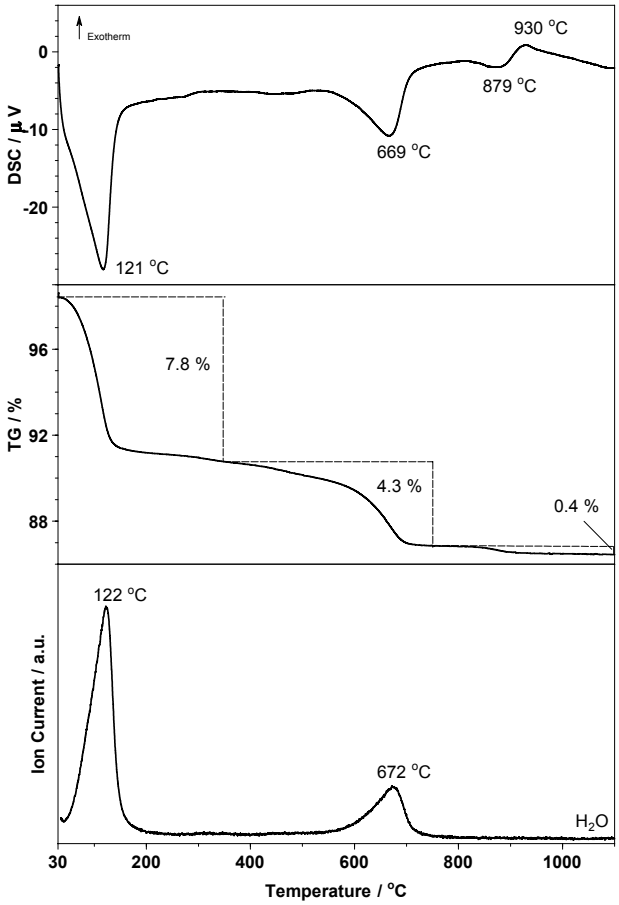

Figure 3 Simultaneous thermal analysis; starting mass of TG: 98.61%.

Grain size distribution

Fraction	%
> 63 µm	-
63 – 20 µm	-
20 – 2 µm	4
< 2 µm	96

Chemical and physical parameters

Method	Value
CEC	84 meq / 100g
ξ (n_c=12)	0.30 eq/FU
BET	28 m^2/g

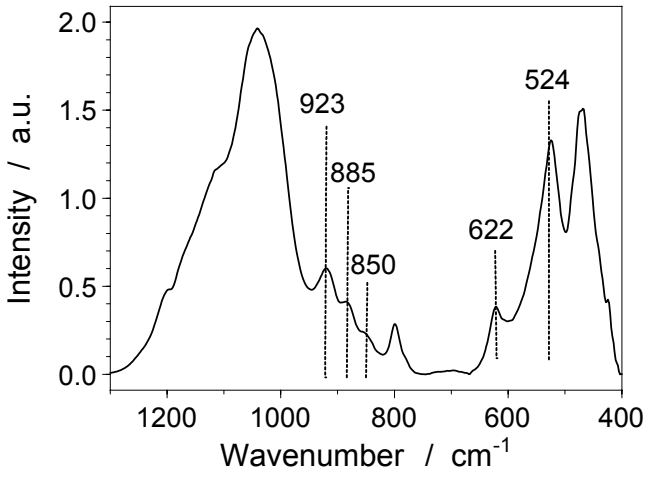

Figure 4 FTIR-spectrum.

Composition of the interlayer

Interlayer composition / FU	Na^+	Ca^{2+}	Mg^{2+}	K^+
[mol]	0.25	0.02	0.005	-

Sample: Bentonite SWy-2 (3_SWy-2)

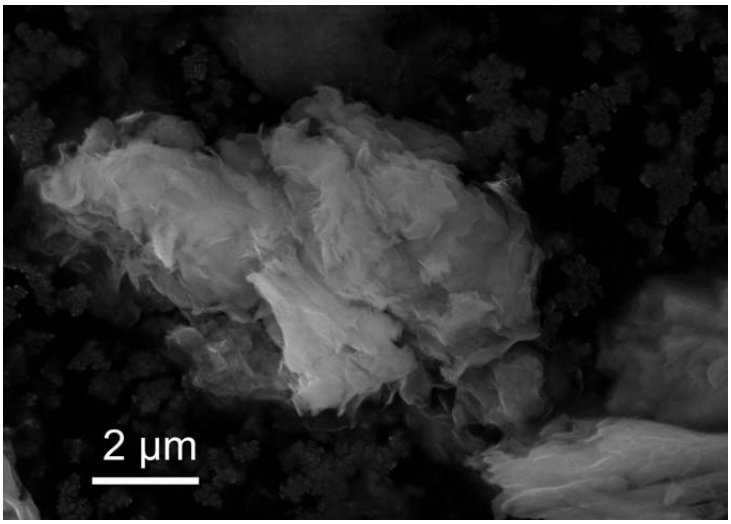

Figure 1 ESEM image.

XRF-Analysis

SiO_2	[%]	61.26
Al_2O_3	[%]	17.98
MgO	[%]	2.41
Fe_2O_3	[%]	3.79
TiO_2	[%]	0.15
MnO	[%]	0.03
Na_2O	[%]	1.34
CaO	[%]	1.54
K_2O	[%]	0.59
P_2O_5	[%]	0.04
LOI	[%]	10.3

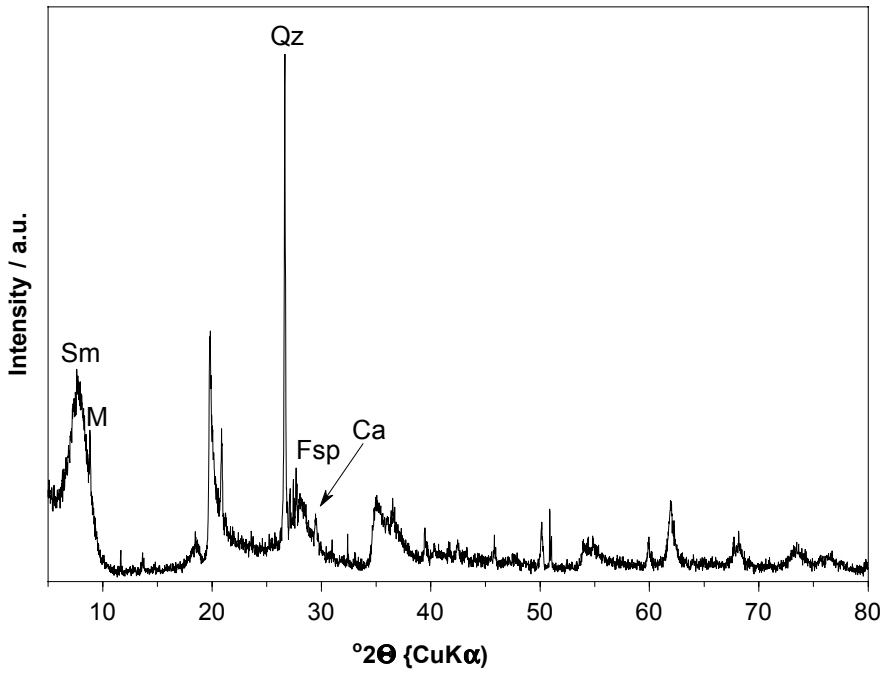

Phase	%
Smectite	79.4
Quartz	10.5
Muscovite	3.7
K-Feldspar (Orthoclase)	4.2
Calcite	2.2

Figure 2 X-ray diffraction analysis (powder sample).
Sm: Smectite (001);
Qz: Quartz; Fsp: Feldspar; Ca: Calcite; M: Muscovite.

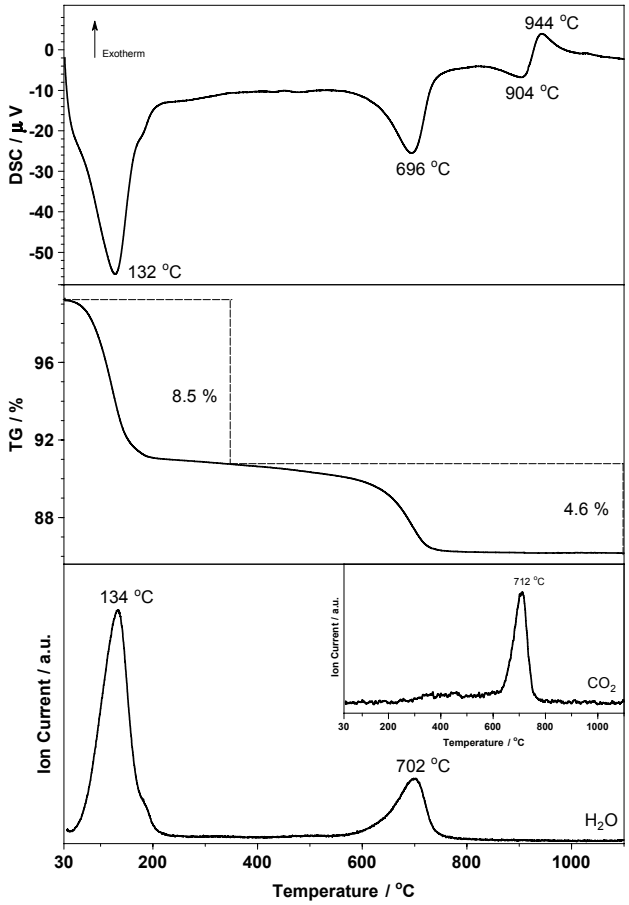

Figure 3 Simultaneous thermal analysis; starting mass of TG: 99.30%.

Grain size distribution

Fraction	%
> 63 µm	1
63 – 20 µm	6
20 – 2 µm	7
< 2 µm	86

Chemical and physical parameters

Method	Value
CEC	78 meq / 100g
ξ (n_c=12)	0.29 eq/FU
BET	24 m^2/g

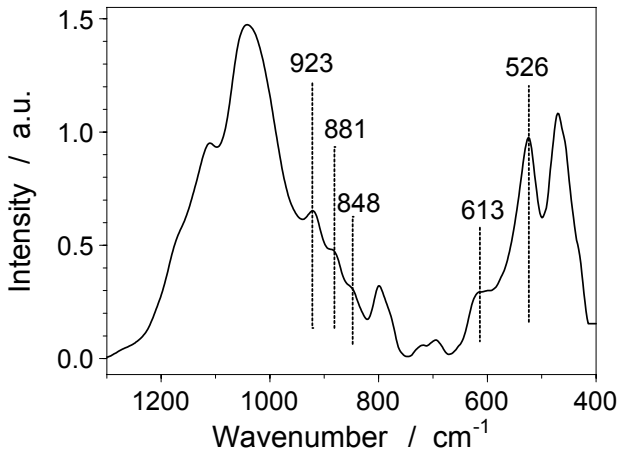

Figure 4 FTIR-spectrum.

Composition of the interlayer

Interlayer composition / FU	Na^+	Ca^{2+}	Mg^{2+}	K^+
[mol]	0.14	0.045	0.03	-

Sample: Bentonite Volclay (4_Vol)

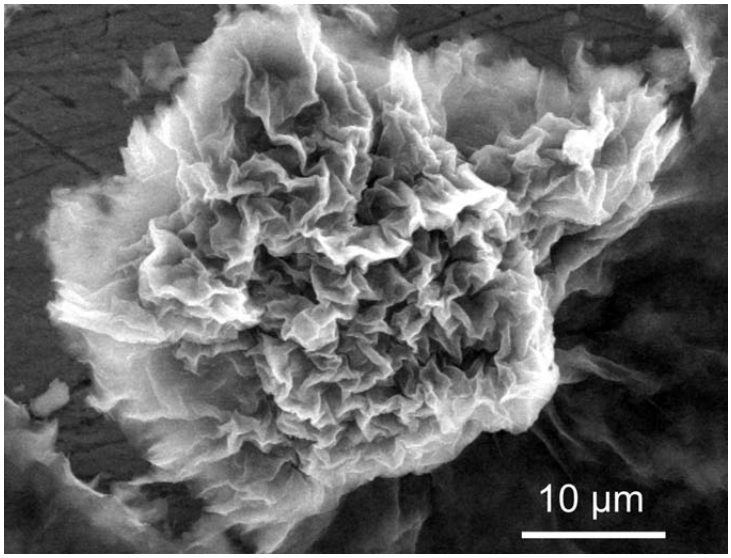

Figure 1 ESEM image.

XRF-Analysis

SiO_2	[%]	56.50
Al_2O_3	[%]	18.56
MgO	[%]	2.26
Fe_2O_3	[%]	3.56
TiO_2	[%]	0.15
MnO	[%]	0.01
Na_2O	[%]	1.88
CaO	[%]	1.14
K_2O	[%]	0.52
P_2O_5	[%]	0.04
LOI	[%]	15.4

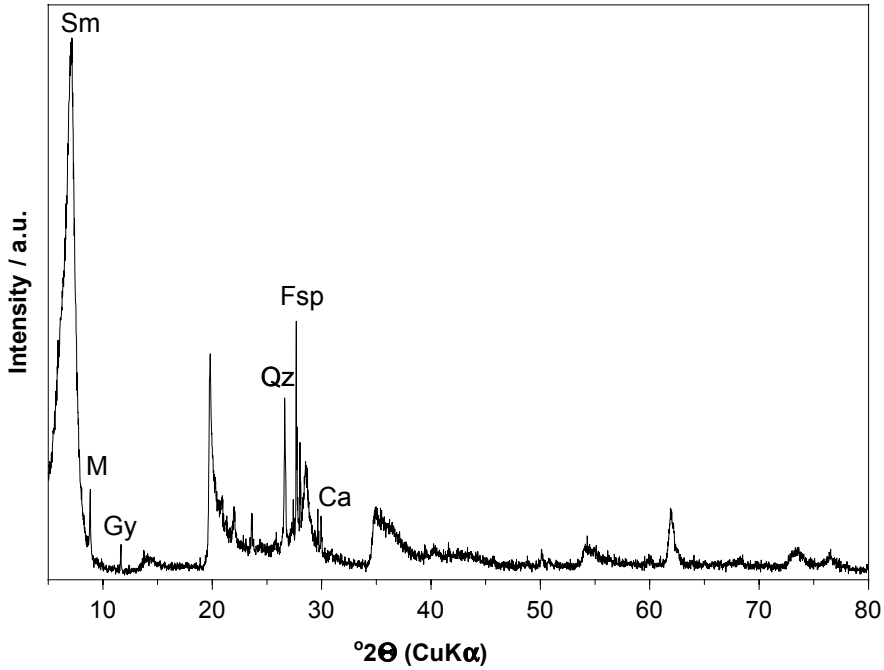

Phase	%
Smectite	79.8
Muscovite	2.8
Quartz	4.4
K-Feldspar (Orthoclase)	4.0
Plagioclase (Albite)	4.1
Calcite	1.2
Gypsum	3.6

Figure 2 X-ray diffraction analysis (powder sample).
Sm: Smectite (001); Qz: Quartz; Fsp: Feldspar; Ca: Calcite;
M: Muscovite; Gy: Gypsum.

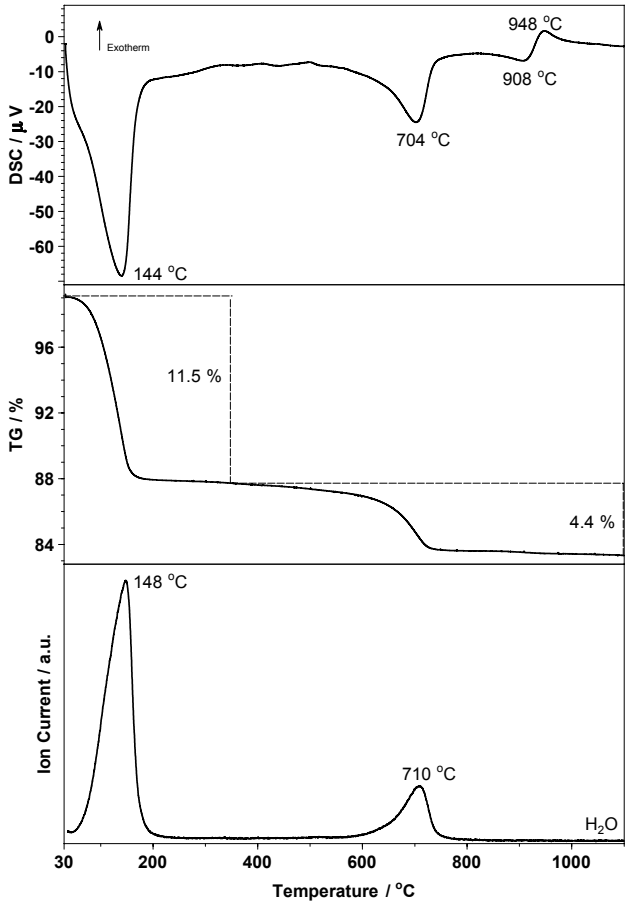

Figure 3 Simultaneous thermal analysis; starting mass of TG: 99.22%.

Grain size distribution

Fraction	%
> 63 µm	2
63 – 20 µm	5
20 – 2 µm	5
< 2 µm	88

Chemical and physical parameters

Method	Value
CEC	85 meq / 100g
ξ (n_c=12)	0.27 eq/FU
BET	30 m^2/g

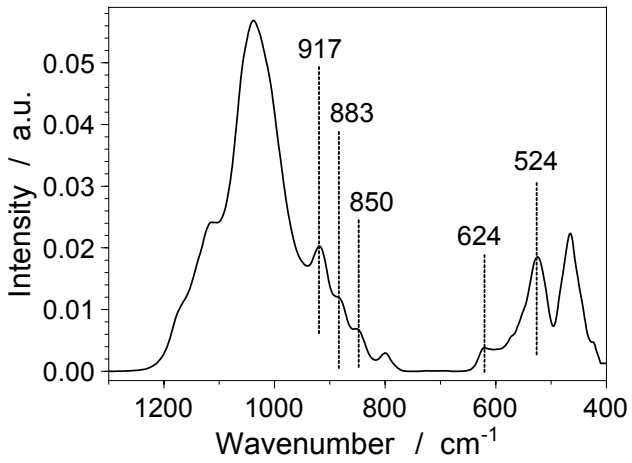

Figure 4 FTIR-spectrum.

Composition of the interlayer

Interlayer composition / FU	Na^+	Ca^{2+}	Mg^{2+}	K^+
[mol]	0.16	0.04	0.01	-

Sample: Bentonite WYO (5_WYO)

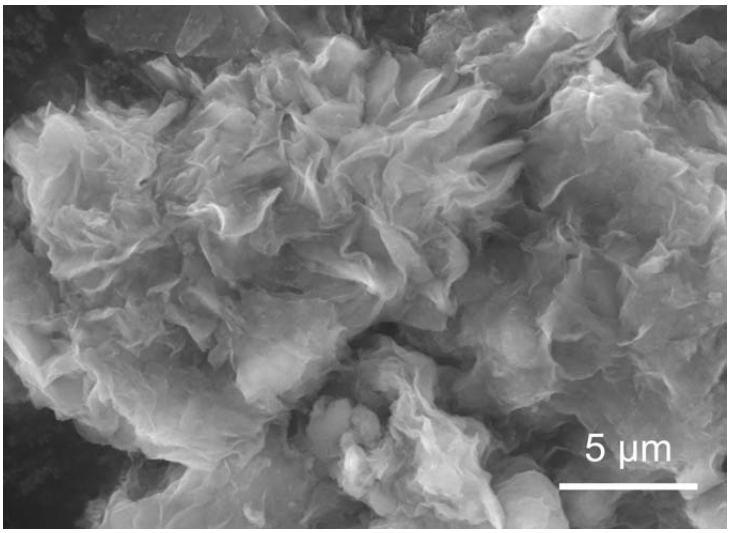

Figure 1 ESEM image.

XRF-Analysis

SiO_2	[%]	59.85
Al_2O_3	[%]	15.21
MgO	[%]	5.41
Fe_2O_3	[%]	1.61
TiO_2	[%]	0.17
MnO	[%]	0.33
Na_2O	[%]	2.17
CaO	[%]	2.37
K_2O	[%]	0.52
P_2O_5	[%]	0.07
LOI	[%]	12.3

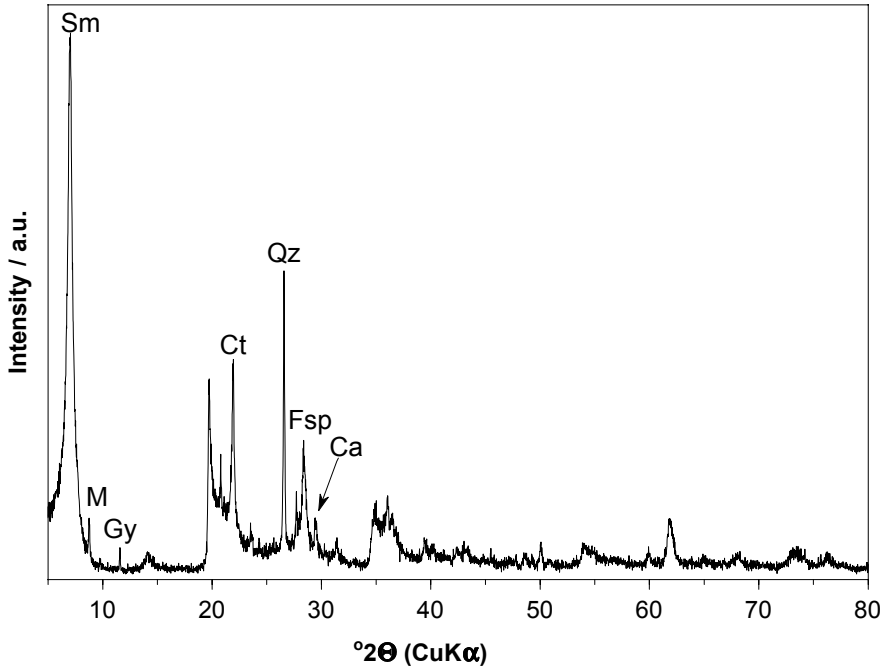

Phase	%
Smectite	67.2
Cristobalite	3.6
Quartz	6.6
Muscovite	2.8
K-Feldspar (Microcline)	3.9
Plagioclase (Oligoclase)	8.0
Calcite	3.5
Gypsum	0.9
Clinoptilolite	1.0

Figure 2 X-ray diffraction analysis (powder sample).
Sm: Smectite (001); Qz: Quartz; Fsp: Feldspar; Ca: Calcite;
M: Muscovite; Gy: Gypsum; Ct: Cristobalite.

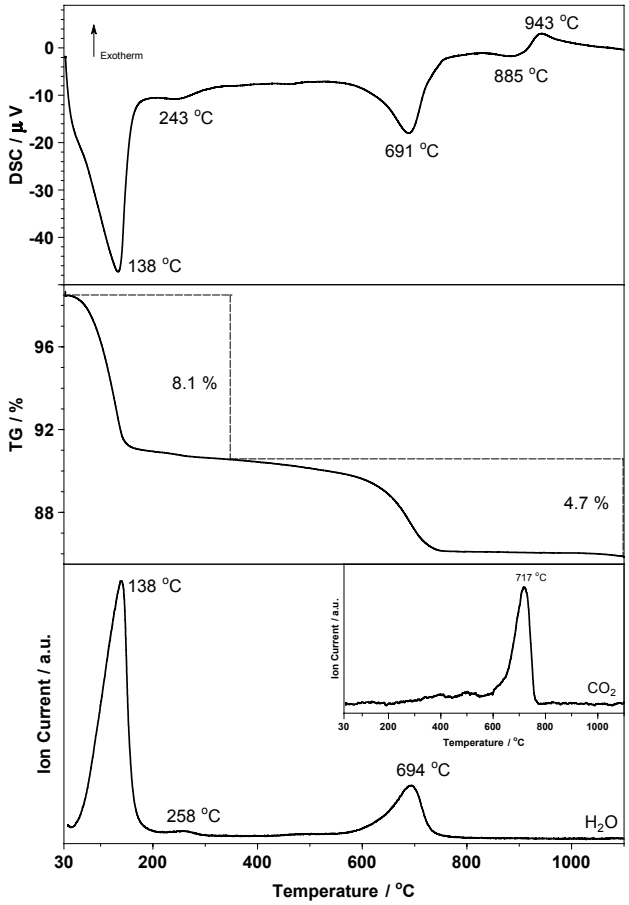

Figure 3 Simultaneous thermal analysis; starting mass of TG: 98.66%.

Grain size distribution

Fraction	%
> 63 µm	4
63 – 20 µm	3
20 – 2 µm	15
< 2 µm	78

Chemical and physical parameters

Method	Value
CEC	68 meq / 100g
ξ (n_c=12)	0.28 eq/FU
BET	32 m^2/g

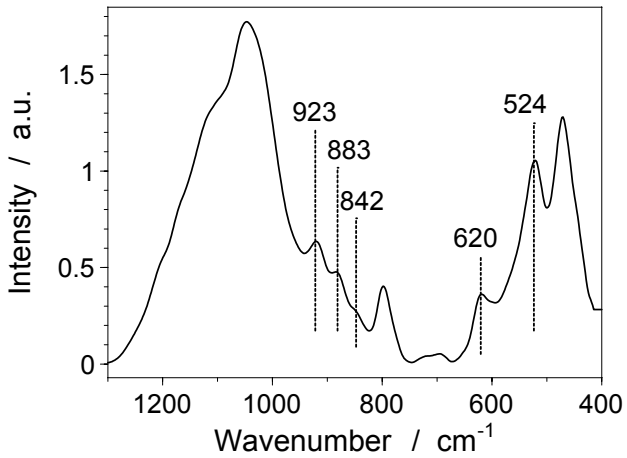

Figure 4 FTIR-spectrum.

Composition of the interlayer

Interlayer composition / FU	Na^+	Ca^{2+}	Mg^{2+}	K^+
[mol]	0.19	0.04	0.005	-

Sample: Indian Bentonite (6_IndBent)

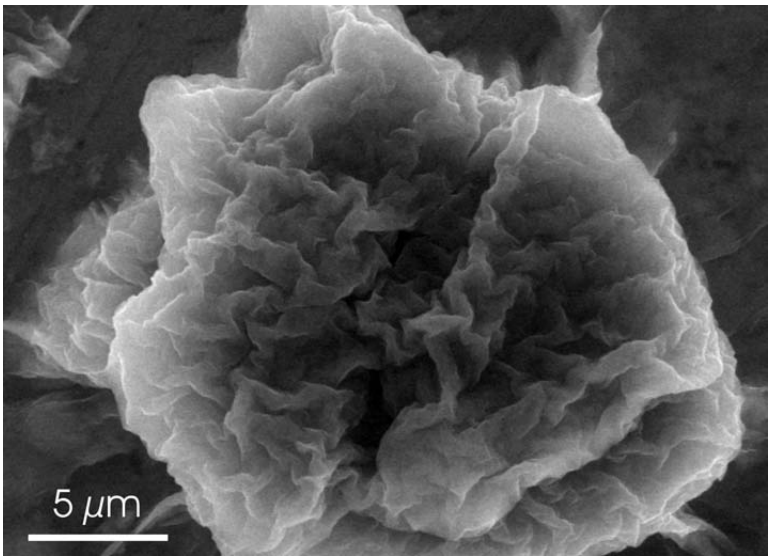

Figure 1 ESEM image.

XRF-Analysis

SiO_2	[%]	43.08
Al_2O_3	[%]	15.59
MgO	[%]	2.40
Fe_2O_3	[%]	13.74
TiO_2	[%]	0.94
MnO	[%]	0.12
Na_2O	[%]	3.39
CaO	[%]	1.23
K_2O	[%]	0.10
P_2O_5	[%]	0.06
LOI	[%]	18.8

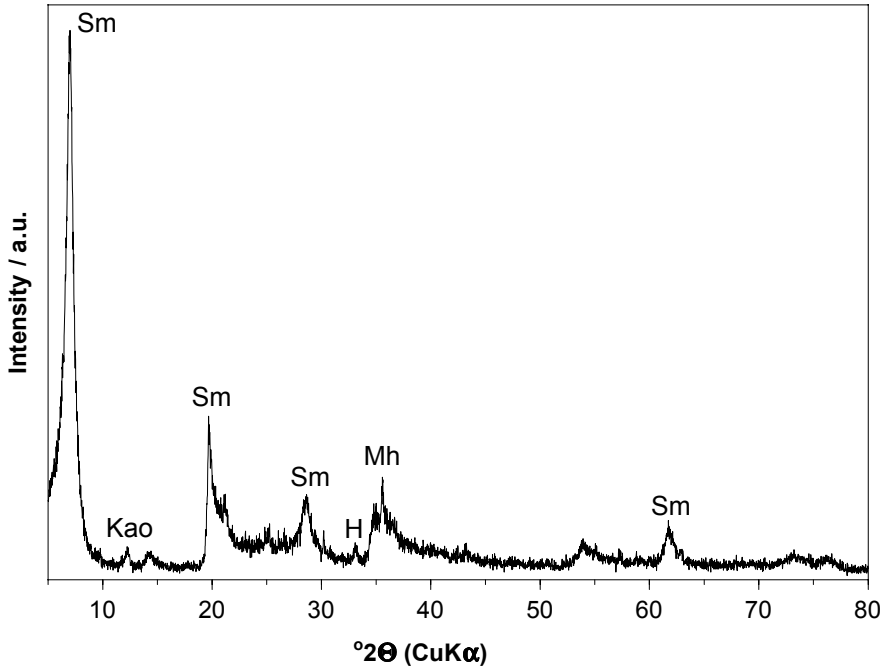

Phase	%
Smectite	88.9
Kaolinite	4.4
Quartz	1.1
Plagioclase (Oligoclase)	3.9
Maghemite	0.9
Hematite	0.8

Figure 2 X-ray diffraction analysis (powder sample).
Sm: characteristic smectite peaks with increasing 2θ (001), (020,110,021), (060);
Kao: Kaolinite; Mh: Maghemite; H: Hematite.

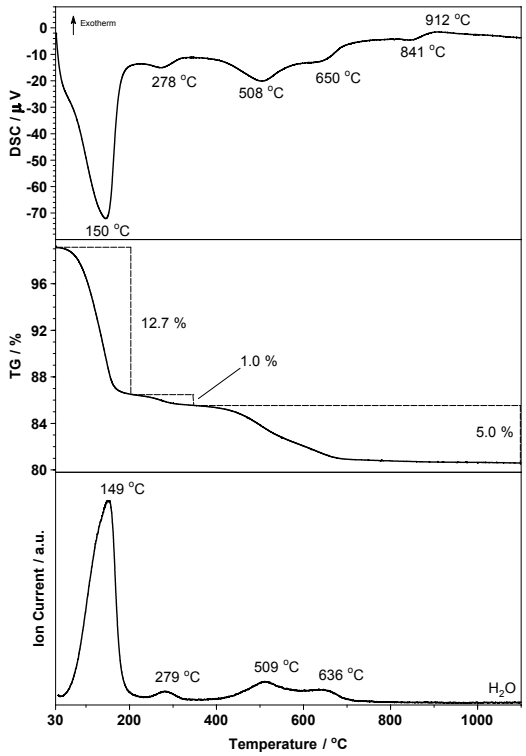

Figure 3 Simultaneous thermal analysis; starting mass of TG: 99.23%.

Grain size distribution

Fraction	%
> 63 µm	3
63 – 20 µm	3
20 – 2 µm	5
< 2 µm	89

Chemical and physical parameters

Method	Value
CEC	91 meq / 100g
ξ (n_c=12)	0.38 eq/FU
BET	29 m^2/g

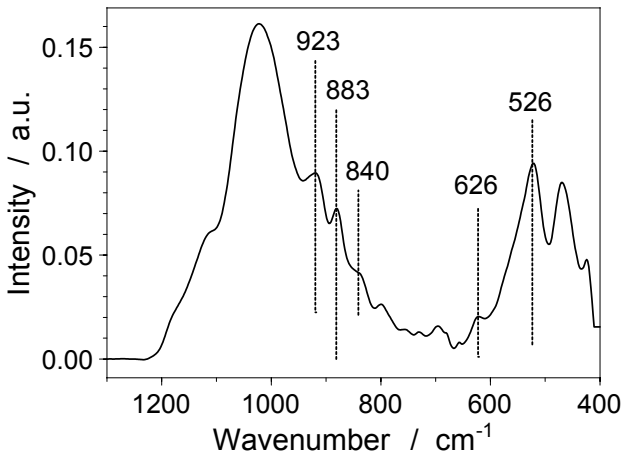

Figure 4 FTIR-spectrum.

Composition of the interlayer

Interlayer composition / FU	Na^+	Ca^{2+}	Mg^{2+}	K^+
[mol]	0.30	0.015	-	-

Sample: Natural Hectorite (7_NHec)

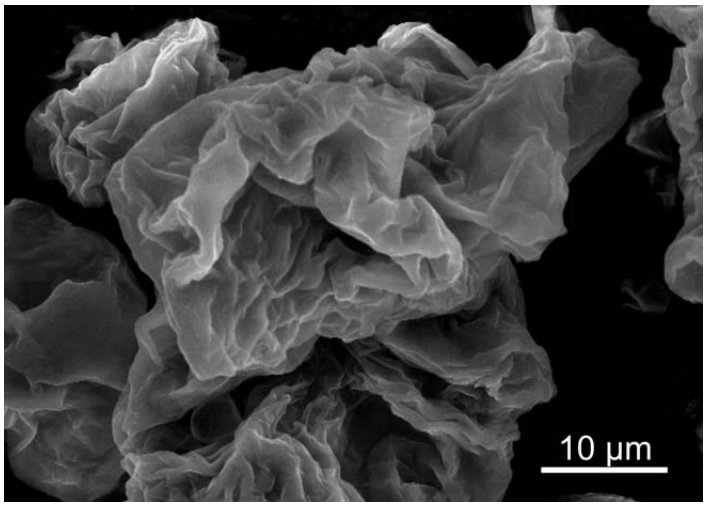

Figure 1 ESEM image.

XRF-Analysis

SiO_2	[%]	55.03
Al_2O_3	[%]	1.61
MgO	[%]	22.84
Fe_2O_3	[%]	0.81
TiO_2	[%]	0.08
MnO	[%]	0.02
Na_2O	[%]	3.31
CaO	[%]	1.88
K_2O	[%]	0.42
P_2O_5	[%]	0.87
LOI	[%]	12.7

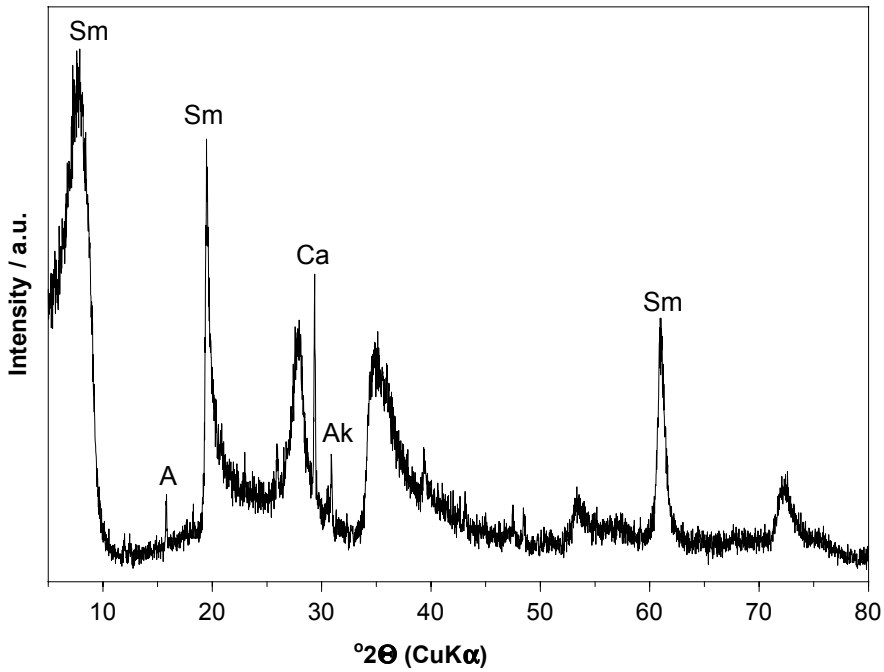

Phase	%
Smectite	93.9
Calcite	3.1
Ankerite	0.7
Analcime	2.1

Figure 2 X-ray diffraction analysis (powder sample).
Sm: characteristic smectite peaks with increasing 2θ (001), (020,110,021), (060);
Ca: Calcite; Ak: Ankerite; A: Analcime.

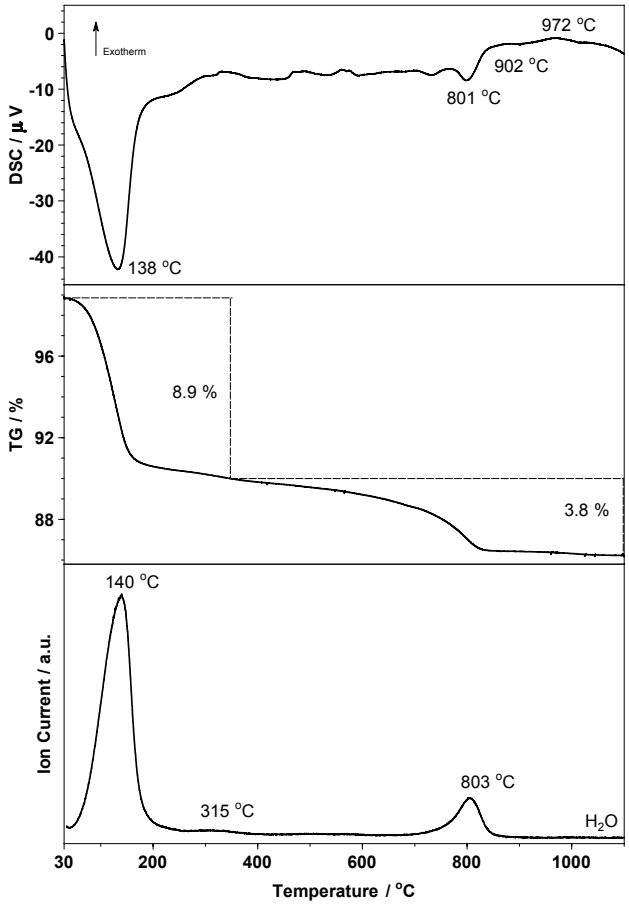

Figure 3 Simultaneous thermal analysis; starting mass of TG: 98.92%.

Grain size distribution

Fraction	%
> 63 µm	-
63 – 20 µm	-
20 – 2 µm	2
< 2 µm	98

Chemical and physical parameters

Method	Value
CEC	89 meq / 100g
ξ (n_c=12)	0.29 eq/FU
BET	48 m^2/g

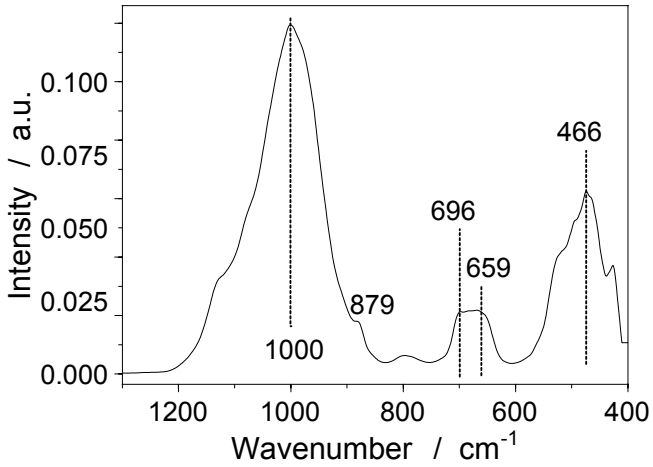

Figure 4 FTIR-spectrum.

Composition of the interlayer

Interlayer composition / FU	Na^+	Ca^{2+}	Mg^{2+}	K^+
[mol]	0.24	0.015	0.005	-

Sample: Vermiculite (8_Verm)

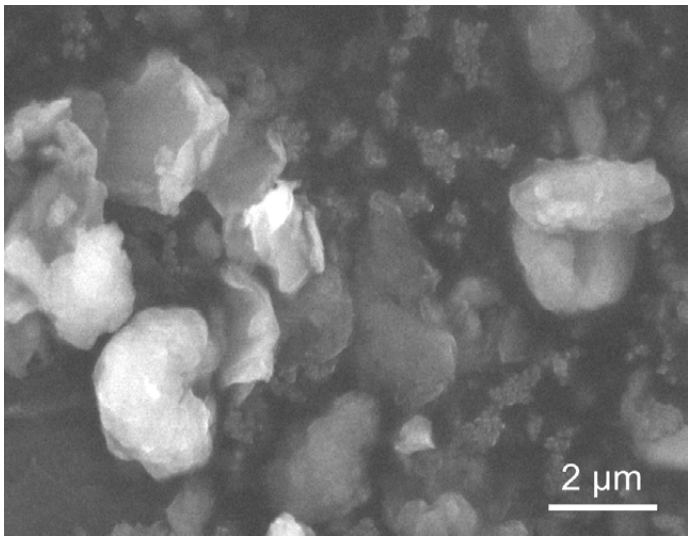

Figure 1 ESEM image.

XRF-Analysis

SiO_2	[%]	36.89
Al_2O_3	[%]	10.21
MgO	[%]	26.08
Fe_2O_3	[%]	5.14
TiO_2	[%]	0.55
MnO	[%]	0.06
Na_2O	[%]	0.00
CaO	[%]	0.57
K_2O	[%]	0.26
P_2O_5	[%]	0.02
LOI	[%]	20.2

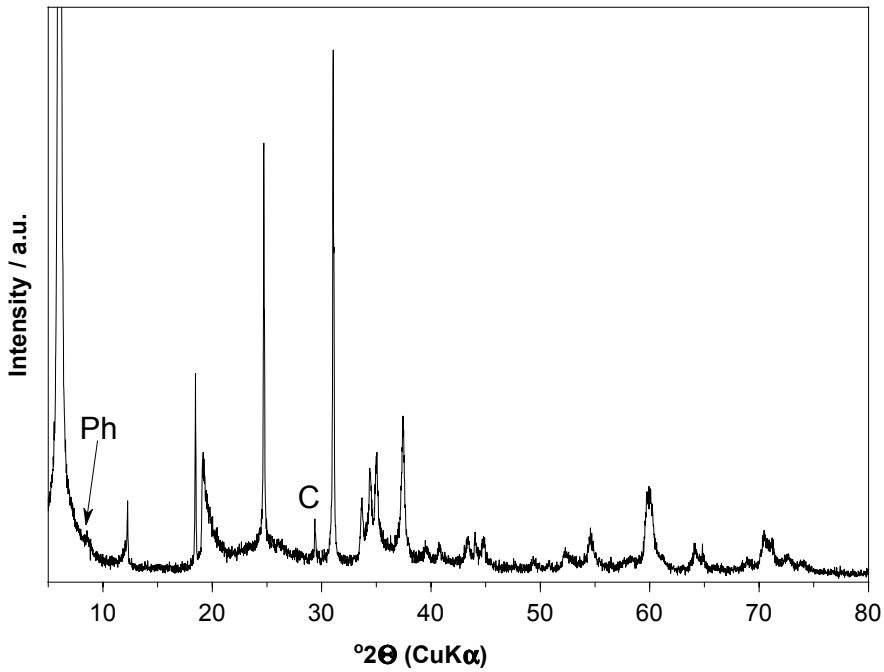

Phase	%
Vermiculite	84.0
Phlogopite	14.0
Calcite	2.0

Figure 2 X-ray diffraction analysis (powder sample).
Ph: Phlogopite; Ca: Calcite;
all not indexed peaks originated from vermiculite.

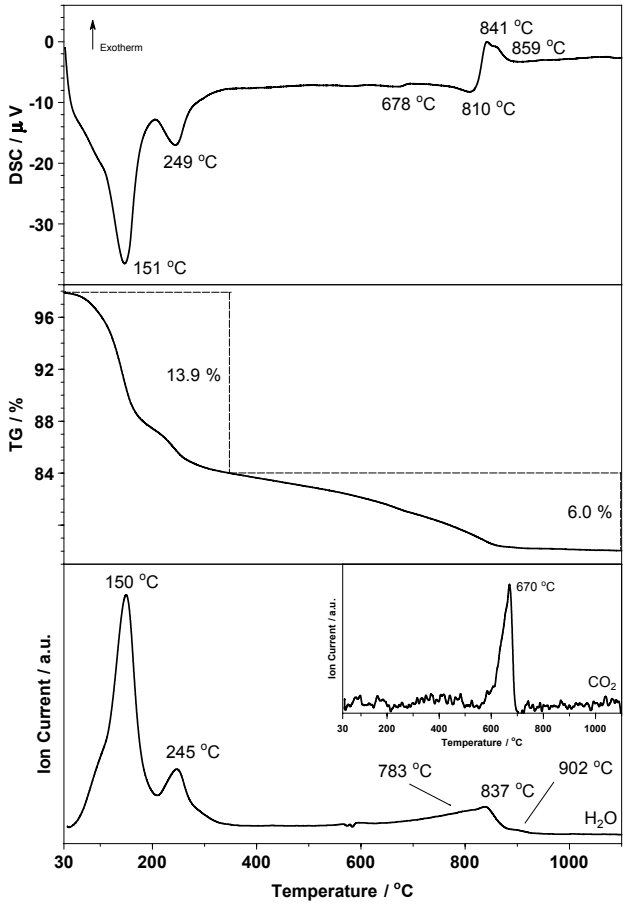

Figure 3 Simultaneous thermal analysis; starting mass of TG: 97.94%.

Grain size distribution

Fraction	%
> 63 µm	74
63 – 20 µm	5
20 – 2 µm	11
< 2 µm	10

Chemical and physical parameters

Method	Value
CEC	159 meq / 100g
ξ (n_c=12)	0.70 eq/FU
BET	36 m^2/g

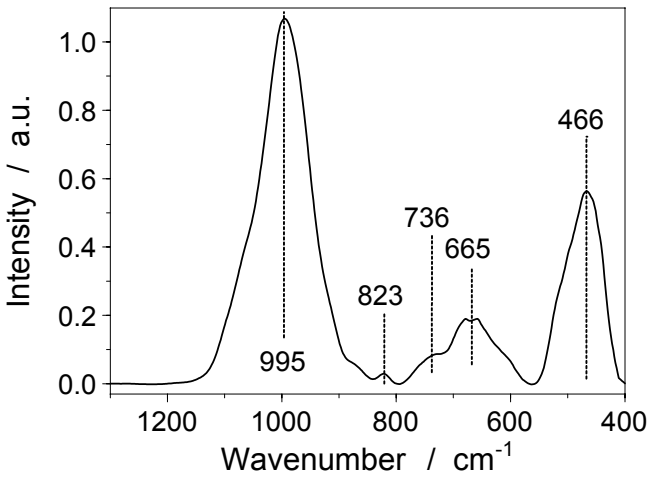

Figure 4 FTIR-spectrum.

Composition of the interlayer

Interlayer composition / FU	Na^+	Ca^{2+}	Mg^{2+}	K^+	Al^{3+}
[mol]	-	0.04	0.22	0.01	0.05

Sample: Illite (9_Illite)

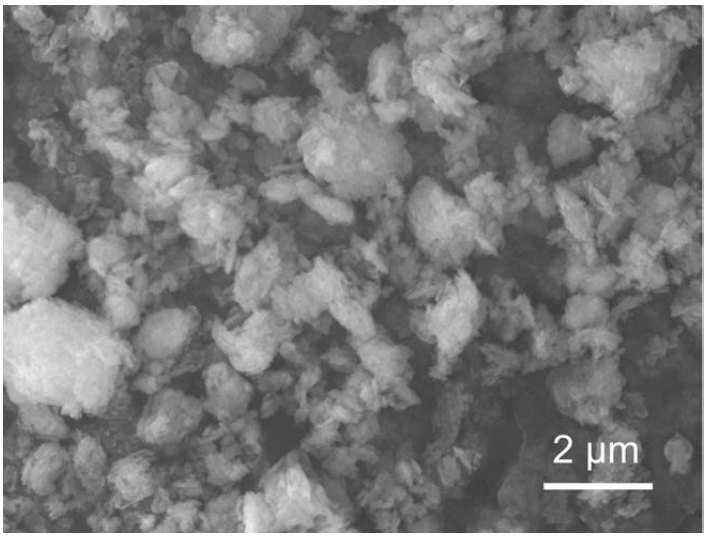

Figure 1 ESEM image.

XRF-Analysis

SiO_2	[%]	47.56
Al_2O_3	[%]	22.02
MgO	[%]	3.65
Fe_2O_3	[%]	7.93
TiO_2	[%]	0.80
MnO	[%]	0.06
Na_2O	[%]	0.00
CaO	[%]	1.46
K_2O	[%]	6.82
P_2O_5	[%]	0.41
LOI	[%]	11.1

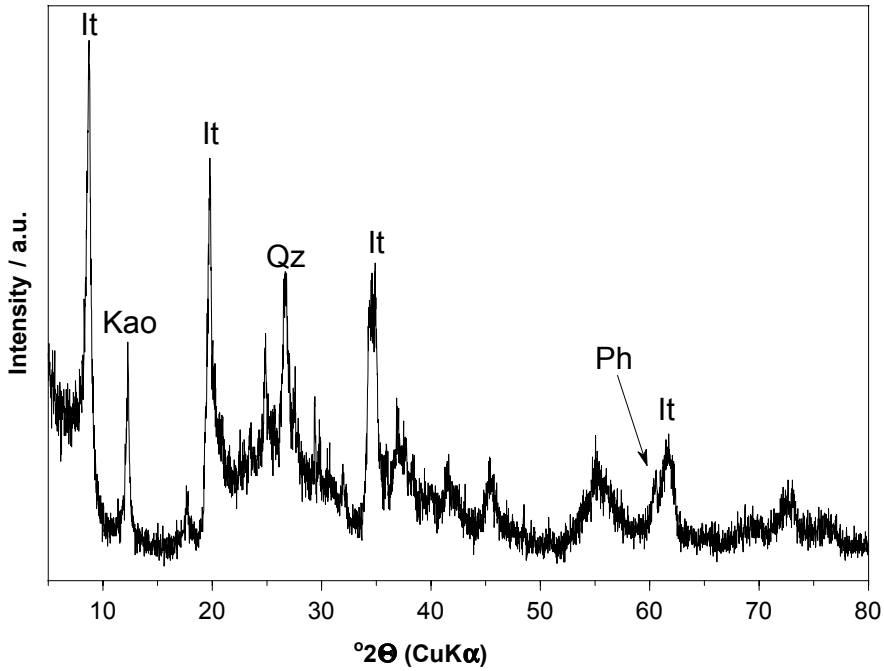

Phase	%
Illite	76.4
Phlogopite	7.8
Kaolinite	5.4
K-Feldspar (Orthoclase)	4.4
Plagioclase (Anorthite)	1.1
Quartz	0.4
Calcite	2.4
Anhydrite	1.4
Apatite	0.7

Figure 2 X-ray diffraction analysis (powder sample).
It: characteristic illite peaks with increasing 2θ (001), (002), (130), (060);
Qz: Quartz; Kao: Kaolinite; Ph: Phlogopite (060).

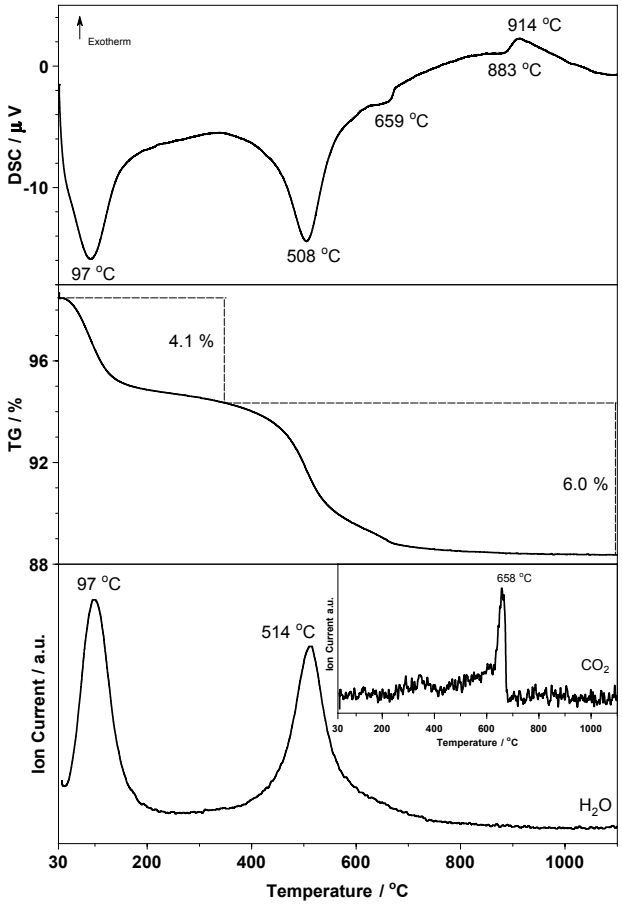

Figure 3 Simultaneous thermal analysis; starting mass of TG: 98.68%.

Grain size distribution

Fraction	%
> 63 µm	-
63 – 20 µm	6
20 – 2 µm	2
< 2 µm	92

Chemical and physical parameters

Method	Value
CEC	-
ξ (n_c=12)	-
BET	94 m^2/g

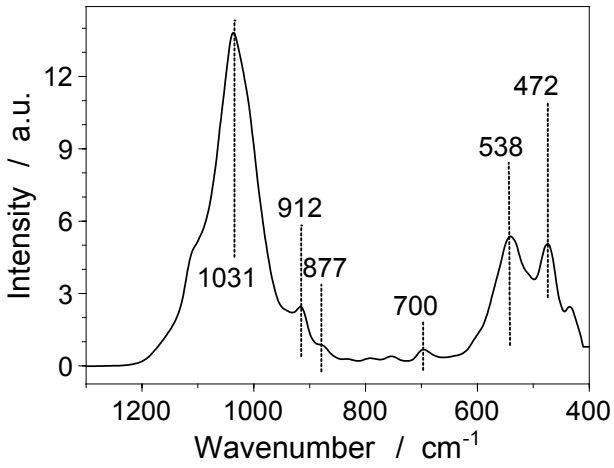

Figure 4 FTIR-spectrum.

Sample: Sepiolite PangelS9 (10_PangelS9)

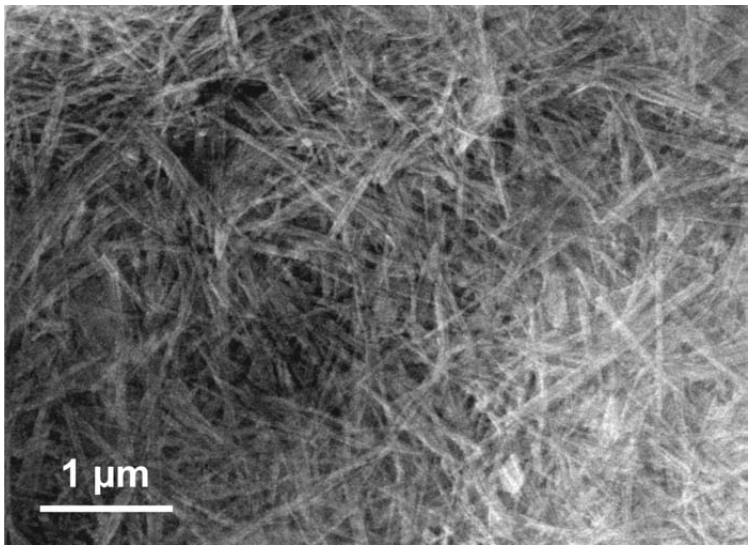

Figure 1 ESEM image.

XRF-Analysis

SiO_2	[%]	53.59
Al_2O_3	[%]	2.51
MgO	[%]	22.93
Fe_2O_3	[%]	0.81
TiO_2	[%]	0.12
MnO	[%]	0.03
Na_2O	[%]	0.09
CaO	[%]	0.34
K_2O	[%]	0.63
P_2O_5	[%]	0.05
LOI	[%]	18.9

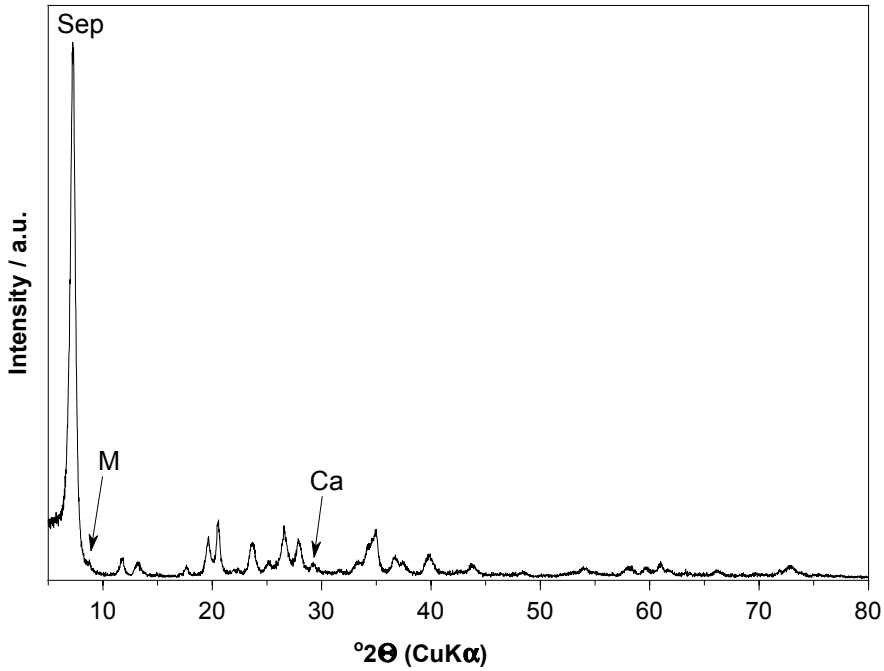

Phase	%
Sepiolite	90.7
Muscovite	8.2
Calcite	1.1

Figure 2 X-ray diffraction analysis (powder sample).
Sep: characteristic sepiolite peak (110);
M: Muscovite/Illite; Ca: Calcite.

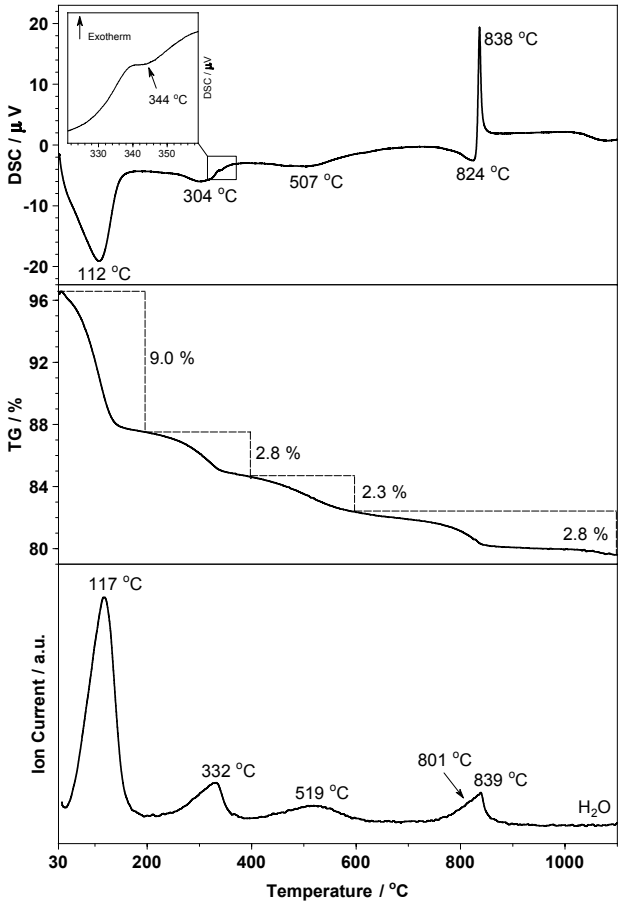

Figure 3 Simultaneous thermal analysis; starting mass of TG: 96.53%.

Grain size distribution

Fraction	%
> 63 µm	1
63 – 20 µm	1
20 – 2 µm	12
< 2 µm	86

Chemical and physical parameters

Method	Value
CEC	14 meq / 100g
ξ (n_c=12)	-
BET	300 m^2/g

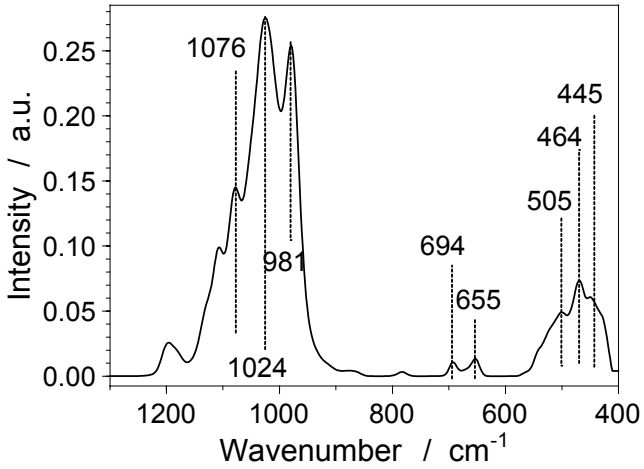

Figure 4 FTIR-spectrum

Composition of the interlayer

Interlayer composition / FU	Na^+	Ca^{2+}	Mg^{2+}	K^+
[mol]	0.01	0.045	0.035	0.01

Sample: Sepiolite Pansil (11_Pansil)

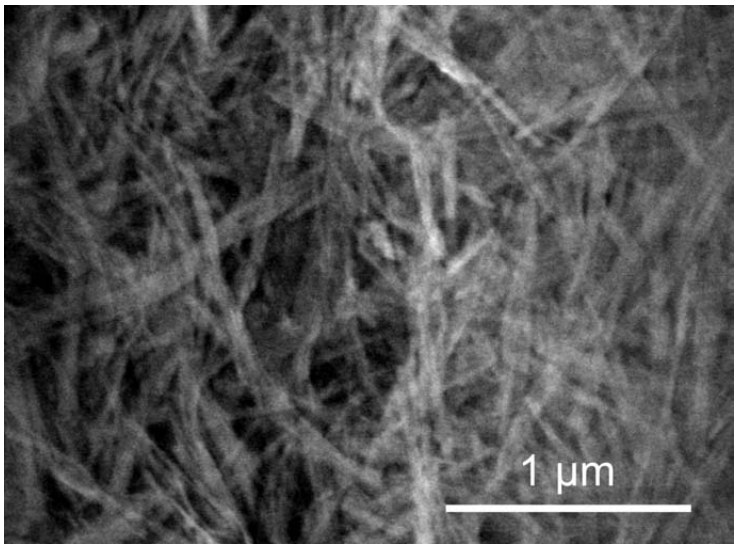

Figure 1 ESEM image.

XRF-Analysis

SiO_2	[%]	57.51
Al_2O_3	[%]	3.17
MgO	[%]	19.23
Fe_2O_3	[%]	0.59
TiO_2	[%]	0.12
MnO	[%]	0.01
Na_2O	[%]	0.36
CaO	[%]	0.90
K_2O	[%]	1.07
P_2O_5	[%]	0.04
LOI	[%]	17.0

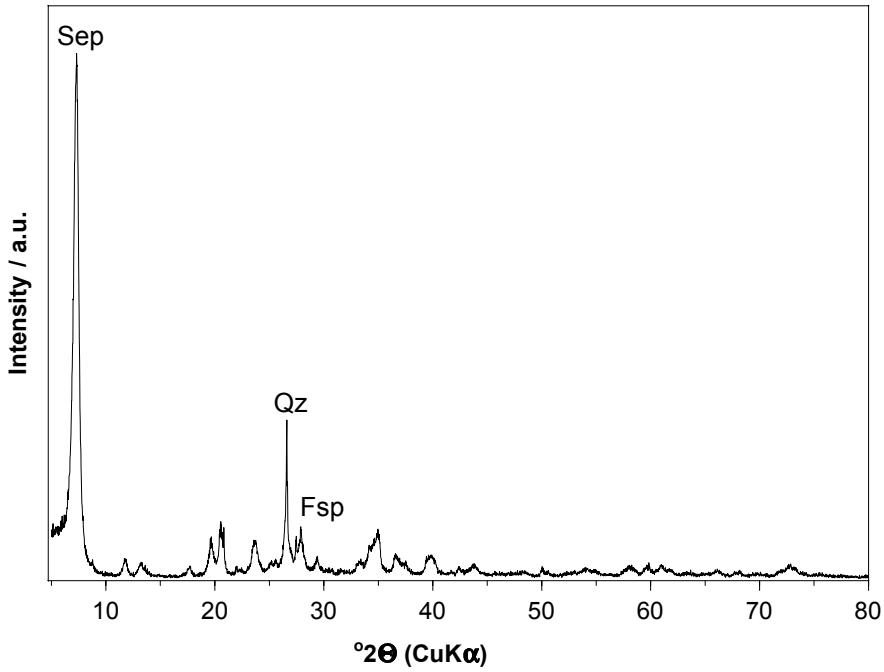

Phase	%
Sepiolite	71.6
Muscovite	8.6
K-Feldspar (Orthoclase)	6.9
Plagioclase (Albite)	7.1
Quartz	4.1
Calcite	1.7

Figure 2 X-ray diffraction analysis (powder sample)
Sep: characteristic sepiolite peak (110);
Qz: Quartz; Fsp: Feldspar

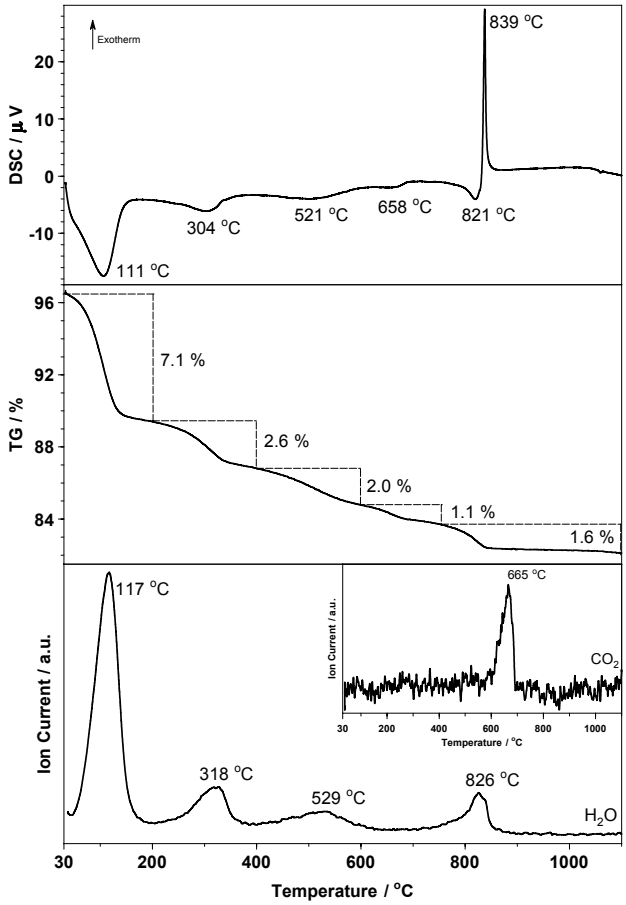

Figure 3 Simultaneous thermal analysis; starting mass of TG: 96.51%.

Grain size distribution

Fraction	%
> 63 µm	-
63 – 20 µm	1
20 – 2 µm	30
< 2 µm	69

Chemical and physical parameters

Method	Value
CEC	11 meq / 100g
ξ (n_c=12)	-
BET	261 m^2/g

Composition of the interlayer

Interlayer composition / FU	Na^+	Ca^{2+}	Mg^{2+}	K^+
[mol]	0.01	0.04	0.02	0.01

Sample: Palygorskite Smectagel (12_Palygorskite)

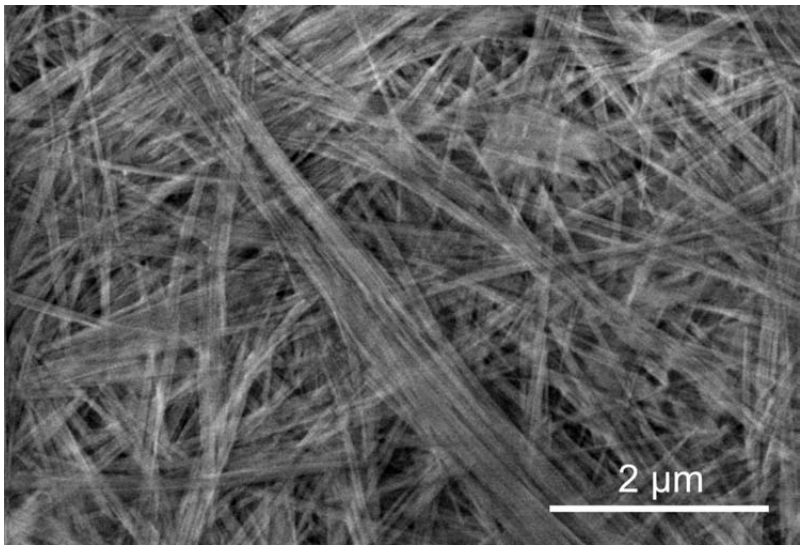

Figure 1 ESEM image.

XRF-Analysis

SiO_2	[%]	52.76
Al_2O_3	[%]	8.54
MgO	[%]	8.62
Fe_2O_3	[%]	2.79
TiO_2	[%]	0.52
MnO	[%]	0.09
Na_2O	[%]	0.12
CaO	[%]	2.83
K_2O	[%]	0.80
P_2O_5	[%]	0.02
LOI	[%]	22.9

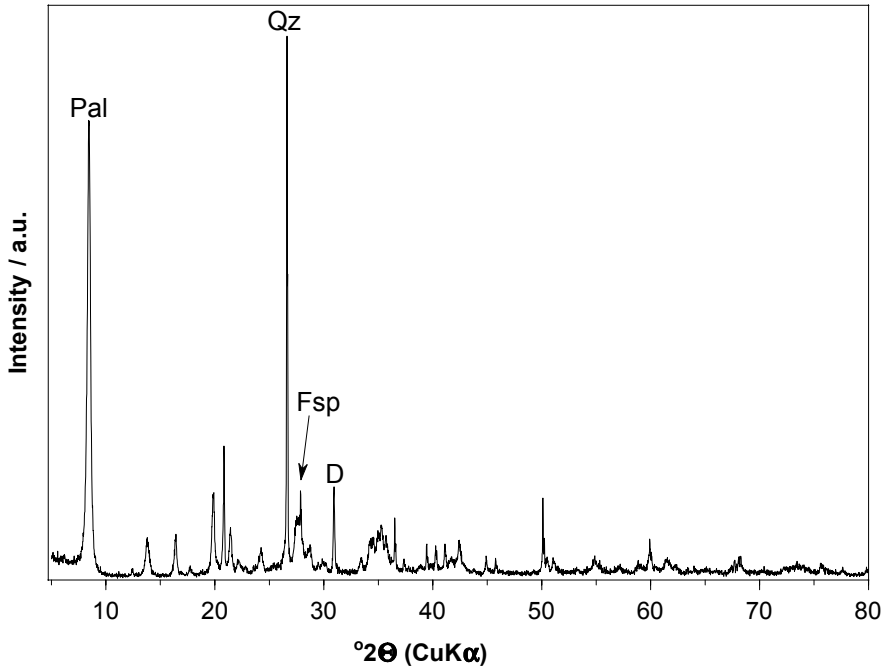

Phase	%
Palygorskite	47.0
Kaolinite	2.9
Chlorite	8.1
K-Feldspar (Orthoclase)	5.9
Quartz	22.6
Dolomite	10.5
Jarosite	3.1

Figure 2 X-ray diffraction analysis (powder sample).
Pal: characteristic palygorskite peak (110);
Qz: Quartz; Fsp: Feldspar; D: Dolomite.

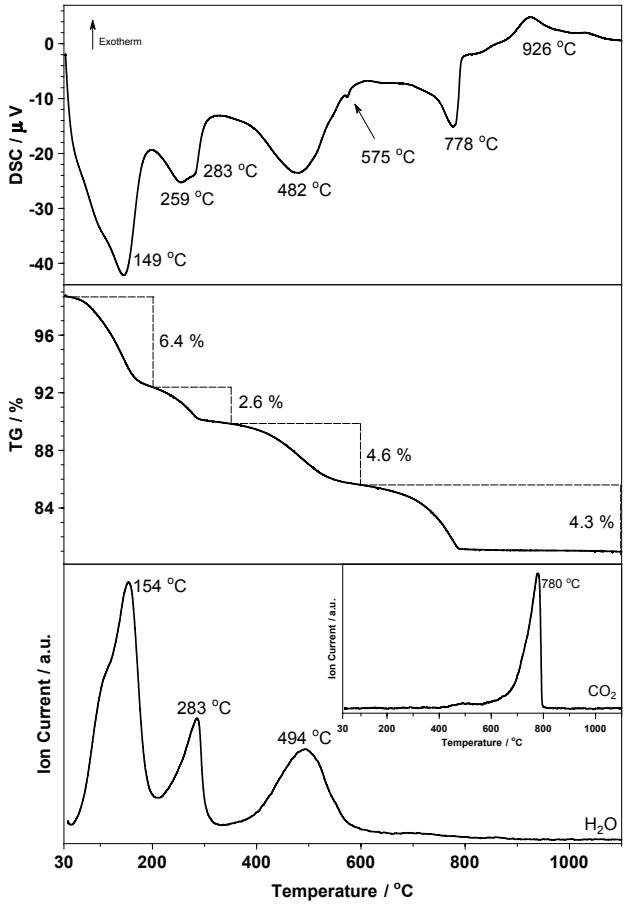

Figure 3 Simultaneous thermal analysis; starting mass of TG: 98.80%.

Grain size distribution

Fraction	%
> 63 µm	5
63 – 20 µm	13
20 – 2 µm	12
< 2 µm	71

Chemical and physical parameters

Method	Value
CEC	5 meq / 100g
ξ (n_c=12)	-
BET	321 m^2/g

Composition of the interlayer

Interlayer composition / FU	Na^+	Ca^{2+}	Mg^{2+}	K^+
[mol]	0.003	0.085	0.01	-

Sample: Kaolinite Polwhite (13_Pol)

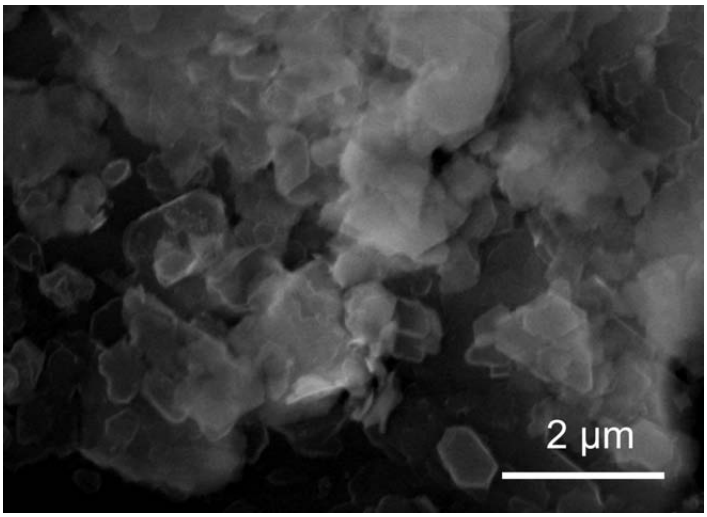

Figure 1 ESEM image.

XRF-Analysis:

SiO_2	[%]	49.72
Al_2O_3	[%]	33.85
MgO	[%]	0.30
Fe_2O_3	[%]	0.96
TiO_2	[%]	0.04
MnO	[%]	0.02
Na_2O	[%]	0.00
CaO	[%]	0.03
K_2O	[%]	3.02
P_2O_5	[%]	0.16
LOI	[%]	11.9

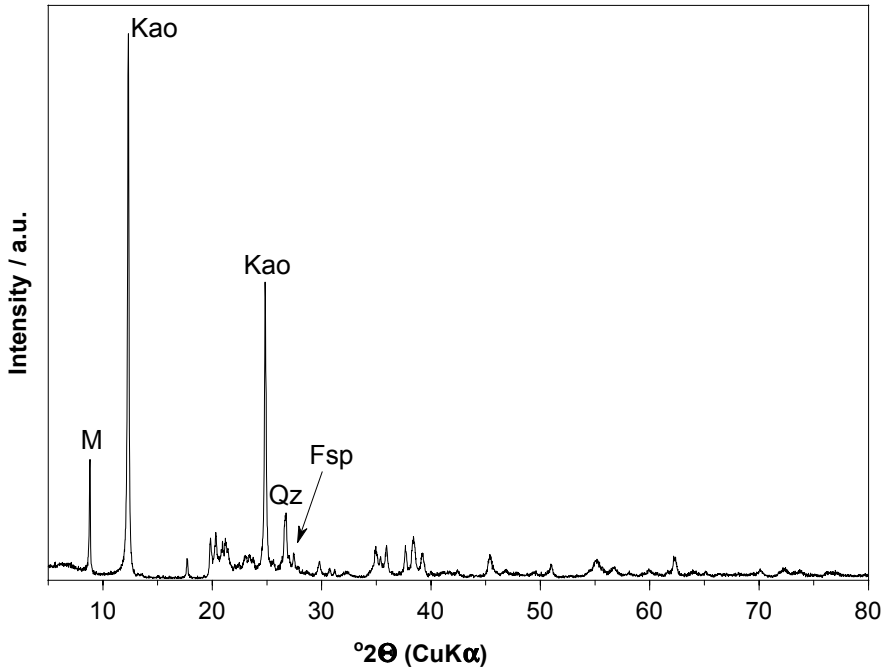

Phase	%
Kaolinite	72.2
Muscovite	8.4
Smectite	6.8
Quartz	1.7
K-Feldspar (Orthoclase)	10.5

Figure 2 X-ray diffraction analysis (powder sample)
Kao: characteristic kaolinite peaks with increasing 2θ (001), (002); Qz: Quartz; M: Muscovite/Illite.

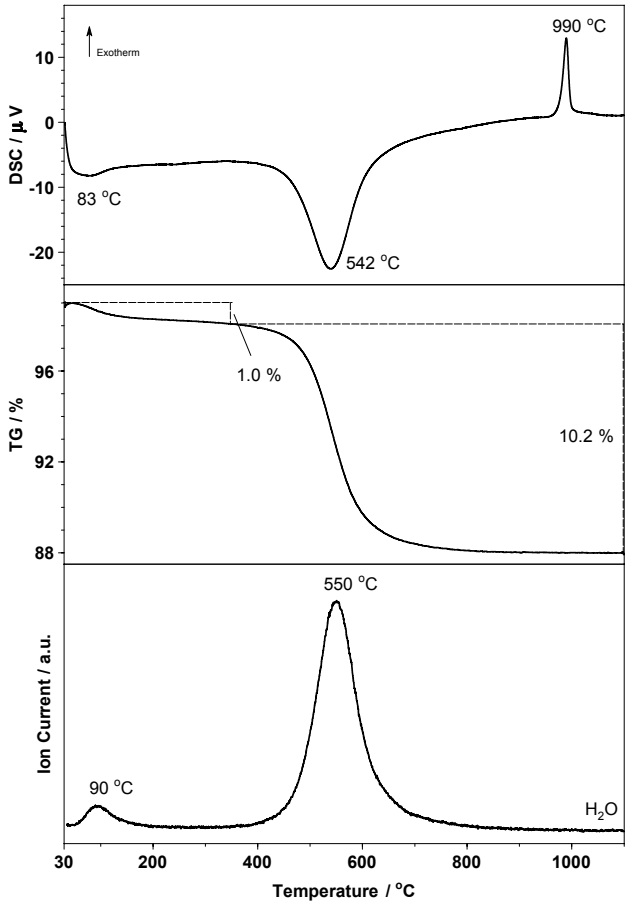

Figure 3 Simultaneous thermal analysis; starting mass of TG: 99.03%.

Grain size distribution:

Fraction	%
> 63 µm	-
63 – 20 µm	6
20 – 2 µm	55
< 2 µm	39

Chemical and physical parameters:

Method	Value
CEC	6 meq / 100g
ξ (n_c=12)	-
BET	11 m^2/g

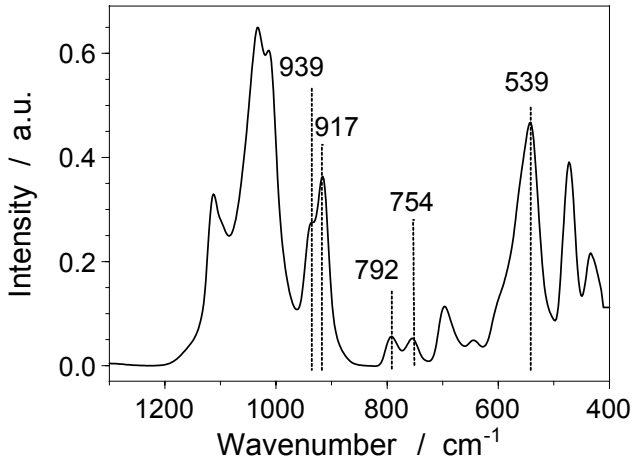

Figure 4 FTIR-spectrum.

Sample: Kaolinite Kaolex (14_Kaolex)

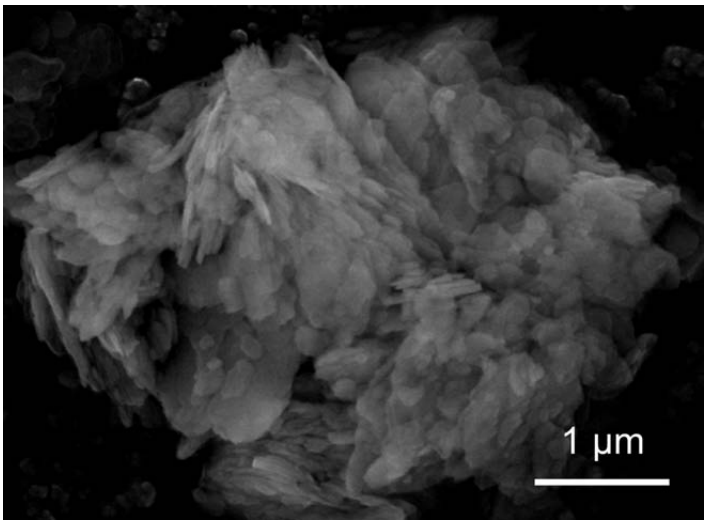

Figure 1 ESEM image.

XRF-Analysis

SiO_2	[%]	44.72
Al_2O_3	[%]	36.34
MgO	[%]	0.08
Fe_2O_3	[%]	1.58
TiO_2	[%]	1.58
MnO	[%]	0.00
Na_2O	[%]	0.00
CaO	[%]	0.00
K_2O	[%]	0.47
P_2O_5	[%]	0.10
LOI	[%]	14.2

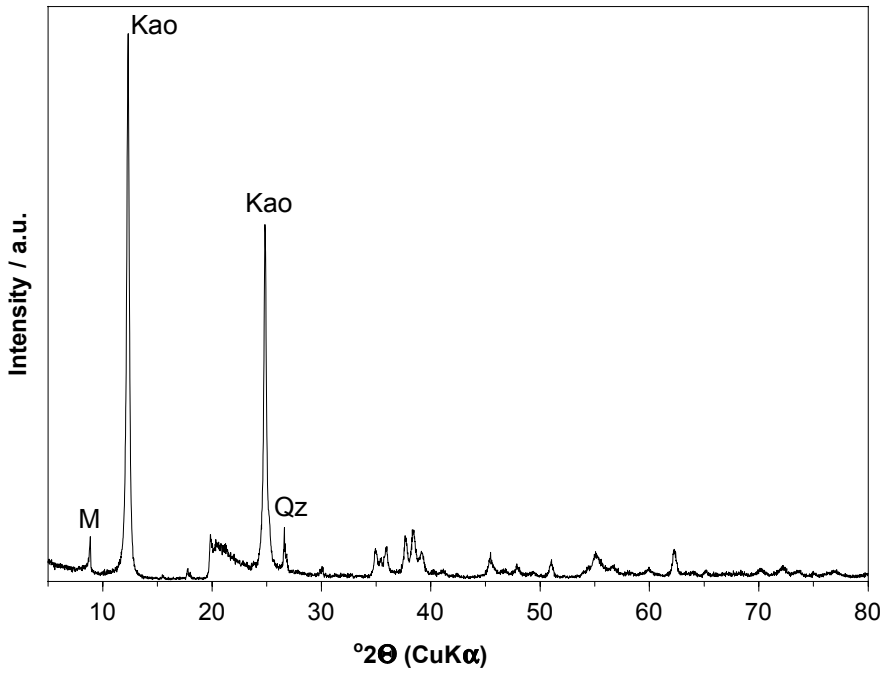

Phase	%
Kaolinite	89.9
Muscovite	7.1
Quartz	1.4
Anatase	1.6

Figure 2 X-ray diffraction analysis (powder sample).
Kao: characteristic kaolinite peaks with increasing 2θ (001), (002); Qz: Quartz; M: Muscovite/Illite.

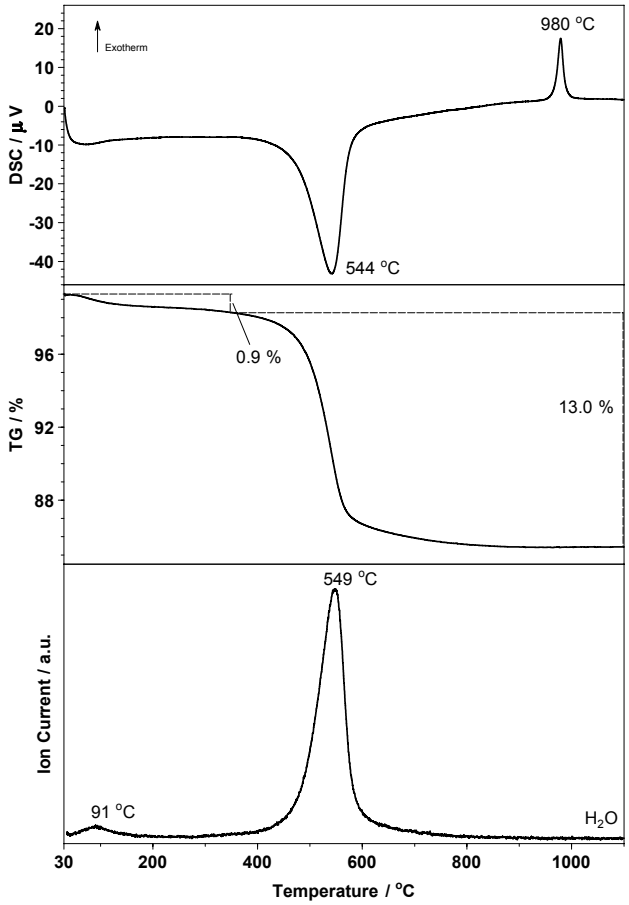

Figure 3 Simultaneous thermal analysis; starting mass of TG: 99.31%.

Grain size distribution

Fraction	%
> 63 µm	-
63 – 20 µm	-
20 – 2 µm	12
< 2 µm	88

Chemical and physical parameters

Method	Value
CEC	4 meq / 100g
ξ (n_c=12)	-
BET	24 m^2/g

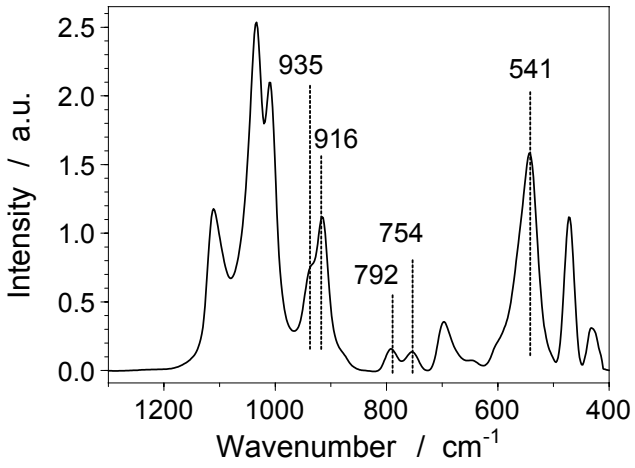

Figure 4 FTIR-spectrum.

Sample: Kaolinite Rogers (15_Rogers)

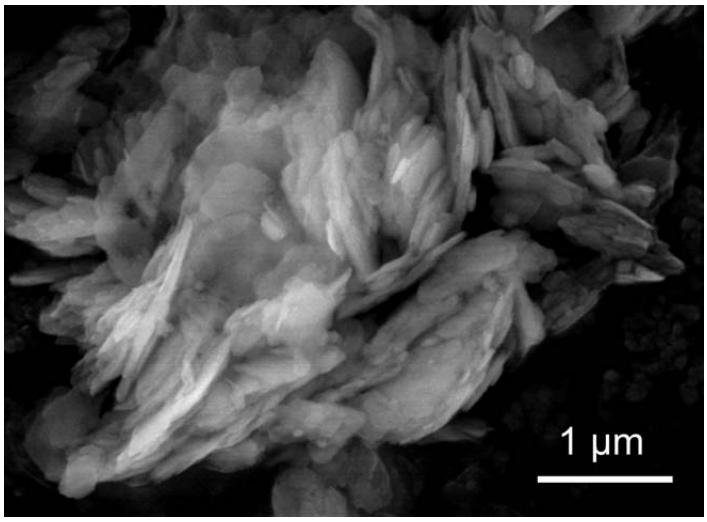

Figure 1 ESEM image.

XRF-Analysis

SiO_2	[%]	45.69
Al_2O_3	[%]	35.98
MgO	[%]	0.33
Fe_2O_3	[%]	0.97
TiO_2	[%]	1.39
MnO	[%]	0.00
Na_2O	[%]	0.00
CaO	[%]	0.16
K_2O	[%]	0.27
P_2O_5	[%]	0.07
LOI	[%]	15.1

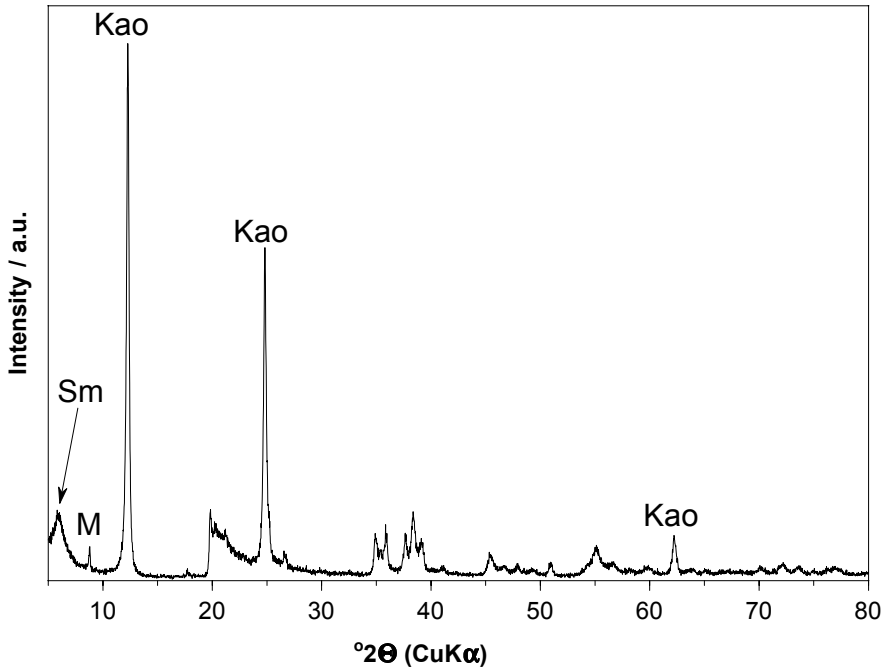

Phase	%
Kaolinite	84.4
Muscovite	3.5
Smectite	10.7
Anatase	1.4

Figure 2 X-ray diffraction analysis (powder sample).
Kao: characteristic kaolinite peaks with increasing 2θ (001), (002), (060); Qz: Quartz; M: Muscovite/Illite; Sm: Smectite.

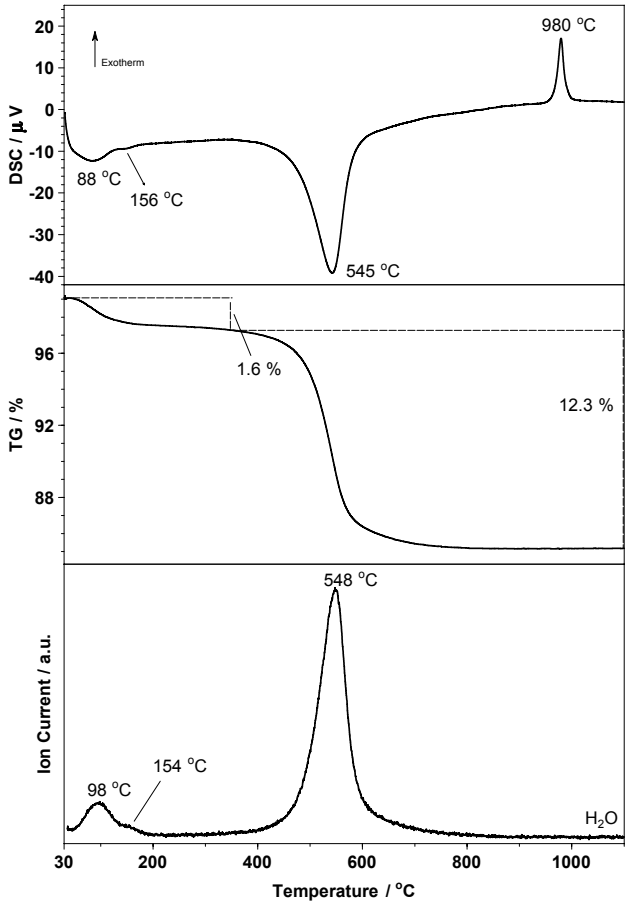

Figure 3 Simultaneous thermal analysis; starting mass of TG: 99.18%.

Grain size distribution

Fraction	%
> 63 µm	-
63 – 20 µm	-
20 – 2 µm	14
< 2 µm	86

Chemical and physical parameters

Method	Value
CEC	10 meq / 100g
BET	24 m^2/g

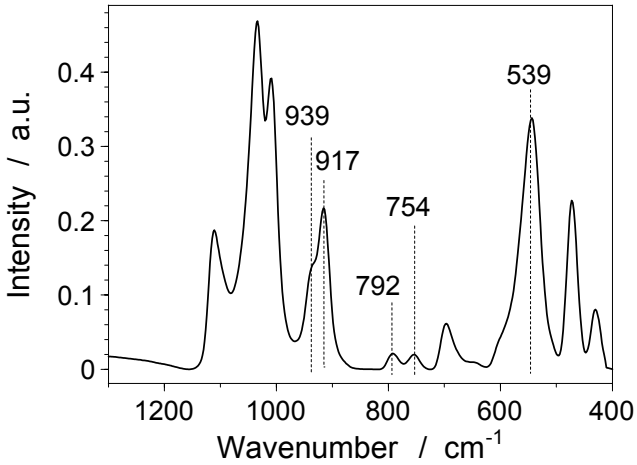

Figure 4 FTIR-spectrum.

Sample: Magadiite (16_Mag)

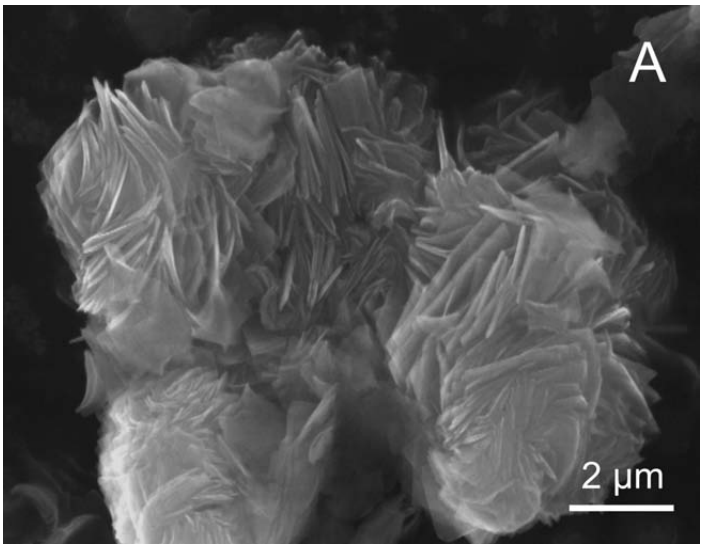

Figure 1 ESEM image.

XRF-Analysis

SiO_2	[%]	77.91
Al_2O_3	[%]	0.36
MgO	[%]	0.00
Fe_2O_3	[%]	0.20
TiO_2	[%]	0.03
MnO	[%]	0.00
Na_2O	[%]	6.09
CaO	[%]	0.00
K_2O	[%]	0.02
P_2O_5	[%]	0.00
LOI	[%]	15.4

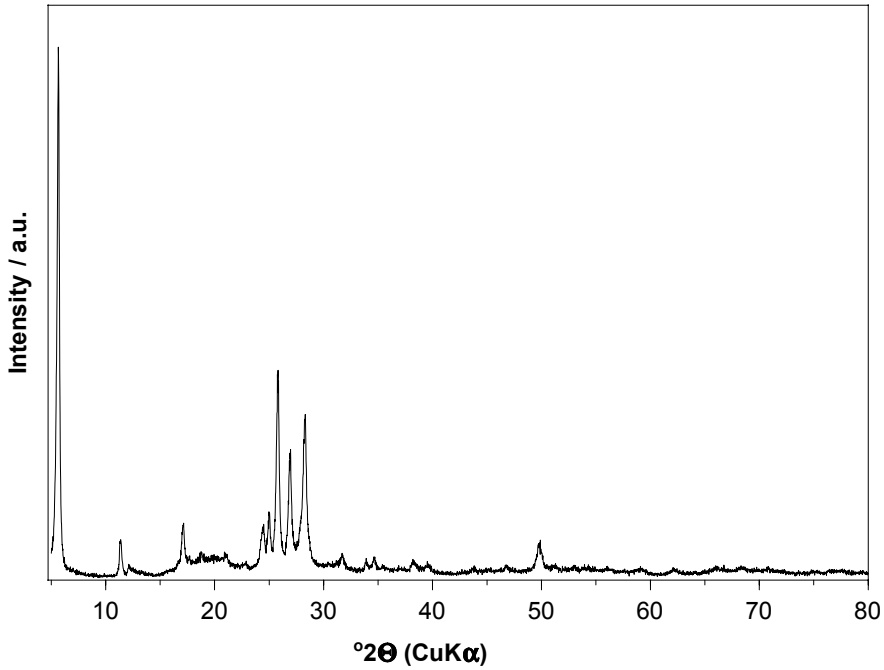

Phase	%
Magadiite	100.0

Figure 2 X-ray diffraction analysis (powder sample).
All peaks originated from magadiite.

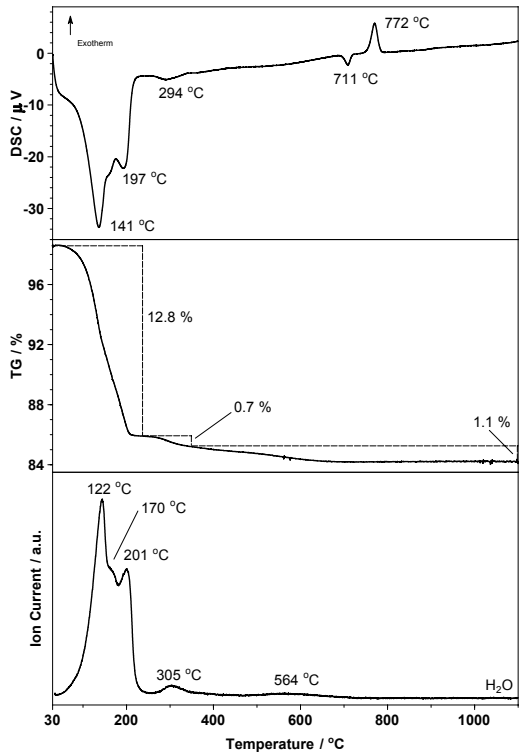

Figure 3 Simultaneous thermal analysis; starting mass of TG: 98.68%.

Chemical and physical parameters

Method	Value
CEC	53 meq / 100g
ξ (n_c=12)	-
BET	30 m^2/g

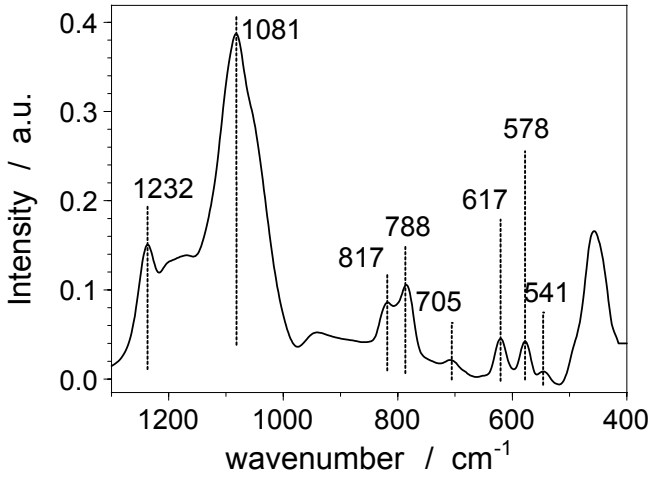

Figure 4 FTIR-spectrum.

Appendix

2 Data sheets “Mineralogical characterisation”

2.2 Fraction < 2 µm and < 0.2 µm

Sample: Calcigel < 2 µm

$$Me^{+}_{0.26}(Si_{3.84}Al^{3+}_{0.16})(Al^{3+}_{1.38}Fe^{3+}_{0.30}Mg^{2+}_{0.43})[O_{10}(OH)_2]$$

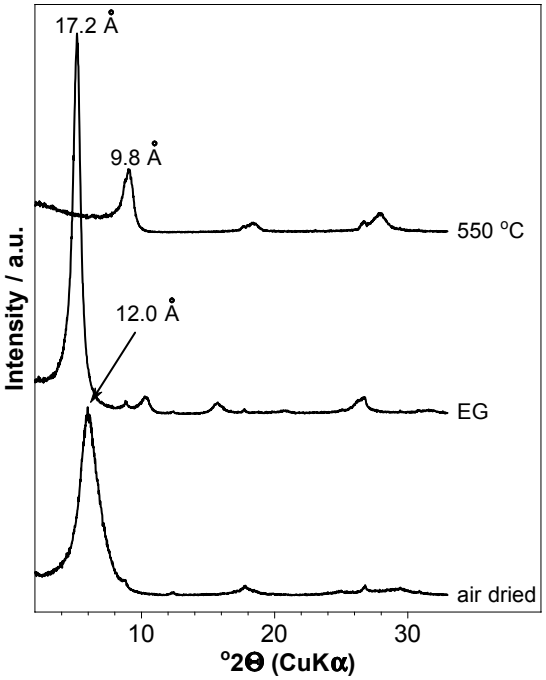

Figure 1 X-ray pattern (texture sample).

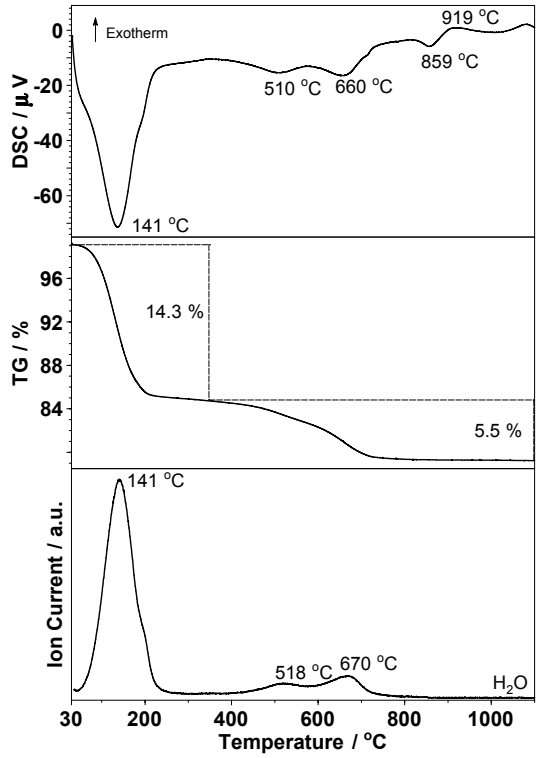

Figure 2 Simultaneous thermal analysis; starting mass of TG: 99.22%.

Basal spacing

d(00l)	air dried [Å]	EG [Å]
d(001)	14.7	17.1
d(002)		8.6
d(003)	4.9	5.6
d(004)		
d(005)	3.3	3.5
d(006)		

Interlayer composition

Interlayer composition / FU	mol
Na^+	0.05
Ca^{2+}	0.085
Mg^{2+}	0.04
K^+	0.01

Layer charge and exchange capacity

Measured		Calculated	
n_c = 12	Cu-trien	Köster (1977)	
ξ [eq/FU]	CEC [meq/100g]	ξ [eq/Fu]	CEC [meq/100g]
0.31	88	0.26	83

Charge location according to Köster (1977)

Charge location [eq/FU]		Tetrahedral charge [%]
tetrahedral	octahedral	
0.16	0.10	62

Sample: EXM757 < 2 µm

$$Me^{+}_{0.32}(Si_{3.95}Al^{3+}_{0.05})(Al^{3+}_{1.53}Fe^{3+}_{0.22}Mg^{2+}_{0.24})[O_{10}(OH)_2]$$

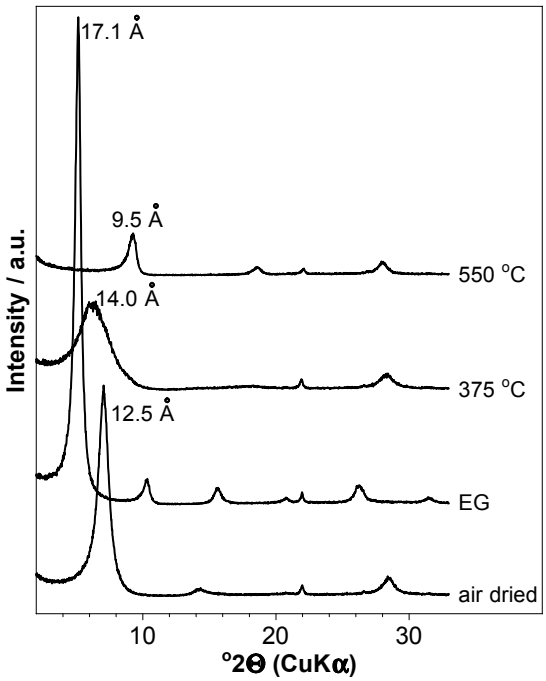

Figure 1 X-ray pattern (texture sample).

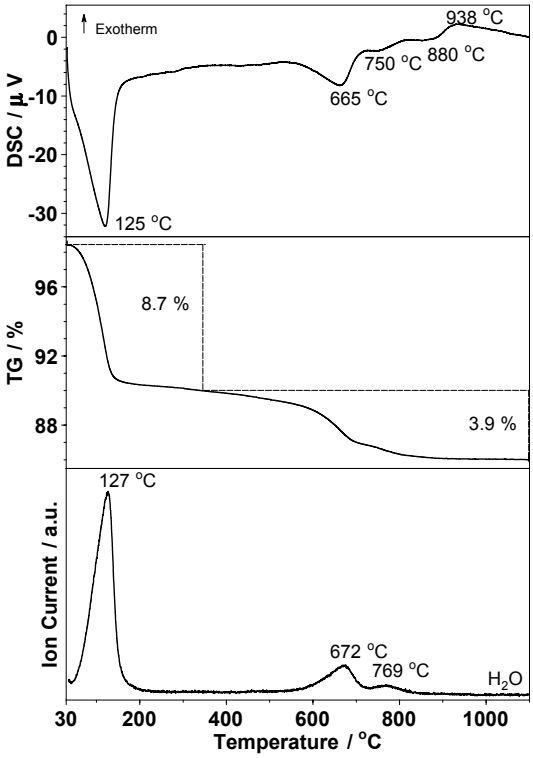

Figure 2 Simultaneous thermal analysis; starting mass of TG: 98.65%.

Basal spacing

d(00l)	air dried [Å]	EG [Å]
d(001)	12.5	17.2
d(002)	6.2	8.6
d(003)		5.7
d(004)	3.13	4.3
d(005)		3.4
d(006)		2.85

Interlayer composition

Interlayer composition / FU	mol
Na^{+}	0.26
Ca^{2+}	0.02
Mg^{2+}	-
K^{+}	-

Layer charge and exchange capacity

Measured		Calculated	
n_c = 12	Cu-trien	Köster (1977)	
ξ [eq/FU]	CEC [meq/100g]	ξ [eq/Fu]	CEC [meq/100g]
0.30	84	0.32	81

Charge location according to Köster (1977)

Charge location [eq/FU]		Tetrahedral charge [%]
tetrahedral	octahedral	
0.05	0.27	16

Sample: SWy-2 < 0.2 µm

$$Me^{+}_{0.29}(Si_{3.79}Al^{3+}_{0.21})(Al^{3+}_{1.53}Fe^{3+}_{0.23}Mg^{2+}_{0.32})[O_{10}(OH)_2]$$

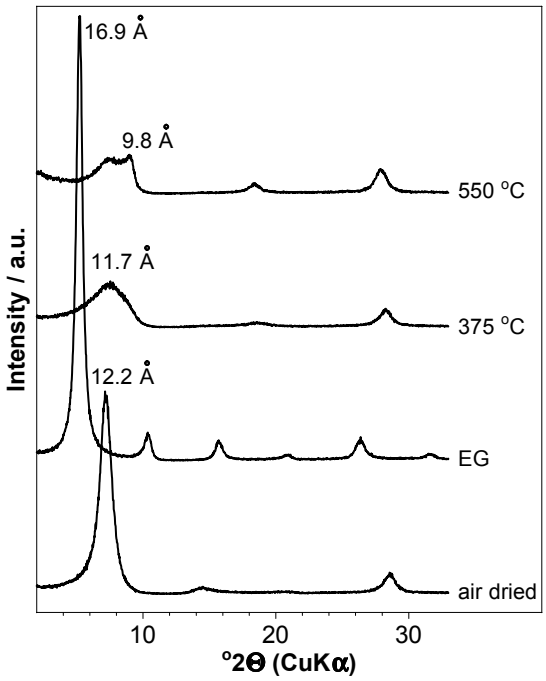

Figure 1 X-ray pattern (texture sample).

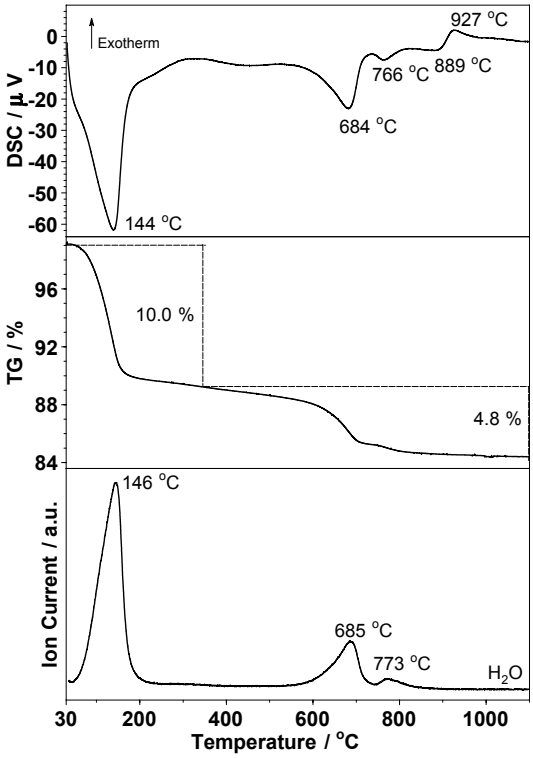

Figure 2 Simultaneous thermal analysis; starting mass of TG: 99.23%.

Basal spacing

d(00l)	air dried [Å]	EG [Å]
d(001)	12.3	16.9
d(002)	6.15	8.5
d(003)		5.6
d(004)	3.1	4.3
d(005)		3.4
d(006)		2.8

Layer charge and exchange capacity

Measured		Calculated	
n_c = 12	Cu-trien	Köster (1977)	
ξ [eq/FU]	CEC [meq/100g]	ξ [eq/Fu]	CEC [meq/100g]
0.31	91	0.29	83

Interlayer composition

Interlayer composition / FU	mol
Na^+	0.21
Ca^{2+}	0.025
Mg^{2+}	0.015
K^+	0.01

Charge location according to Köster (1977)

Charge location [eq/FU]		Tetrahedral charge [%]
tetrahedral	octahedral	
0.21	0.08	72

Sample: Volclay < 2 µm

$$Me^{+}_{0.28}(Si_{3.97}Al^{3+}_{0.03})(Al^{3+}_{1.58}Fe^{3+}_{0.19}Mg^{2+}_{0.22})[O_{10}(OH)_2]$$

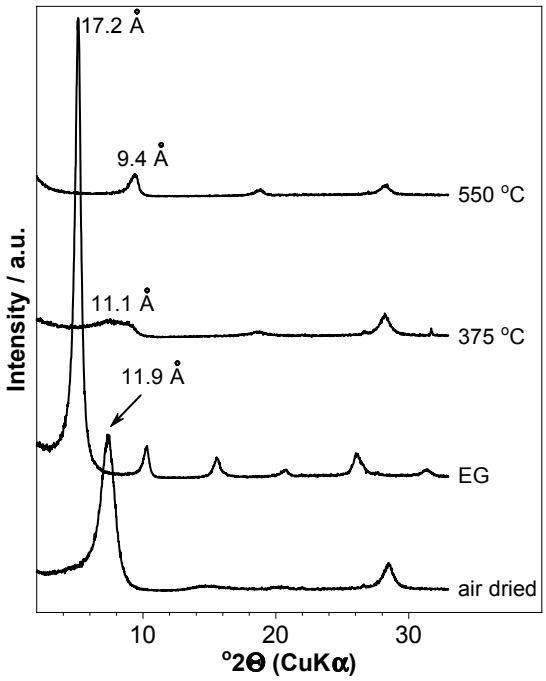

Figure 1 X-ray pattern (texture sample).

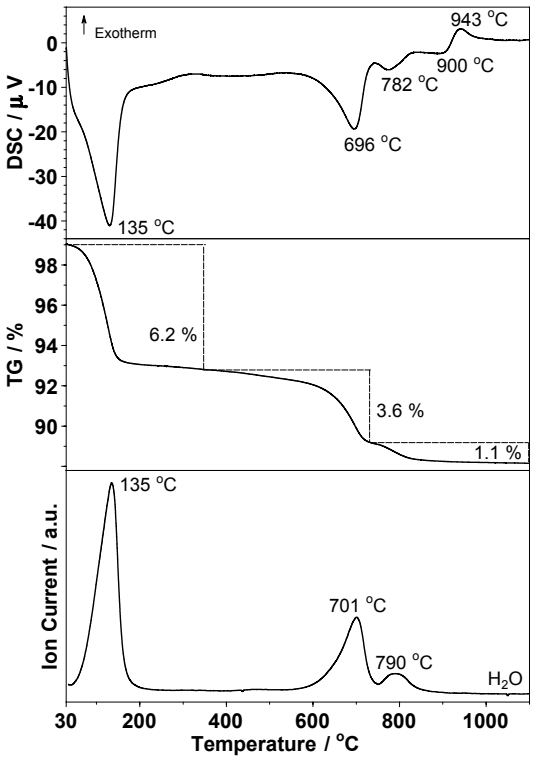

Figure 2 Simultaneous thermal analysis; starting mass of TG: 99.04%.

Basal spacing

d(00l)	air dried [Å]	EG [Å]
d(001)	11.9	17.2
d(002)		8.6
d(003)		5.6
d(004)	3.1	4.3
d(005)		3.4
d(006)		2.8

Interlayer composition

Interlayer composition / FU	mol
Na^+	0.26
Ca^{2+}	-
Mg^{2+}	-
K^+	-

Layer charge and exchange capacity

Measured		Calculated	
n_c = 12	Cu-trien	Köster (1977)	
ξ [eq/FU]	CEC [meq/100g]	ξ [eq/Fu]	CEC [meq/100g]
0.26	85	0.28	70

Charge location according to Köster (1977)

Charge location [eq/FU]		Tetrahedral charge [%]
tetrahedral	octahedral	
0.03	0.25	11

Sample: Volclay < 0.2 µm

$$Me^{+}_{0.25}(Si_{3.95}Al^{3+}_{0.05})(Al^{3+}_{1.58}Fe^{3+}_{0.20}Mg^{2+}_{0.23})[O_{10}(OH)_2]$$

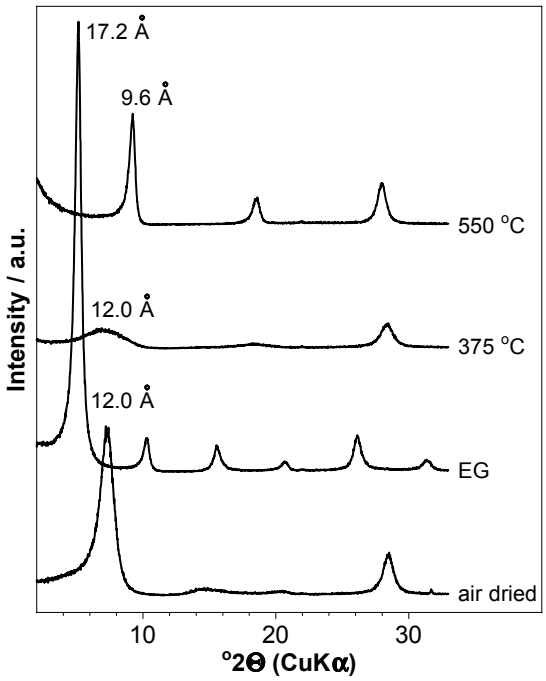

Figure 1 X-ray pattern (texture sample).

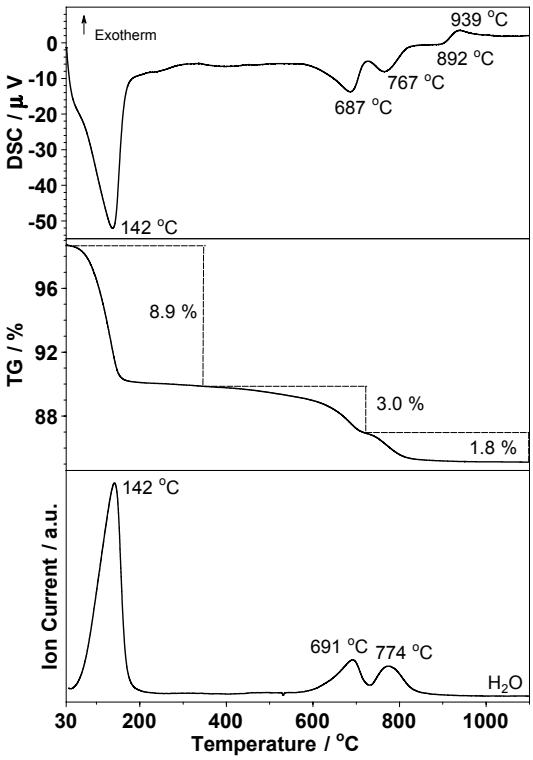

Figure 2 Simultaneous thermal analysis; starting mass of TG: 98.76%.

Basal spacing

d(00l)	air dried [Å]	EG [Å]
d(001)	12.1	17.2
d(002)		8.6
d(003)		5.6
d(004)	3.1	4.3
d(005)		3.4
d(006)		2.85

Interlayer composition

Interlayer composition / FU	mol
Na^+	0.26
Ca^{2+}	-
Mg^{2+}	-
K^+	-

Layer charge and exchange capacity

Measured		Calculated	
n_c = 12	Cu-trien	Köster (1977)	
ξ [eq/FU]	CEC [meq/100g]	ξ [eq/Fu]	CEC [meq/100g]
0.26	90	0.25	70

Charge location according to Köster (1977)

Charge location [eq/FU]		Tetrahedral charge [%]
tetrahedral	octahedral	
0.05	0.20	20

Sample: WYO < 2 µm

$$Me^{+}_{0.28}(Si_{3.89}Al^{3+}_{0.11})(Al^{3+}_{1.53}Fe^{3+}_{0.26}Mg^{2+}_{0.23})[O_{10}(OH)_2]$$

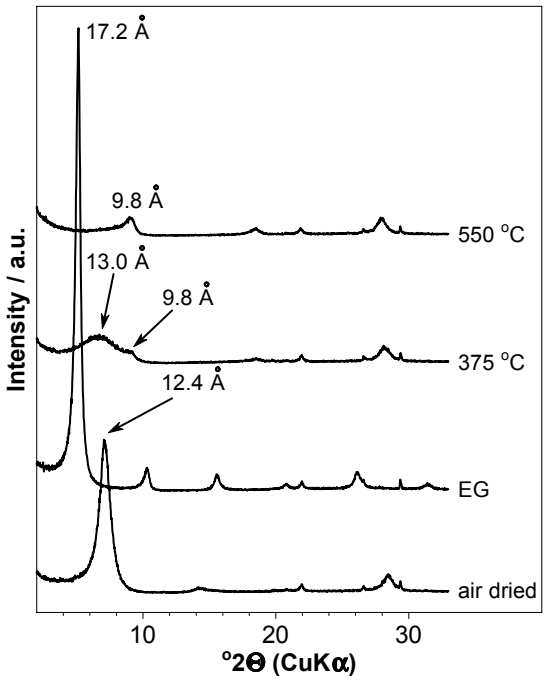

Figure 1 X-ray pattern (texture sample).

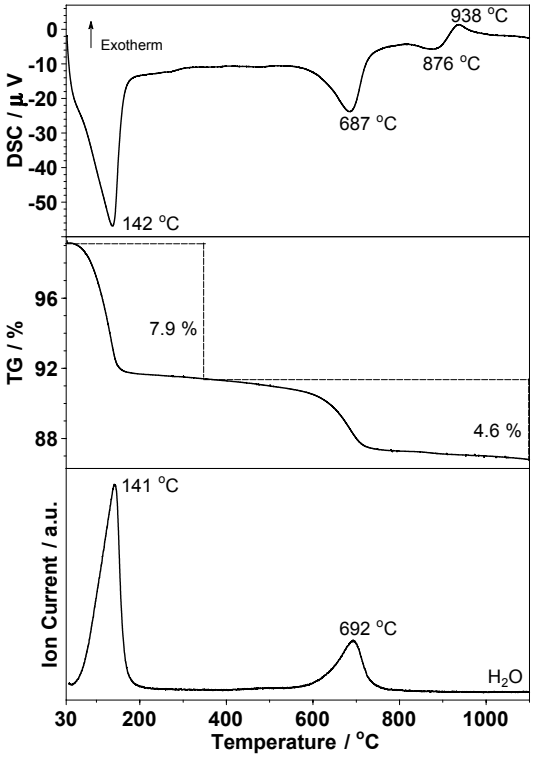

Figure 2 Simultaneous thermal analysis; starting mass of TG: 99.27%.

Basal spacing

d(00l)	air dried [Å]	EG [Å]
d(001)	12.4	17.2
d(002)	6.2	8.6
d(003)		5.6
d(004)	3.1	4.3
d(005)		3.4
d(006)		2.8

Interlayer composition

Interlayer composition / FU	mol
Na^{+}	0.20
Ca^{2+}	0.035
Mg^{2+}	0.005
K^{+}	-

Layer charge and exchange capacity

Measured		Calculated	
n_c = 12	Cu-trien	Köster (1977)	
ξ [eq/FU]	CEC [meq/100g]	ξ [eq/Fu]	CEC [meq/100g]
0.27	80	0.28	73

Charge location according to Köster (1977)

Charge location [eq/FU]		Tetrahedral charge [%]
tetrahedral	octahedral	
0.11	0.17	39

Sample: Indian Bentonite < 2 µm

$$Me^{+}_{0.33}(Si_{3.69}Al^{3+}_{0.31})(Al^{3+}_{1.29}Fe^{3+}_{0.53}Mg^{2+}_{0.26})[O_{10}(OH)_2]$$

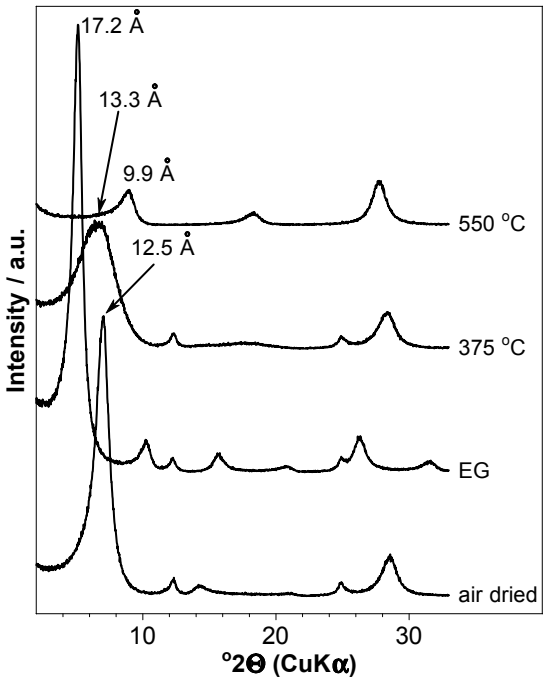

Figure 1 X-ray pattern (texture sample).

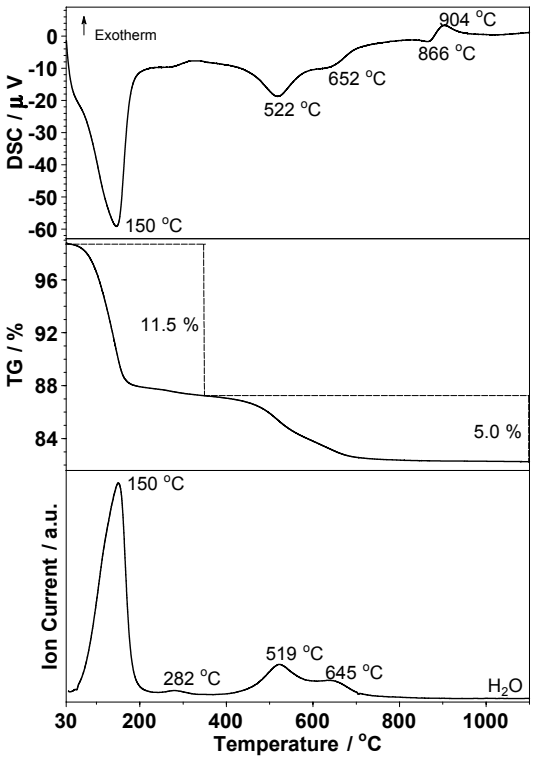

Figure 2 Simultaneous thermal analysis; starting mass of TG: 98.78%.

Basal spacing

d(00l)	air dried [Å]	EG [Å]
d(001)	12.4	16.8
d(002)	6.2	8.4
d(003)		5.6
d(004)	3.1	4.2
d(005)		3.4
d(006)		2.8

Interlayer composition

Interlayer composition / FU	mol
Na^{+}	0.33
Ca^{2+}	-
Mg^{2+}	-
K^{+}	-

Layer charge and exchange capacity

Measured		Calculated	
n_c = 12	Cu-trien	Köster (1977)	
ξ [eq/FU]	CEC [meq/100g]	ξ [eq/Fu]	CEC [meq/100g]
0.33	96	0.33	86

Charge location according to Köster (1977)

Charge location [eq/FU]		Tetrahedral charge [%]
tetrahedral	octahedral	
0.31	0.02	94

Sample: Indian Bentonite < 0.2 µm

$$Me^{+}_{0.34}(Si_{3.71}Al^{3+}_{0.29})(Al^{3+}_{1.32}Fe^{3+}_{0.49}Mg^{2+}_{0.26})[O_{10}(OH)_2]$$

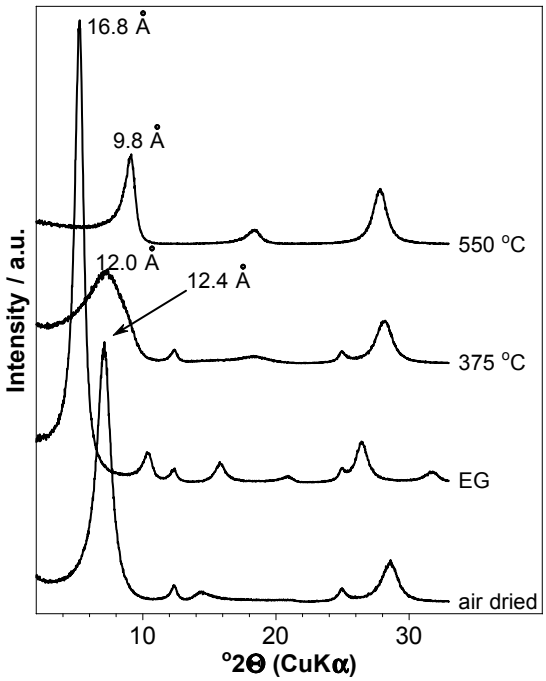

Figure 1 X-ray pattern (texture sample).

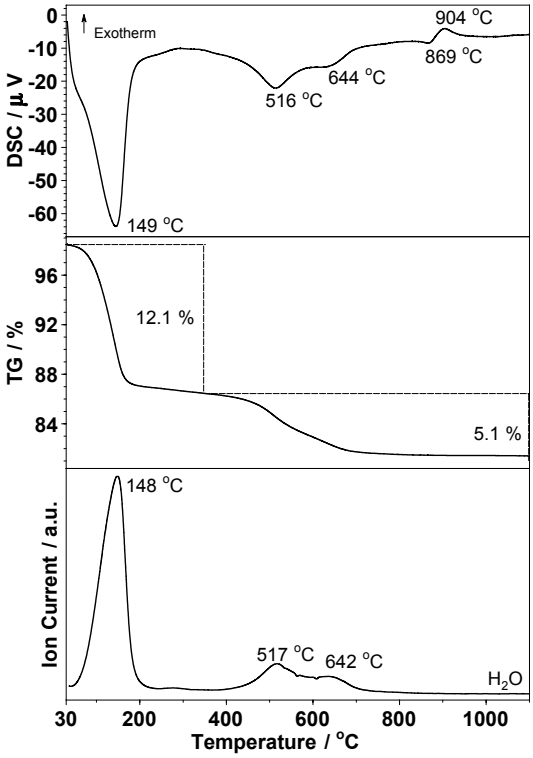

Figure 2 Simultaneous thermal analysis; starting mass of TG: 98.54%.

Basal spacing

d(00l)	air dried [Å]	EG [Å]
d(001)	12.6	17.2
d(002)	6.2	8.6
d(003)		5.6
d(004)	3.1	4.3
d(005)		3.4
d(006)		2.85

Interlayer composition

Interlayer composition / FU	mol
Na^{+}	0.33
Ca^{2+}	-
Mg^{2+}	-
K^{+}	-

Layer charge and exchange capacity

Measured		Calculated	
n_c = 12	Cu-trien	Köster (1977)	
ξ [eq/FU]	CEC [meq/100g]	ξ [eq/Fu]	CEC [meq/100g]
0.33	98	0.34	86

Charge location according to Köster (1977)

Charge location [eq/FU]		Tetrahedral charge [%]
tetrahedral	octahedral	
0.29	0.05	85

Sample: Natural Hectorite < 2 µm

$$Me^{+}_{0.26}(Si_{3.90}Al^{3+}_{0.10})(Mg^{2+}_{2.64}Li^{+}_{0.29}Al^{3+}_{0.05}Fe^{3+}_{0.04})[O_{10}(OH)_2]$$

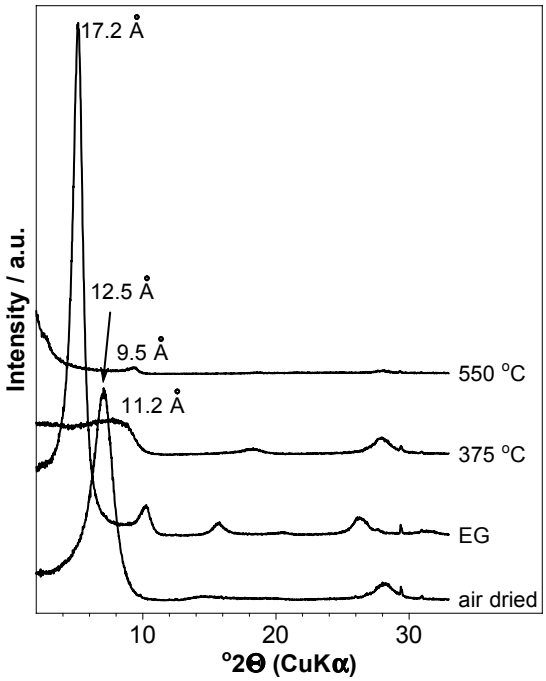

Figure 1 X-ray pattern (texture sample).

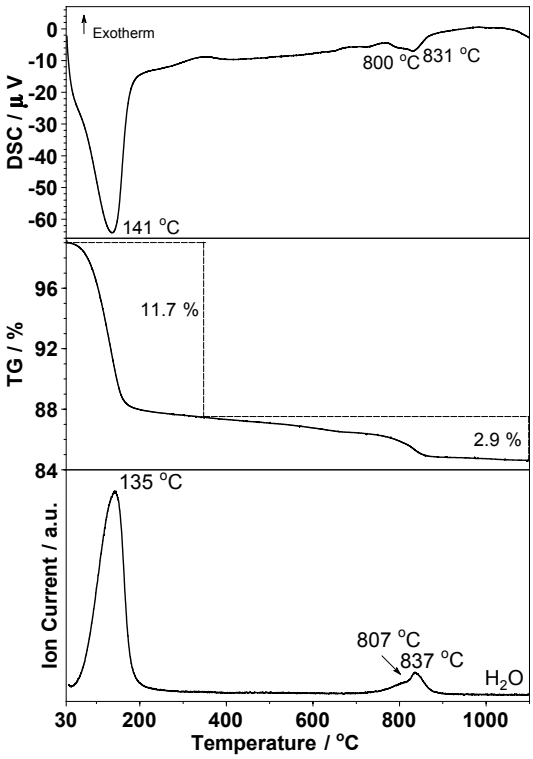

Figure 2 Simultaneous thermal analysis; starting mass of TG: 99.13%.

Basal spacing

d(00l)	air dried [Å]	EG [Å]
d(001)	12.5	17.2
d(002)		8.6
d(003)		5.6
d(004)	3.2	
d(005)		3.4
d(006)		

Interlayer composition

Interlayer composition / FU	mol
Na^+	0.24
Ca^{2+}	0.01
Mg^{2+}	0.005
K^+	-

Layer charge and exchange capacity

Measured		Calculated	
n_c = 12	Cu-trien	Köster (1977)	
ξ [eq/FU]	CEC [meq/100g]	ξ [eq/Fu]	CEC [meq/100g]
0.27	90	0.26	71

Charge location according to Köster (1977)

Charge location [eq/FU]		Tetrahedral charge [%]
tetrahedral	octahedral	
0.10	0.16	38

Sample: Vermiculite < 2 µm

$$Me^{+}_{0.70}(Si_{3.04}Al^{3+}_{0.96})(Mg^{2+}_{2.65}Fe^{3+}_{0.31}Al^{3+}_{0.01})[O_{10}(OH)_2]$$

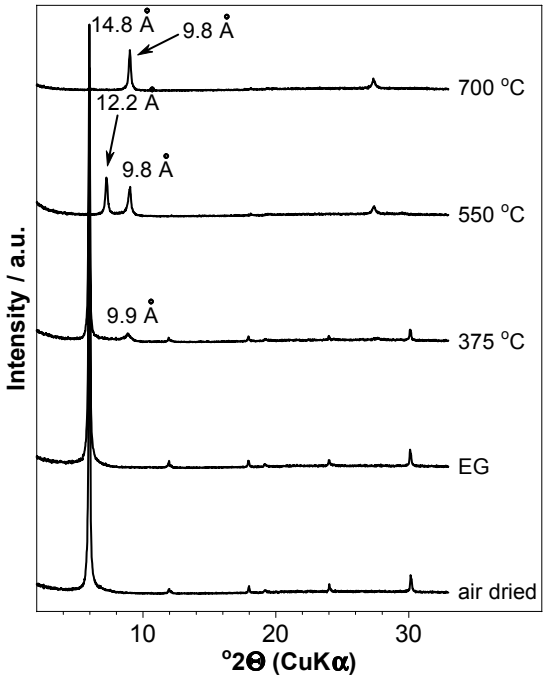

Figure 1 X-ray pattern (texture sample).

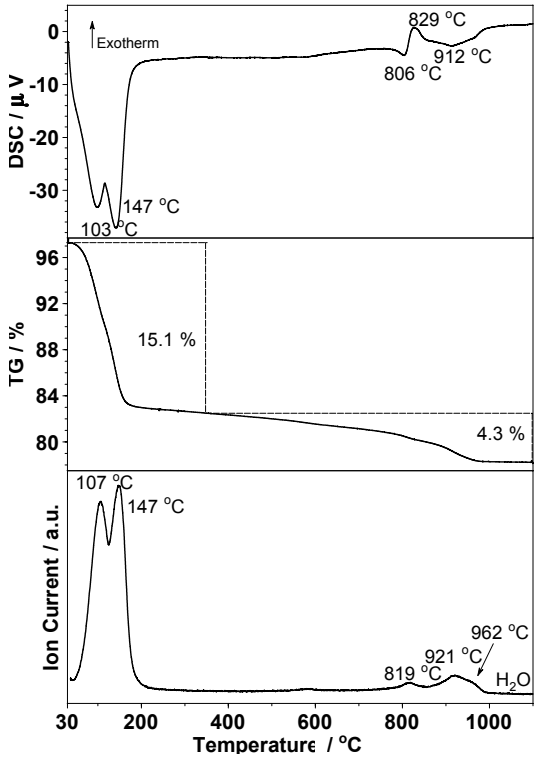

Figure 2 Simultaneous thermal analysis; starting mass of TG: 98.58%.

Basal spacing

d(00l)	air dried [Å]	EG [Å]
d(001)	14.8	14.8
d(002)	7.4	7.4
d(003)	4.93	4.93
d(004)	3.7	3.7
d(005)	2.96	2.96
d(006)	14.8	14.8

Interlayer composition

Interlayer composition / FU	mol
Na^{+}	0.68
Ca^{2+}	0.01
Mg^{2+}	-
K^{+}	-

Layer charge and exchange capacity

Measured		Calculated	
n_c = 12	Ammonium	Köster (1977)	
ξ [eq/FU]	CEC [meq/100g]	ξ [eq/Fu]	CEC [meq/100g]
0.70	176	0.70	174

Sample: Sepiolite Pangel S9 < 2 µm

$$Me^{+}_{0.10}(Si_{5.90}Al^{3+}_{0.10})(Mg^{2+}_{3.55}Al^{3+}_{0.23}Fe^{3+}_{0.07})[O_{15}(OH)_2]\cdot 2H_2O + 4H_2O$$

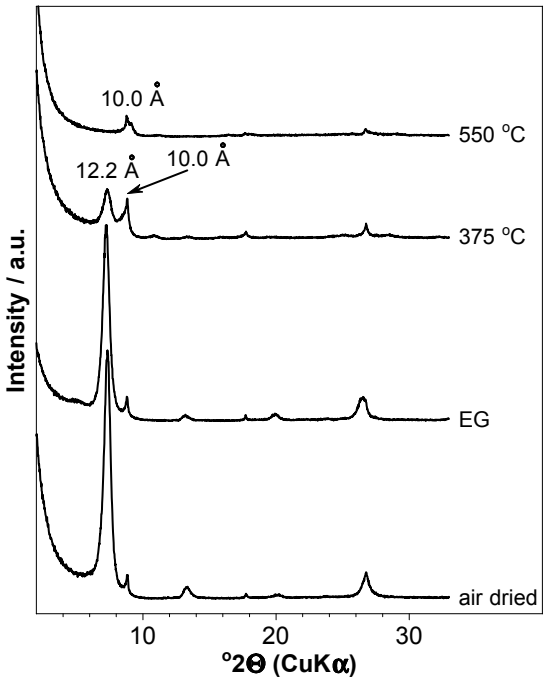

Figure 1 X-ray pattern (texture sample).

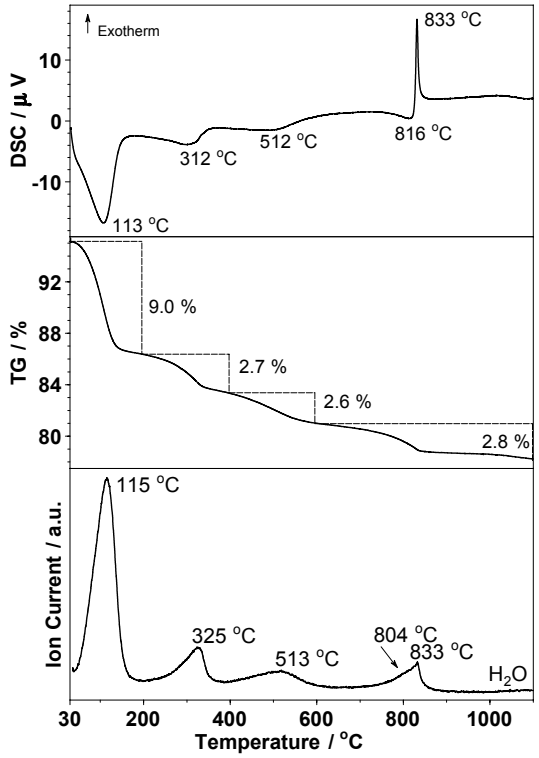

Figure 2 Simultaneous thermal analysis; starting mass of TG: 95.38%.

Interlayer composition

Interlayer composition / FU	mol
Na^+	0.07
Ca^{2+}	-
Mg^{2+}	0.015
K^+	-

Charge location according to Stevens (1945)

Charge location [eq/FU]		Tetrahedral charge [%]
tetrahedral	octahedral	
0.10	0.00	100

Layer charge and exchange capacity

Measured		Calculated	
n_c = 12	Cu-trien	Stevens (1945)	
ξ [eq/FU]	CEC [meq/100g]	ξ [eq/Fu]	CEC [meq/100g]
-	19	0.10	22

Sample: Sepiolite Pangel S9 < 0.2 µm

$$Me^{+}_{0.11}(Si_{5.91}Al^{3+}_{0.09})(Mg^{2+}_{3.63}Al^{3+}_{0.18}Fe^{3+}_{0.06})[O_{15}(OH)_2]\cdot 2H_2O + 4H_2O$$

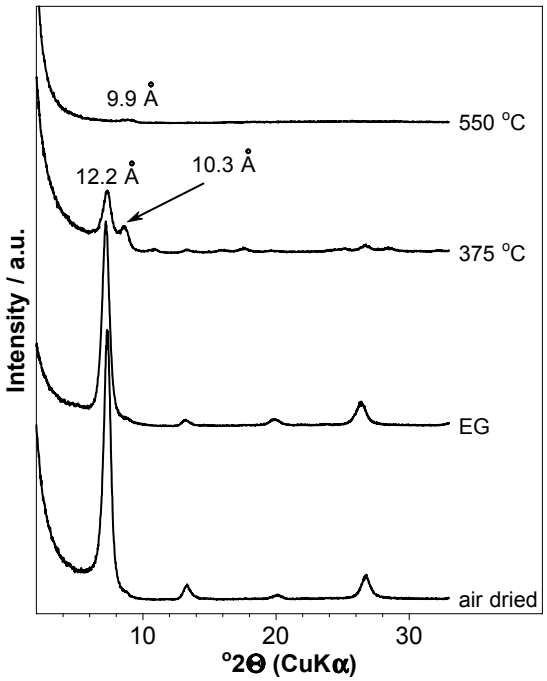

Figure 1 X-ray pattern (texture sample).

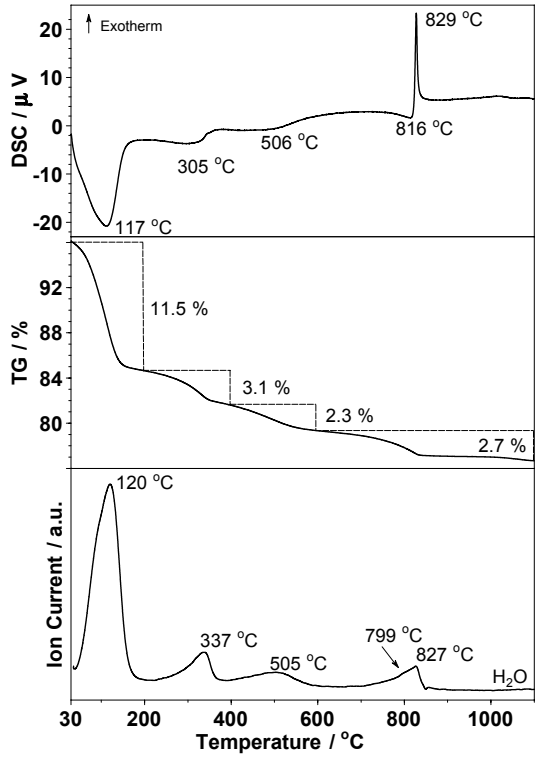

Figure 2 Simultaneous thermal analysis; starting mass of TG: 96.15%.

Interlayer composition

Interlayer composition / FU	mol
Na^+	0.07
Ca^{2+}	-
Mg^{2+}	0.015
K^+	-

Charge location according to Stevens (1945)

Charge location [eq/FU]		Tetrahedral charge [%]
tetrahedral	octahedral	
0.09	0.02	82

Layer charge and exchange capacity

Measured		Calculated	
n_c = 12	Cu-trien	Stevens (1945)	
ξ [eq/FU]	CEC [meq/100g]	ξ [eq/Fu]	CEC [meq/100g]
-	16	0.11	24

Appendix

3 Data sheets “Acid treatment”

3.1 Bulk material

Sample: Bentonite Calcigel (1_Calci)

Treatment conditions: 5 M H_2SO_4 at 80 °C for 0, 1.5, 5, 20, 72 and 96 h

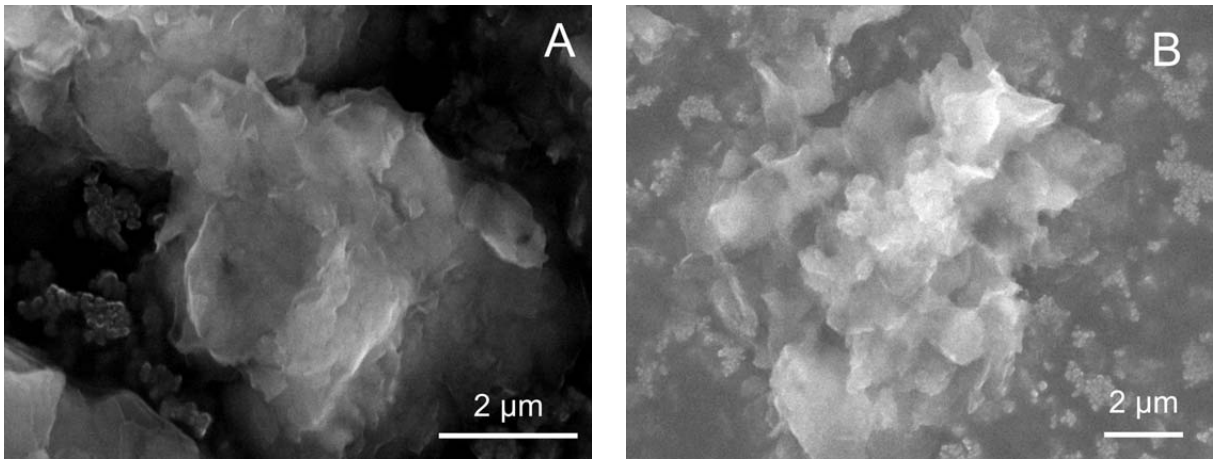

Figure 1 ESEM image of the raw (A) and acid treated (96 h) Calcigel (1_Calci) (B).

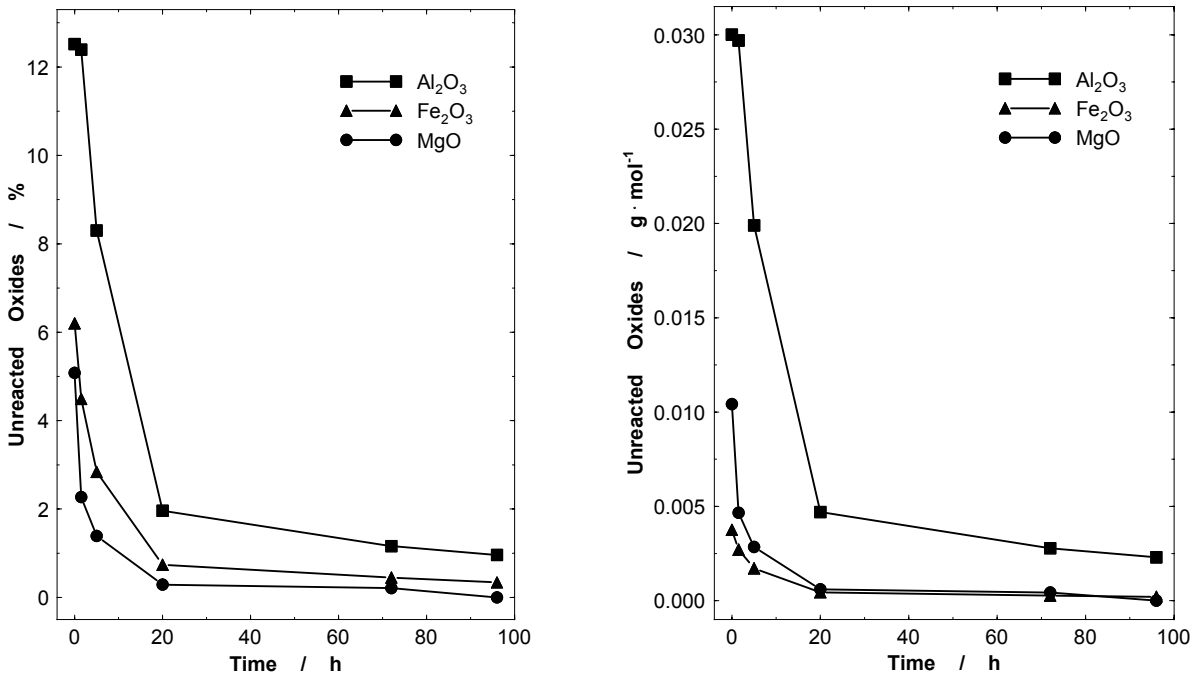

Figure 2 Both graphs show the chemical composition of the residual solid. The graph A shows the unreacted oxides in %. The graph B shows the unreacted oxides [g·mol^{-1}] related to the molecular weight of the formula unit (half unit cell).

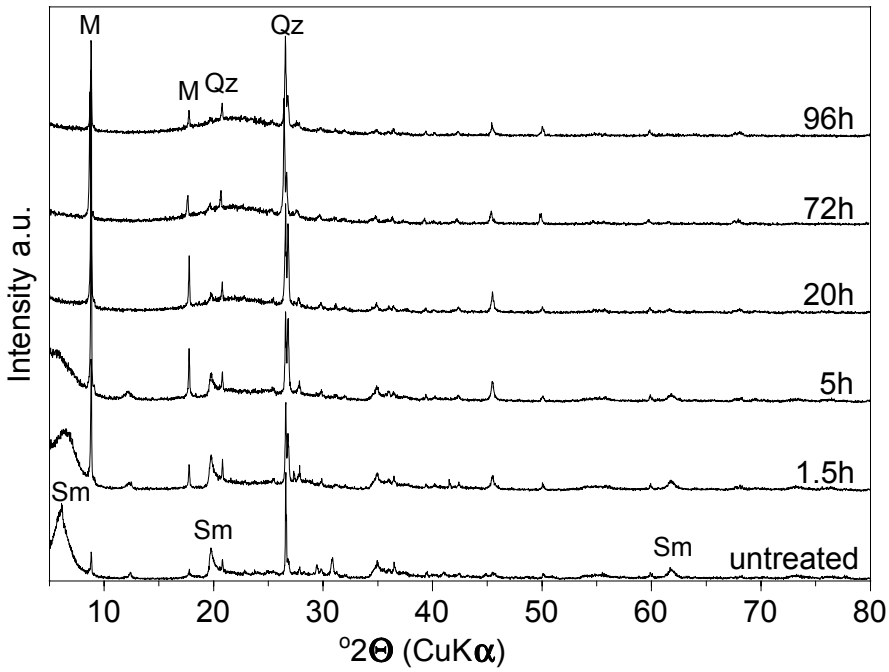

Figure 3 X-ray diffraction analysis (powder sample) of the raw and acid treated material. Sm: characteristic Smectite peaks with increasing 2θ (001), (020,110,021), (060); M: Muscovite; Qz: Quartz.

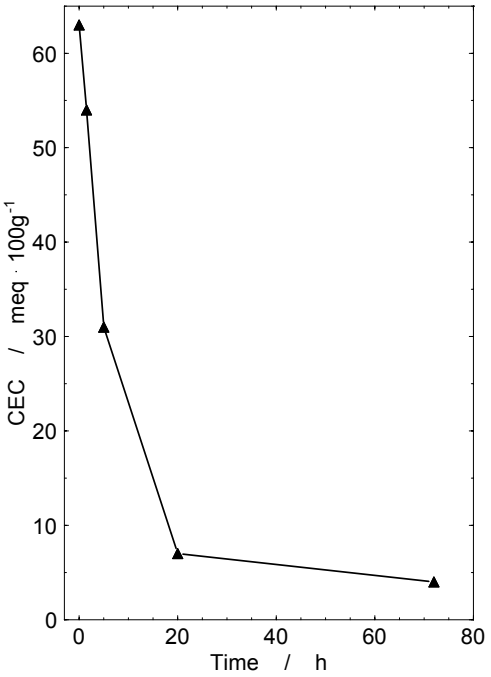

Figure 4 CEC in dependency of the time.

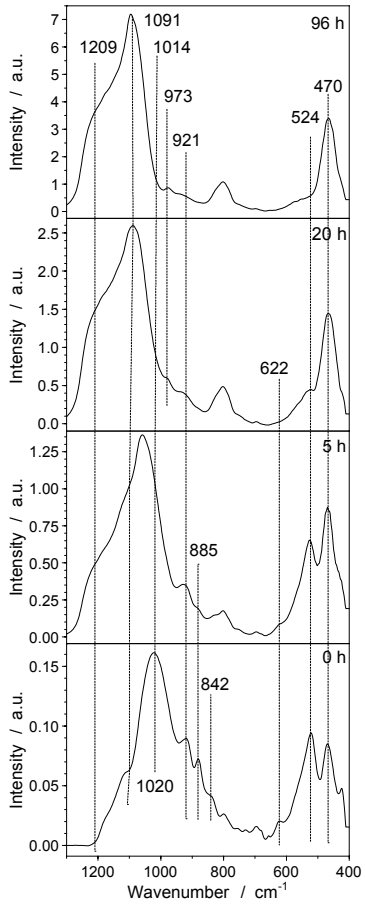

Figure 5 FTIR-spectra.

Sample: Bentonite EXM757 (2_EXM757)

Treatment conditions: 5 M H_2SO_4 at 80 °C for 0, 1.5, 5, 20, 72 and 96 h

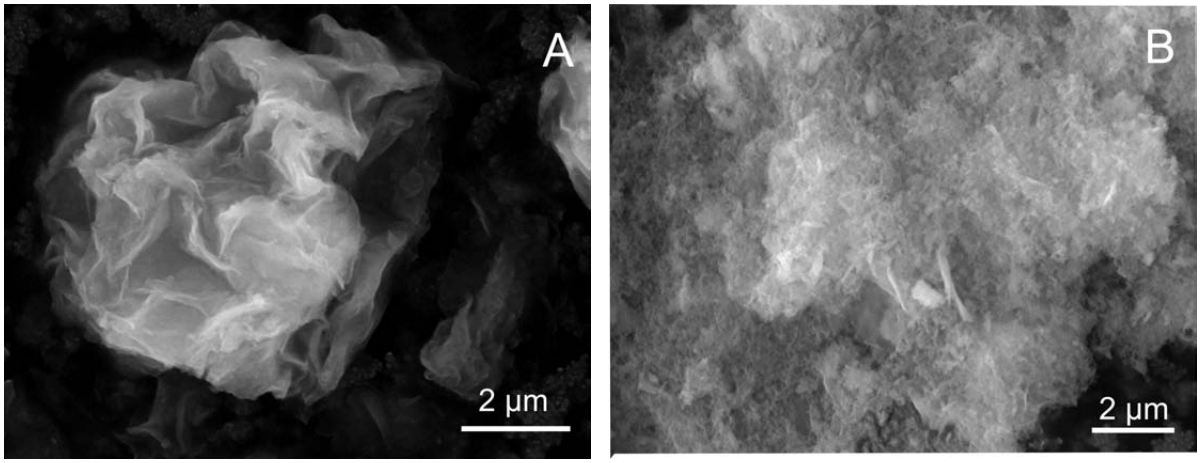

Figure 1 ESEM image of the raw (A) and acid treated (96 h) bentonite EXM757 (2_EXM757) (B).

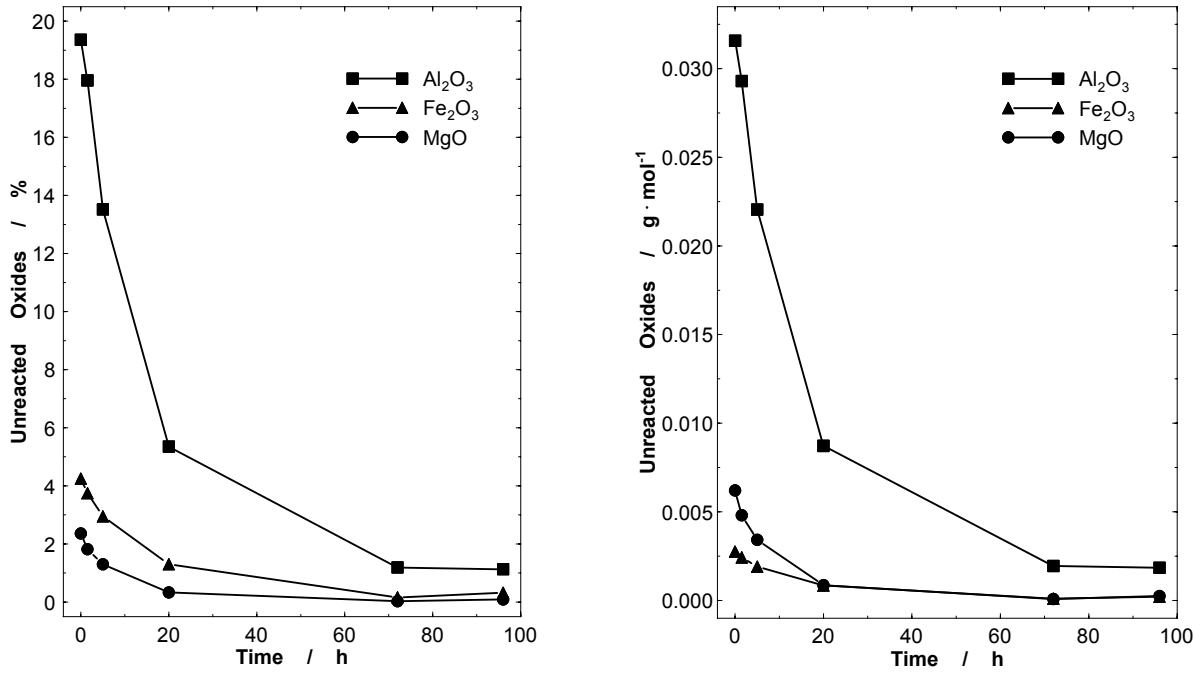

Figure 2 Both graphs show the chemical composition of the residual solid. The graph A shows the unreacted oxides in %. The graph B shows the unreacted oxides [g·mol^{-1}] related to the molecular weight of the formula unit (half unit cell).

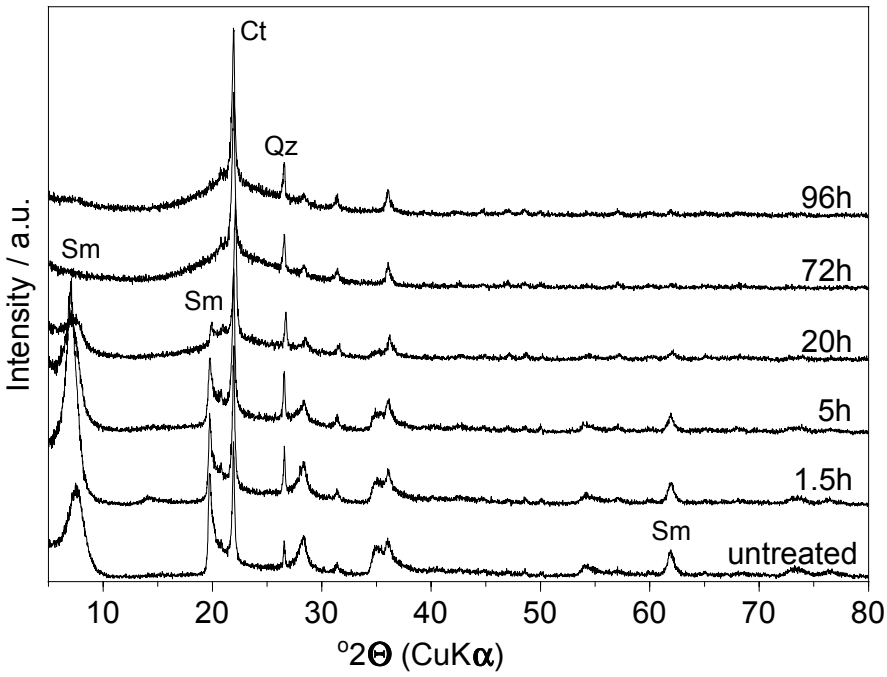

Figure 3 X-ray diffraction analysis (powder sample) of the raw and acid treated material. Sm: characteristic Smectite peaks with increasing 2θ (001), (020,110,021), (060); Qz: Quartz; Ct: Cristobalite.

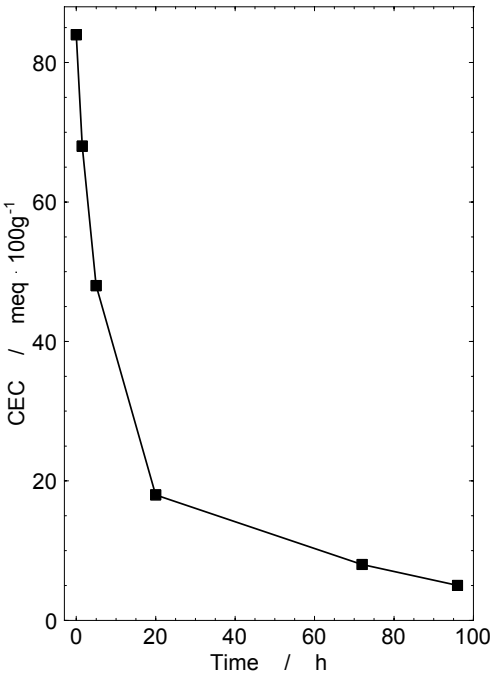

Figure 4 CEC in dependency of the time.

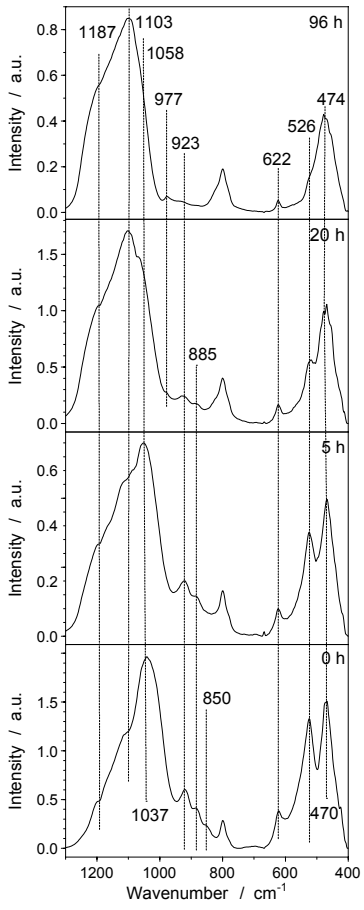

Figure 5 FTIR-spectra.

Sample: Bentonite SWy-2 (3_SWy-2)

Treatment conditions: 5 M H_2SO_4 at 80 °C for 0, 20 and 96 h

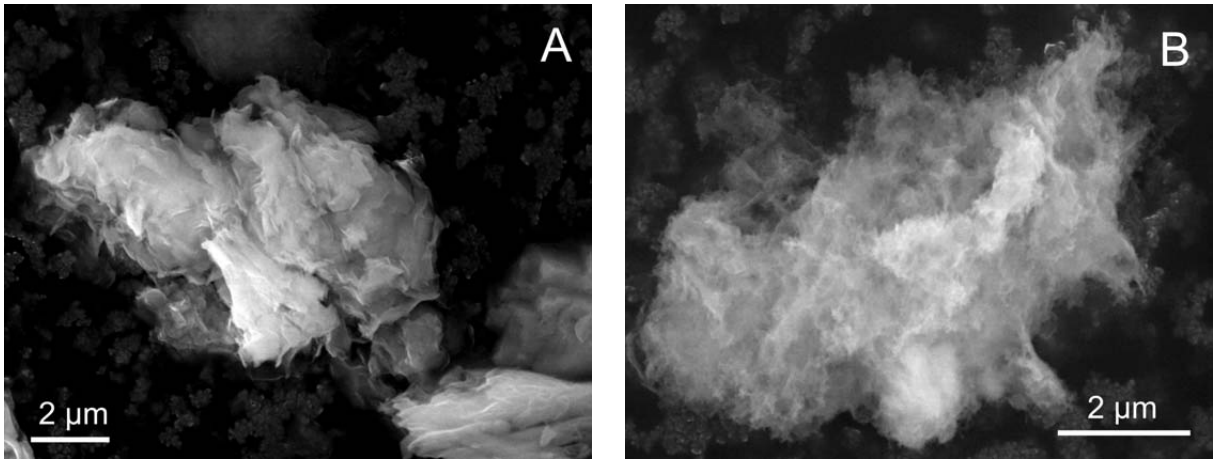

Figure 1 ESEM image of the raw (A) and acid treated (96 h) bentonite SWy-2 (3_SWy-2) (B).

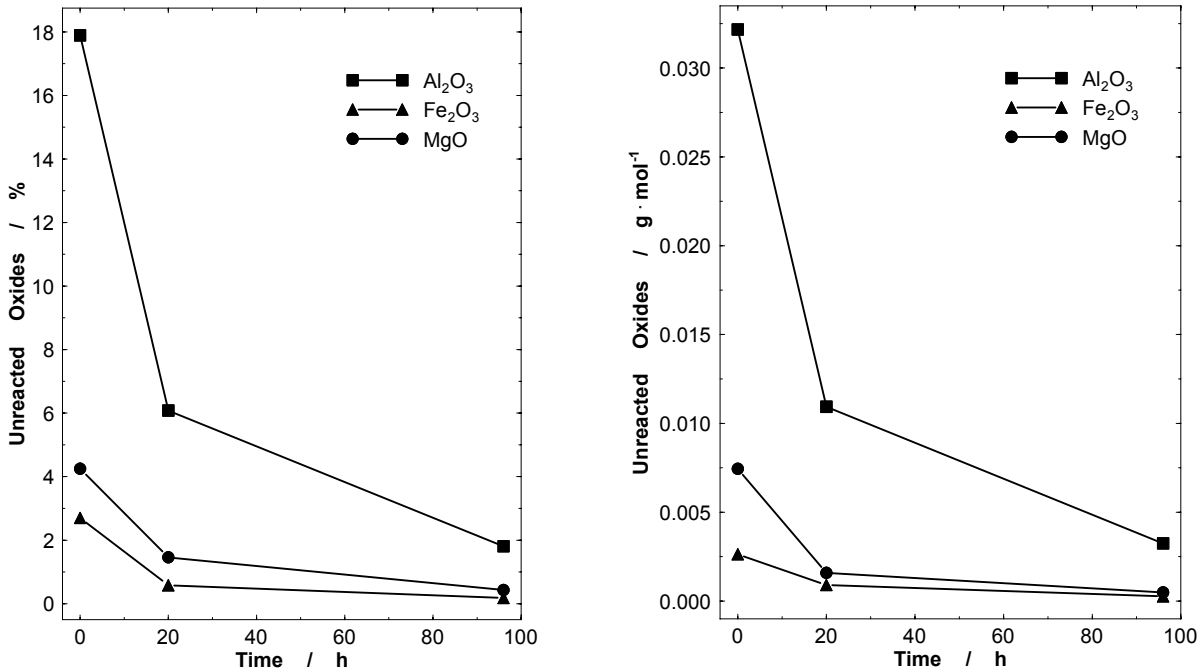

Figure 2 Both graphs show the chemical composition of the residual solid. The graph A shows the unreacted oxides in %. The graph B shows the unreacted oxides [g·mol^{-1}] related to the molecular weight of the formula unit (half unit cell).

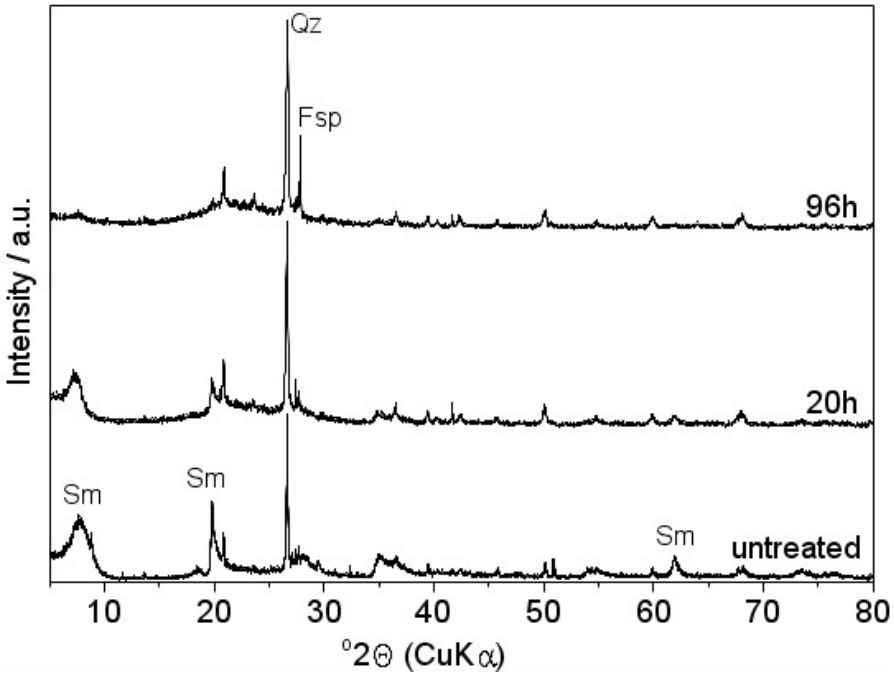

Figure 3 X-ray diffraction analysis (powder sample) of the raw and acid treated material. Sm: characteristic Smectite peaks with increasing 2θ (001), (020,110,021), (060); Qz: Quartz; Fsp: Feldspars.

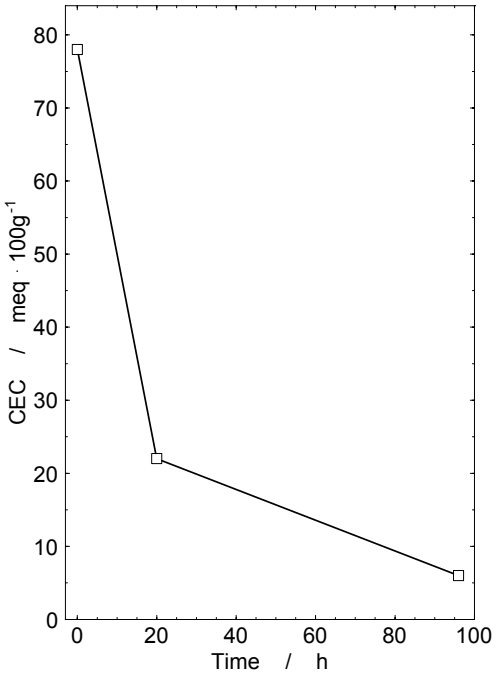

Figure 4 CEC in dependency of the time.

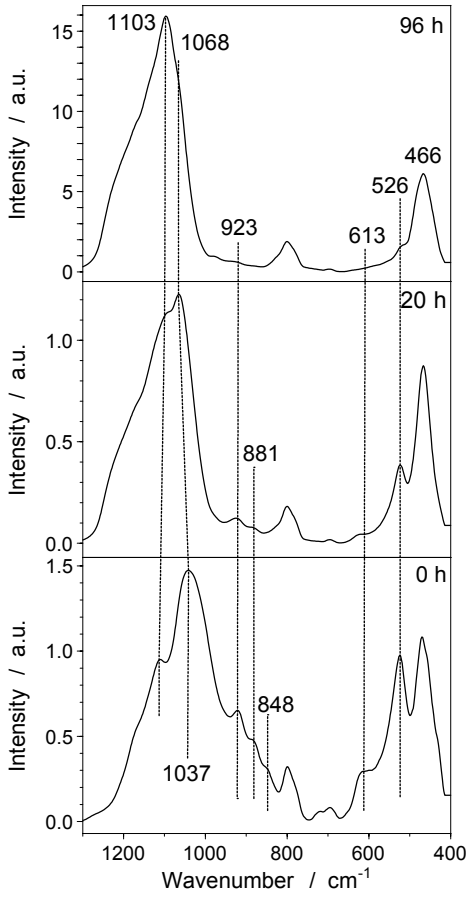

Figure 5 FTIR-spectra.

Sample: Bentonite Volclay (4_Vol)

Treatment conditions: 5 M H_2SO_4 at 80 °C for 0, 1.5, 5, 20, 72 and 96 h

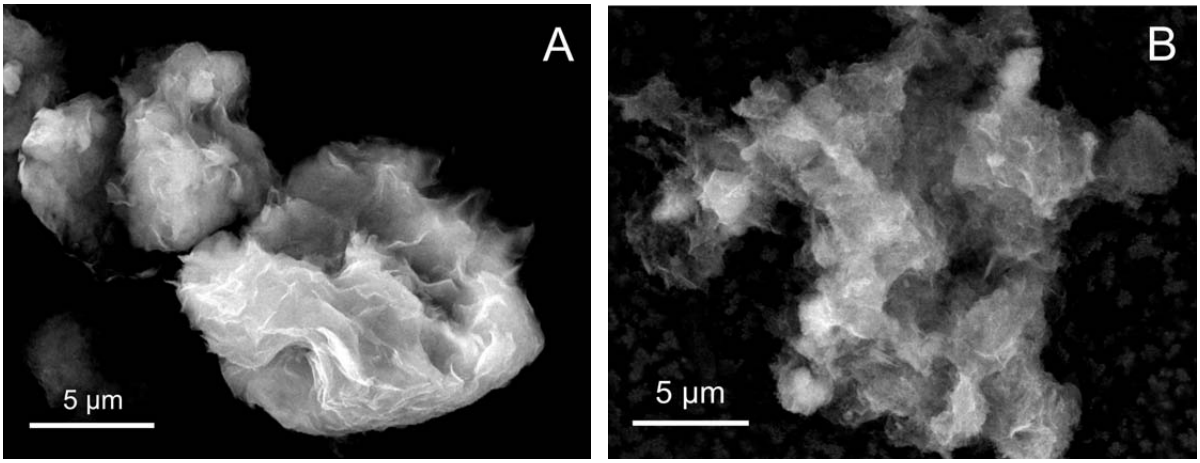

Figure 1 ESEM image of the raw (A) and acid treated (96 h) Volclay (4_Vol) (B).

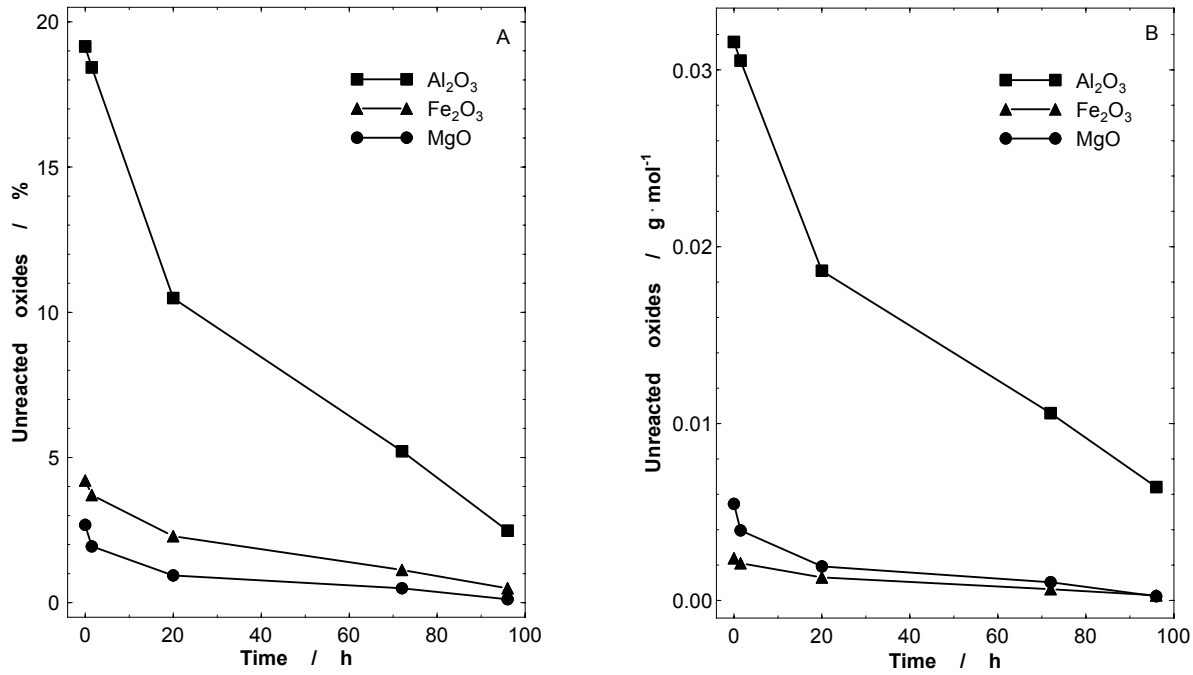

Figure 2 Both graphs show the chemical composition of the residual solid. The graph A shows the unreacted oxides in %. The graph B shows the unreacted oxides [g·mol^{-1}] related to the molecular weight of the formula unit (half unit cell).

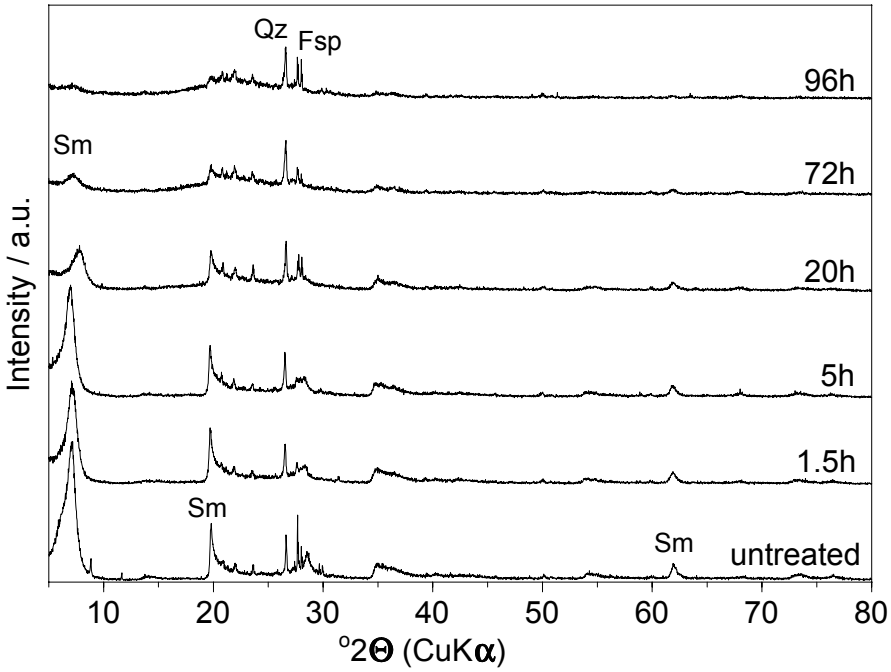

Figure 3 X-ray diffraction analysis (powder sample) of the raw and acid treated material. Sm: characteristic Smectite peaks with increasing 2θ (001), (020,110,021), (060); Qz: Quartz; Fsp: Feldspars.

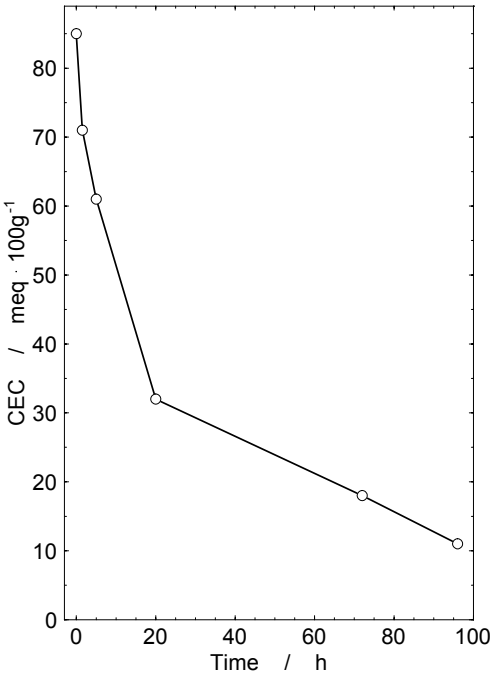

Figure 4 CEC in dependency of the time.

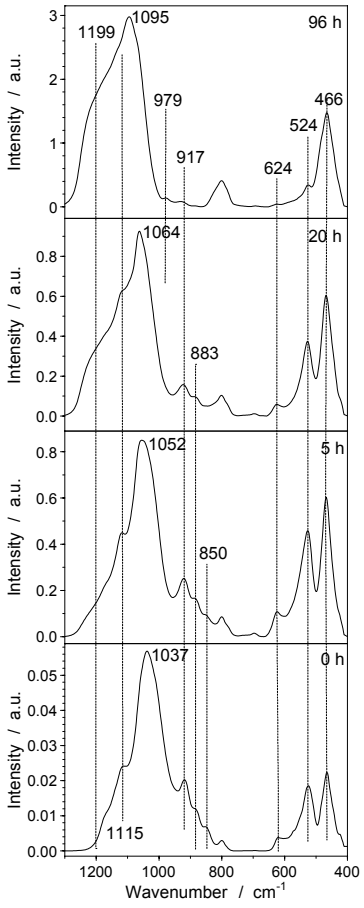

Figure 5 FTIR-spectra.

Sample: Bentonite WYO (5_WYO)

Treatment conditions: 5 M H_2SO_4 at 80 °C for 0, 20 and 96 h

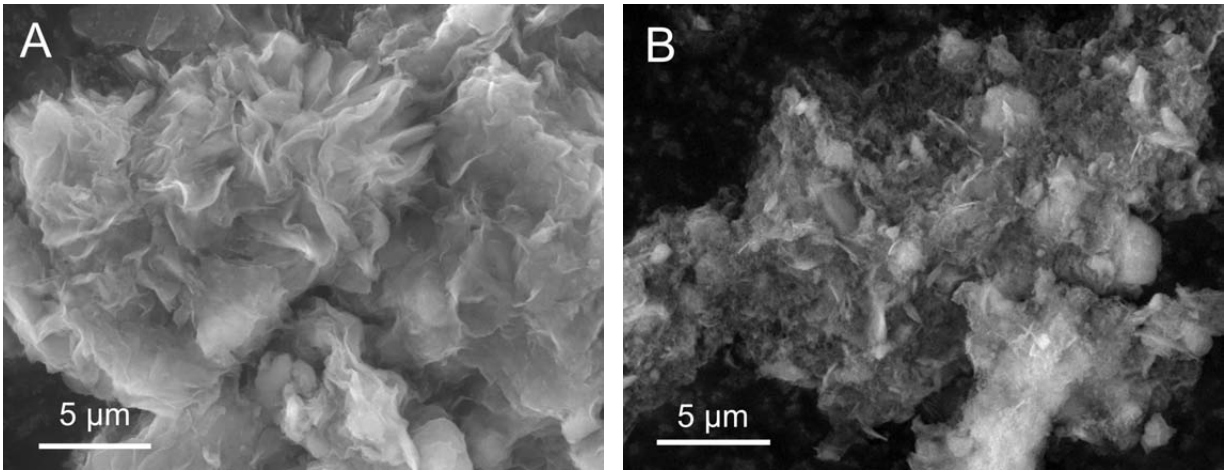

Figure 1 ESEM image of the raw (A) and acid treated (96 h) bentonite WYO-Bent (5_WYO) (B).

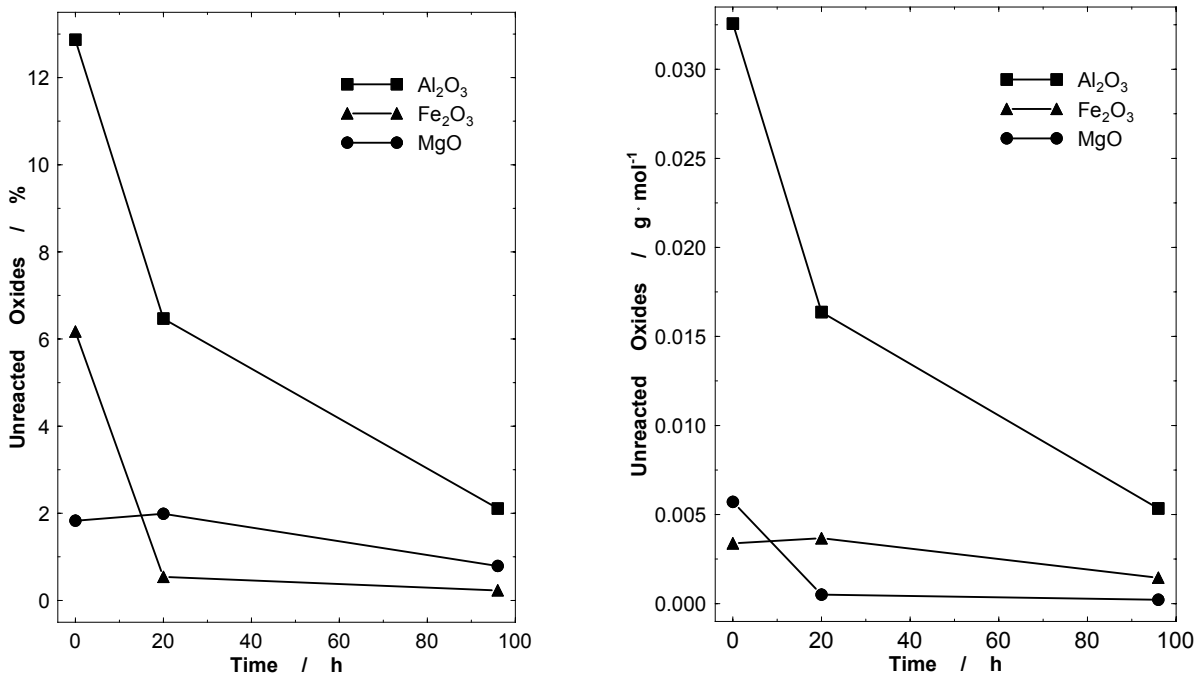

Figure 2 Both graphs show the chemical composition of the residual solid. The graph A shows the unreacted oxides in %. The graph B shows the unreacted oxides [g·mol^{-1}] related to the molecular weight of the formula unit (half unit cell).

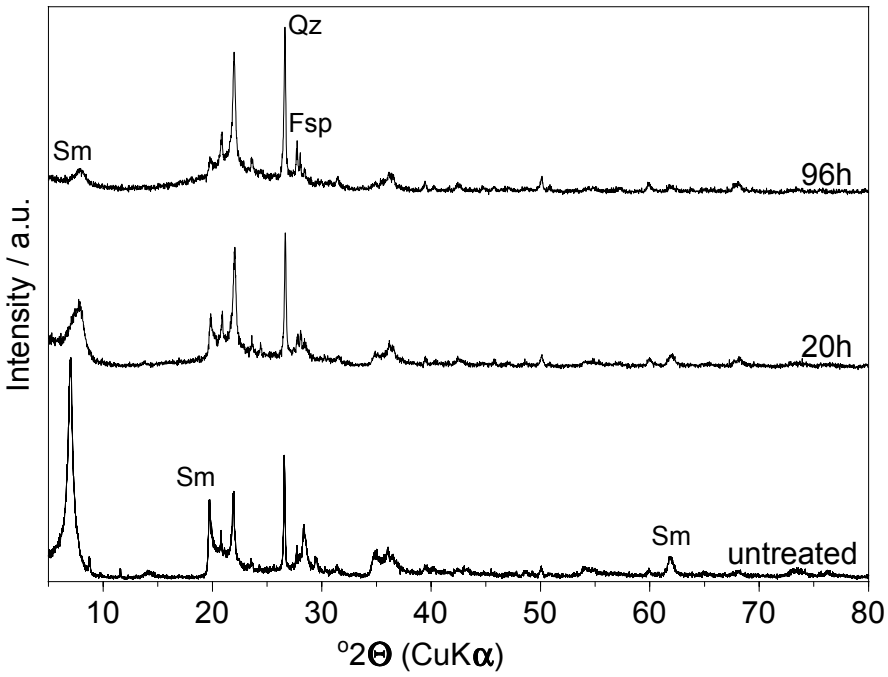

Figure 3 X-ray diffraction analysis (powder sample) of the raw and acid treated material. Sm: characteristic Smectite peaks with increasing 2θ (001), (020,110,021), (060); Qz: Quartz; Fsp: Feldspars.

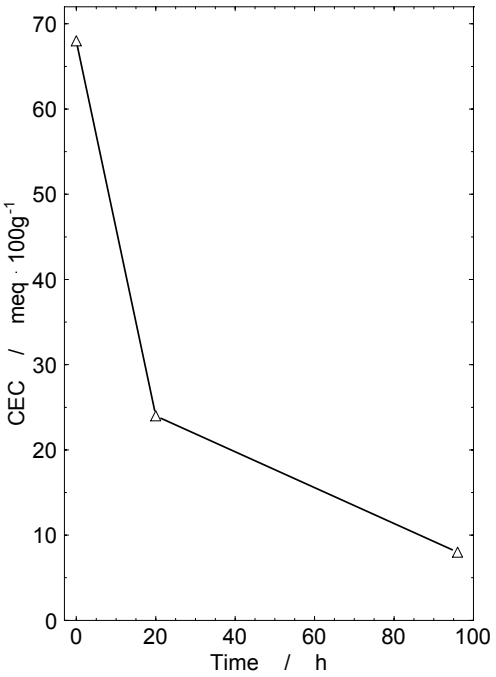

Figure 4 CEC in dependency of the time.

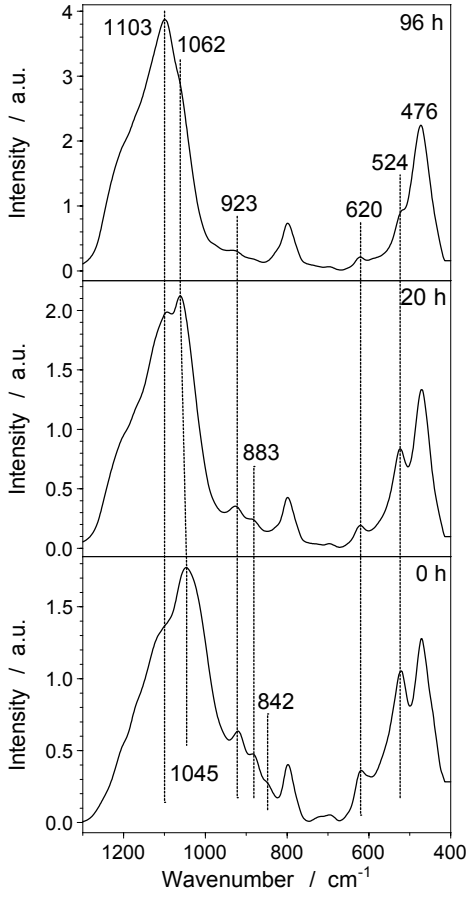

Figure 5 FTIR-spectra.

Sample: Indian Bentonite (6_IndBent)

Treatment conditions: 5 M H_2SO_4 at 80 °C for 0, 1.5, 5, 20 and 96 h

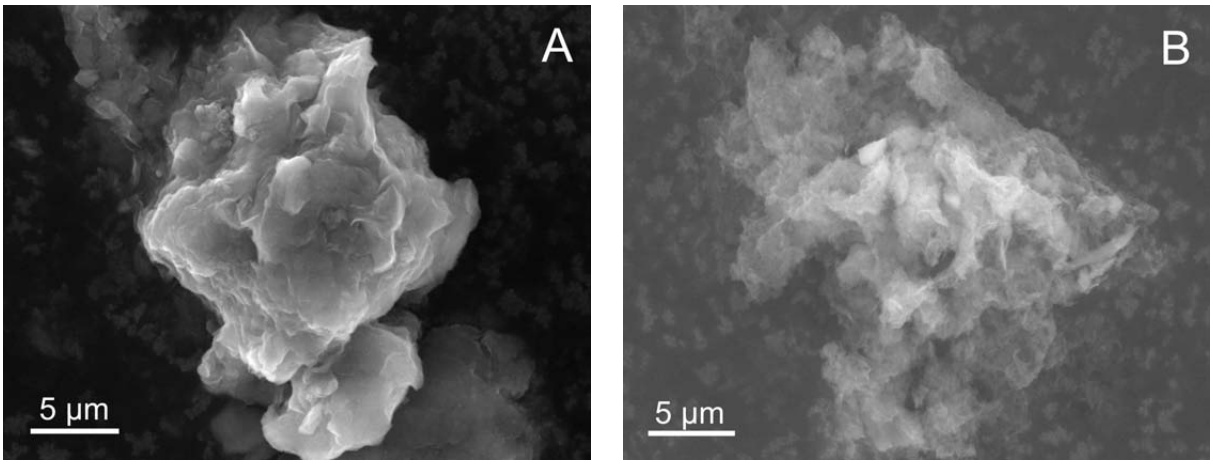

Figure 1 ESEM image of the raw (A) and acid treated (96 h) Indian Bentonite (6_IndBent) (B).

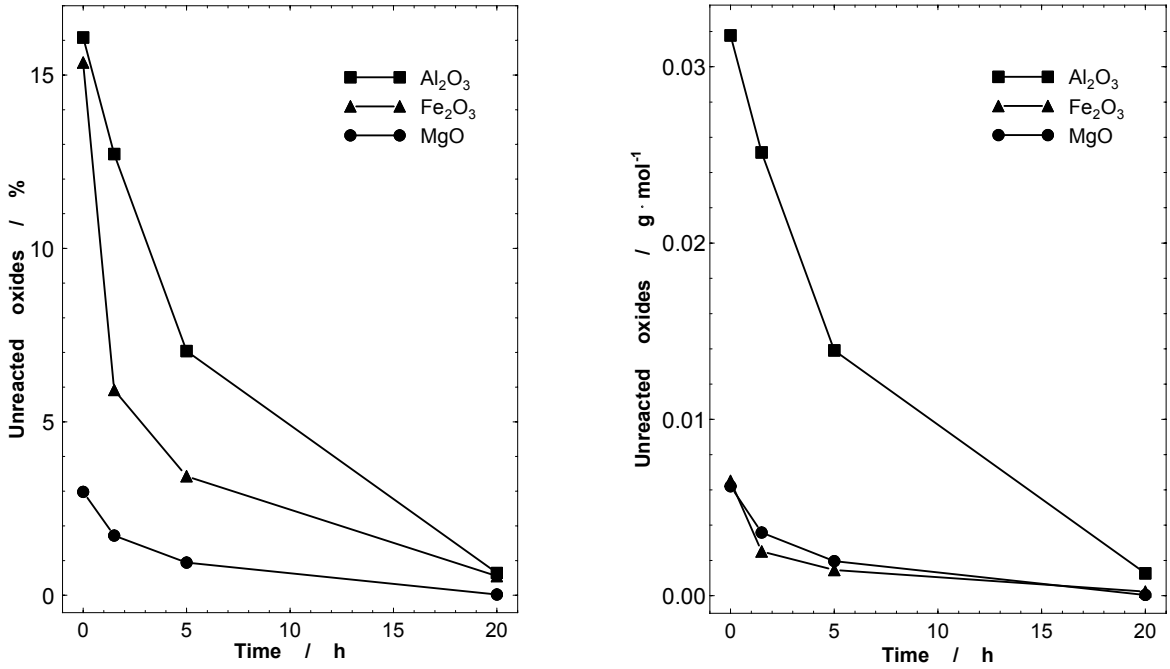

Figure 2 Both graphs show the chemical composition of the residual solid. The graph A shows the unreacted oxides in %. The graph B shows the unreacted oxides [g·mol^{-1}] related to the molecular weight of the formula unit (half unit cell).

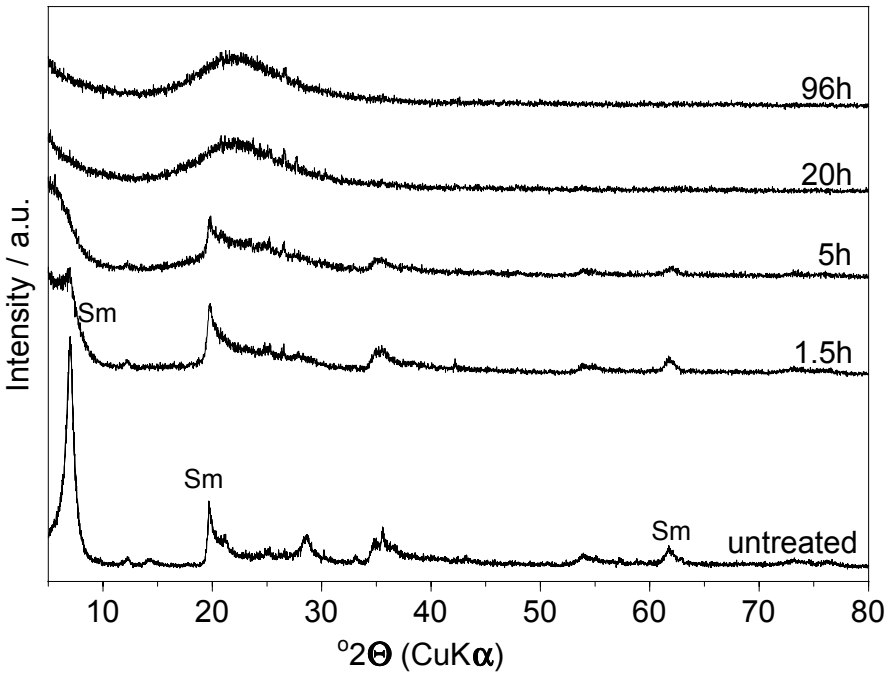

Figure 3 X-ray diffraction analysis (powder sample) of the raw and acid treated material. Sm: characteristic Smectite peaks with increasing 2θ (001), (020,110,021), (060).

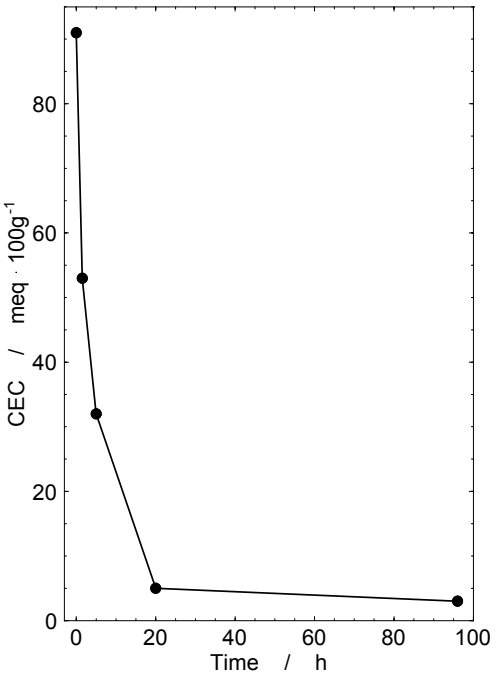

Figure 4 CEC in dependency of the time.

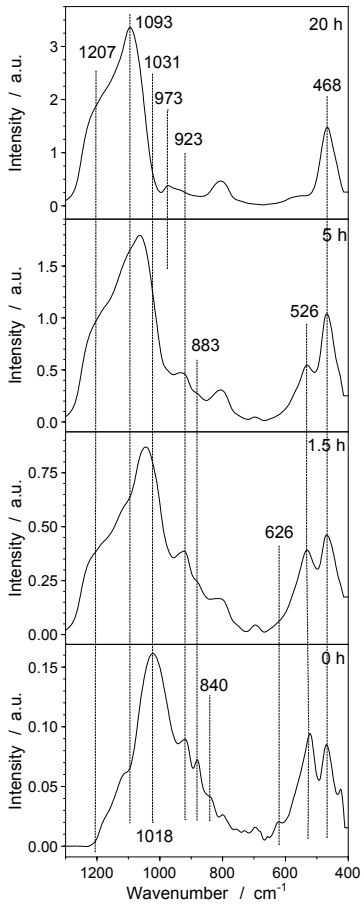

Figure 5 FTIR-spectra.

Sample: Natural Hectorite (7_NHec)

Treatment conditions: 5 M H_2SO_4 at 80 °C for 0, 1.5, 5, 20 and 96 h

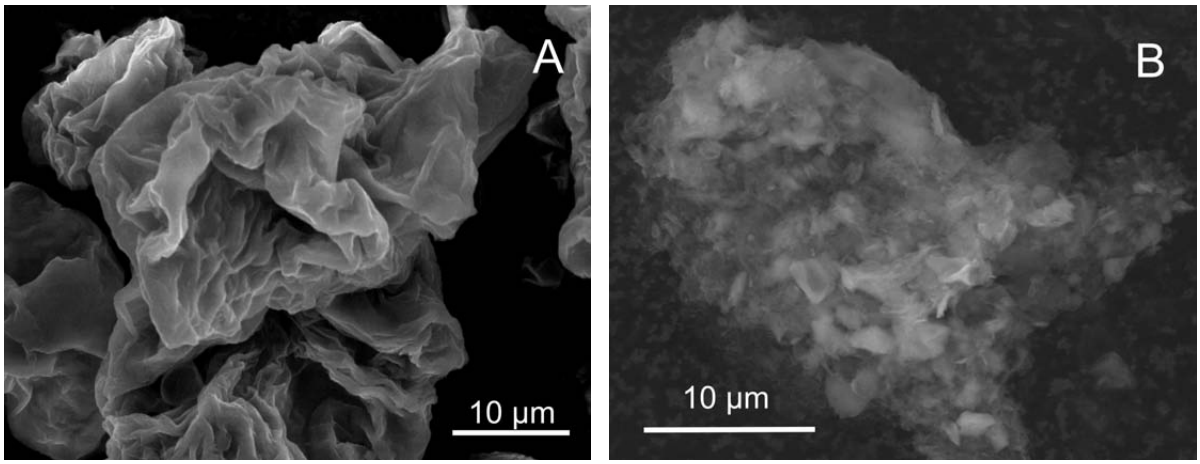

Figure 1 ESEM image of the raw (A) and acid treated (96 h) hectorite (7_NHec) (B).

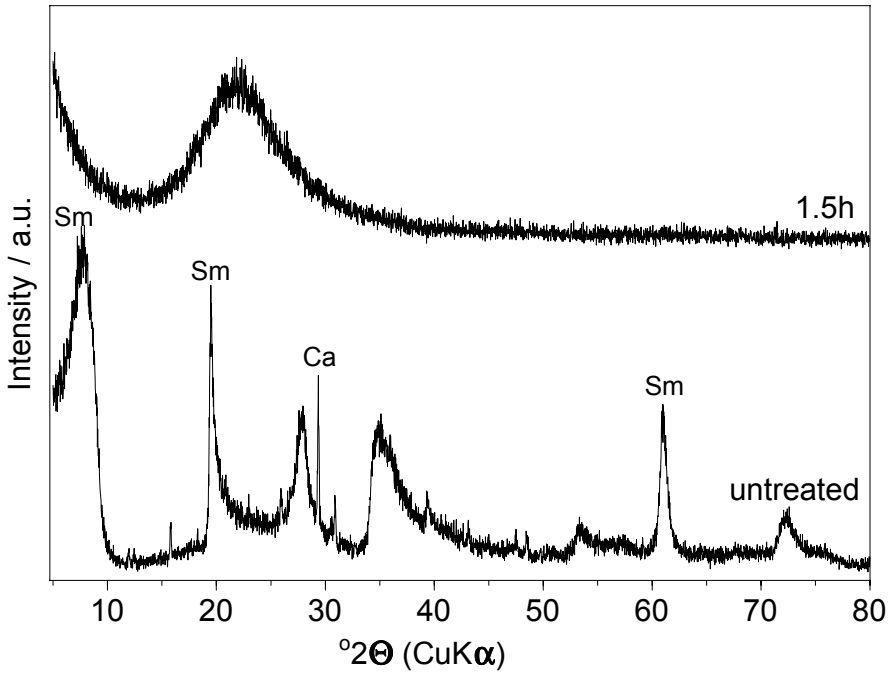

Figure 2 X-ray diffraction analysis (powder sample) of the raw and acid treated material. Sm: characteristic Smectite peaks with increasing 2θ (001), (020,110,021), (060); Ca: Calcite.

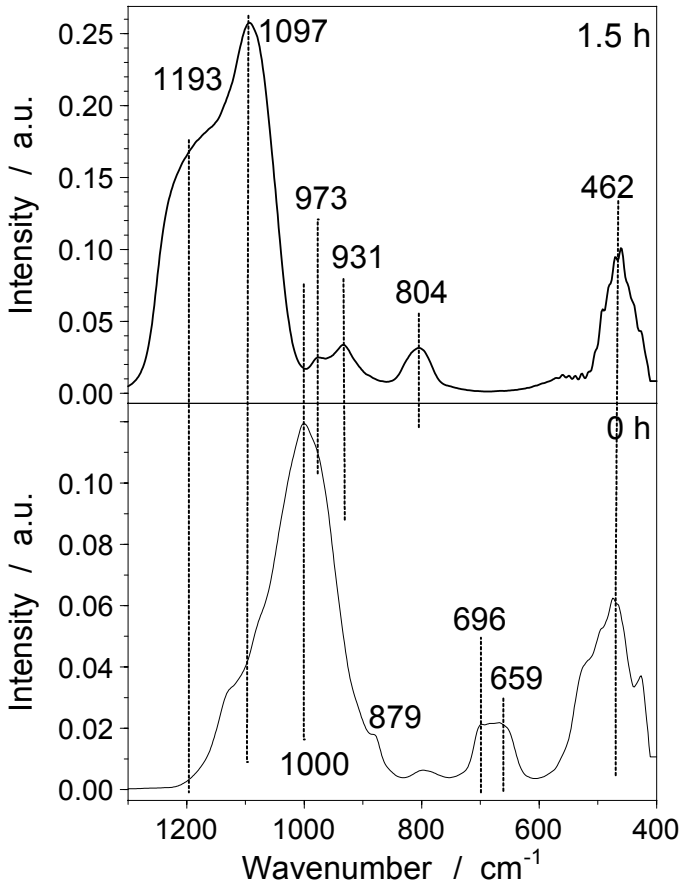

Figure 3 FTIR-spectra.

Sample: Vermiculite (8_Verm)

Treatment conditions: 5 M H_2SO_4 at 80 °C for 0, 1.5, 5, 20 and 72 h

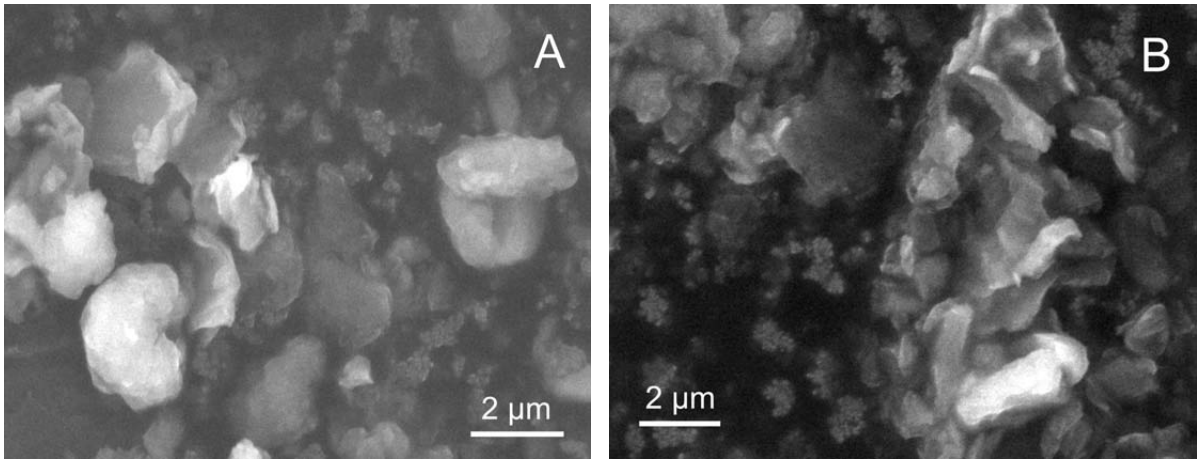

Figure 1 ESEM image of the raw (A) and acid treated (20 h) vermiculite (8_Verm) (B).

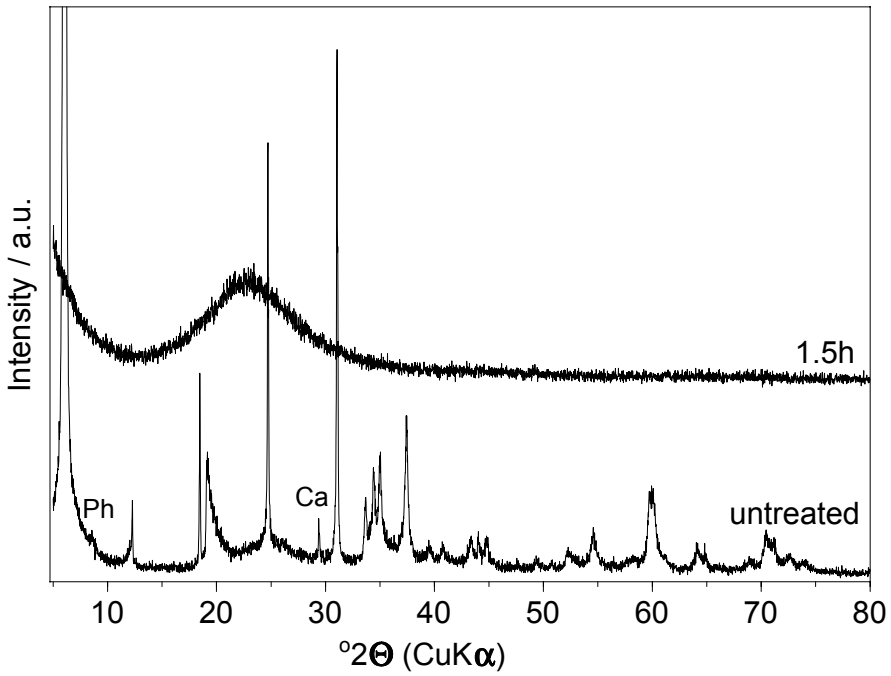

Figure 2 X-ray diffraction analysis (powder sample) of the raw and acid treated material. Ph: Phlogopite; Ca: Calcite; all not indexed peaks originated from vermiculite.

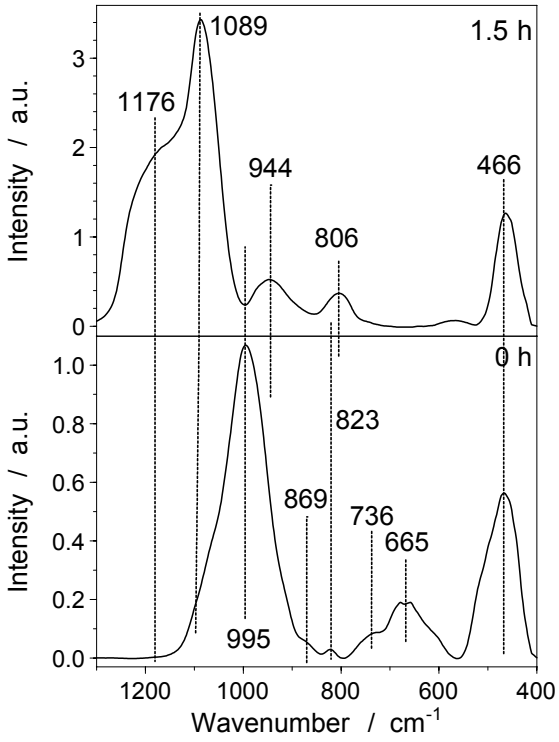

Figure 3 FTIR-spectra.

Sample: Illite (9_Illite)

Treatment conditions: 5 M H_2SO_4 at 80 °C for 0, 20 and 96 h

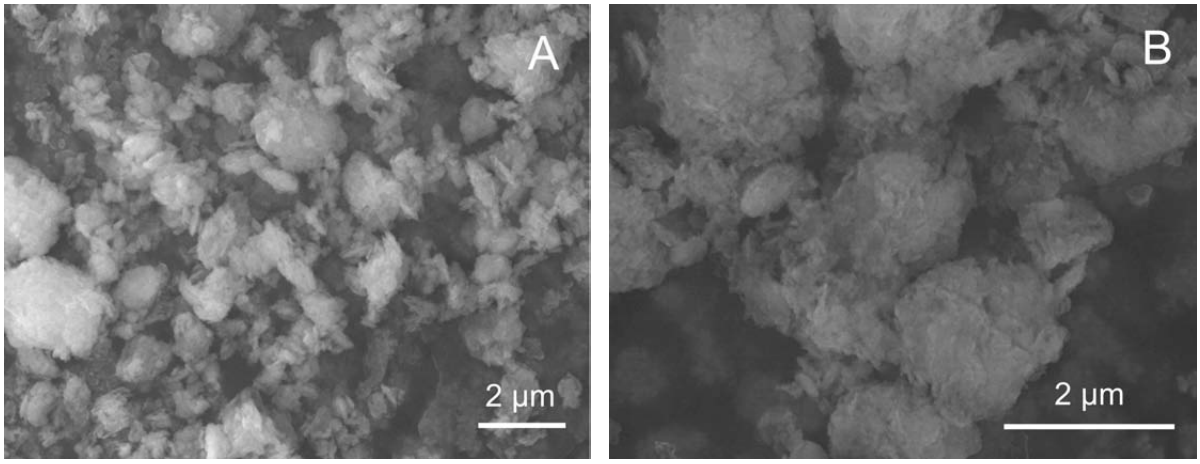

Figure 1 ESEM image of the raw (A) and acid treated (96 h) illite (9_Illite) (B).

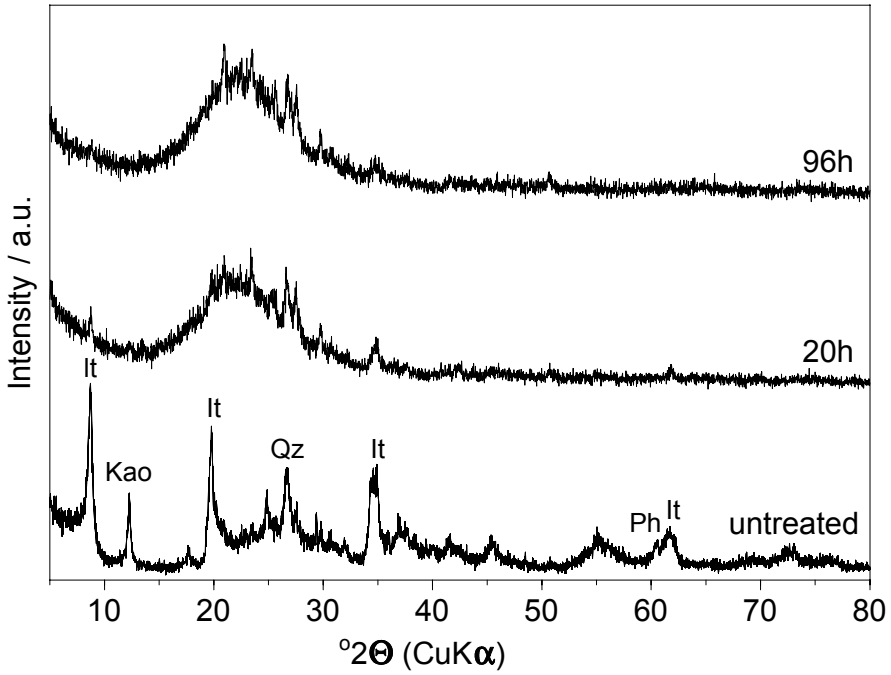

Figure 2 X-ray diffraction analysis (powder sample) of the raw and acid treated material. It: characteristic illite peaks with increasing 2θ (001), (002), (130), (060); Qz: Quartz; Kao: Kaolinite; Ph: Phlogopite (060).

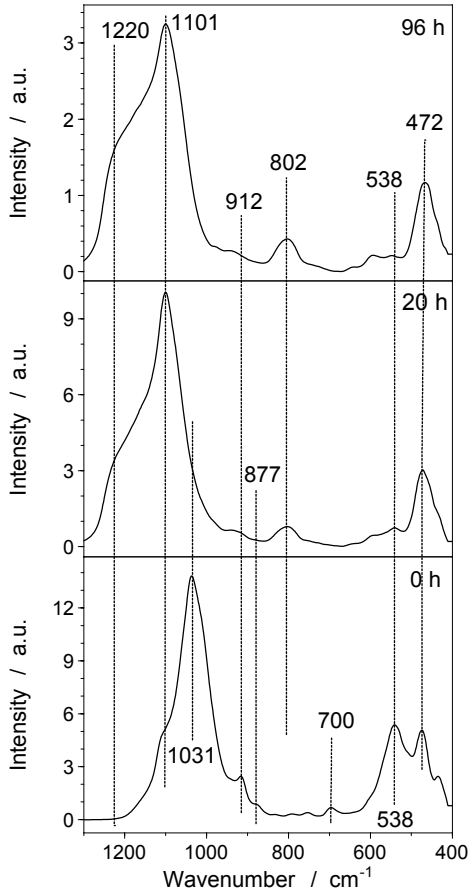

Figure 3 FTIR-spectra.

Sample: Sepiolite Pangel S9 (10_PangelS9)

Treatment conditions: 5 M H_2SO_4 at 80 °C for 0, 1.5, 5, 20 and 72 h

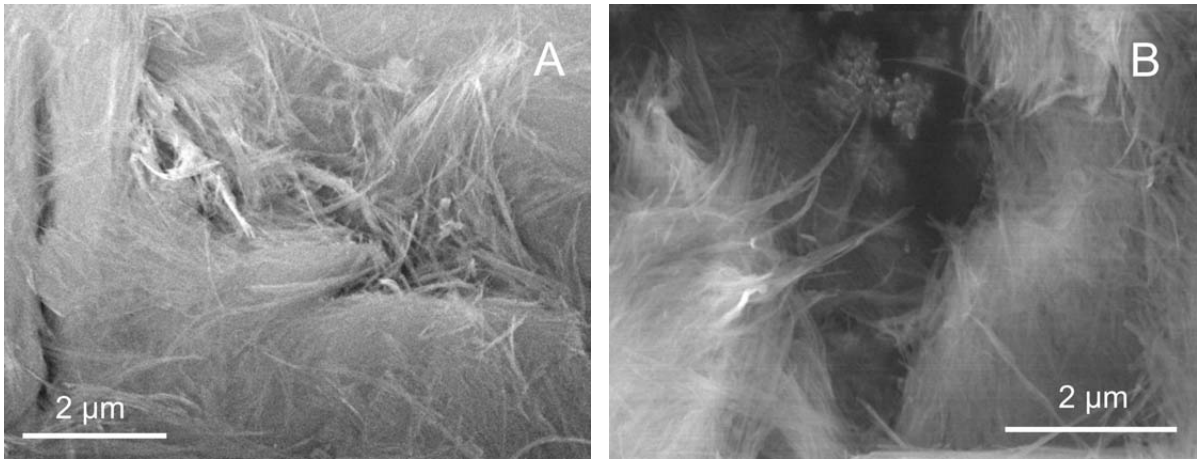

Figure 1 ESEM image of the raw (A) and acid treated (20 h) sepiolite (10_PangelS9) (B).

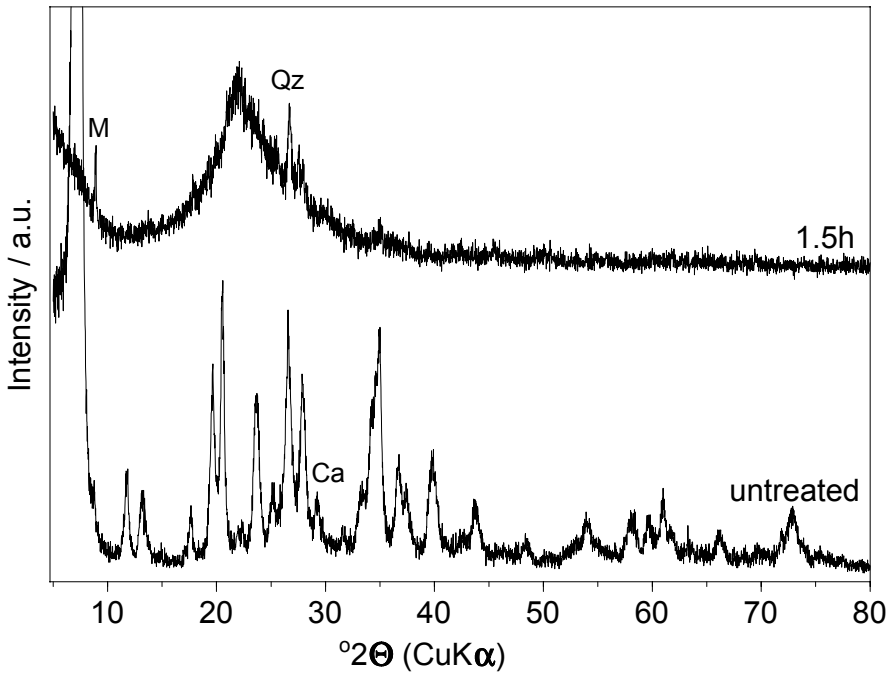

Figure 2 X-ray diffraction analysis (powder sample) of the raw and acid treated material. M: Muscovite; Qz: Quartz; Fsp: Feldspars; all not indexed peaks originated from sepiolite.

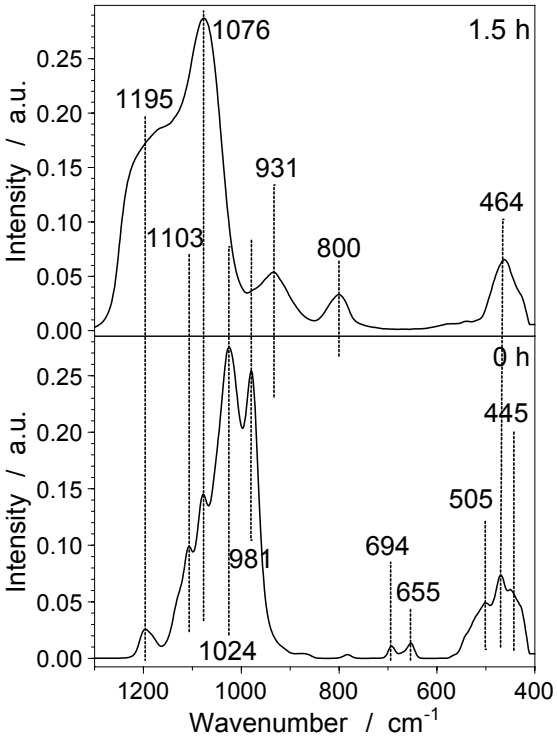

Figure 3 FTIR-spectra.

Sample: Kaolinite Polwhite (13_Pol)

Treatment conditions: 5 M H_2SO_4 at 80 °C for 0, 1.5, 5, 20, 72 and 96 h

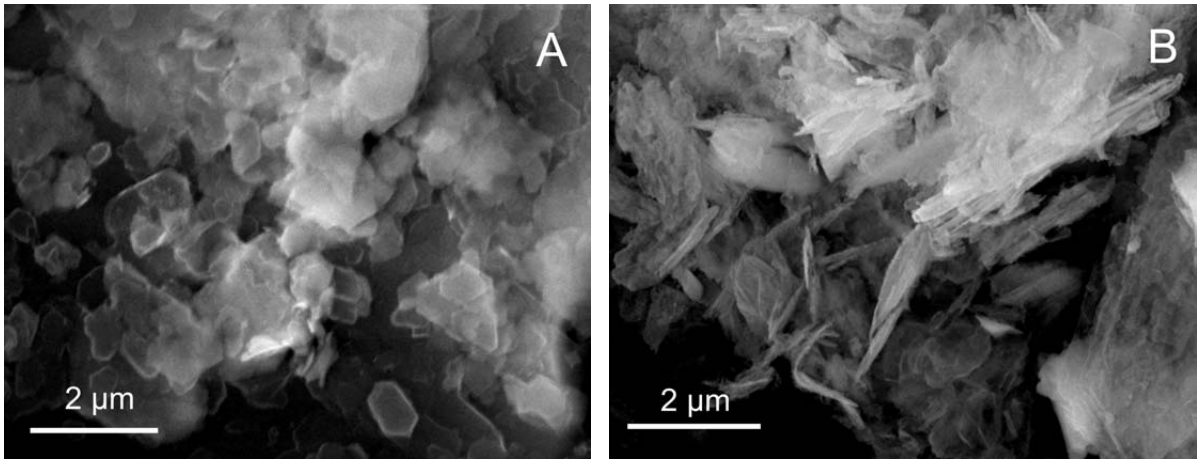

Figure 1 ESEM image of the raw (A) and acid treated (96 h) kaolinite Polwhite (13_Pol) (B).

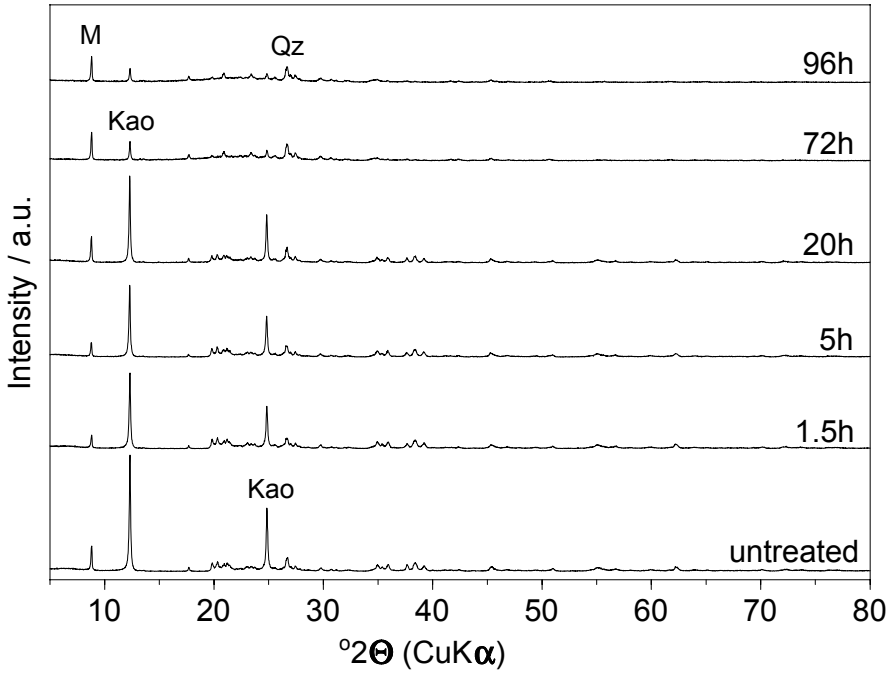

Figure 2 X-ray diffraction analysis (powder sample) of the raw and acid treated material.
Kao: characteristic kaolinite peaks with increasing 2θ (001), (002);
Qz: Quartz; M: Muscovite.

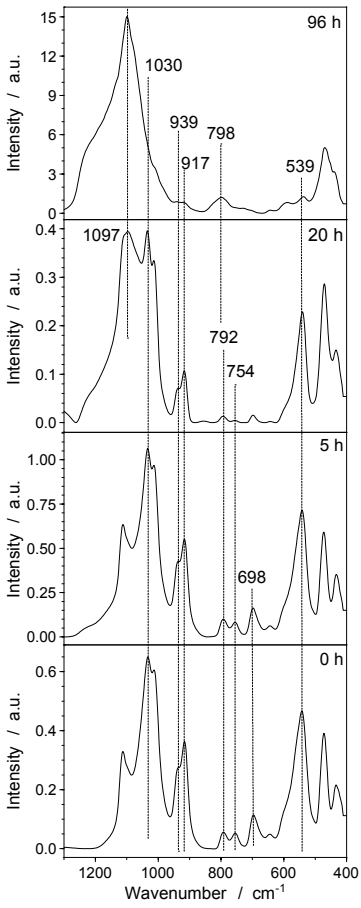

Figure 3 FTIR-spectra.

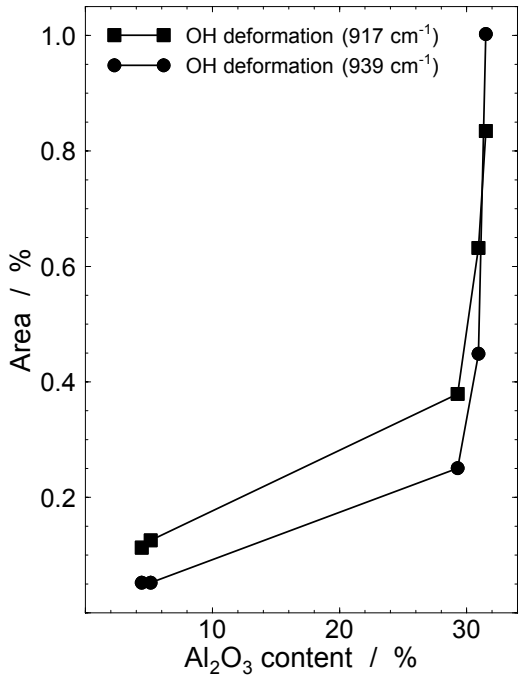

Figure 4 Comparison between the unreacted aluminium content and the area of the OH vibrations.

Sample: Kaolinite Rogers (15_Rogers)

Treatment conditions: 5 M H_2SO_4 at 80 °C for 0, 20 and 96 h

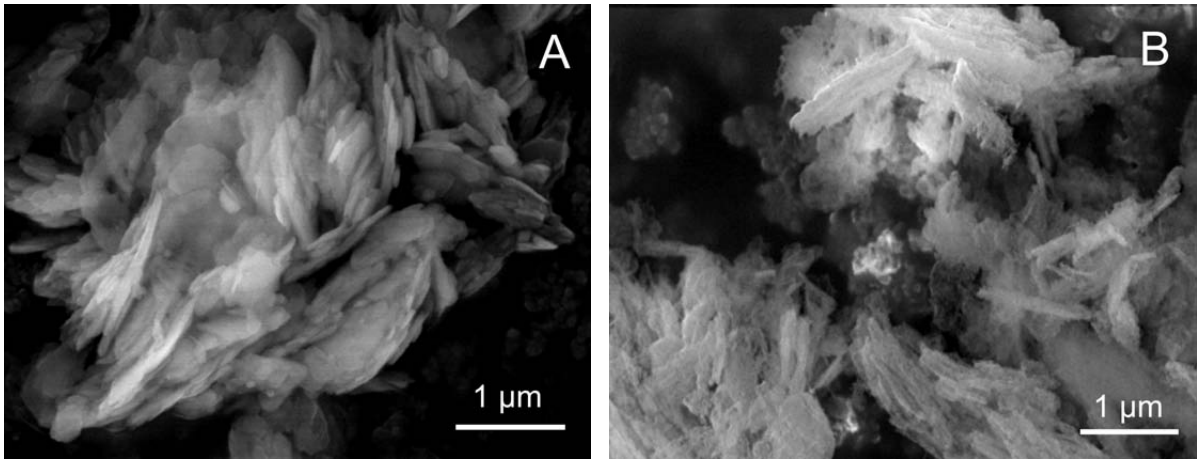

Figure 1 ESEM image of the raw (A) and acid treated (96 h) kaolinite Rogers (15_Rogers) (B).

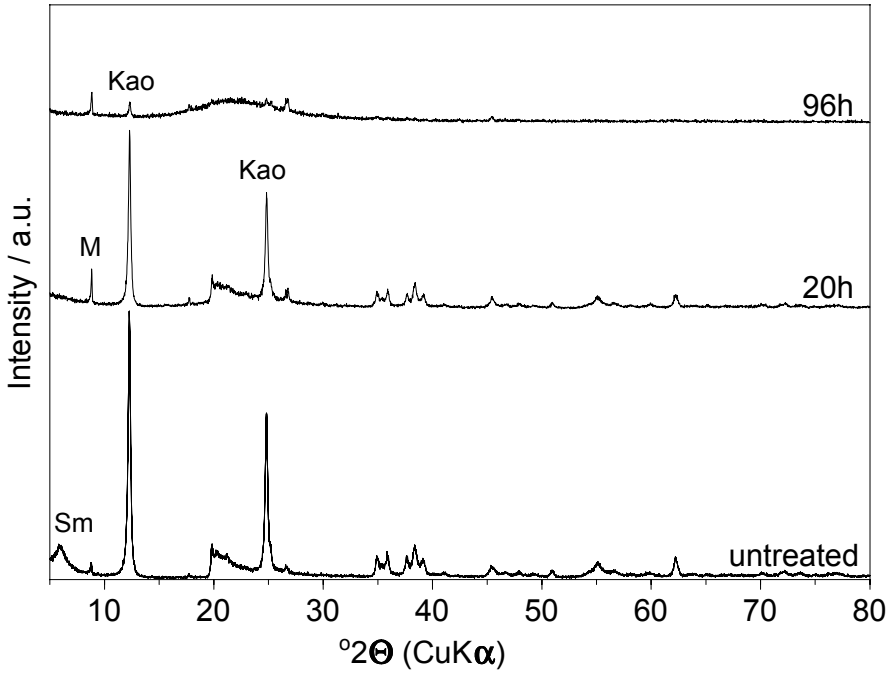

Figure 2 X-ray diffraction analysis (powder sample) of the raw and acid treated material.
Kao: characteristic kaolinite peaks with increasing 2θ (001), (002);
Sm: Smectite; M: Muscovite.

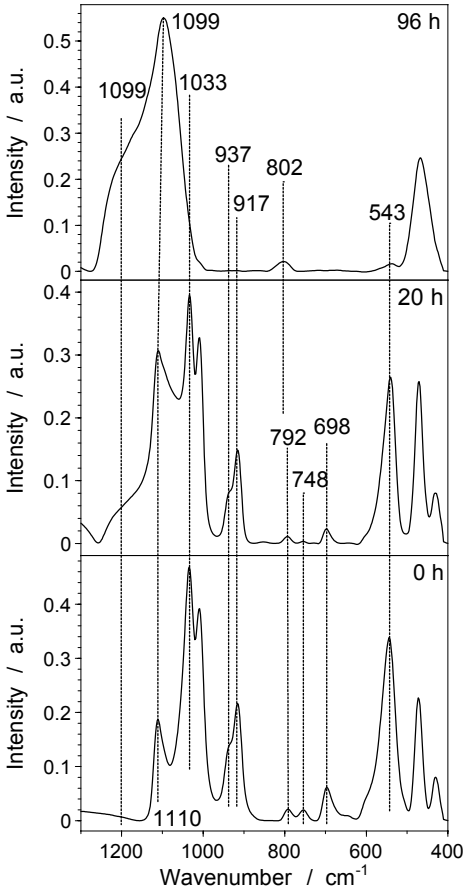

Figure 3 FTIR-spectra.

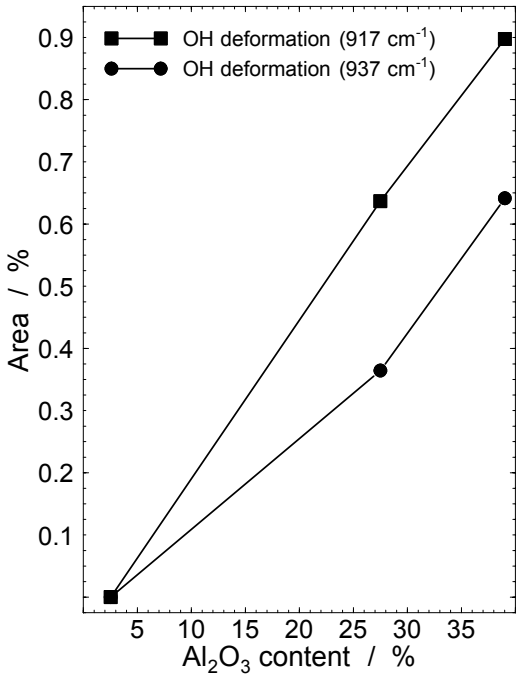

Figure 4 Comparison between the unreacted aluminium content and the area of the OH vibrations.

Sample: Magadiite (16_Mag)

Treatment conditions: 5 M H_2SO_4 at 80 °C for 0, 1.5, 5, 20 and 72 h

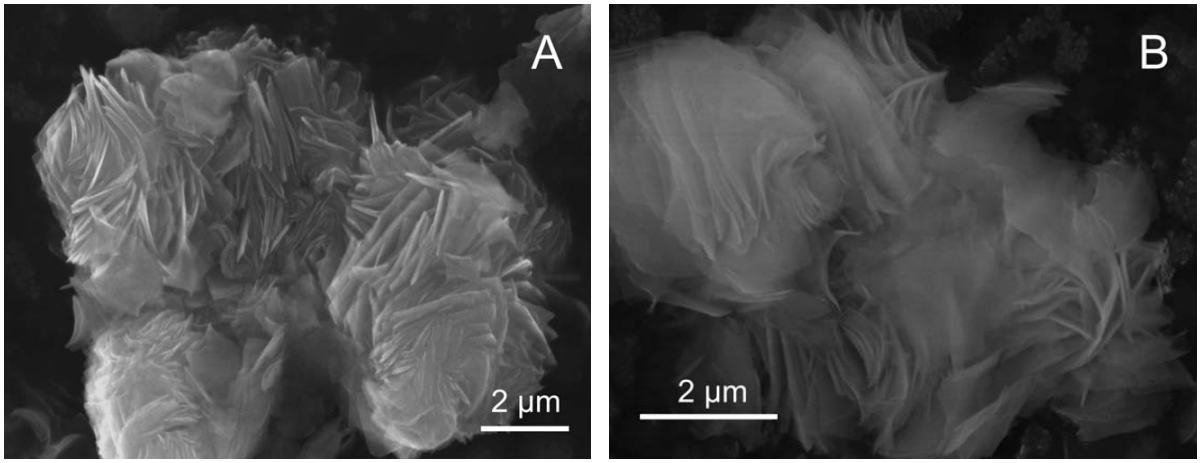

Figure 1 ESEM image of the raw (A) and acid treated (72 h) magadiite (16_Mag) (B).

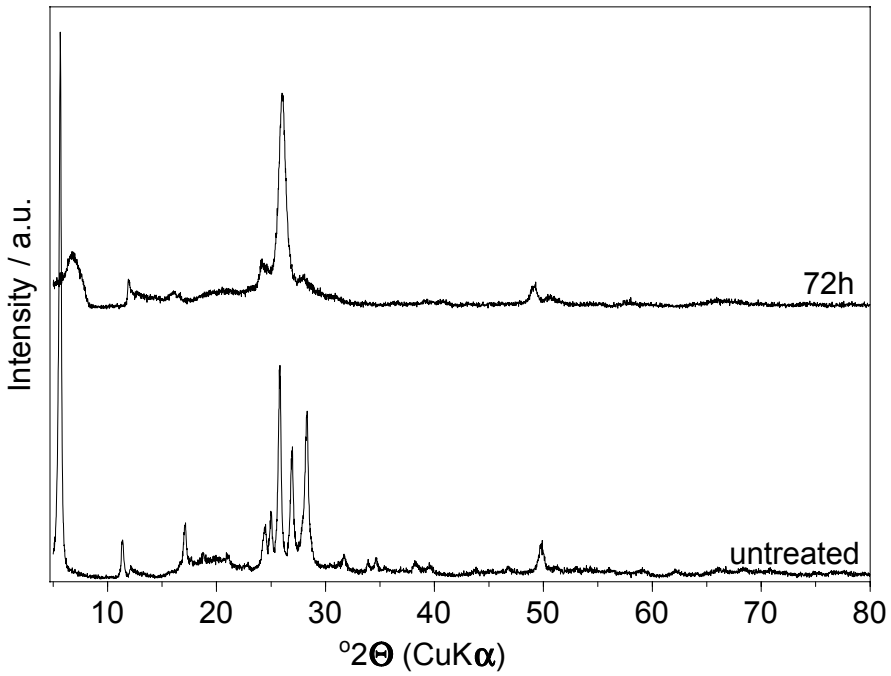

Figure 2 X-ray diffraction analysis (powder sample) of the raw and acid treated material. All peaks originated from magadiite.

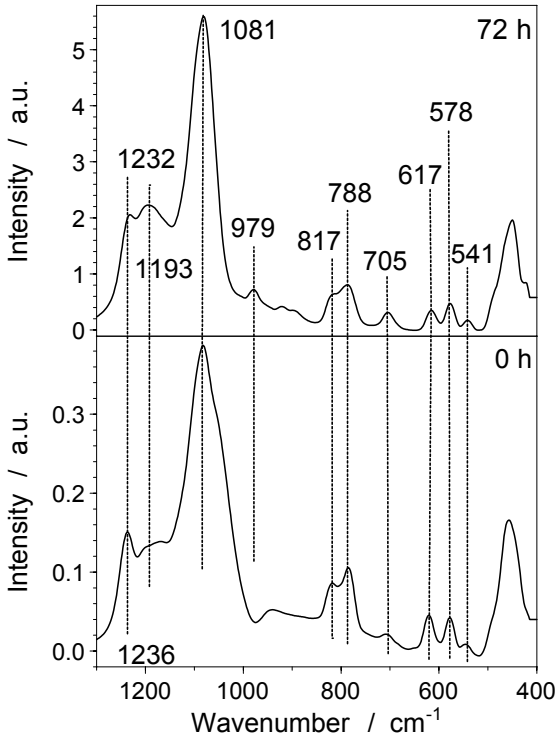

Figure 3 FTIR-spectra.

Appendix

3 Data sheets “Acid treatment”

3.2 Nitrogen adsorption / surface properties

Overview about the surface properties

1. Smectites in Bentonites

Calcigel (1_Calci)

Time [h]	A_E [m^2/g]	A_{MP} [m^2/g]	A_S [m^2/g]	A_{MP} / A_S [%]
0	38	26	64	41
1.5	134	38	172	22
5	237	11	248	4
20	183	32	215	15
72	159	25	184	14
96	153	27	180	15

EXM757 (2_EXM757)

Time [h]	A_E [m^2/g]	A_{MP} [m^2/g]	A_S [m^2/g]	A_{MP} / A_S [%]
0	26	2	28	7
1.5	102	29	131	22
5	134	41	175	23
20	141	40	180	22
72	126	34	159	21
96	123	30	153	20

SWy-2 (3_SWy-2)

Time [h]	A_E [m^2/g]	A_{MP} [m^2/g]	A_S [m^2/g]	A_{MP} / A_S [%]
0	17	7	24	29
20	102	25	127	20
96	105	30	135	22

Volclay (4_Vol)

Time [h]	A_E [m^2/g]	A_{MP} [m^2/g]	A_S [m^2/g]	A_{MP} / A_S [%]
0	20	10	30	33
1.5	63	14	77	18
5	93	7	100	7
20	119	26	145	18
72	110	38	148	26
96	131	21	152	14

WYO (5_WYO)

Time [h]	A_E [m^2/g]	A_{MP} [m^2/g]	A_S [m^2/g]	A_{MP} / A_S [%]
0	24	8	32	25
20	75	12	88	14
96	67	18	85	21

Indian Bentonite (6_IndBent)

Time [h]	A_E [m^2/g]	A_{MP} [m^2/g]	A_S [m^2/g]	A_{MP} / A_S [%]
0	27	2	29	7
1.5	340	37	378	10
5	396	56	452	12
20	391	40	431	9
96	250	62	312	20

Natural hectorite (7_NHec)

Time [h]	A_E [m^2/g]	A_{MP} [m^2/g]	A_S [m^2/g]	A_{MP} / A_S [%]
0	34	15	48	31
1.5	235	45	280	16
5	168	33	201	16
20	111	32	143	22
96	95	27	122	22

2. Kaolinites

Kaolinite Polwhite (13_Pol)

Time [h]	A_E [m^2/g]	A_{MP} [m^2/g]	A_S [m^2/g]	A_{MP} / A_S [%]
0	11	0	11	0
1.5	17	3	21	14
5	26	5	31	15
20	40	6	46	13
72	42	15	57	26
96	42	16	58	31

Kaolinite Kaolex (14_Kaolex)

Time [h]	A_E [m^2/g]	A_{MP} [m^2/g]	A_S [m^2/g]	A_{MP} / A_S [%]
0	22	2	24	8
20	94	20	114	17
96	97	23	120	19

Kaolinite Rogers (15_Rogers)

Time [h]	A_E [m^2/g]	A_{MP} [m^2/g]	A_S [m^2/g]	A_{MP} / A_S [%]
0	23	1	24	4
20	77	15	92	16
96	87	24	111	22

Appendix

3 Data sheets “Acid treatment”

3.2 Peak area in dependence on the chemistry

Comparison between peak area and chemistry of the bentonites SWy-2 and WYO

Treatment conditions: 5 M H_2SO_4 at 80 °C at 20 h and 96 h

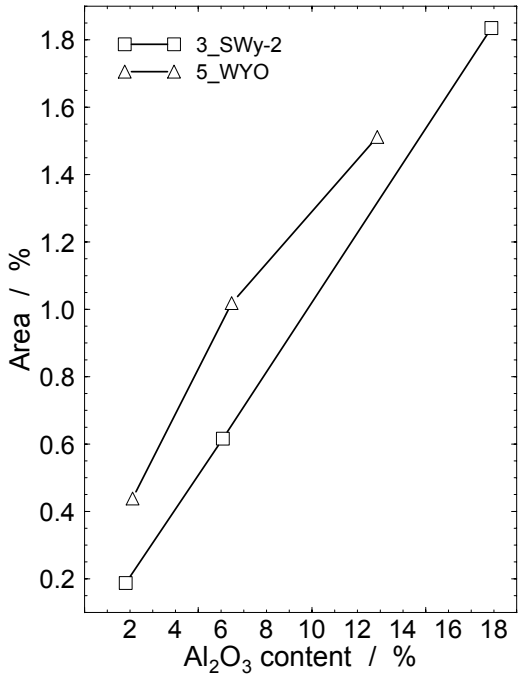

Figure 1 Comparison between unreacted Al content and area of the AlAlOH band (920 cm^{-1}).

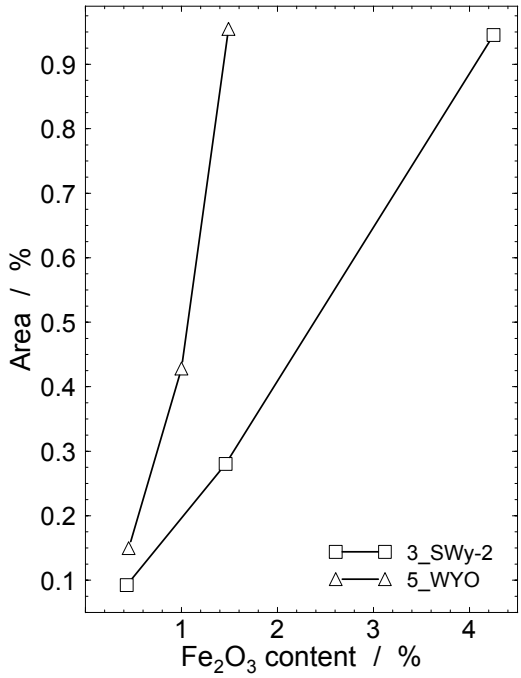

Figure 2 Comparison between unreacted Fe content and area of the AlFeOH band (885 cm^{-1}).

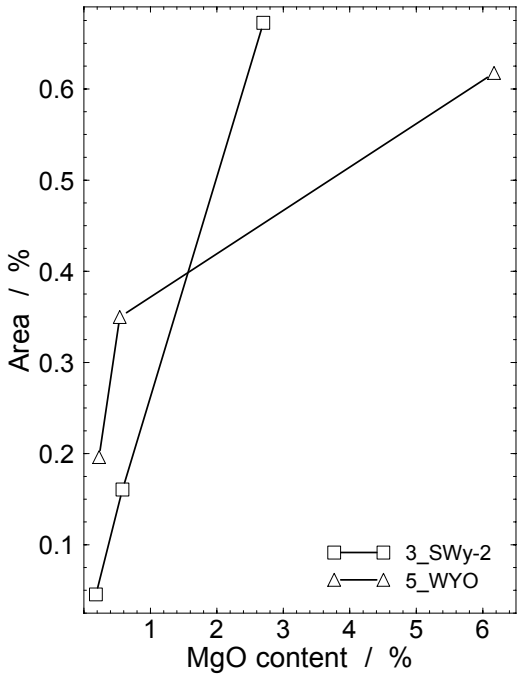

Figure 3 Comparison between unreacted Mg content and area of the AlMgOH band (850 cm^{-1}).

In der Reihe "Karlsruher Geochemische Hefte" (ISSN 0943-8599) sind erschienen:

Band 1: U. Kramar (1993)
Methoden zur Interpretation von Daten der geochemischen Bachsedimentprospektion am Beispiel der Sierra de San Carlos/ Tamaulipas Mexiko

Band 2: Z. Berner (1993)
S-Isotopengeochemie in der KTB - Vorbohrung und Beziehungen zu den Spuren-elementmustern der Pyrite

Band 3: J.-D. Eckhardt (1993)
Geochemische Untersuchungen an jungen Sedimenten von der Galapagos-Mikroplatte:
Hydrothermale und stratigraphisch signifikante Signale

Band 4: B. Bergfeldt (1994)
Lösungs- und Austauschprozesse in der ungesättigten Bodenwasserzone und Auswirkungen auf das Grundwasser

Band 5: M. Hodel (1994)
Untersuchungen zur Festlegung und Mobilisierung der Elemente As, Cd, Ni und Pb an ausgewählten Festphasen unter besonderer Berücksichtigung des Einflusses von Huminstoffen.

Band 6: T. Bergfeldt (1995)
Untersuchungen der Arsen- und Schwermetallmobilität in Bergbauhalden und kontaminierten Böden im Gebiet des Mittleren Schwarzwaldes.

Band 7: M. Manz (1995)
Umweltbelastungen durch Arsen und Schwermetalle in Böden, Halden, Pflanzen und Schlacken ehemaliger Bergbaugebiete des Mittleren und Südlichen Schwarzwaldes.

Band 8: J. Ritter (1995)
Genese der Mineralisation Herrmanngang im Albtalgranit (SE-Schwarzwald) und Wechselwirkungen mit dem Nebengestein.

Band 9: J. Castro (1995)
Umweltauswirkungen des Bergbaus im semiariden Gebiet von Santa Maria de la Paz, Mexiko.

Band 10: T. Rüde (1996)
Beiträge zur Geochemie des Arsens.

Band 11: J. Schäfer (1998)
Einträge und Kontaminationspfade Kfz-emittierter Platin-Gruppen-Elemente (PGE) in verschiedenen Umweltkompartimenten.

Band 12: M. A. Leosson (1999)
A Contribution to the Sulphur Isotope Geochemistry of the Upper Continental Crust: The KTB Main Hole - A Case Study

Band 13: B. A. Kappes (2000)
Mobilisierbarkeit von Schwermetallen und Arsen durch saure Grubenabwässer in Bergbaualtlasten der Ag-Pb-Zn-Lagerstätte in Wiesloch

Band 14: H. Philipp (2000)
The behaviour of platinum-group elements in petrogenetic processes:
A case study from the seaward-dipping reflector sequence (SDRS), Southeast Greenland volcanic rifted margin

Band 15: E. Walpersdorf (2000)
Nähr- und Spurenelementdynamik im Sediment/Wasser-Kontaktbereich nach einer Seekreideaufspülung - Pilotstudie Arendsee -

Band 16: R. H. Kölbl (2000)
Models of hydrothermal plumes by submarine diffuse venting in a coastal area: A case study for Milos, South Aegean Volcanic Arc, Greece

Band 17: U. Heiser (2000)
Calcium-rich Rhodochrosite layers in Sediments of the Gotland Deep, Baltic Sea, as Indicators for Seawater Inflow

In der Fortsetzungsreihe "Karlsruher Mineralogische und Geochemische Hefte" (ISSN 1618-2677) sind bisher erschienen:

Band 18: S. Norra (2001)
Umweltgeochemische Signale urbaner Systeme am Beispiel von Böden, Pflanzen, und Stäuben in Karlsruhe

Band 19: M. von Wagner, Alexander Salichow, Doris Stüben (2001)
Geochemische Reinigung kleiner Fließgewässer mit Mangankiesen, einem Abfallsprodukt aus Wasserwerken (GReiFMan)

Band 20: U. Berg (2002)
Die Kalzitapplikation als Restaurierungsmaßnahme für eutrophe Seen – ihre Optimierung und Bewertung

Band 21: Ch. Menzel (2002)
Bestimmung und Verteilung aquatischer PGE-Spezies in urbanen Systemen

Band 22: P. Graf (2002)
Meta-Kaolinit als latent-hydraulische Komponente in Kalkmörtel

Band 23: D. Buqezi-Ahmeti (2003)
Die Fluidgehalte der Mantel-Xenolithe des Alkaligesteins-Komplexes der Persani-Berge, Ostkarpaten, Rumänien: Untersuchungen an Fluid-Einschlüssen

Band 24: B. Scheibner (2003)
Das geochemische Verhalten der Platingruppenelemente bei der Entstehung und Differenzierung der Magmen der Kerguelen-Flutbasaltprovinz (Indischer Ozean)

Ab Band 25 erscheinen die Karlsruher Mineralogischen und Geochemischen Hefte im Karlsruher Universitätsverlag online unter der Internetadresse

http://www.uvka.de/univerlag/institut.php?fakultaet=1

Auf Wunsch sind beim Karlsruher Universitätsverlag gedruckte Exemplare erhältlich („print on demand").

Band 25: A. Stögbauer (2005)
Schwefelisotopenfraktionierung in abwasserbelasteten Sedimenten - Biogeochemische Umsetzungen und deren Auswirkung auf den Schwermetallhaushalt

Band 26: X. Xie (2005)
Assessment of an ultramicroelectrode array (UMEA) sensor for the determination of trace concentrations of heavy metals in water

Band 27: F. Friedrich (2005)
Spectroscopic investigations of delaminated and intercalated phyllosilicates

Band 28: L. Niemann (2005)
Die Reaktionskinetik des Gipsabbindens: Makroskopische Reaktionsraten und Mechanismen in molekularem Maßstab

Band 29: F. Wagner (2005)
Prozessverständnis einer Naturkatastrophe: eine geo- und hydrochemische Untersuchung der regionalen Arsen-Anreicherung im Grundwasser West-Bengalens (Indien)

Band 30: F. Pujol (2005)
Chemostratigraphy of some key European Frasnian-Famennian boundary sections (Germany, Poland, France)

Band 31: Y. Dikikh (2006)
Adsorption und Mobilisierung wasserlöslicher Kfz-emittierter Platingruppenelemente (Pt, Pd, Rh) an verschiedenen bodentypischen Mineralen

Band 32: F. I. Müller (2007)
Influence of cellulose ethers on the kinetics of early Portland cement hydration

Band 33: H. Haile Tolera (2007)
Suitability of local materials to purify Akaki Sub-Basin water

Band 34: M. Memon (2008)
Role of Fe-oxides for predicting phosphorus sorption in calcareous soils

Band 35: S. Bleeck-Schmidt (2008)
Geochemisch-mineralogische Hochwassersignale in Auensedimenten und deren Relevanz für die Rekonstruktion von Hochwasserereignissen

Schriftenreihe des Instituts für
Mineralogie und Geochemie

Clay minerals show a large variability, e.g., in chemical composition, morphology, layer charge, layer charge density and exchange behaviour. Thus, for technical applications a comprehensive characterisation is essential. The focus of this work was the structural characterisation and modification of different and apparently similar clay minerals, allowing technical applications.

In this study, samples were selected with respect to their layer charge and morphology. Sixteen bulk materials were pre-selected, which contained either swellable clay minerals (smectite, vermiculite) or non-swelling clay minerals (kaolinite, illite, sepiolite, palygorskite, magadiite). A comprehensive characterisation of all materials was carried out.
One topic of this work was a comprehensive determination of layer and edge charge and exchange properties of clay minerals, because the exchange capacity is the most important feature of swellable clay minerals.
In addition to the layer charge, the charges of the edges were investigated using the purified and fractionated material of two smectites (Volclay, Indian Bentonite), one vermiculite and one sepiolite.
A further topic in this study concerned the modification of swellable and non-swelling clay minerals with mineral acids, e.g., HCl and H_2SO_4.

ISSN: 1618-2677
ISBN: 978-3-86644-352-5

www.uvka.de